

2012

Microelectromechanical Actuator and Sensor System for Measuring the Mechanical Compliance of Biological Cells

Markus Hans Gnerlich
Lehigh University

Follow this and additional works at: <http://preserve.lehigh.edu/etd>

Recommended Citation

Gnerlich, Markus Hans, "Microelectromechanical Actuator and Sensor System for Measuring the Mechanical Compliance of Biological Cells" (2012). *Theses and Dissertations*. Paper 1246.

This Dissertation is brought to you for free and open access by Lehigh Preserve. It has been accepted for inclusion in Theses and Dissertations by an authorized administrator of Lehigh Preserve. For more information, please contact preserve@lehigh.edu.

**Microelectromechanical Actuator and Sensor System for Measuring
the Mechanical Compliance of Biological Cells**

by

Markus Hans Gnerlich

Presented to the Graduate and Research Committee
of Lehigh University
in Candidacy for the Degree of
Doctor of Philosophy

in

Electrical Engineering

Lehigh University

January 2012

Copyright

Approved and recommended for acceptance as a dissertation in partial fulfillment of the requirements for the degree of Doctor of Philosophy.

Date

Dissertation Director

Accepted Date

Svetlana Tatic-Lucic
Electrical & Computer Engineering
Lehigh University

Peter Butler
Bioengineering
The Pennsylvania State University

Xuanhong Cheng
Materials Science and Engineering
Lehigh University

Susan Perry
Chemical Engineering
Lehigh University

Marvin White
Electrical & Computer Engineering
Lehigh University

Arkady Voloshin
Mechanical Engineering & Mechanics
Lehigh University

Acknowledgements

Foremost, I would like to thank my wife, Anne, and my family for their support and patience over the years. I have been reminded that there was a lot of patience. It has been a long and twisty path to finally complete my doctorate, but I feel the education of a curious mind never ends. This marks an end that is a new beginning.

I would like to thank my advisor, Professor Svetlana Tatic-Lucic who has supported and advised me with knowledge, candor and humor over the past six years. My committee has also provided indispensable advice during my research: Prof. Peter Butler, Prof. Xuanhong Cheng, Prof. Susan Perry, Prof. Marvin White, and Prof. Arkady Voloshin.

I would like to thank the people at the Sherman Fairchild Center who have provided the support and training without which my research accomplishments would not have been possible: Dr. Floyd Miller, Mr. Raymond Filozof, and Mr. Grant Reed. In addition, Dr. Wenyue (Lydia) Zhang provided the training and introduction to this research project that laid the foundation for my work. I would also like to thank those at Lehigh University who have offered their technical advice and support: Prof. Richard Vinci and Prof. H. Daniel Ou-Yang. I would like to thank my colleagues, Negar Moghimi, Tianyi Zhou, Umar Izhar, Gaoshan Jing, Yaohua Sun, and Kanlun Li. Finally, I would like to thank my undergraduate thesis advisor at the Penn State Bioengineering Dept., Prof. Roger Gaumond, who supervised me during my first serious research project.

My experience at Lehigh University would not have been the same without the Office of Graduate Student Life and the Graduate Student Senate. In particular, Kathleen

Hutnik (Director of Graduate Student Life) has encouraged many of us to strive to make a great community for graduate students at Lehigh. I would also like to thank my students over the years who have made me more thoughtful and open minded. It has been good to see them succeed, as well.

This project was supported by the start-up funds of Professor Svetlana Tatic-Lucic and the Howard Hughes Medical Institute (HHMI) Biosystems Dynamics Summer Institute (BDSI) program. Thanks to the Sherman Fairchild Foundation, the Esty, NJ Zinc Co., and Baldwin Fellowships, as well as the Lehigh University Electrical & Computer Engineering and Bioengineering departments for their financial support.

Contents

Abstract.....	1
Chapter 1: Introduction.....	2
Objectives	2
Significance.....	3
Bone Tissue Summary	3
Mechanical Sensing and Osteogenesis	4
System Overview	7
Piezoresistive Force Sensor.....	7
Electrostatic Actuator	9
Fabrication.....	10
Layout	11
Cell Mechanical Properties	14
Typical Microplate Compression	16
Expected Forces in this Research	18
Chapter 2: Piezoresistive Force Sensor	22
Principle of Operation.....	22
Cantilever Beam Force Sensor	22
Fabrication Methods	22
Lateral Sensing for Cell Mechanics.....	23

Lateral Force Sensor Architecture	24
Modeling	27
Linear Beam Bending	27
Piezoresistors.....	34
Signal to Noise Ratio	36
Fabrication Process and Layout	44
Fabrication.....	44
Layout	45
Estimates of Mechanical Behavior	48
Parametric Calculations	48
FEA Simulation with CoventorWare.....	56
Sensitivity Characterization	65
Cantilever Reference Springs.....	65
Piezo-Driver for Precise Movement	68
Reference Spring Verification.....	71
Sensitivity Measurement in LabView.....	72
Actual Dimensions and Measured Sensitivity	75
Conclusion	77
Chapter 3: Electrostatic Actuator	80

Principle of Operation.....	80
Electrostatic Clamp.....	80
Discrete Stepped Motion.....	81
Operation in Liquid.....	82
FEA Contact Simulation.....	83
Material Properties.....	83
Simulation Results.....	84
Layout.....	86
Design Revision 1: Complete Encapsulation.....	88
Fabrication.....	88
Characterization.....	89
Results.....	91
Design Revision 2: Native Oxide.....	95
Fabrication.....	95
Characterization.....	96
Results.....	98
Conclusion.....	102
Future Work.....	106
Chapter 4: Supporting Electronics.....	108

Force Sensor Driver and Preamplifier	108
Notes	111
Actuator Driver	117
Temperature Regulation	120
On-Chip RTD	120
Temperature-Compensated Current Source	122
Heater Driver	123
LabView Interface	123
Chapter 5: Cell Biomechanics.....	127
Model of Cell Behavior	127
Contact Mechanics	127
Viscoelastic Model	129
Measured Stress Relaxation	132
Tests with On-chip Actuator	132
Test with External Piezo-driver	133
NIH3T3 and MC3T3 Comparison.....	137
Conclusion	142
Bibliography	143
Appendices.....	147

Appendix I: Layout.....	148
Design Rules	148
Resolution Tests of DRIE Silicon	148
Mask Layout.....	151
Appendix II: Fabrication.....	167
Revision 1.....	168
Revision 2.....	195
Equipment and Materials	200
Appendix III: Fabrication Process #1	202
Starting Materials	202
Device Layer Photoresist Patterning (DEVICE mask).....	202
Deep Reactive Ion Etching.....	203
Metal Layer Photoresist Patterning (METAL mask)	203
Metallization and Lift-Off.....	204
Device Undercut.....	204
Insulation Layer Photoresist Patterning (ISOLATION mask).....	205
Device Release	206
Protection Layer & Wafer Dicing	206
Appendix IV: Fabrication Process #2.....	208

Starting Materials	208
Device Layer Photoresist Patterning (DEVICE mask).....	208
Deep Reactive Ion Etching.....	209
Native Oxide Removal.....	209
Metal Layer Photoresist Patterning (METAL mask)	209
Metallization and Lift-Off.....	210
Oxide Pre-release Etch.....	211
Insulation Layer Photoresist Patterning (ISOLATION2 mask)	212
Clean & Harden.....	213
Protection Layer & Wafer Dicing	213
Device Release	214
Prepare for Packaging	215
Addendum: Descum	215
Addendum: Dry Strip.....	215
Appendix V: Fabrication Process – DRIE Configuration	216
STEP 1: 10 D 8MBAR (Thermalization)	216
STEP 2: TEMPO 30S 8MBAR (Temporization)	216
STEP 3: LOWROUGHNESS (Process)	216
Etch Rate Characterization.....	217

Appendix VI: Measured Force Sensor Transducer Widths	218
Appendix VII: Measured Spring Constants	221
Appendix VIII: NIH3T3 Test Data	223
Raw Data and Model Fit Figures.....	223
Tabulated Model Fit Parameters	231
Appendix IX: MC3T3 Test Data.....	234
Raw Data and Model Fit Figures.....	234
Tabulated Model Fit Parameters	238
Publications.....	240
Journals	240
Conferences.....	240
Vita	242

List of Tables

Table 1: Viscoelastic parameters for different cell types using several different experimental techniques (adapted from [49])	15
Table 2: Mechanical properties of osteoblasts (from [47])	15
Table 3: Mechanical properties of fibroblasts (from [47])	16
Table 4: Microplate compression results [49] for avian chick fibroblast cells	18
Table 5: Sources of electronic noise.....	39
Table 6: Summary of parameter effects on sensitivity and signal to noise ratio	44
Table 7: Force Sensor Parameters and Dimensions Summary	48
Table 8: Parametric estimates from simple cantilever beam bending at 1 μ N applied force with $t_r = 1 \mu$ m.	49
Table 9: Parametric estimates from simple cantilever beam bending plus yoke at 1 μ N applied force with $t_r = 1 \mu$ m.	49
Table 10: Parametric estimation of sensitivity at 1 μ N applied force with $t_r = 1 \mu$ m. ...	50
Table 11: Intrinsic noise estimate parameters.....	50
Table 12: Noise estimate for $f_{\min}=0.1$ Hz to $f_{\max}=100$ Hz.	51
Table 13: Noise estimate for $f_0=3000$ Hz and bandwidth of 100 Hz.	51
Table 14: Silicon material properties used in FEA simulation [34].....	57
Table 15: Parametric simulation results from the MemMech mechanical solver (stress).	60
Table 16: Parametric simulation results from the MemMech mechanical solver (displacement).	61
Table 17: Parametric simulation results from the MemPZR piezoresistive solver.....	63
Table 18: Harmonic 1 – Vertical (out of plane) vibration.	64
Table 19: Harmonic 2 – Lateral (xy plane) vibration.....	64
Table 20: Harmonic 3 – Twist along beam axis vibration.....	65
Table 21: Gold wire cantilever specifications using diameter error $\pm 0.25 \mu$ m and length error $\pm 50 \mu$ m.	67
Table 22: nanoScience FCL-5 reference spring cantilever specifications.	68
Table 23: PSM-1000 microscope calibration with Moticam 2300 using 0.5X c-mount.70	
Table 24: LabView internal calibration of the piezo actuator coupled with NI USB-6009 DAQ.	71
Table 25: Measured spring stiffness of fine wire beams.	72
Table 26: Measured force sensor sensitivity.....	75
Table 27: Measured force sensor sensitivity.....	77
Table 28: Measured sensitivity of force sensors ((V/V)/N).	77
Table 29: Bulk mechanical properties of silicon for FEA simulation [34].	84
Table 30: Bulk mechanical and electrical properties of silicon dioxide for FEA simulation.....	84
Table 31: Bulk mechanical properties of soft body for FEA simulation.....	84
Table 32: Predicted pull-in voltages for various electrode separations.....	86
Table 33: Layout parameters of actuator array (revision 1).	87
Table 34: Layout parameters of actuator array (revision 2).	87
Table 35: Statistics of measured displacement (all values in μ m).	101

Table 36: Statistics of measured displacement (all values in μm).	102
Table 37: Measured RTD parameters.	122
Table 38: Gold / Chrome layer thicknesses	122
Table 39: Cell Testing Procedure.	135
Table 40: Nonlinear fit algorithm upper and lower search bounds.	136
Table 41: Summary of a single repeated cell compression.	137
Table 42: Summary of measured NIH3T3 and MC3T3 elastic modulus.	137
Table 43: Measured values for mouse fibroblast (NIH3T3) mechanical properties.	138
Table 44: Reported results for avian chick fibroblast mechanical properties [49].	139
Table 45: Summary of deviation from feature and field in OCG 825	149
Table 46: Summary of etching deviation from photoresist mask.	150
Table 47: Design parameters of all devices dies (revision 1).	153
Table 48: Design parameters of all devices dies (revision 2).	154
Table 49: Silicon-on-insulator (SOI) wafer specifications.	167
Table 50: Fabrication process flow (revision 1).	168
Table 51: Description of DIP pin assignment.	187
Table 52: Wafer SOI_02 resistivity measurement using AT2 test die.	190
Table 53: Measured dimensions for DIE AT2 ($l_s=160 \mu\text{m}$).	192
Table 54: Measured dimensions for DIE AT2 ($l_s=240 \mu\text{m}$).	193
Table 55: Parameters for elastic modulus measurement.	193
Table 56: Wafer SOI_01 silicon elastic modulus (E) measurement using AT2 test die.	194
Table 57: Fabrication process flow (revision 2).	195
Table 58: Wafer SOI_06 resistivity measurement using AT2 test die.	199
Table 59: Materials listing.	200
Table 60: Equipment listing.	201
Table 61: Measured force sensor transducer widths (left side).	218
Table 62: Measured force sensor transducer widths (right side).	219
Table 63: Measured force sensor transducer widths (summary).	220
Table 64: Measured weights for reference cantilever No. 5 at various positions.	221
Table 65: Measured forces (converted from above) for reference cantilever No. 5 at various positions.	222
Table 66: Measured weights for reference cantilever No. 9 at various positions.	222
Table 67: Measured forces (converted from above) for reference cantilever No. 9 at various positions.	222
Table 68: NIH3T3 fit to pure elastic model.	231
Table 69: NIH3T3 fit to pure elastic model.	232
Table 70: NIH3T3 fit to standard linear solid model.	233
Table 71: MC3T3 fit to pure elastic model.	238
Table 72: MC3T3 fit to standard linear solid model.	239

List of Figures

Figure 1: Diagram of bone tissue [2] (left) and detail diagram of transverse section of body of human fibula, decalcified, X 250 [3] (right).	4
Figure 2: First layer (silicon is shown in red) of a single device die which corresponds to mask #1. The entire die is shown on the left, and a close-up is shown on the right. .	11
Figure 3: Second layer (metal is shown in green) of a single device die which corresponds to mask #2. The entire die is shown on the left, and a close-up is shown on the right.	11
Figure 4: Third layer (isolation material is shown in blue) of a single device die which corresponds to mask #2. The entire die is shown on the left, and a close-up is shown on the right.	11
Figure 5: Color coded masks and layout: DEVICE layer is red, METAL layer is green, and ISOLATION layer is light blue. Each device die is 4 mm by 4 mm square.	12
Figure 6: Labeled features in the force sensing and cell trapping regions.	13
Figure 7: Labeled features of the actuator array. During operation, a single pair of anchored electrodes is energized and all suspended electrodes are grounded.	13
Figure 8: A color-coded fabricated BioMEMS chip (4 mm by 4 mm) showing the location of the force sensor (red), actuator array and shuttle (blue), DEP electrodes (green), temperature sensor (violet), and heater ring (orange).	14
Figure 9: Standard linear solid model of a viscoelastic material	16
Figure 10: Schematic of the system for measuring the mechanical compliance of a biological cell.	19
Figure 11: Plot of displacement (Δd) and corresponding reaction force (F) for expected upper and lower limits of cell elastic modulus. The diameter of the cell is 15 μm and the Poisson ratio is 0.5.	19
Figure 12: Plot of displacement (Δd) and corresponding reaction force (F) for expected upper and lower limits of cell elastic modulus. The diameter of the cell is 15 μm and the Poisson ratio is 0.5.	20
Figure 13: Expected elastic modulus (E) as a function of minimum detectable force for various cell compressions ($\Delta d=1,2,3$ or 4 μm). The diameter of the cell is 15 μm and the Poisson ratio is 0.5.	21
Figure 14: The force sensor is based on a pair of cantilevers each connected to a central yoke which allows each cantilever to bend in a fixed-free configuration.	25
Figure 15: Force applied to the center of the force sensor creates compressive and tensile stress in the piezoresistor regions.	26
Figure 16: The electrical equipotentials in the full bridge are color coded and labeled, and equivalent resistors are labeled.	26
Figure 17: Piezoresistor pairs (e.g. R_{1A} and R_{1B}) act in parallel, and each pair forms one quarter of a full bridge.	26
Figure 18: Force sensor mechanical diagram with labels.	28
Figure 19: The dimensions for the cantilever beam with periodic holes are shown with a top-down view (left) and a cross section of the beam (right).	29

Figure 20: The dimensions for the cantilever beam are shown in a in the transducer region with a cross section (top) and a top-down view (bottom).....	30
Figure 21: The piezoresistors in the force sensor are connected in a full bridge configuration and the output of the sensor is taken as V/V_b so that $V/V_b=\Delta R/R$	36
Figure 22: Piezoresistive coefficient π_{11} as a function of doping concentration in n-type silicon [22]. Figure adapted from [23] (see fig 3 at 300 Kelvin).	38
Figure 23: Fit for lookup table of piezoresistive coefficient π_{11} as a function of doping concentration in n-type based on previous figure.	38
Figure 24: Silicon resistivity and doping concentration [32]	41
Figure 25: Carrier concentration values (figures adapted from [31], Table 10 (pg. 34) and Table 14 (pg. 40) and [32]).	42
Figure 26: Force sensor mechanical diagram with typical dimensions (in micrometers).	45
Figure 27: Estimated sensitivity (left) and SNR (right) of the force sensor as a function of applied voltage and silicon resistivity.	53
Figure 28: Estimated maximum temperature rise of the force sensor as a function of applied voltage and silicon resistivity.	54
Figure 29: Estimated sensitivity (left) and SNR (right) of the force sensor as a function of the cantilever beam length and the piezoresistive element length.	54
Figure 30: Estimated sensitivity (left) and SNR (right) of the force sensor as a function of the piezoresistive element width and the piezoresistive element length.	55
Figure 31: Estimated sensitivity (left) and SNR (right) of the force sensor as a function of parasitic trace resistance and silicon resistivity.	56
Figure 32: Illustration showing the primary and secondary flats of {100} and {111} wafers for both n-type and p-type doping (SEMI M1-0302) [35].	57
Figure 33: Illustration identifying various crystal planes in a wafer of {100} orientation [35].	58
Figure 34: A load of 0.5 μN was applied to the front face of the cantilever (labeled in white, left side) which corresponds to 1 μN for both halves of the model. The outer faces of the three rectangular blocks at the base of the cantilever are fixed in all directions (labeled in white, right side).	59
Figure 35: Representative results of stress in the transducer region for 1 μN load. The beam length is 450 μm and the transducer length is 32 μm . The height of the structure is 10 μm , and it is fabricated from highly doped n-type silicon.	59
Figure 36: An XY slice through the transducer region of the previous figure. The figure has been exaggerated in the y-direction to show the stress distribution in the 1 μm wide transducer region can be seen.	60
Figure 37: Representative results from the piezoresistive solver showing the applied voltage potential.	62
Figure 38: Representative results from the piezoresistive solver showing the resulting current density while under stress.	62
Figure 39: Representative results for the first three modes of vibration where the beam length is 450 μm and the transducer length is 32 μm	63
Figure 40: Gold bonding wire attached to a tungsten probe tip which can be mounted in a probe station micromanipulator.....	66

Figure 41: Gold bonding wire cantilever reference of length 4910 μm and width 25 μm	66
Figure 42: Mounting diagrams for SUSS MicroTek PH120 with Physik Instrument P-216.4S piezo actuator (all measurements in mm).	69
Figure 43: A piezo actuator mounted to the micromanipulator using a machined aluminum clamp.	69
Figure 44: Screenshot from the piezo controller portion of the LabView control panel.	73
Figure 45: A typical force sensor measurement while it undergoes loading and loading with a calibration cantilever of known spring constant. Smooth unloading and loading without sudden changes in applied force or excessive noise indicate good mechanical contact.	73
Figure 46: Typical sensitivity plot in LabView showing repeated loading and unloading.	74
Figure 47: Typical SEM inspection of the force sensor transducer area (Wafer SOI 02, Die A39 - right).	76
Figure 48: Typical SEM inspection of each of the force sensor transducer beam widths on one side (Wafer SOI 02, Die A39 - right).	76
Figure 49: Predicted sensitivity based on beam bending model.	78
Figure 50: Predicted sensitivity based on FEA simulations.	79
Figure 51: Actual measured sensitivity.	79
Figure 52: Angled electrostatic clamp which makes use of a small-gap starting zone on the right to reduce the required pull-in voltage.	81
Figure 53: The key components of an electrostatic clamp are shown before actuation (left) and after actuation (right).	82
Figure 54: CoSolveEM results of $\frac{1}{2}$ symmetric model at 50V with 6 μm designed displacement shown without geometry scaling (left) and with geometry scaling (right). The electrodes are 500 μm long; the suspension beams supporting the shuttle are 6 μm wide, 10 μm high and 600 μm long; and the shuttle itself is 350 μm long and 40 μm wide.	85
Figure 55: Actuator mechanical diagram with labeled dimensions.	86
Figure 56: A central shuttle surrounded by an array of electrostatic clamps which translate their forward displacement to the shuttle. The separation of each pair of clamps varies, but the distance to the shuttle is always 2 μm	88
Figure 57: SEM micrograph of central shuttle and surrounding electrostatic actuators. The fixed actuators are encapsulated with AZ 4035 negative photoresist.	89
Figure 58: The black box on this image shown the region of interest captured in a series of time-stamped images while the actuators are tested at various voltages.	90
Figure 59: A small region of interest is defined (see top right) where each line of the image region can be averaged together to form a one-dimensional trace of the brightness (see bottom right). The dark edges of the two faces can be programmatically found (see red circles in bottom right).	91
Figure 60: A typical test result showing the behavior of one of the actuator pairs (no. 3) . The plates require 60 volts to clamp shut completely, at which point the shuttle moves forward repeatedly by 2.3 μm	92

Figure 61: Designed vs. actual displacement for devices having a 4 μm wide moving electrostatic plate and a minimum gap of 2 μm . Error bars indicate standard deviation and the value is shown below each point (N=6 devices). 93

Figure 62: Designed vs. actual displacement for devices having a 6 μm wide moving electrostatic plate and a minimum gap of 2 μm . Error bars indicate standard deviation and the value is shown below each point (N=6 devices). 94

Figure 63: Designed vs. actual displacement for devices having a 6 μm wide moving electrostatic plate and a minimum gap of 4 μm . Error bars indicate standard deviation and the value is shown below each point (N=6 devices). The displacement “droop” at points 6 and 7 are due to incomplete clamping of the actuator pairs at the maximum voltage of 100V DC. 94

Figure 64: Second generation layout based on 6 μm wide springs. DEVICE layer is gray, METAL layer is yellow, and ISOLATION layer is blue. 96

Figure 65: Second generation layout based on 4 μm wide springs. DEVICE layer is gray, METAL layer is yellow, and ISOLATION layer is blue. 96

Figure 66: A typical image captured during the actuator test. Each original in the stack (left) is sequentially loaded into MATLAB, and a 200 px by 400 px region of interest is defined (middle). Next, the image is converted to grayscale followed by 8X oversampled and histogram normalized (left). 97

Figure 67: One-dimensional trace obtained by taking the average of the intensity of each row of pixels in the image. The feature extraction finds the edges of gap by looking for the bright area in the middle (green circle), and then finding the local minima (red circles) in the adjacent areas that are below a dark level threshold (blue circles). 97

Figure 68: The actuator array on die B63 (Wafer SOI_06), which is based on 6 μm wide springs. 98

Figure 69: The actuator array of Wafer SOI_06 Die A06, which is based on 4 μm wide springs. 99

Figure 70: Measured displacement during sequential actuation (left) and the average measured displacement versus designed displacement (right).100

Figure 71: Measured displacement during sequential actuation (left) and the average measured displacement versus designed displacement (right).101

Figure 72: Critical electrostatic actuation frequency at selected values of b/g (directly from [36]).104

Figure 73: Minimum gap where screening effects do not dominate at 2 MHz and 20 MHz (native oxide thickness b=2nm and oxide permittivity $\epsilon_{\text{ox}}=4$). Conductivity of 1 $\mu\text{S/cm}$ on the left corresponds to very pure water, and 1000 $\mu\text{S/cm}$ on the right corresponds to typical biological media.105

Figure 74: Proposed actuator array which adds mechanical stops in a compact layout.106

Figure 75: Close-up of mechanical stops which limit the minimum gap to 2 μm while providing 1 μm forward displacement to the moveable shuttle at the left.107

Figure 76: Schematic of force sensor driver and preamplifier circuit.109

Figure 77: Simulated signal levels (top), signal gains (middle), and the proportional bridge signal which is comparable to $\Delta R/R_0$ (bottom).110

Figure 78: Wiring and Shielding diagram for NI PCI-6225 DAQ break-out box (NI SCC-68) and custom PCB. The six-wire cable for analog signals is IEEE 1394 firewire (double-shielded, 8-inches), and the 14 wire cable for digital signals is a shielded ribbon cable (18-inches).	114
Figure 79: The digital control lines from the ADC are buffered with an N-channel MOSFET transistor before connecting to the actuator control transistors (Q1 and Q2 below).	118
Figure 80: Each actuator pair is driven by a single high frequency voltage source, but the signal to each actuator pair is regulated by a set of NPN pull-down transistors.	118
Figure 81: On-state versus off-state comparison of the actuator driver showing the voltage at the transistors Q1 and Q2.	119
Figure 82: On-state versus off-state comparison of the actuator driver showing the voltage after removing the DC component.	119
Figure 83: On-state versus off-state comparison of the actuator driver showing the expected voltage at the surface of the electrostatic electrodes.	120
Figure 84: Typical RTD resistance for chips from wafer SOI 02 as a function of temperature. The RTD is made from thin film gold with a chrome adhesion layer.	121
Figure 85: Typical RTD resistance for chips from wafer SOI 06 as a function of temperature. The RTD is made from thin film gold with a chrome adhesion layer.	121
Figure 86: LabView process flow showing inputs, outputs, user display and user input (part 1).	124
Figure 87: LabView process flow showing inputs, outputs, user display and user input (part 2).	125
Figure 88: LabView front panel.	126
Figure 89: Two models of viscoelastic material: a Kelvin-Voigt unit (spring in parallel with dashpot) in series with a second spring (right) or a Maxwell unit (spring in series with dashpot) in parallel with a second spring (left).	129
Figure 90: A single MC3T3 cell is compressed by 1.7 μm in 10% sucrose using the on-chip actuator array.	133
Figure 91: Four compression tests on MC3T3 cells using the on-chip actuator in 10% sucrose. The difference between Force 1 (with cell) and Force 2 (without cell) does not reveal useable measurements of forces on the cell due to the strong interference.	133
Figure 92: NIH3T3 cell (16.4 μm diameter) compressed by 3.7 μm (SOI 06 A47, Number 2, 20110708_122341).	134
Figure 93: Bulk elastic modulus (E) of NIH3T3 and MC3T3 cells derived by fit to a purely elastic contact model.	138
Figure 94: Equilibrium elastic modulus (E_1) of NIH3T3 and MC3T3 cells derived by fit to a viscoelastic (SLS) contact model.	140
Figure 95: Elastic modulus (E_2) of NIH3T3 and MC3T3 cells derived by fit to a viscoelastic (SLS) contact model.	140
Figure 96: Viscosity (η) of NIH3T3 and MC3T3 cells derived by fit to a viscoelastic (SLS) contact model.	141
Figure 97: Relaxation time (τ) of NIH3T3 and MC3T3 cells derived by fit to a viscoelastic (SLS) contact model.	141

Figure 98: OCG 825 photoresist (positive) resolution characterization showing slightly narrower lines and wider trenches than present on the mask.	149
Figure 99: DRIE resolution characterization showing very little change in size (features become ridges, and field becomes trenches) during the 10 minute etching.	150
Figure 100: The location of each numbered die on the wafer. Each die number is unique to a particular design, but some are duplicated across the 4 quadrants (A,B,C,D).....	152
Figure 101: DEVICE mask (same for revision 1 and revision 2) layout for 3-inch wafer (4-inch quartz AR chrome mask). Wafer flat alignment mark is visible at the bottom.	155
Figure 102: METAL mask (same for revision 1 and revision 2) layout for 3-inch wafer (4-inch quartz AR chrome mask).	156
Figure 103: ISOLATION mask (revision 1) layout for 3-inch wafer (4-inch quartz AR chrome mask).....	157
Figure 104: ISOLATION mask (revision 2) layout for 3-inch wafer (4-inch quartz AR chrome mask).	158
Figure 105: Precision alignment marks are positioned at the edges of the wafer.....	159
Figure 106: Precision alignment mark that includes an inverted cross and Vernier scales [55].	160
Figure 107: Typical layout showing DEVICE layer in grey and METAL layer in yellow.	161
Figure 108: Typical device die layout showing DEVICE layer in grey, METAL layer in yellow, and ISOLATION layer in blue.	162
Figure 109: Test Die #1 for piezoresistive constant which was based on beam stretching induced by an electrostatic clamp.	163
Figure 110: Test Die #2 for bulk resistivity (right), critical dimensions (center) and silicon elastic modulus (left) [56].....	164
Figure 111: Test die #3 for resolution (line & spacing).	165
Figure 112: Test die #4 containing a piezoresistive full bridge.	166
Figure 113: SU-8 3010 T-Topping with 16 second dose (left) 8 second dose (right).	171
Figure 114: SU-8 3010 (16 sec dose / 1 min develop) where "cobwebs" are visible in narrow trenches at standard development time.	171
Figure 115: SU-8 3010 (16 sec dose / 5 min develop) where longer development time does not improve resolution.	172
Figure 116: SU-8 3010 (16 sec dose / 15 min develop) where longer development removes more material but does not eliminate "cobweb" effect.	172
Figure 117: SU-8 3010 (16 sec dose / 15 min develop) where a set of four SU-8 lines have fused together.....	173
Figure 118: SU-8 2015 (8 sec dose / 1 min develop) formulation has similar resolution limitations as SU-8 3010.	173
Figure 119: SU-8 2015 (12 sec dose / 1 min develop) formulation has similar resolution limitations as SU-8 3010.	174
Figure 120: SU-8 2 (12 sec dose / 1 min develop) formulation has similar resolution limitations as SU-8 3010.	174
Figure 121: AZ n4035 with 6 second exposure was found to have clear trenches but negative sidewalls which left the bottom of encapsulated structures exposed.	175

Figure 122: AZ n4035 with 10 second exposure was found to have straight sidewalls but residue left in trenches.	175
Figure 123: Silicon block after DRIE, metal and oxide pre-etch with 5:1 BHF for 10 min.	176
Figure 124: Device wafer (SOI) showing unreleased structures after bulk silicon etch and Cr/Au metal lift-off.	177
Figure 125: Close-up showing transducer region of the force sensor; the thin transducer beams are 0.6 μm wide (left).	177
Figure 126: Close-up of actuator array region before encapsulation showing zip-mode electrostatic actuators and central shuttle (right).	178
Figure 127: A typical chip from wafer SOI 01.	179
Figure 128: Typical results from the actuator region on wafer SOI_01.	179
Figure 129: Actuator region from wafer SOI_01 showing straight sidewalls and clear trenches. An 8 second exposure was found to be optimal. Partially etched buried oxide layer is shown beneath the silicon device layer structures.	180
Figure 130: SOI_01 transducer region.	180
Figure 131: SOI_01 Alignment mark with 1 μm Vernier scales. Alignment to within 1 μm between all layers was achieved.	181
Figure 132: SOI_01 DEVICE Layer line (left) and spacing (right) test structures.	181
Figure 133: SOI_01 METAL Layer line (left) and spacing (right) test structures.	181
Figure 134: SOI_01 ISOLATION Layer line (left) and spacing (right) test structures.	182
Figure 135: A typical device die following the last release step, but before wafer dicing.	183
Figure 136: Over-etch on wafer SOI 02, Die A08 transducer region (1 μm mask width) following final release step.	184
Figure 137: A hairline crack is visible in an over-etched 1 μm beam, but 2 μm beams do not suffer from is problem.	184
Figure 138: Following dicing with 0.003 inch (76 μm) blade. The wafer was then manually broken into individual chips with a pair of tweezers.	185
Figure 139: Each chip is mounted in a 28-bin empty cavity dual-inline-package (DIP).	186
Figure 140: Wire bonding diagram for the chip in a 28-pin DIP.	187
Figure 141: A blunt needle was filled with Dow-Corning Sylgard 184 (silicone elastomer) and used to encapsulate each chip.	188
Figure 142: A typical 28-pin DIP following PDMS encapsulation and final packaging.	189
Figure 143: Die T2 which contains a resistivity test structure on the right side.	190
Figure 144: Die T2 which contains resistivity test structure on the left side as well as test structures for elastic modulus. A close up of one of the spring-and-plate elastic modulus test structures is shown on the right.	192
Figure 145: Corner of silicon actuator with SU-8 encapsulation showing DRIE scallops and typical sidewall profile.	197
Figure 146: Structures to be free-standing are not encapsulated (such as this electrostatic actuator) while everything else is encapsulated in SU-8.	197

Figure 147: PDMS was carefully placed on the chip while it was heated using the on-chip heater.....	198
Figure 148: On-chip heating helped cure the PDMS more rapidly as it neared the center of the chip.	198
Figure 149: A completed chip with PDMS encapsulation and polypropylene dish.	199
Figure 150: Etch rate on a <100> silicon wafer as a function of trench width. OCG 825 photoresist was used as an etch mask with the LOWROUGHNESS process described above.....	217
Figure 151: The spring constant of a specially prepared fine gold wire is verified using a CAHN C-30 microbalance in 0.000 mg range setting.	221

Abstract

An integrated biological microelectromechanical system (BioMEMS) has been developed for *in vitro* cell biomechanics experiments. This system combines a lateral force sensor, an electrostatic actuator array, an on-chip heater, resistance temperature detector and cell positioning dielectrophoresis electrodes in a fully submersible and reusable 4 mm by 4 mm chip. All mechanical structures, including the piezoresistive elements in the force sensor, are defined by a single mask on a silicon-on-insulator (SOI) wafer without the need for a patterned doping or annealing step. The optimal design of this force sensor is examined, as well as the sensitivity characterization results from fabricated devices. The operation of the electrostatic actuator array is also examined in the liquid environment. Finally, a calibrated force sensor is used to measure the reaction forces of suspended mouse fibroblast cells (NIH3T3) and osteoblast cells (MC3T3) during compression, and the data is fit to a combined viscoelastic-contact model.

Chapter 1: Introduction

Objectives

The objective of this research is to measure the mechanical response of a single cell to a step compression. This response will be measured as a reaction force during the step displacement, which will allow an estimate of the elastic modulus and viscosity of the interior of the cell once the force curve has been fit to a viscoelastic model. This system is targeted towards the development of a diagnostic device which can apply a pre-defined mechanical compression to a cell and measure the reaction force signature to be used as a mechanical biomarker. Although this device does not produce a simulation of *in vivo* conditions, it is intended to extract useful information from single cells in a way that can be adapted to a high-throughput or highly paralleled testing apparatus. We are investigating whether this diagnostic information is related to diseases in which mechanotransduction in cells may play a role. Bone tissue cells are of particular interest due to their apparent mechanical sensing ability and the important role they may play in osteoporosis.

There are a number of constraints which make measurement of forces on cells difficult. First, cells are very soft, requiring sensitive force sensors that operate while submerged in liquid (see discussion below and Figure 12). Second, operation in a conductive liquid introduces undesirable parasitic resistances, requiring standard MEMS designs to be adapted to this environment. Third, the living cells require maintenance of on-chip temperature at 37 °C, and the various designs must generally be constrained to low-power to limit self-heating.

Significance

Bone Tissue Summary

Bone tissue responds to its mechanical environment, and it has the remarkable ability to become stronger in response to exercise. However, the exact mechanism that bone tissue is able to sense its mechanical environment and respond with increased bone density is not well understood. For an excellent review of the subject the reader is directed to “Mechanical Strain and Bone Cell Function: A Review” [1]. Bone tissue is comprised of bone cells, as well as a structural matrix of protein (collagen) and minerals (hydroxyapatite). A balance between the deposition and absorption of the structural matrix is maintained between osteoblasts (which deposit collagen and hydroxyapatite) and osteoclasts (which break down hydroxyapatite). The life of an osteoblast cell is complex. It begins as an osteoprogenitor cell in the bone marrow, but the cell differentiates into an osteoblast under the influence of certain growth factors. The bone generating osteoblast cells eventually become trapped in the bone matrix, after which they are known as osteocytes and stop secreting the bone matrix. As shown in Figure 1, osteocytes are interconnected through very small channels (canaliculi) and surround larger interstitial pathways (Haversian canals).

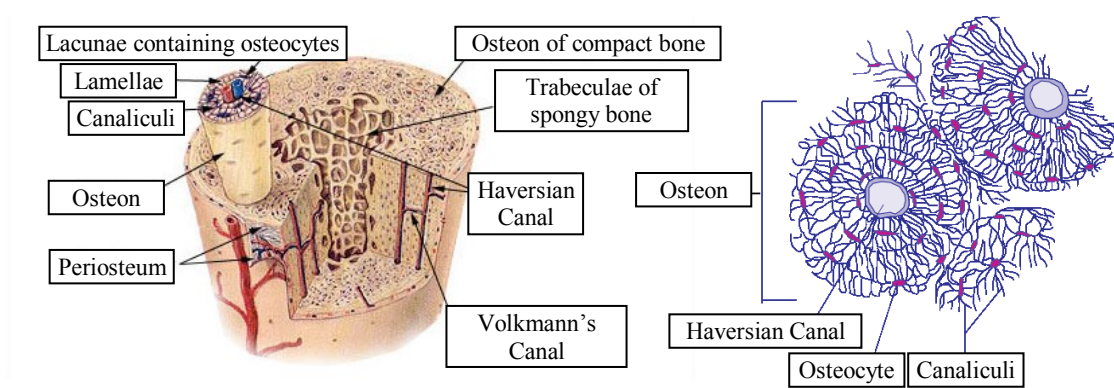


Figure 1: Diagram of bone tissue [2] (left) and detail diagram of transverse section of body of human fibula, decalcified, X 250 [3] (right).

In human beings, bone tissue becomes weaker if the body is deprived of impact exercise such as tennis or jogging. This may affect disabled people and hospital patients, but also astronauts in low gravity environments. Furthermore, some humans lose bone density and develop osteoporosis as they grow older, since they are unable to maintain the same bone density given the same level of physical activity that they had when younger. This may be simply caused by an age-related decrease in the total number of osteoblast cells in bone tissue [5], but it theoretically may also be caused by an age-related decrease in the ability of bone tissue to sense and respond to mechanical stimuli. The mechanism of how bone tissue senses and responds to mechanical conditions is of significant scientific interest.

Mechanical Sensing and Osteogenesis

A number of realistic possibilities could exist by which bone strength could be controlled by a person's activity. One possibility is that the rate of osteoblast deposition is increased or the rate of osteoclast resorption is decreased in response to activity. Another possibility is that the rate of deposition and resorption of individual cells is not affected, but bone tissue under stress somehow recruits osteoblasts to increase the total

capacity of bone tissue generation. A third possibility is that the body can regulate nutrients and energy used by osteoblasts in response to exercise, thereby increasing osteoblast activity.

From an engineering standpoint, it is interesting to think where the control levers for this system could be located and where the boundaries of the osteoblast or osteoclast cells lie with respect to the functional activity. Instructions to alter the osteoblast / osteoclast balance of deposition / resorption could be based on internal cell signaling, extra cellular signaling, or an increase or decrease of available minerals / energy to the bone cells. The extra cellular signals could be produced directly by cells in nearby tissue or by a larger control system in the body. The options can be explored by with different possible answers to the following question:

Can osteoblasts control bone density by directly sensing their mechanical environment?

1. Yes, osteoblasts can directly sense mechanical forces inside their cell body while embedded in bone tissue.
 - a. *Possibility A:* In addition to this sensing, the sensitivity of the strain measurement is dependent on the stiffness of the cell, which implies that the cytoskeleton is involved in the mechanical transduction.
 - b. *Possibility B:* Although this sensing occurs, the sensitivity of the strain measurement is not dependent on the stiffness of the cell, which implies that the cytoskeleton may not be involved in the mechanical transduction.
2. No, the osteoblasts cannot directly sense mechanical loading while embedded in bone tissue.
 - a. *Possibility A:* There is some other structure in bone tissue that can do this, and it somehow signals the osteoblasts.
 - i. Local signaling occurs directly between sense structure and bone cell through a released chemical factor (paracrine signaling).
 - ii. Signaling from the sense structure to the bone cell is mediated through a broader system in the body.

- b. *Possibility B*: The body can sense stress / strain in an indirect way
 - i. By sensing pain in joints and muscles, which is mediated through the central nervous system.
- c. *Possibility C*: The body cannot sense stress / strain either.
 - i. Instead it uses information related to activity and fatigue to manage bone density.

Existing research has already narrowed the possibilities by providing some counter-evidence to a few of the options. In particular, options 2.b. and 2.c. are unlikely. Research involving baseball players has shown that hypertrophy of bone tissue occurs in the playing arm only [1] and also that animals with higher than ordinary loading applied to a limb will experience hypertrophy in the bone tissue of that limb [7][1]. In addition, it has been well established that impact loading induces a morphological change where static loading does not [1]. This research demonstrates that a certain kind of mechanical loading – and not necessarily exercise – causes bone hypertrophy.

Currently, the most likely explanation is that the mechanical sensing occurs directly within bone tissue, and a control signal is sent from the mechanical sensing unit to the osteoblast / osteoclast so that increased impact loading results in increased bone tissue. Also, the search is focused on the individual osteoblast / osteoclast cells because there are no known innervations and nociceptors in bone tissue (which might be similar to pain sensory cells) that provide input to a central nervous system mediated response (option 2.b.). In particular, the osteoblast cell is a promising candidate in which the entire mechanical sensing / internal signaling / bone tissue production loop could be located (options 1.a. and 1.b.). Studies of osteoblasts *in vitro* have shown increased bone matrix formation in response to mechanical stimulation [8].

A small specialized cell may exist whose purpose is to sense mechanical loading and produce paracrine signals in nearby bone tissue to recruit osteoblasts / inhibit osteoclasts or modulate activity in nearby osteoblasts / osteoclasts (option 2.a.). It is possible that the osteocytes rather than the osteoblasts can directly sense mechanical impact loading by way of pressure transmitted through the fluid filled network of canals in bone [8][9]. In addition, chondrocytes from bovine intervertebral discs subjected to compressive strain of various frequencies (dynamic compression) have been shown to alter the production of the extra-cellular matrix as a function of the strain amplitude and maturity of the subject [6].

System Overview

Piezoresistive Force Sensor

Robust force sensors with high sensitivity and low minimum detectable force are needed for cellular biomechanics applications where forces are typically below 100 nN [49]. Many types of transducers exist which can convert a force into an electrical signal.

- Capacitive: the force is converted to a small movement, and the distance between two electrodes can be accurately measured by the capacitance between them.
- Piezoresistive: the force is converted to a stress in a special material which exhibits piezoresistivity, and the change in the material resistivity can be measured through a direct resistance measurement
- Strain: the force causes a thin film to stretch, and the change in length can be measured through a direct resistance measurement

- Optical: the force is converted to a small movement, and the movement causes a beam of light to deflect, which can be measured with a light sensitive detector

For this particular application, where the force sensor is to be submerged in electrically conductive cell medium, the transducer itself must be either isolated from the environment or designed to be immune to interference from the environment. The previous generation design [10] used an SU-8 cantilever with a thin film metallic strain gauge, but subsequent fabrication and testing showed that interference from the environment caused measurement problems. For instance, the exposed metallic strain gauge not only measured the strain in the metal trace, but also excessive environmental interference. Possible sources of this interference were the temperature of the environment, and fluid flow as the heat (due to self-heating) was transported away from the immediate surroundings.

The ideal situation would be immunity from all these sources of interference. Of the above four transduction methods, piezoresistive is the most robust when the sensor is exposed directly to the hostile environment. A capacitor would be short circuited by the conductive cell medium. Light from optical methods would need to shine through the cell medium, and the light emitter and sensor would be difficult to integrate on-chip. The metal strain gauge exhibits from relatively low sensitivity compared to a semiconductor piezoresistor of similar dimensions. By using a single material – highly doped silicon – as both the piezoresistor and the structural material of the entire chip, the force sensor could be easily integrated. The piezoresistive elements would be more

conductive than the environment, and naturally develop an insulating native oxide thus reducing interference.

Electrostatic Actuator

In addition to precise force detection, precision motion is important for cell biomechanics experiments since it is the combined measure of force and displacement that determines the measure of stiffness. A cell is compressed by a specified amount (a so-called controlled strain environment), while the corresponding reaction force is measured. These measurements and their fit to a model of cell behavior are discussed in detail in Chapter 5: Cell Biomechanics. Numerous experiments using this basic methodology have been carried out [47]. The uncertainty in the compression displacement and the uncertainty in the force measurement both add to the overall uncertainty of the stiffness measurement.

Two general methods to achieve precision motion exist. One method uses a position sensor to monitor actuator displacement, and this information can be incorporated into a feedback loop – the ubiquitous servo motor is a prime example. On the other hand, an actuator can incorporate predefined mechanical stops so that it may move repeatedly to set positions without the need for feedback control – a stepper motor exemplifies this strategy.

Electrostatic MEMS actuators have proven to be well suited for a variety of applications when the operational environment is air or vacuum. Recently, electrostatic comb-drive actuators have been demonstrated that work in liquids as well, as long as a high-frequency driving voltage is applied [36]. In addition, an electrostatic comb-drive

driven at high-frequency has been used for cell biomechanics studies [37]. Electrostatic actuators which utilize plates that clamp together are an alternative to comb drives. Two examples are a zip-mode actuator with a shuttle that offers continuous motion [38] and a single-electrode cascading electrostatic clamp which offers motion in discrete steps [39].

The electrostatic MEMS actuator described here uses a high-frequency driving voltage and operates in liquids, but makes use of a series of independent electrostatic clamps to provide precise stepped motion. Since the controlled strain condition that is applied to a cell is a repeatable step displacement and does not need to be continuously variable, the added complexity of a feedback sensor and control loop is unnecessary.

Fabrication

The fabrication is based on a 3-mask process which is described in detail in Appendix I: Layout. First, the device layer is formed in highly-doped N-type silicon by deep-reactive-ion-etching (DRIE) using a photoresist mask (see Figure 2). This forms all the function elements of various parts of the MEMS chip. Next, a layer consisting of gold with a thin layer of adhesion metal is patterned using lift-off, and this forms the interconnects between the functional elements and the bonding pads for off-chip connections (see Figure 3). Finally, a special electrical isolation layer made from an electrically insulating photopatternable material covers all areas that do not have free-standing mechanical parts (see Figure 4).

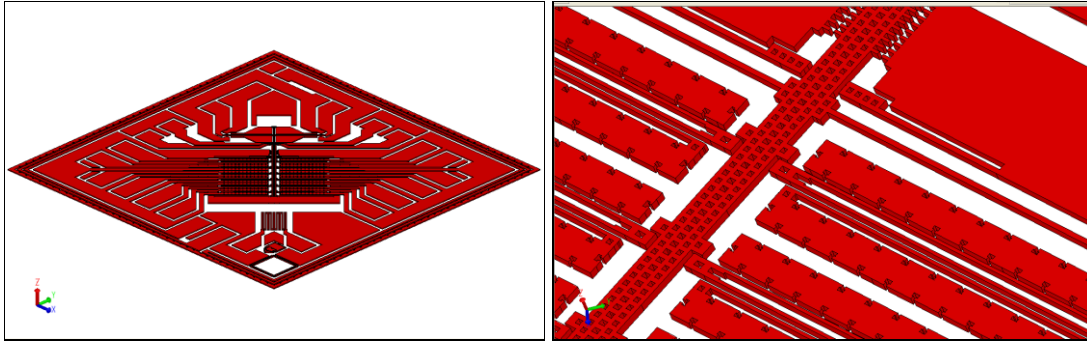


Figure 2: First layer (silicon is shown in red) of a single device die which corresponds to mask #1. The entire die is shown on the left, and a close-up is shown on the right.

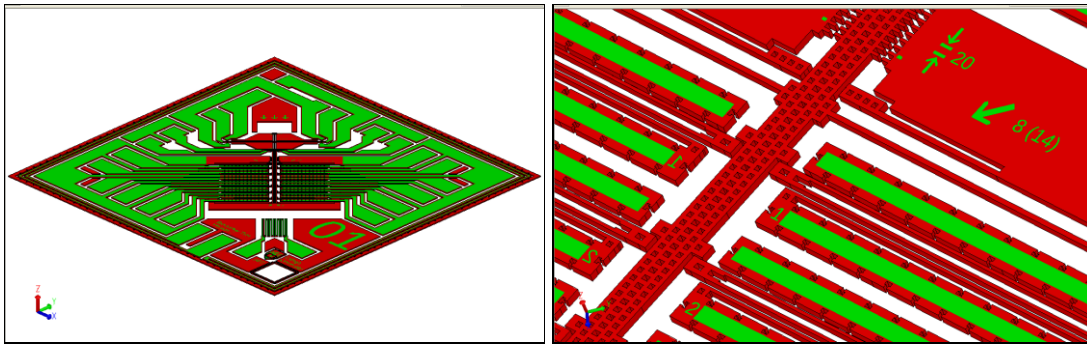


Figure 3: Second layer (metal is shown in green) of a single device die which corresponds to mask #2. The entire die is shown on the left, and a close-up is shown on the right.

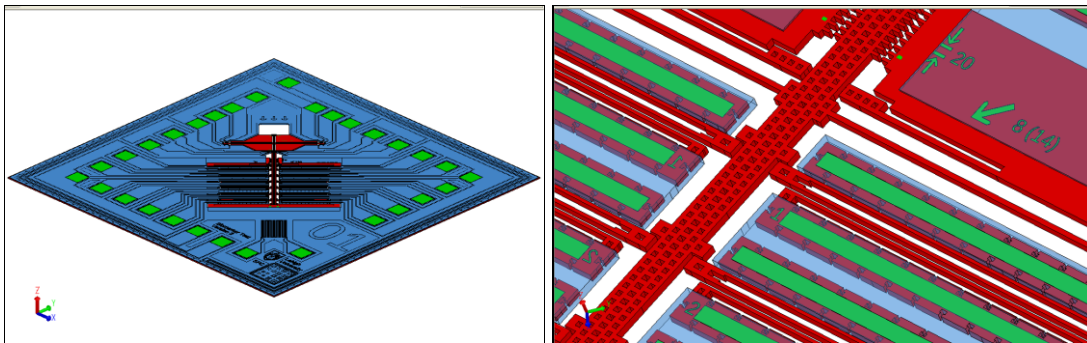


Figure 4: Third layer (isolation material is shown in blue) of a single device die which corresponds to mask #2. The entire die is shown on the left, and a close-up is shown on the right.

Layout

This force sensor is part of an integrated system for measuring the mechanical properties of single cells, and it includes an actuator, dielectrophoretic trapping

electrodes, a temperature sensor and an on-chip heater. See Figure 5 for an overview of the location of the major parts of the chip.

A close-up view of the force sensor and cell measurement area is shown in Figure 6. The design, calibration and characterization of the force sensor are discussed in detail in Chapter 2: Piezoresistive Force Sensor, and the cell mechanics results are discussed in Chapter 5: Cell Biomechanics. A close-up view of the actuator array is shown in Figure 7, and the function of the actuator array is discussed in Chapter 3: Electrostatic Actuator. Finally, see Figure 8 for a look at a fabricated chip following release but before packaging. The fabrication techniques and layout variations are discussed in Appendix I: Layout.

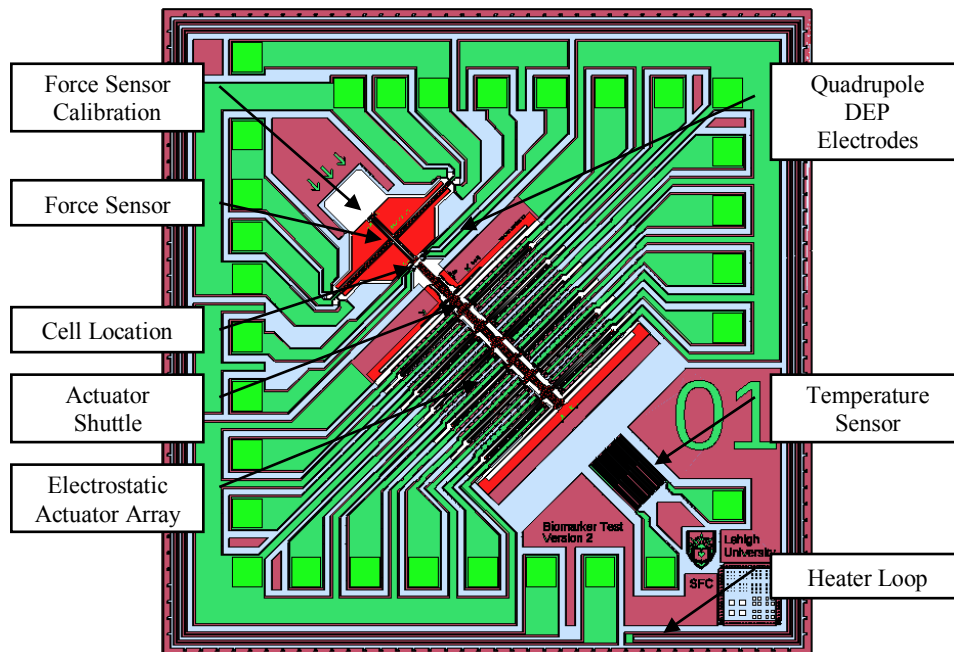


Figure 5: Color coded masks and layout: DEVICE layer is red, METAL layer is green, and ISOLATION layer is light blue. Each device die is 4 mm by 4 mm square.

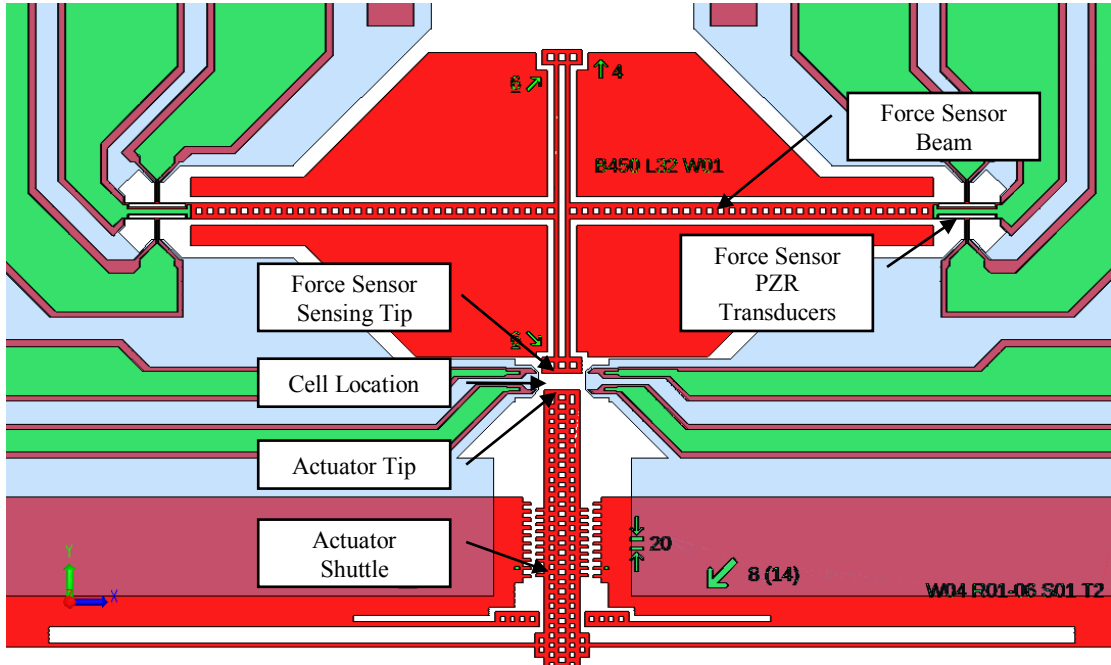


Figure 6: Labeled features in the force sensing and cell trapping regions.

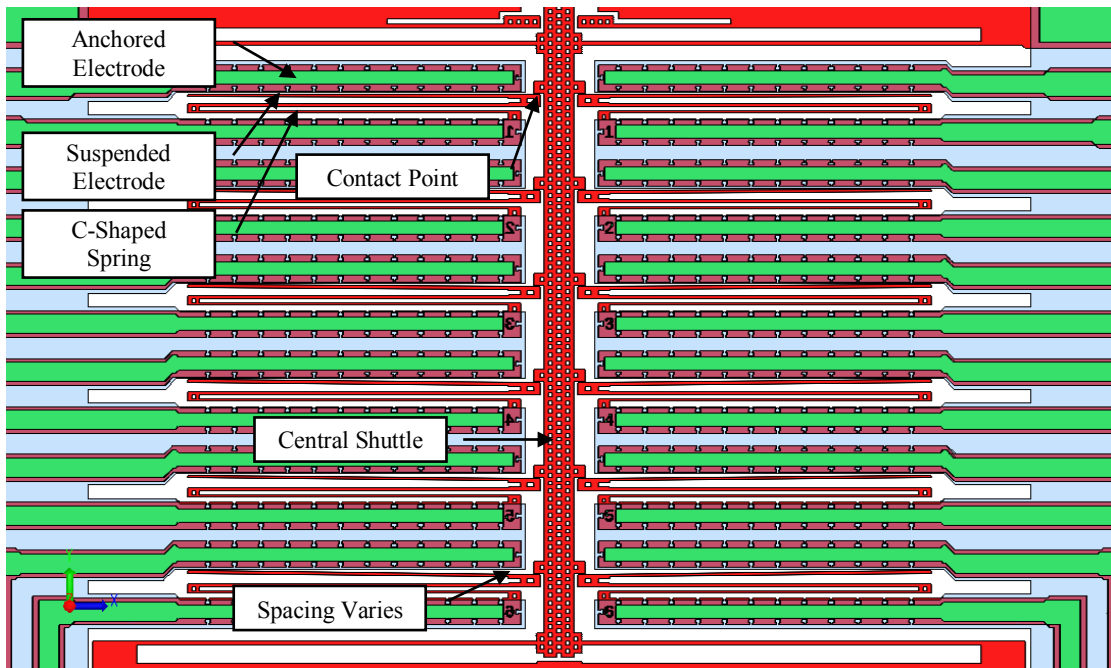


Figure 7: Labeled features of the actuator array. During operation, a single pair of anchored electrodes is energized and all suspended electrodes are grounded.

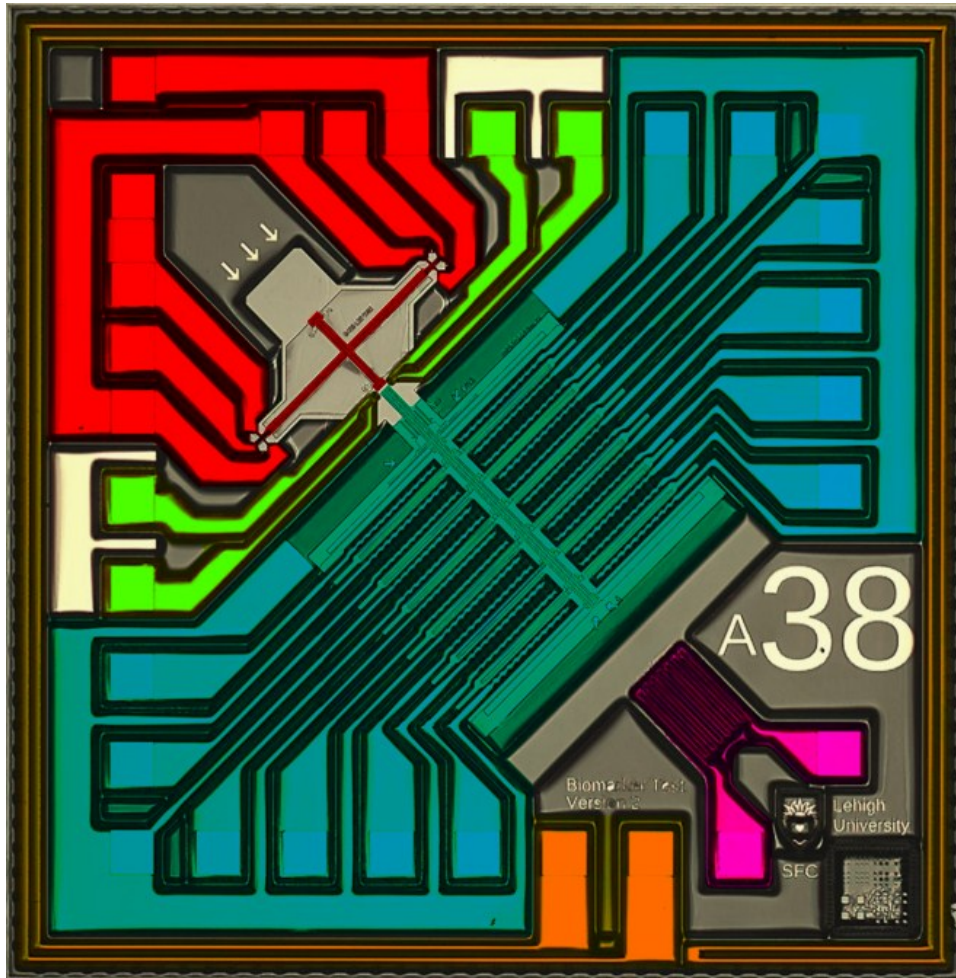


Figure 8: A color-coded fabricated BioMEMS chip (4 mm by 4 mm) showing the location of the force sensor (red), actuator array and shuttle (blue), DEP electrodes (green), temperature sensor (violet), and heater ring (orange).

Cell Mechanical Properties

A number of measurements for the elastic modulus of cells has already been made, and the results vary quite a bit depending on the cell, its morphological state, the substrate, and the method of measurement. A number of these important measurements have already been compiled [47] as part of research work on the viscoelastic properties of osteoblasts, chondrocytes and adipocytes, and the measurements relevant to osteoblasts and fibroblasts have been summarized below in Table 2 and Table 3 (notice that the majority of measurements have been accomplished using AFM).

Table 1: Viscoelastic parameters for different cell types using several different experimental techniques (adapted from [49])

Author (Year)	Cell Type	Test Method	Force ⁵ (nN)	Pressure ⁵ (Pa)	k ₁ (Pa)	k ₂ (Pa)	τ _r (sec)	η (Pa-s) ⁴
Koay (2003)	chondrocyte	indentation	50	-	1090	1140	1.32	1439
Tedrow (2000)	chondrocyte	micropipette	-	100-500	200	300	10	2000
Wu (2000)	Hepatocyte	micropipette	-	300	87	33	0.18	15.7
Thoumine (1997)	Fibroblast	microplate ¹	80-120	-	960	510	13	12480
Thoumine (1997)	Fibroblast	microplate ²	70-110	-	960	840	12	11520
Sato (1990)	Endothelial	micropipette	-	200	100	200	39.5	3950
Chien (1984)	Neutrophil	micropipette	-	40	31	76	0.22	6.8
Schmid-Schönbein (1981)	Neutrophil	micropipette	-	20	28	74	0.18	5.0
Peeters (2005)	Myoblast	compression ³	100-1000	-	2120	1960	0.30	636

¹ microplate step compression and step stretch

² microplate sinusoidal oscillation stretch/compress at 1 Hz

³ bulk sinusoidal compression oscillation

⁴ converted using $\eta = \tau k_1$

⁵ compression is reported either as a pressure or a force on the cell depending on the method

Table 2: Mechanical properties of osteoblasts (from [47])

Author, Year	E (kPa) ¹	Cell Source	Testing Method	Morphology, Substrate ²	Notes
Charras & Horton, (2002a)	14	Murine, neonatal long bones	AFM	Spread, glass	pyramidal AFM tip
Charras & Horton, (2002b)	3.175	Murine, neonatal long bones	AFM	Spread, glass	spherical AFM tip
Domke et al., (2000)	5.4–7.6	Human, SaOS2 osteoblast cell line	AFM	Spread, glass/TCP	pyramidal AFM tip
Jaasma et al., (2006)	3–5 (converted)	Murine, MC3T3-E1 osteoblast cell line	AFM	Spread, Col-I glass	spherical AFM tip
Shin & Athanasiou, (1999)	0.92-1.09	Human, MG63 osteosarcoma cell line	Cyto-indentation	Spherical, silicon	Flat tip
Takai et al., (2005)	1.2	Murine, MC3T3-E1 osteoblast cell line	AFM	Spread, PLL	pyramidal AFM tip

¹ When applicable, apparent moduli values were converted by assuming $\nu=0.5$

² PLL is poly-L-lysine; TCP is tissue culture plastic

Table 3: Mechanical properties of fibroblasts (from [47])

Author, Year	E (kPa) ¹	Cell Source	Testing Method	Morphology, Substrate ²	Notes
Jaasma et al., (2006)	1–2 (converted)	Murine, NIH3T3 fibroblast cell line	AFM	Spread, Col-I glass	spherical AFM tip
Mahaffy et al., (2000)	0.75–1.4	Murine, NIH3T3 fibroblast cell line	AFM	Spread, glass	spherical AFM tip
Mahaffy et al., (2004)	0.6	Murine, NIH3T3 fibroblast cell line	AFM	Spread, glass	spherical AFM tip
Petersen et al., (1982)	4–14	Murine, 3T3 fibroblast cell Line	cell poker	Spread, glass	spherical-tipped poker
Wu et al., (1998)	4	Murine, L929 fibroblast cell Line	AFM	Spread, TCP	pyramidal AFM tip

¹ When applicable, apparent moduli values were converted by assuming $\nu=0.5$

² PLL is poly-L-lysine; TCP is tissue culture plastic

Typical Microplate Compression

A cell can be modeled as a viscoelastic material using the standard linear solid model [49]. On one side is a spring (k_0) and the other side is the series combination of a spring (k_1) and a dashpot with viscosity μ . The combined elements determine the relationship between the stress (σ) and strain (ϵ) as shown in Figure 9.

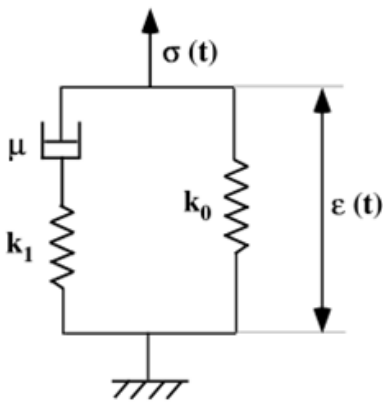


Figure 9: Standard linear solid model of a viscoelastic material

For time-dependent deformation, the governing equation for this system is given by equation 1.

$$\sigma(t) + \frac{\mu}{k_1} \frac{d\sigma(t)}{dt} = k_0 \epsilon(t) + \mu(k_0 + k_1) \frac{d\epsilon(t)}{dt} \quad 1$$

Assuming the strain is constant after the initial loading, or $\epsilon' = 0$, then the stress as a function of time is given by equation 2, or alternately by equation 3.

$$\sigma(t) = \epsilon_0 (k_0 + k_1 e^{-t/\tau}) \quad 2$$

$$\frac{\sigma(t)}{\epsilon_0} = k_0 + k_1 e^{-t/\tau} \quad 3$$

The initial strain ϵ_0 occurs right after compression and the relaxation time τ is related to μ and k by equation 4.

$$\mu = \tau k_1 \quad 4$$

The stress is measured as force over area (equation 5) where the area of the cell is given by equation 6, where, d_{cross} is cross sectional diameter of the cell perpendicular to direction of force (f).

$$\sigma(t) = \frac{f(t)}{A_{cell}} \quad 5$$

$$A_{cell} = \pi \left(\frac{1}{2} d_{cross} \right)^2 \quad 6$$

The strain is measured as a change in the diameter over time (equation 7) where d_{axial} is diameter of cell parallel to direction of force.

$$\epsilon(t) = \frac{d_{axial}(t)}{d_{axial}(0)} - 1 \quad 7$$

The simplified mechanics used to interpret these experiments are justified by the fact that the cells were subjected to large strains where their shape was no longer spherical, and more similar to short wide cylinders under compression or long thin cylinders being stretched.

The results of these tests are shown in Table 4 for two methods. First, chick fibroblast cells were either stretched or compressed by 12 μm after attachment to a pair of microplates. Second, the fibroblast cells were attached to a pair of microplates and then stretched and compressed using an oscillating sinusoidal motion of $\pm 12 \mu\text{m}$ with period of 4, 40, 400 or 4000 seconds.

Table 4: Microplate compression results [49] for avian chick fibroblast cells

Test	k_0 (N/m ²)	k_1 (N/m ²)	τ (s)	μ (kPa-s)
step compression & step stretch	960	510	13	12.5
oscillation	960	840	12	11.5

Expected Forces in this Research

Two flat blocks (one fixed and one moveable) compress a cell which is modeled as a sphere of radius R (see Figure 10). The reaction force exerted by the cell on the fixed block is modeled by equation 8. This is equation is discussed in more detail in Chapter 5: Cell Biomechanics (see equation 69).

$$F = \frac{4}{3} \left(\frac{E}{1 - \nu^2} \right) \sqrt{R} \Delta d^{3/2} \quad 8$$

Here, Δd is the compression displacement, E is the elastic modulus of the cell, d is the diameter of the cell body, and ν is the Poisson ratio of the cell body (which is assumed to be 0.5).

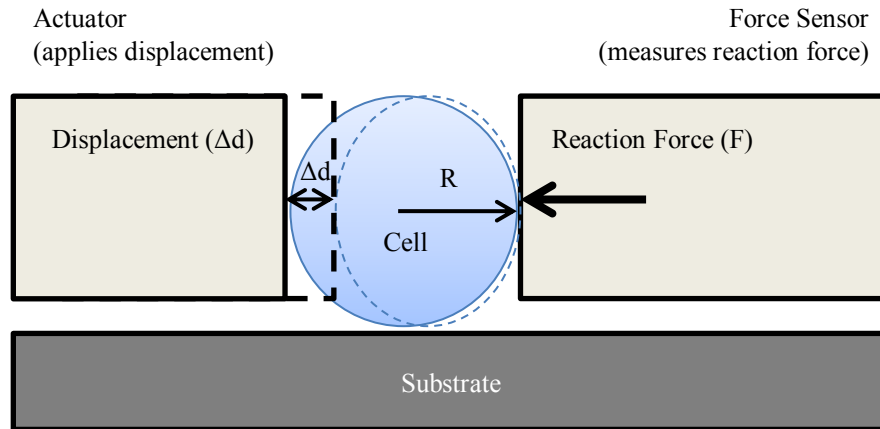


Figure 10: Schematic of the system for measuring the mechanical compliance of a biological cell.

Based on literature research of the maximum and minimum elastic modulus reported for cells (see Table 1), a graph of the operating region of a force/displacement sensor system can be made (see Figure 11 and Figure 12).

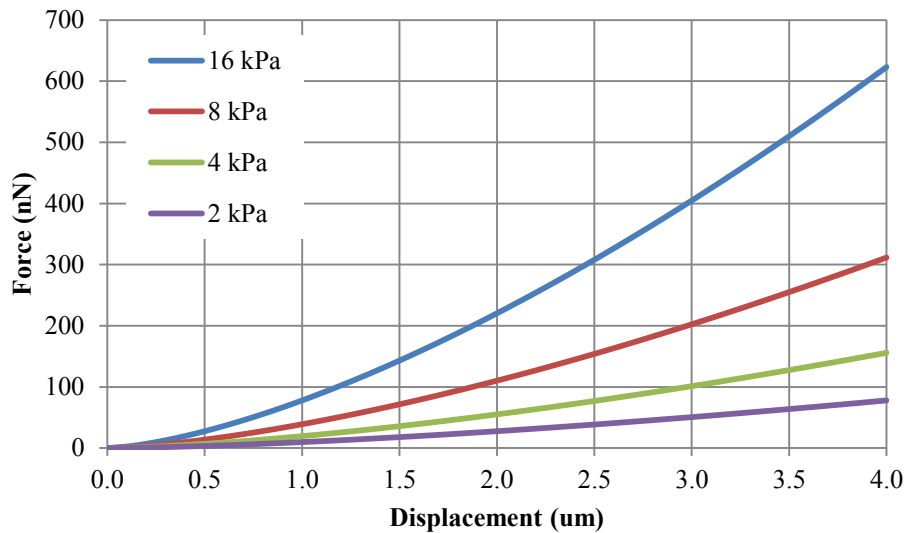


Figure 11: Plot of displacement (Δd) and corresponding reaction force (F) for expected upper and lower limits of cell elastic modulus. The diameter of the cell is 15 μm and the Poisson ratio is 0.5.

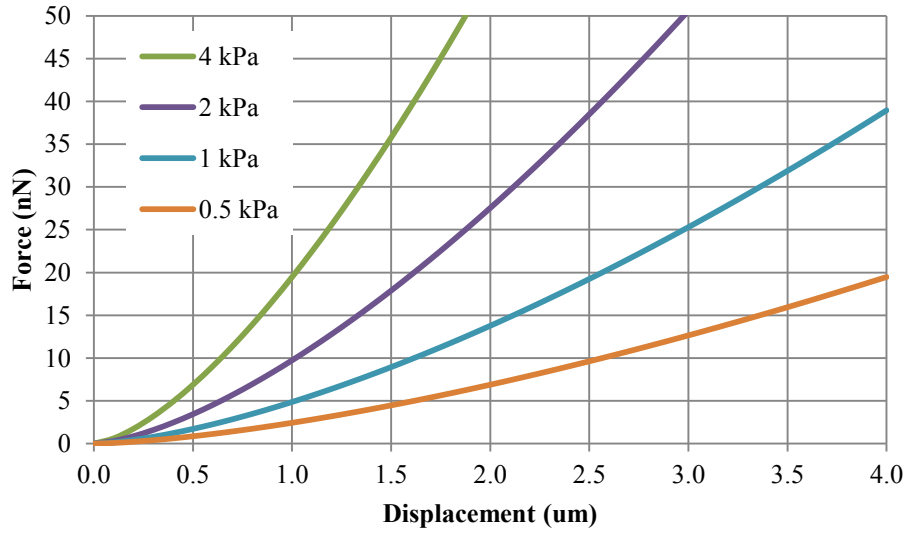


Figure 12: Plot of displacement (Δd) and corresponding reaction force (F) for expected upper and lower limits of cell elastic modulus. The diameter of the cell is $15 \mu\text{m}$ and the Poisson ratio is 0.5.

For studies of cell mechanical properties where the elastic modulus of the cell interior is 1 kPa, it is necessary for the force sensor to resolve forces of 25 nN when a cell of 15 μm in diameter is compressed by 3.0 μm . The expected elastic modulus of the cell is given by equation 9, which is based on equation 8.

$$E = \frac{3 F(1 - \nu^2)}{4 \sqrt{R} \Delta d^{3/2}} \quad 9$$

When the elastic modulus is plotted as a function of minimum detectable force while the cell is compressed by a certain Δd , then the limitations of the minimum measurable elastic modulus are apparent (see Figure 13). For a cell compressed by 3 μm and a minimum detectable force of 10 nN, the softest object that can be measured has an elastic modulus of 395 Pa. For a cell compressed by 4 μm and a minimum detectable force of 5 nN, the softest object that can be measured has an elastic modulus of 128 Pa.

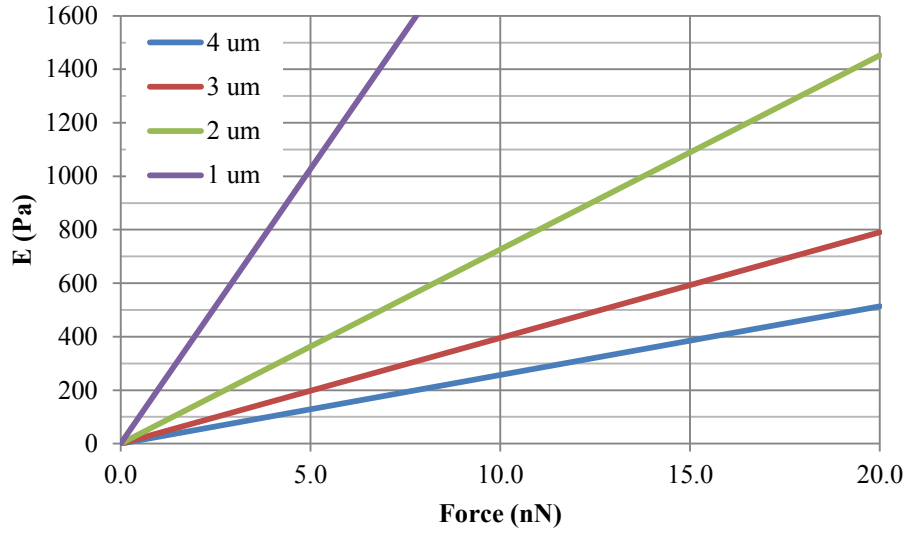


Figure 13: Expected elastic modulus (E) as a function of minimum detectable force for various cell compressions ($\Delta d=1,2,3$ or $4 \mu\text{m}$). The diameter of the cell is $15 \mu\text{m}$ and the Poisson ratio is 0.5 .

The expected elastic modulus of chondrocytes and fibroblasts is 100 to 1000 Pa, so a force resolution of below 5 nN is highly desirable for the study of these types of cells.

Chapter 2: Piezoresistive Force Sensor

Principle of Operation

Cantilever Beam Force Sensor

This force sensor design is based on a free-standing cantilever beam combined with piezoresistive materials which act as stress transducers. When a fixed-free cantilever beam is subjected to a force at the free end, the free end deflects and stress is created along the edges of the beam. This stress is greatest at the base of the cantilever where it is fixed and greatest at the edges parallel to the axis of bending. The piezoresistive transducers are placed in the region of maximum stress and oriented so that they are in the pathway of electrical current so the resistance can be measured.

Fabrication Methods

A number of options exist for force sensing with a cantilever beam, and they can be generally categorized by fabrication method and force sensing direction. The methods for defining piezoresistors are: (1) thin film or surface-doped, (2) sidewall-doped, and (3) integral. The sensing directions are: (1) perpendicular and (2) lateral to the surface of the silicon wafer.

Thin film or surface doped

This is the most common method and uses standard semiconductor processes to either create a thin film piezoresistor on the surface or directly dope silicon to form a piezoresistor. These methods naturally imply that the sensing direction is perpendicular

to the plane of silicon and thin film fabrication. Numerous references for the optimization of these types of cantilevers exist [11] [12].

Sidewall doped

It is very difficult to deposit thin films on the sides of silicon structures using standard methods, but sidewall doping can be used to create a piezoresistor for force sensing in the lateral direction [14] [15].

Integral

Instead of patterned doping or thin films, both the structural regions and the sensing regions can be made from the same piezoresistive material. Integral sensors have been used for a single-mask accelerometer [16] as well as for position feedback in MEMS actuators [17]. Although this method limits the possibilities for electrical routing, it simplifies the fabrication of the force sensor. This method naturally limits the sensing direction to the lateral direction.

Lateral Sensing for Cell Mechanics

For the cell biomechanics application discussed in this thesis, the direction of the force to be measured is lateral to the plane of fabrication of the silicon wafer, and the sensor will be a cantilever beam with a stress transducer at the base. This makes patterning and electrical isolation techniques that rely on thin films to define the stress transducer unsuitable, since it should be located on the side of the beam, rather than the top.

The integral piezoresistive transducer design is an attractive alternative since it can simplify the fabrication process to just one mask by defining the piezoresistive regions

purely with mask geometry rather than patterned doping or electrical isolation layers. This is also a disadvantage, since the mechanical structure will act as an electrical short circuit unless all areas are physically separated. Creating “islands” of electrically separated mechanical structures is straightforward when using DRIE on a silicon-on-insulator (SOI) wafer. But since there is only one layer, electrical routing is rather limited. Despite these limitations, a new design has been developed which can take advantage of the simplified fabrication [18].

Lateral Force Sensor Architecture

The force sensor consists of a transducer region, a cantilever beam, and a central wishbone (see Figure 14). At the base of each cantilever is a thin transducer ribbon which is defined in bulk silicon by two rectangular cut-outs. The transducer length and beam length of the force sensor are varied to find the best geometry for maximum sensitivity. The dashed line shows plane of symmetry, and the hatched blocks show anchor points. The regularly spaced square cut-outs along the length of the cantilever beam are etch holes to speed release of the cantilever, which is defined from the device layer of SOI wafer where the buried oxide acts as a sacrificial release layer.

An external force is applied to the wishbone which translates the force to the cantilever tip. The cantilever beam acts as a lever which concentrates stress at the base in the transducer region. The transducer region converts stress to a change in resistance and the resistors are connected in a full bridge configuration. As long as the central yoke at the center is significantly less stiff than the two symmetric cantilevers, the two

cantilevers can behave as a pair of fixed-free beams which increases the stress at the base compared to a fixed-fixed cantilever of equal length.

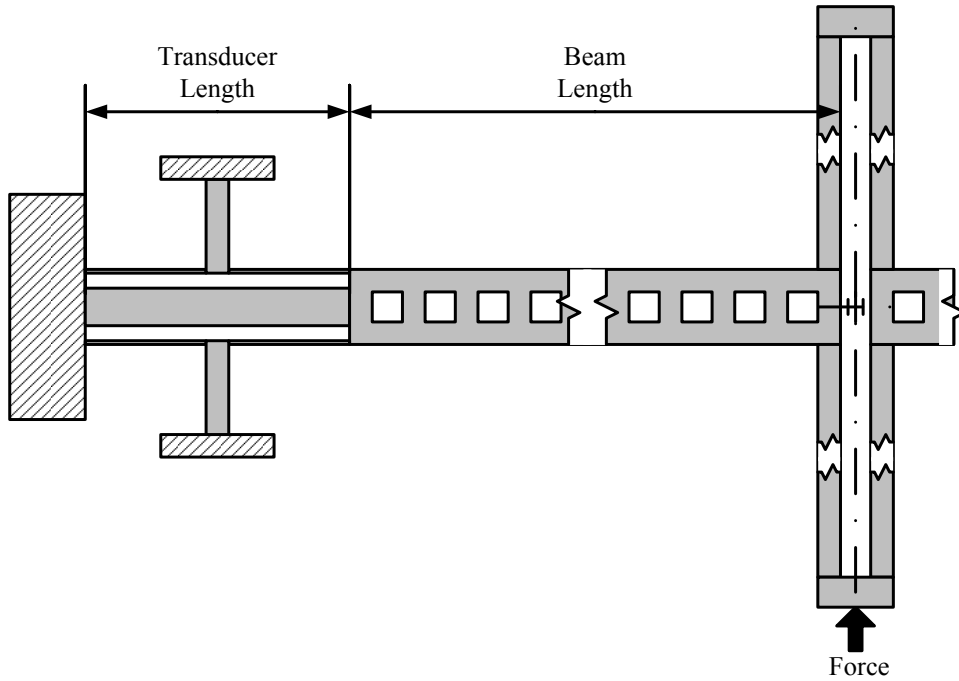


Figure 14: The force sensor is based on a pair of cantilevers each connected to a central yoke which allows each cantilever to bend in a fixed-free configuration.

According to Euler–Bernoulli beam theory, the maximum stress in the beam occurs at the base, and the cut-outs act both as stress concentration regions and also electrical pathways that guide the current flow through piezoresistive elements (see Figure 17). In order to organize the piezoresistors into a full bridge configuration without disturbing the geometry which allows for stress concentration at the base of the cantilever, small beams were added in the middle of the piezoresistive ribbons to give them a “T” shape. This allows an electrical potential to be applied at opposite ends of the pair of cantilevers while an applied force unbalances the full bridge and produces a voltage $V_1 - V_2$ (see Figure 16 and Figure 17). On-chip metal traces tie the potentials at V_1 and V_2 together; $V_S - V_0$ drives the bridge and the output voltage is taken across $V_1 - V_2$. Note that

R_{beam} and other parasitic resistances do not affect sensitivity, but may increase overall power dissipation.

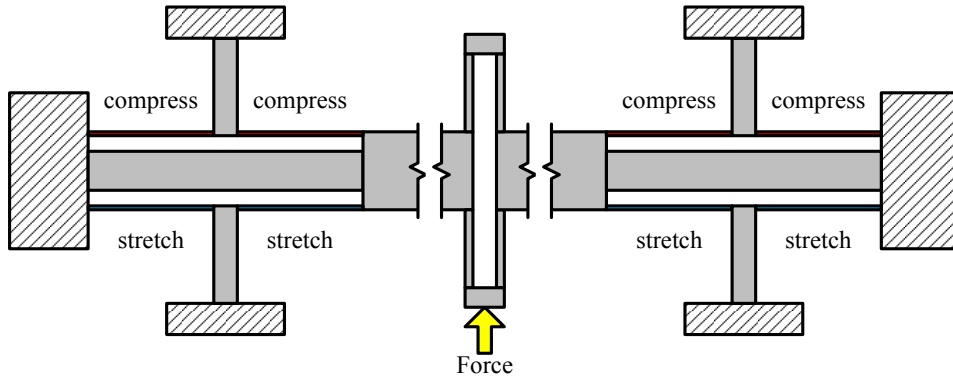


Figure 15: Force applied to the center of the force sensor creates compressive and tensile stress in the piezoresistor regions.

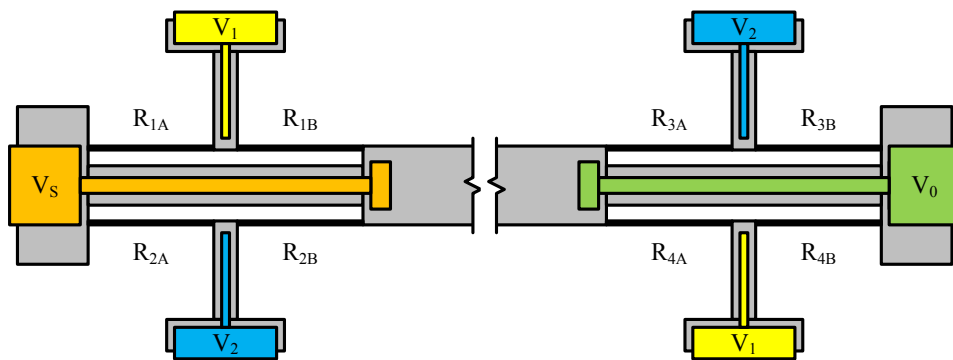


Figure 16: The electrical equipotentials in the full bridge are color coded and labeled, and equivalent resistors are labeled.

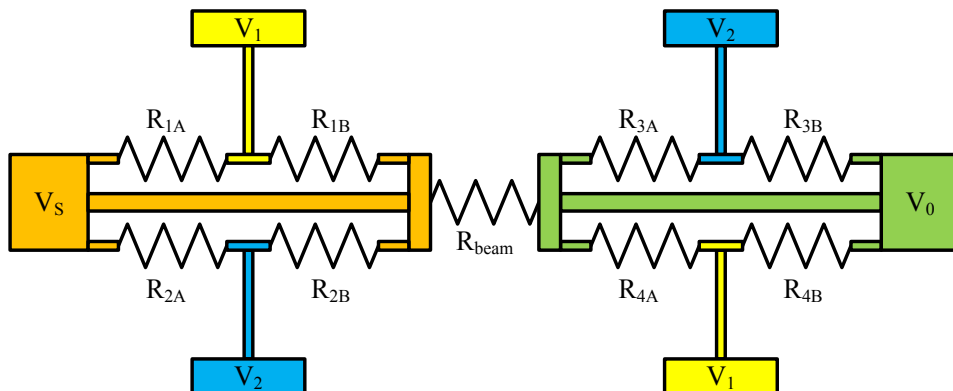


Figure 17: Piezoresistor pairs (e.g. R_{1A} and R_{1B}) act in parallel, and each pair forms one quarter of a full bridge.

A short circuit is possible between V_S and V_1 or V_2 , which would bypass the piezoresistors and degrade the sensitivity of the bridge. In practice this does not pose a problem since the silicon itself forms an insulating native oxide layer and the resistivity of the silicon (just 2.5 m Ω -cm) is significantly lower than the resistivity of the cell medium (approximately 62 Ω -cm [in-house measurement] to 72 Ω -cm [33]). The metal traces leading from the bonding pads to the resistors are covered with an electrically insulating encapsulation layer.

Modeling

Linear Beam Bending

In order to model the effect of the cut-out regions and the overall sensitivity of the force sensor, one of the two cantilever pairs is modeled as a uniform beam with two different area moments of inertia. The result of this model produces predictions for tip displacement (and hence spring stiffness of the structure) and the stress in the piezoresistive ribbon region. The stress can then be converted to a change in resistivity, and finally the expected voltage of the full bridge due to a particular force applied at the tip of the cantilever can be computed.

A detailed diagram of the force sensor is shown in Figure 18. This diagram is referred to throughout the following sections. The choice of physical dimensions is discussed further in Appendix I: Layout.

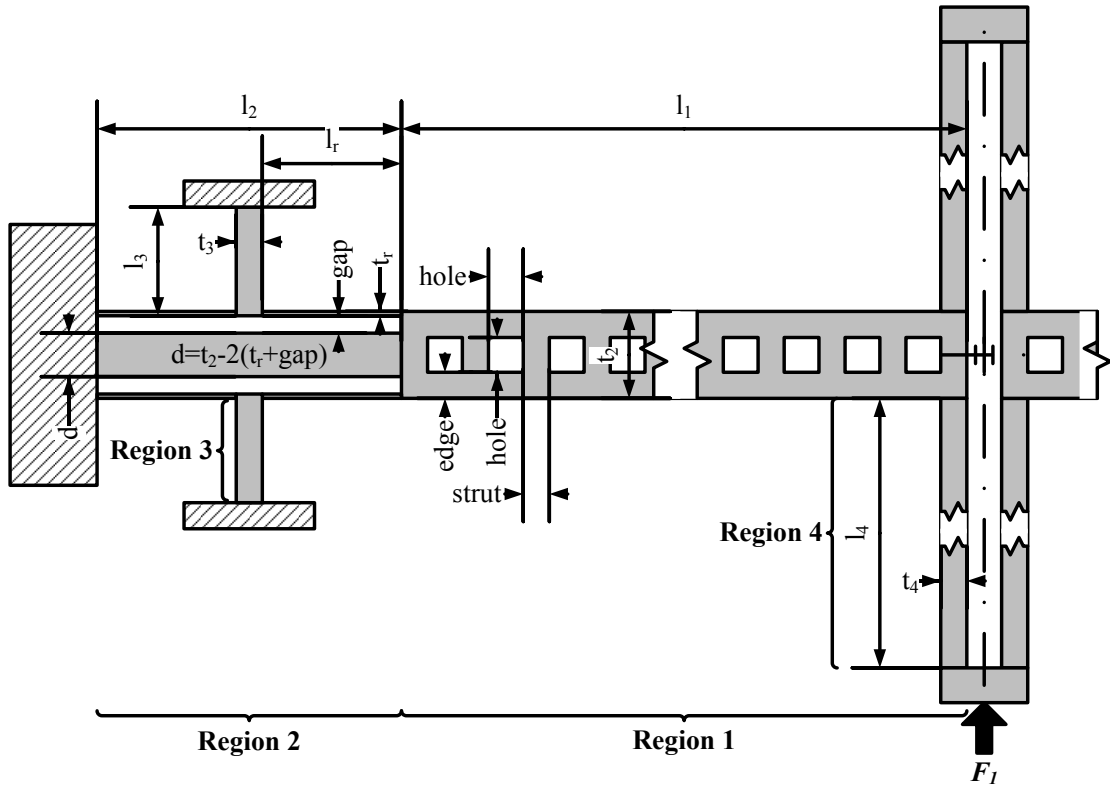


Figure 18: Force sensor mechanical diagram with labels

Area Moment of Inertia (I_x)

By applying the formula for the area moment of inertia (Equation 10), to the cross-sections of the cantilever beam (Region 1 in Figure 18) and transducer (Region 2 in Figure 18) of the force sensor, a model of the bending behavior can be developed.

$$I_x = \int y^2 dA \tag{10}$$

Along the length of the cantilever beam, a series of periodic square cut-outs are needed to speed the release of the cantilever during the final etching step. The structure is defined from the device layer of SOI wafer where the buried oxide acts as a sacrificial release layer (Appendix I: Layout).

Region 1: Beam region ($l_2 < x < l_1$)

For a beam with periodic square holes in the center (see Figure 19) the area moment of inertia in the portion without a hole is I_{x1a} (see equation 11), and it is I_{x1b} (see equation 12) in the portion with a hole.

$$I_{x1a} = \frac{wt^3}{12} \quad 11$$

$$I_{x1b} = \frac{2w}{3} \left(\left(\frac{t}{2} \right)^3 - \left(\frac{t}{2} - t_e \right)^3 \right) \quad 12$$

The weighted sum for a long cantilever beam is I_{x1} (see equation 13), where w is beam width (perpendicular to force), t is beam thickness (in direction of force), a is strut width, b is hole width, and t_e is edge width.

$$I_{x1} = \frac{b}{a+b} \left[\frac{2w}{3} \left(\left(\frac{t}{2} \right)^3 - \left(\frac{t}{2} - t_e \right)^3 \right) \right] + \frac{a}{a+b} \left[\frac{wt^3}{12} \right] \quad 13$$

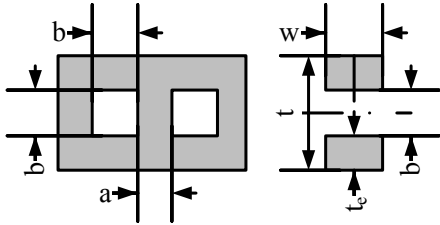


Figure 19: The dimensions for the cantilever beam with periodic holes are shown with a top-down view (left) and a cross section of the beam (right).

Region 2: Transducer region ($0 < x < l_2$)

For a beam with two gaps at each edge (see Figure 20), the area moment of inertia is I_{x2} (see equation 14) where w is beam width (perpendicular to force), t is beam thickness (in direction of force), t_r is transducer “ribbon” width, and g is transducer gap at base.

$$I_{x2} = \frac{2w}{3} \left[\left(\frac{t}{2} \right)^3 - \left(\frac{t}{2} - t_r \right)^3 + \left(\frac{t}{2} - t_r - g \right)^3 \right] \quad 14$$

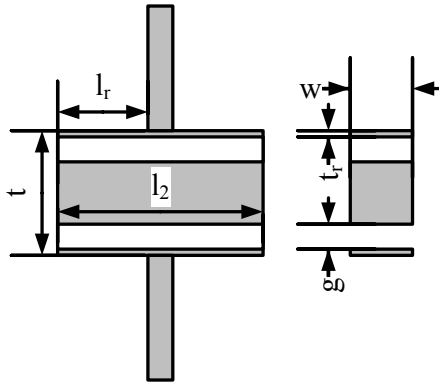


Figure 20: The dimensions for the cantilever beam are shown in a in the transducer region with a cross section (top) and a top-down view (bottom).

Mechanical Behavior of Beam with Two Regions of Different Area Moment of Inertia

The modeling of stress and deflection is based on Euler-Bernoulli beam theory. Since the beams are relatively thin compared to their length (width of 20 μm and length of 300 μm to 600 μm) and the expected deflections are small (below 1 μm) the deficiencies of this model are ignored. It under-predicts deflection and over-predicts stiffness compared to more complex beam theories such as Timoshenko beam theory which accounts for the effects of transverse shear strain [19]. These effects are normally neglected for beams which are significantly longer than they are wide and when there is small displacement of the beam tip.

Applied Force

The initial assumption in Euler-Bernoulli beam theory is shown in equation 15, where E is the elastic modulus, I is the area moment of inertia, and q is the distributed load.

$$\frac{d^2}{dx^2} \left(EI \frac{d^2 y(x)}{dx^2} \right) = q \quad 15$$

This can be rewritten as equation 16 for the case when I is uniform, and E is constant.

$$EI \frac{d^4 y}{dx^4} = q \quad 16$$

In the case where there is point force loading at the end of cantilever beam under fixed-free bending, then those boundary conditions produce equation 17.

$$\frac{d^3 y(x)}{dx^3} = \frac{F}{EI_x(x)} \quad 17$$

The deflection in the two regions described earlier is $y(x) = \begin{cases} y_2(x), & x \leq l_2 \\ y_1(x), & x > l_2 \end{cases}$ and the

corresponding moments of inertia are $I(x) = \begin{cases} I_{x2}, & x < l_2 \\ I_{x1}, & x \geq l_2 \end{cases}$. Here, F is force, E is elastic

modulus, and I_x is the moment of inertia around the x -axis. Furthermore, let $L = l_1 + l_2$

so that $x = L$ is at the end of the beam, $x = 0$ is at the base, and $x = l_2$ is at the edge

between the two different cross sections.

Moment and Stress

Moment does not depend on moment of inertia I_x and is simply given by equation 18.

$$M(x) = F(L - x) \quad 18$$

The stress in the beam is given by equation 19 where $Z(x)$ is the section modulus

defined by equation 20.

$$\sigma(x) = \frac{M(x)}{Z(x)} \quad 19$$

$$Z(x) = \frac{I_x(x)}{y} \quad 20$$

The resulting stress along the beam is given by equation 21 where y is 0 at the center of the beam and $t/2$ at the edge.

$$\sigma(x, y) = \frac{M(x)}{I_x(x)} y \quad 21$$

Transverse Shear

The constraints at the boundaries of region 1 and region 2 are given by equations 22 and 23.

$$\left. \frac{d^2 y_1(x)}{dx^2} \right|_{x=L} = 0 \text{ for } x > l_2 \quad 22$$

$$\left. \frac{d^2 y_2(x)}{dx^2} \right|_{x=l_2} = \left. \frac{d^2 y_1(x)}{dx^2} \right|_{x=l_2} \text{ for } x = l_2 \quad 23$$

Integrating $\frac{d^3 y_2(x)}{dx^3}$ for $x \geq l_2$ results in equation 24.

$$\frac{d^2 y_1(x)}{dx^2} = -\frac{F}{E} \left(\frac{L-x}{I_{x1}} \right) \quad 24$$

Integrating $\frac{d^3 y_1(x)}{dx^3}$ for $x \leq l_2$ results in equation 25.

$$\frac{d^2 y_2(x)}{dx^2} = -\frac{F}{E} \left(\frac{L-l_2}{I_{x1}} + \frac{l_2-x}{I_{x2}} \right) \quad 25$$

Slope or Rotation

The constraints at the boundaries of region 1 and region 2 are given by equations 26 and 27.

$$\left. \frac{dy_2(x)}{dx} \right|_{x=0} = 0 \text{ for } x > l_2 \quad 26$$

$$\left. \frac{dy_2(x)}{dx} \right|_{x=l_2} = \left. \frac{dy_1(x)}{dx} \right|_{x=l_2} \text{ for } x = l_2 \quad 27$$

Integrating $\frac{d^2y_2(x)}{dx^2}$ for $x \geq l_2$ results in equation 28.

$$\frac{dy_1(x)}{dx} = \left. \frac{dy_2(x)}{dx} \right|_{x=l_2} + \frac{F}{E} \left(\left(\frac{1/2}{I_{x1}} \right) x^2 - \left(\frac{L}{I_{x1}} \right) x + \left(\frac{Ll_2 - 1/2 l_2^2}{I_{x1}} \right) \right) \quad 28$$

Integrating $\frac{d^2y_2(x)}{dx^2}$ for $x \leq l_2$ results in equation 29.

$$\frac{dy_2(x)}{dx} = + \frac{F}{E} \left(\left(\frac{1/2}{I_{x2}} \right) x^2 - \left(\frac{L - l_2}{I_{x1}} + \frac{l_2}{I_{x2}} \right) x \right) \quad 29$$

Deflection

The constraints at the boundaries of region 1 and region 2 are given by equations 30 and 31.

$$y_2(x)|_{x=0} = 0 \text{ for } x > l_2 \quad 30$$

$$y_2(x)|_{x=l_2} = y_1(x)|_{x=l_2} \text{ for } x = l_2 \quad 31$$

Integrating $\frac{dy_1(x)}{dx}$ for $x \geq l_2$ results in equation 32

$$\begin{aligned}
y_1(x) = y_2(x)|_{x=l_2} + \frac{F}{E} \left(\left(\frac{1/6}{I_{x1}} \right) x^3 - \left(\frac{L/2}{I_{x1}} \right) x^2 + \left(\frac{Ll_2 - 1/2 l_2^2}{I_{x1}} + \frac{E}{F} \frac{dy_2(x)}{dx} \Big|_{x=l_2} \right) x \right) \\
- \frac{F}{E} \left(\left(\frac{1/6}{I_{x1}} \right) l_2^3 - \left(\frac{L/2}{I_{x1}} \right) l_2^2 + \left(\frac{Ll_2 - 1/2 l_2^2}{I_{x1}} + \frac{E}{F} \frac{dy_2(x)}{dx} \Big|_{x=l_2} \right) l_2 \right)
\end{aligned} \tag{32}$$

Or equivalently, equation 33.

$$\begin{aligned}
y_1(x) = y_2(x)|_{x=l_2} + \frac{F}{E} \left(\left(\frac{1/6}{I_{x1}} \right) x^3 - \left(\frac{L/2}{I_{x1}} \right) x^2 + \left(\frac{Ll_2 - 1/2 l_2^2}{I_{x1}} \right) x \right) \\
+ \left(\frac{dy_2(x)}{dx} \Big|_{x=l_2} \right) x - \frac{F}{E} \left(\left(\frac{1/6}{I_{x1}} \right) l_2^3 - \left(\frac{L/2}{I_{x1}} \right) l_2^2 + \left(\frac{Ll_2 - 1/2 l_2^2}{I_{x1}} \right) l_2 \right) \\
- \left(\frac{dy_2(x)}{dx} \Big|_{x=l_2} \right) l_2
\end{aligned} \tag{33}$$

Integrating $\frac{dy_2(x)}{dx}$ for $x \leq l_2$ results in equation 34.

$$y_2(x) = + \frac{F}{E} \left(\left(\frac{1/6}{I_{x2}} \right) x^3 - 1/2 \left(\frac{L - l_2}{I_{x1}} + \frac{l_2}{I_{x2}} \right) x^2 \right) \tag{34}$$

Piezoresistors

A simplified equation describing the way normal (σ) and shear (τ) stress affects the change in resistivity ($\Delta\rho/\rho$) through the piezoresistive coefficient (π) is shown below in equation 35 [21].

$$\begin{bmatrix} \Delta\rho_{xx}/\rho_0 \\ \Delta\rho_{yy}/\rho_0 \\ \Delta\rho_{zz}/\rho_0 \\ \Delta\rho_{xz}/\rho_0 \\ \Delta\rho_{yz}/\rho_0 \\ \Delta\rho_{xy}/\rho_0 \end{bmatrix} = \begin{bmatrix} \pi_{11} & \pi_{12} & \pi_{12} & 0 & 0 & 0 \\ \pi_{12} & \pi_{11} & \pi_{12} & 0 & 0 & 0 \\ \pi_{12} & \pi_{12} & \pi_{11} & 0 & 0 & 0 \\ 0 & 0 & 0 & \pi_{44} & 0 & 0 \\ 0 & 0 & 0 & 0 & \pi_{44} & 0 \\ 0 & 0 & 0 & 0 & 0 & \pi_{44} \end{bmatrix} \begin{bmatrix} \sigma_{xx} \\ \sigma_{yy} \\ \sigma_{zz} \\ \tau_{xz} \\ \tau_{yz} \\ \tau_{xy} \end{bmatrix} \quad 35$$

The most interesting coefficients are the π_{11} for n-type silicon and the π_{44} for p-type silicon since they are the largest. Although the p-type π_{44} coefficient is larger, the n-type π_{11} coefficient is convenient to work with from the design perspective since an elongated sensing element can be oriented in one of the principle directions (x , y , or z) and current flow along the axial direction is directly affected through the change in resistance. This is clear in equation 36, but it also reveals that transverse stresses are undesirable because the n-type π_{12} coefficient is opposite in sign.

$$\Delta\rho_{xx}/\rho_0 = \pi_{11}\sigma_{xx} + \pi_{12}\sigma_{yy} + \pi_{12}\sigma_{zz} \quad 36$$

When transverse stresses are neglected, equation 36 simplifies to 37,

$$\Delta\rho/\rho_0 = \pi_{11}\sigma_{xx} \quad 37$$

The four piezoresistive transducers in the force sensor are arranged in a full bridge so the ratiometric voltage output V/V_b is directly proportional to $\Delta R/R$ (see Figure 21). The sensitivity of the force sensor is measured as volts per volt per newton $((V/V)/N)$ since the output of the bridge is measured as the ratio of the bridge offset voltage to the bridge driving voltage in response to an applied force.

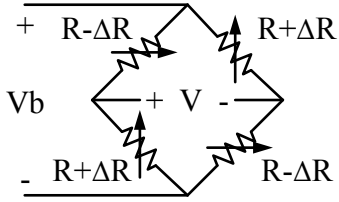


Figure 21: The piezoresistors in the force sensor are connected in a full bridge configuration and the output of the sensor is taken as V/V_b so that $V/V_b = \Delta R/R$.

Signal to Noise Ratio

Expected Signal

The signal to noise ratio can be estimated by combining the mechanical behavior model, the expected piezoresistive change, and the noise model. The output from the piezoresistor full bridge can be written as equation 38 which simplifies to equation 39.

$$\frac{V}{V_b} = \frac{\Delta R}{R} = \frac{R - R_0}{R_0} = \frac{\sigma \pi_{11} \rho \left(\frac{l_r}{t_r w} \right) - \rho \left(\frac{l_r}{t_r w} \right)}{\rho \left(\frac{l_r}{t_r w} \right)} = \frac{\pi_{11} \sigma - 1}{1} \quad 38$$

$$V = V_b (\pi_{11} \sigma - 1) \quad 39$$

The stress in equation 39 is determined by equations 18 and 21, and equation 14 is used for the corresponding cross section moment of inertia I_{x2} . The stress at edge of region 2

(where $x = l_2$ and $= t/2$) is $\sigma = \frac{F(L-l_2)}{I_x(l_2)} \left(\frac{t}{2} \right)$ and $l_2 = 2l_r + t_3$.

For the transducer region with gaps, the expected signal as a function of the applied force is described by equation 40.

$$V = V_b \left[\pi_{11} \left(\frac{F(L - l_2) \left(\frac{t}{2}\right)}{\frac{2w}{3} \left[\left(\frac{t}{2}\right)^3 - \left(\frac{t}{2} - t_r\right)^3 + \left(\frac{t}{2} - t_r - g\right)^3 \right]} \right) - 1 \right] \quad 40$$

Alternately, consider the limiting case where the beam has a uniform rectangular cross-section (see equation 41).

$$I_x = \frac{ht_2^3}{12} \quad 41$$

For a homogenous beam, the expected signal as a function of the applied force is described by equation 42.

$$V_u = V_b \left[\pi_{11} \left(\frac{F(L - l_2) \left(\frac{t}{2}\right)}{\frac{wt^3}{12}} \right) - 1 \right] \quad 42$$

In addition to the geometric dimensions which affect stress in the piezoresistor region, the expected signal depends on the piezoresistive factor which is a function of the doping level above $1 \times 10^{17} \text{ cm}^{-3}$. This effect is hard to estimate accurately over a wide range of doping levels, but a fit to the logarithmic function $\pi_{11} = f \ln(N) + g$ is possible where $f = -107 \text{ Pa}^{-1}$ and $g = 6784 \text{ Pa}^{-1}$ are fitting parameters valid over the range of $1 \times 10^{24} \text{ m}^{-3}$ ($1 \times 10^{18} \text{ cm}^{-3}$) to $1 \times 10^{26} \text{ m}^{-3}$ ($1 \times 10^{20} \text{ cm}^{-3}$).

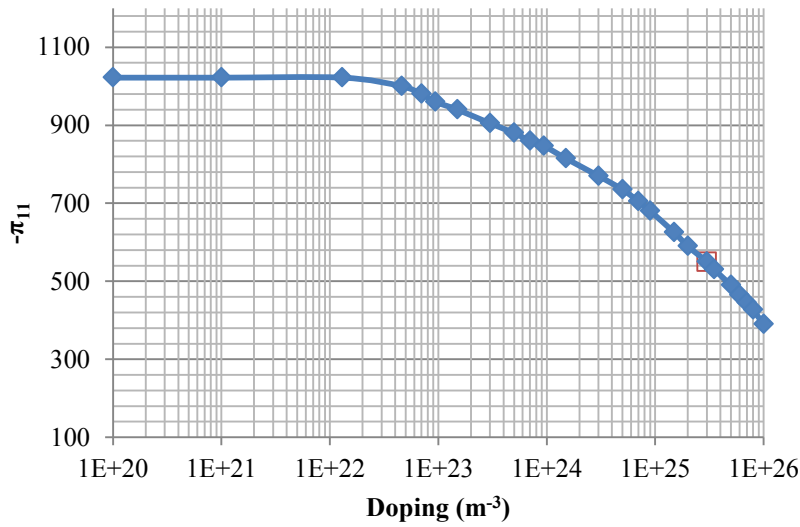


Figure 22: Piezoresistive coefficient π_{11} as a function of doping concentration in n-type silicon [22]. Figure adapted from [23] (see fig 3 at 300 Kelvin).

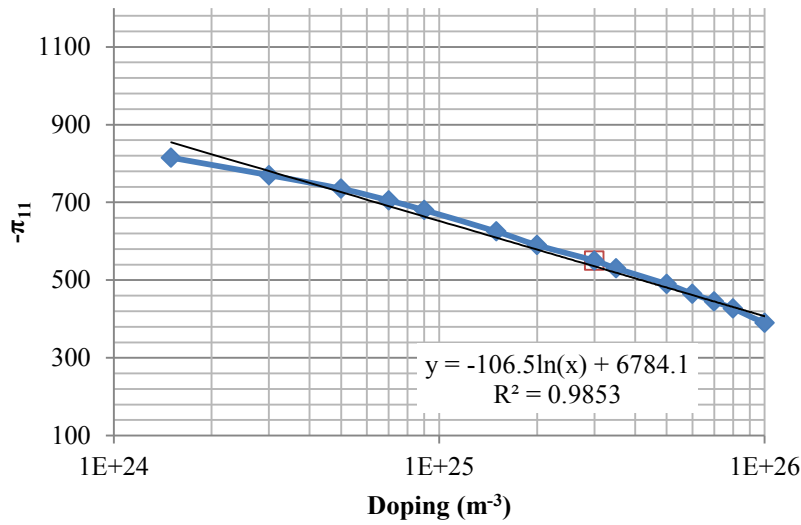


Figure 23: Fit for lookup table of piezoresistive coefficient π_{11} as a function of doping concentration in n-type based on previous figure.

For a homogenous beam, the expected signal as a function of the applied force is then given by equation 43.

$$V_u = V_b \left[(6784 - 107 \ln(N)) \left(\frac{F(L - l_2) \left(\frac{t}{2}\right)}{\frac{wt^3}{12}} \right) - 1 \right] \quad 43$$

For the transducer region with gaps, the expected signal as a function of the applied force is then given by equation 44.

$$V = V_b \left[(6784 - 107 \ln(N)) \left(\frac{F(L - l_2) \left(\frac{t}{2}\right)}{\frac{2w}{3} \left[\left(\frac{t}{2}\right)^3 - \left(\frac{t}{2} - t_r\right)^3 + \left(\frac{t}{2} - t_r - g\right)^3 \right]} \right) - 1 \right] \quad 44$$

Expected Noise

In order to determine the signal to noise ratio of the sensor, we consider the following sources of electronic noise: thermal (Johnson-Nyquist), 1/f (Hooge), and shot (Schottky) which are shown below in Table 5. In addition to their normal form, the equations have also been written using the bridge voltage V_b where the voltage V across an element is $V = \frac{1}{2} V_b$.

Table 5: Sources of electronic noise

Type of Noise	Noise Model
Thermal Noise [25][26]	$V_{th}^2 = 4k_B RT(f_{max} - f_{min})$
1/f Noise [27]	$V_f^2 = \alpha \frac{V^2}{n} \ln \left(\frac{f_{max}}{f_{min}} \right)$ $V_f^2 = \alpha \frac{\left(\frac{V_b}{2}\right)^2}{n} \ln \left(\frac{f_{max}}{f_{min}} \right) = \alpha \frac{V_b^2}{4n} \ln \left(\frac{f_{max}}{f_{min}} \right)$
Shot Noise [28]	$I_I^2 = 2qI(f_{max} - f_{min})$ $V_I^2 = 2qRI(f_{max} - f_{min}) = V_b q(f_{max} - f_{min})$

The variables used here (see Table 11) are defined as:

- k_B Boltzmann's constant
- q electron charge
- T temperature
- V_b V_{rms} bridge voltage
- V V_{rms} bias voltage
- α Hooge constant
- N doping concentration
- n total number of carriers

The total noise voltage is given by equations 45 and 46.

$$e_{total} = \sqrt{V_{th}^2 + V_f^2 + V_I^2} \quad 45$$

$$e_{total} = \sqrt{[4k_B RT(f_{max} - f_{min})]^2 + \left[\alpha \frac{V_b^2}{4n} \ln \left(\frac{f_{max}}{f_{min}} \right) \right]^2 + [V_b q(f_{max} - f_{min})]^2} \quad 46$$

Of these variables, only n and R are dependent on design geometry choices. First, the total number of carriers in the volume, n (equation 47), impacts the 1/f noise.

$$n = N(wt_r l_r) \quad 47$$

Second, the resistance, R (equation 48), impacts the thermal noise, but the silicon resistivity ρ is a function of the doping concentration N .

$$R = \rho \frac{wt_r}{l_r} \quad 48$$

An approximate relationship between the doping concentration and resistivity for n-type material is formulated based on a fit to the power law $\rho = cN^d$ where $c = 1.07 \times 10^{14} \Omega\text{-m}$ and $d = -0.735$ are fitting parameters (Figure 25). The units of resistivity are expressed as $\Omega\text{-m}$ and doping as $1/\text{m}^3$.

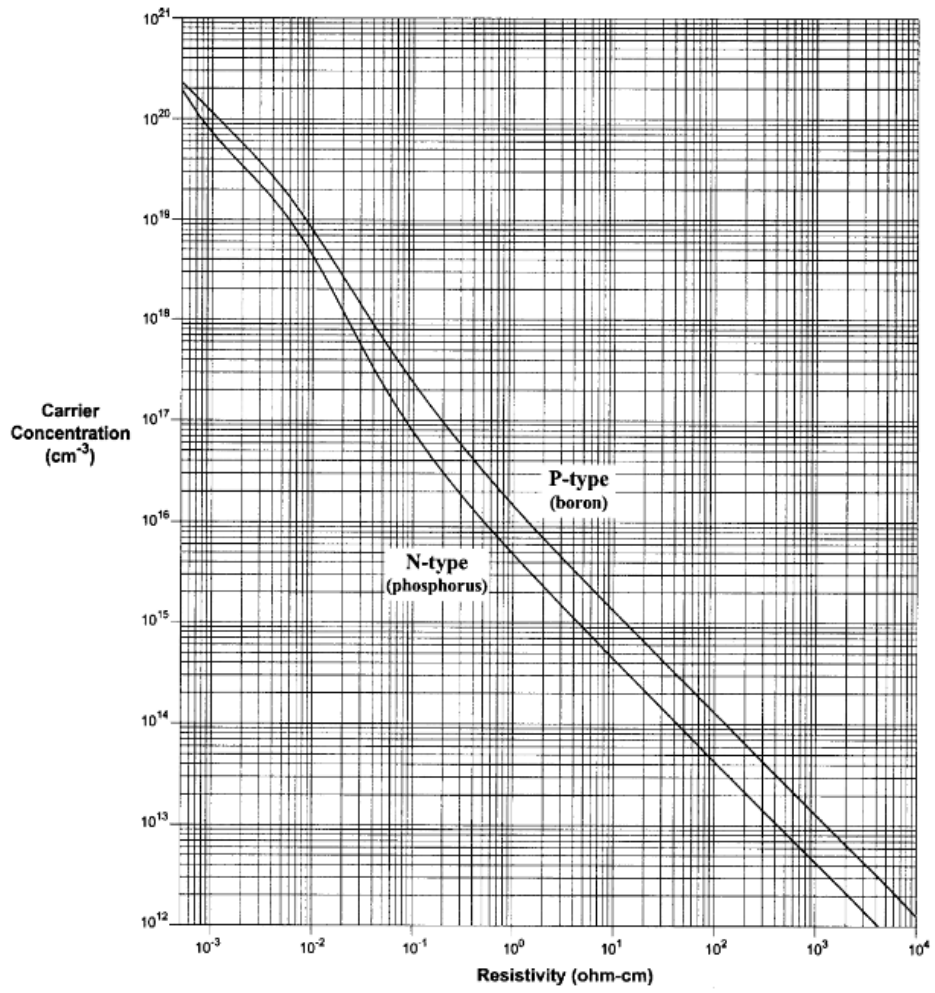


Figure 24: Silicon resistivity and doping concentration [32]

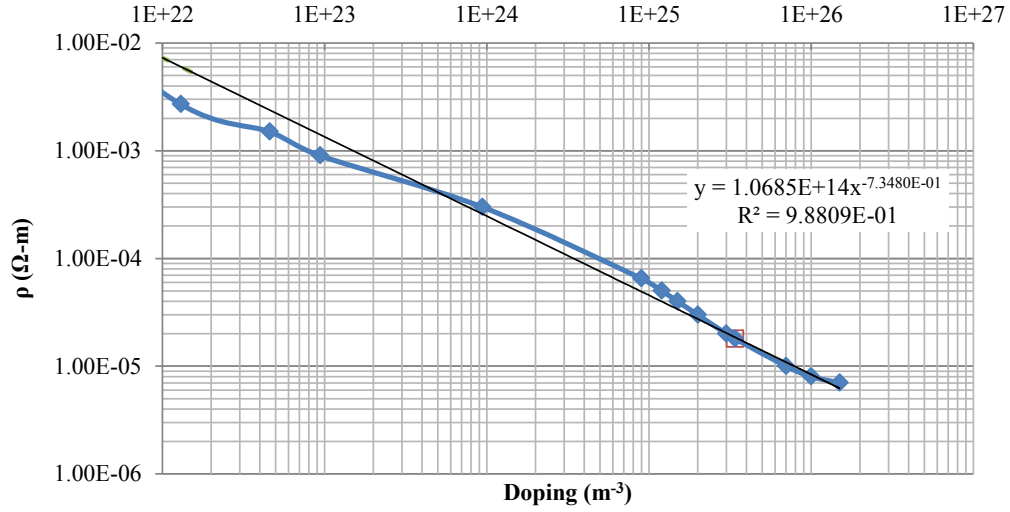


Figure 25: Carrier concentration values (figures adapted from [31], Table 10 (pg. 34) and Table 14 (pg. 40) and [32]).

In this case, the resistance R results in equation 49 and the total noise voltage is given by equation 50.

$$R = (1.07 \times 10^{14} N^{-0.735}) \frac{wt_r}{l_r} \quad 49$$

$$e_{total} = \sqrt{\left[4k_B T \left(\frac{1.07 \times 10^{14} wt_r}{N^{0.735} l_r} \right) (f_{max} - f_{min}) \right]^2 + \left[\frac{1}{4} \frac{V_b^2 \alpha}{N (wt_r l_r)} \ln \left(\frac{f_{max}}{f_{min}} \right) \right]^2 + [V_b q (f_{max} - f_{min})]^2} \quad 50$$

Expected Signal to Noise Ratio

The signal to noise ratio is the most significant figure of merit for the force sensor for this cell biomechanics application since it determines the minimum detectable force.

The signal to noise ratio for a homogeneous beam is shown in equation 51, and the signal to noise ratio for a beam with two cutouts of width g which leave a remaining ribbon at the edge of width t_r is shown in equation 52.

$$\frac{V_u}{e_{total}} = \frac{V_b \left[(6784 - 107 \ln(N)) \left(\frac{F(L - l_2) \left(\frac{t}{2} \right)}{\frac{wt^3}{12}} \right) - 1 \right]}{\sqrt{\left[4k_B T \left(\frac{1.07 \times 10^{14} wt_r}{N^{0.735} l_r} \right) (f_{max} - f_{min}) \right]^2 + \left[\frac{1}{4} \frac{V_b^2 \alpha}{N(wt_r l_r)} \ln \left(\frac{f_{max}}{f_{min}} \right) \right]^2 + [V_b q (f_{max} - f_{min})]^2}} \quad 51$$

$$\frac{V}{e_{total}} = \frac{V_b \left[(6784 - 107 \ln(N)) \left(\frac{F(L - l_2) \left(\frac{t}{2} \right)}{\frac{2w}{3} \left[\left(\frac{t}{2} \right)^3 - \left(\frac{t}{2} - t_r \right)^3 + \left(\frac{t}{2} - t_r - g \right)^3 \right]} \right) - 1 \right]}{\sqrt{\left[4k_B T \left(\frac{1.07 \times 10^{14} wt_r}{N^{0.735} l_r} \right) (f_{max} - f_{min}) \right]^2 + \left[\frac{1}{4} \frac{V_b^2 \alpha}{N(wt_r l_r)} \ln \left(\frac{f_{max}}{f_{min}} \right) \right]^2 + [V_b q (f_{max} - f_{min})]^2}} \quad 52$$

These equations are used to produce a set of figures which reveal the optimal design choices (see Estimates of Mechanical Behavior below). The general effects of various parameters which are important to the force sensor design are summarized in Table 6.

Table 6: Summary of parameter effects on sensitivity and signal to noise ratio

Parameter	Effect on Sensitivity		Effect on Noise Level	
Silicon Resistivity (↓)	↓	Piezoresistivity coefficient decreases ↓ Reduced sensitivity	↓	Thermal noise and 1/f noise decrease
Bridge Voltage (↑)	↔	None	↓	Signal level is higher compared to background noise
			↑	All noise levels increase at differing rates
Piezoresistor Width (↓)	↓	Reduced cross-sectional area	↓	Reduced cross-sectional area
	↑	Increased stress	↑	Increased resistance
	↑	Increased resistivity change (piezoresistivity)	↑	Increased noise
	↑	Increased sensitivity		
Piezoresistor Length (↑)	↔	None <i>Expect that very long beams cause the model to deviate from actual stresses</i>	↑	Increased length
			↑	Increased resistance
			↑	Increased noise
Cantilever Beam Length (↑)	↑	Stress at base of cantilever increases for given force	↔	None
	↑	Increased sensitivity		<i>Dominant noise source is not thermal-mechanical noise and so is not dependent on the harmonic frequencies of the structure</i>
Parasitic Bridge Resistance (↑)	↓	Reduced sensitivity <i>Combined with the piezoresistor width and length, this sets the lower limit for Si resistivity</i>	↔	None

Fabrication Process and Layout

Fabrication

The fabrication process (Appendix I: Layout) is based on SOI wafers that are n-type doped by the manufacturer to a conductivity of between 1 and 5 mΩ-cm. The actual resistivity after fabrication was measured to be between 1.3 and 2.5 mΩ-cm (see Device Test Results in Appendix I: Layout). The detailed fabrication process developed for the Sherman Fairchild Laboratory clean room is listed in Appendix I: Layout.

Layout

A number of the dimensions of the force sensor are chosen to optimize the performance of the force sensor. Detailed diagrams of the force sensor are shown in Figure 18 and Figure 26, and a summary of parameters is listed in Table 7. All variations included in the layout (revision 1) are listed in Appendix I: Layout.

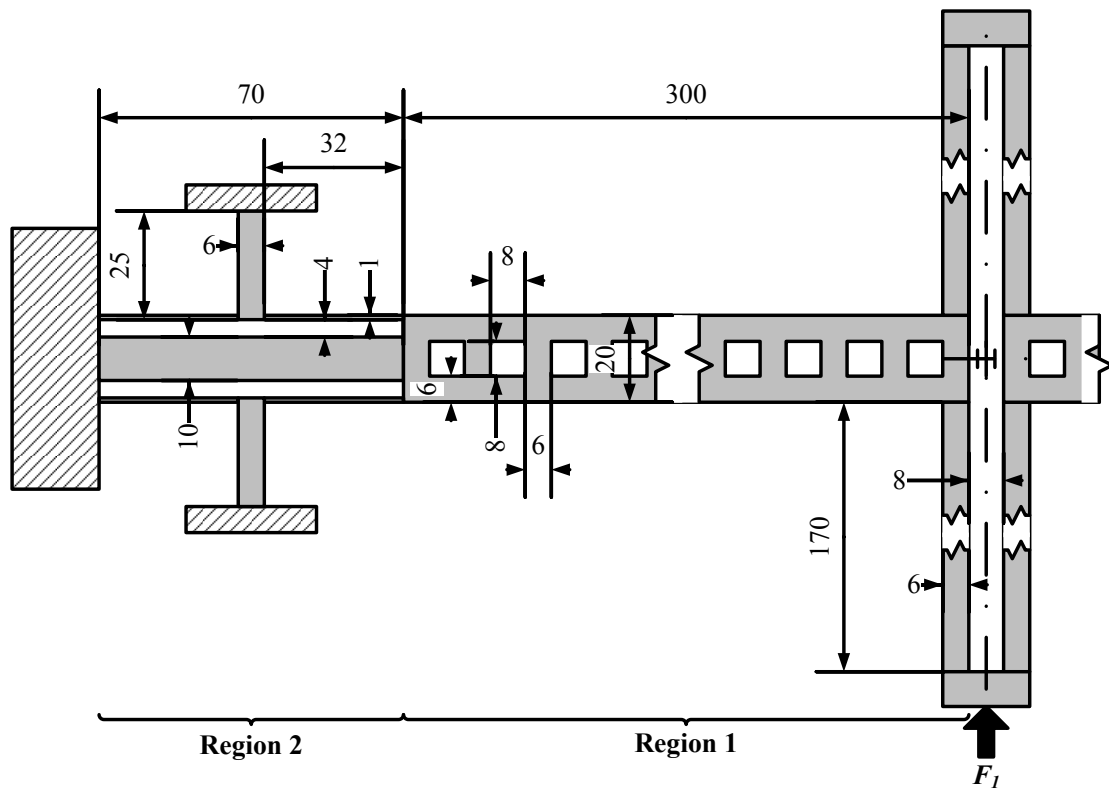


Figure 26: Force sensor mechanical diagram with typical dimensions (in micrometers).

The optimization of SNR is discussed in detail above, and the combination of layout rules and optimal design parameters resulted in the following design choices.

Free-Standing Beam Length

Stiction limits the length of all free-standing beams defined in the device layer, since low out-of-plane stiffness may allow them to stick to the handle wafer surface $2 \mu\text{m}$

below them. When the design was developed, it was unclear what the maximum permissible length would be, but subsequent fabrication indicated that the 600 μm beams were too long and stiction was a common problem.

Etch Release

Free-standing structural beams (such as the struts (t_e) in the cantilever beam) should be wide enough to be rigid, but still allow them to be under-etched in a reasonable time. Typical beam size was chosen to be 6 μm as a compromise between strength and etch release time.

Force Sensor Dimensions

The beam length (l_l) should be long to increase sensitivity and various lengths were fabricated to verify modeled behavior.

The transducer width (t_r) should be narrow to maximize stress in the piezoresistor, but it is limited by the fabrication resolution of 1 μm and the tendency of thin free-standing silicon structures to break during fabrication. Subsequent fabrication showed that 1 μm beams frequently broke, but 2 μm beams rarely broke.

Beam width (t_2) should be narrow to increase the stress at the base, and the transducer gap width (gap) acts as a stress concentrator and should be wide. However, these choices are limited by the need to place a metal trace at the base (d) to connect the piezoresistive transducers. Starting with the metal trace width of 6 μm , which runs along the base of the cantilever, the center part of the transducer (d) should be 2 μm wider on each side leading to a width of 10 μm . If transducer isolation gap is 4 μm and

the transducer width (t_r) is 1 μm , then the beam width (t_2) is 20 μm . Using a strut size (a) of 6 μm , this results in an etch hole size (b) of 8 μm .

Yoke beam length should be long enough that it does not add significant stiffness to the force sensor. This was chosen to be 170 μm , which adds approximately 5% stiffness to the force sensor based on the 300 μm beam length.

The side beam length (l_3) should be long enough to prevent significant distortion of the stress in the transducer piezoresistors, but additional length adds parasitic resistance to the bridge. Finite element simulations indicated that 25 μm was sufficient to limit this unbalancing effect to about 10% of overall stress (see Figure 36 and Table 15).

Device Layer Thickness

The device layer height was chosen to be 10 μm , causing the top of the device layer to be 12 μm above the surface of the handle wafer following the oxide etch release step. This was considered sufficient to compress a 10-15 μm diameter cell resting on the surface, *but future designs should use a device layer height at least 20 μm in order to allow bigger cells to be tested.* Since the force sensor's sensitivity is independent of the device layer height, the only limitation is the aspect ratio capability of the DRIE fabrication step.

Table 7: Force Sensor Parameters and Dimensions Summary

Region	Variable*	Value	Description
1	l_1	300, 450, or 600 μm	Cantilever beam length
1	<i>Strut (a)</i>	6 μm	Beam strut width
1	<i>Hole (b)</i>	8 μm	Beam hole width
1	<i>Edge (t_e)</i>	6 μm	Beam edge width
1	t_2	20 μm	Total beam width
2	t_r	1 or 2 μm	Transducer ribbon width
2	l_r	16, 32, or 64 μm	Transducer ribbon length
2	<i>gap</i>	4 μm	Transducer isolation gap
2	l_2	$t_3+2(l_r)$	Region 1 length
3	t_3	6 μm	Side beam width
3	l_3	25 μm	Side beam length
4	l_4	170 μm	Yoke beam length
4	t_4	8 μm	Yoke beam width
-	h	10 μm	Device layer height

* see Figure 26 which shows a force sensor with variables labeled

For a complete listing of die variations included in fabrication, see Appendix I: Layout.

Estimates of Mechanical Behavior

Parametric Calculations

Sensitivity Estimate

Based on the mechanical model described above, the expected stress in the transducer region was calculated for a variety of geometries, as well as the tip displacement and overall spring stiffness (see Table 8). A small test force of 1 μN was applied at the tip, and the stress was calculated at $x = l_2$ and $y = t/2 - l_r/2$.

Table 8: Parametric estimates from simple cantilever beam bending at 1 μ N applied force with $t_r = 1 \mu\text{m}$.

Beam Length (μm)	Transducer Length (μm)	Ave Stress (MPa)	Max. Displace (nm)	Spring Stiffness (N/m)
300	16	0.450	7.4	67.3
300	32	0.450	9.7	51.3
300	64	0.450	16	31.8
450	16	0.675	22	22.4
450	32	0.675	27	18.5
450	64	0.675	38	13.1
600	16	0.900	50	10.0
600	32	0.900	58	8.64
600	64	0.900	76	6.57

The effect of the central yoke, which links the two cantilever beams in the force sensor, was estimated by combining its stiffness with that of the cantilever beams (see Table 9). The central yoke increases the bending stiffness of the force sensor and makes it slightly less sensitive. Although a certain test force is applied, the force sensor deflects as if a lower force is applied due to this added stiffness, and for estimation purposes, the test force was proportionally reduced.

Table 9: Parametric estimates from simple cantilever beam bending plus yoke at 1 μ N applied force with $t_r = 1 \mu\text{m}$.

Beam Length (μm)	Transducer Length (μm)	Ave Stress (MPa)	Max. Displace (nm)	Spring Stiffness (N/m)
300	16	0.459	7.1	70.3
300	32	0.448	9.5	52.6
300	64	0.423	16	31.2
450	16	0.622	19	26.2
450	32	0.604	23	21.8
450	64	0.566	32	15.4
600	16	0.732	37	13.4
600	32	0.709	43	11.7
600	64	0.661	54	9.2

Based on the stress computed for the transducer region, as well as the material properties of the doped silicon, the resistance (R) and change in resistance (ΔR) due to the piezoresistive effect are estimated (see Table 10).

Table 10: Parametric estimation of sensitivity at 1 μN applied force with $t_r = 1 \mu m$.

Beam Length (μm)	Transducer Length (μm)	R (Ω)	ΔR (Ω)	$\Delta R/R$	$(\Delta R/R)/F$ ($(\Omega/\Omega)/N$)
300	16	28.8	0.0070	0.000243	243
300	32	57.6	0.0137	0.000238	238
300	64	115.2	0.0258	0.000224	224
450	16	28.8	0.0095	0.000330	330
450	32	57.6	0.0184	0.000319	319
450	64	115.2	0.0345	0.000299	299
600	16	28.8	0.0111	0.000385	385
600	32	57.6	0.0216	0.000375	375
600	64	115.2	0.0402	0.000349	349

Noise Estimate

The expected intrinsic noise levels are computed below using the parameters in Table 11.

Table 11: Intrinsic noise estimate parameters.

Parameter	Value	Units	Description
k_B	1.3807×10^{-23}	J/K	Boltzmann's constant [29]
q	1.6022×10^{-19}	C	electron charge [29]
T	300	Kelvin	temperature
V_{bridge}	0.500	V_{rms}	bridge voltage
V_b	0.250	V_{rms}	bias voltage
α	5.00×10^{-6}		Hooke constant [24]
N	3.50×10^{25}	$1/m^3$	doping concentration
w_r	1.00×10^{-6}	m	piezoresistor width
t_r	10.0×10^{-6}	m	piezoresistor thickness

For direct DC measurements where the 1/f noise is the most significant factor, the overall noise decreases as the volume of the piezoresistor element increases and

decreases as the doping concentration increases (see Table 12). For measurements based on an AC bridge where thermal noise is the most significant factor, the overall noise decreases as the cross-section area to length ratio decreases and decreases as the doping concentration increases (see Table 13). Practically, this means that shorter piezoresistive elements are better when an AC bridge is used since the thermal noise is lower, and longer piezoresistive elements are better when a direct DC bridge is used since the $1/f$ noise is lower.

Table 12: Noise estimate for $f_{min}=0.1$ Hz to $f_{max}=100$ Hz.

l_r (μm)	R (Ω)	V_i (nV)	V_t (nV)	V_f (nV)	e_n (nV)
4	7	2.0	3.4	39.3	39.5
8	14	2.0	4.8	27.8	28.3
16	28	2.0	6.8	19.6	20.9
32	56	2.0	9.6	13.9	17.0
64	112	2.0	13.6	9.8	16.9

Table 13: Noise estimate for $f_0=3000$ Hz and bandwidth of 100 Hz.

l_r (μm)	R (Ω)	V_i (nV)	V_t (nV)	V_f (nV)	e_n (nV)
4	7	2.0	3.4	2.7	4.8
8	14	2.0	4.8	1.9	5.6
16	28	2.0	6.8	1.4	7.2
32	56	2.0	9.6	1.0	9.9
64	112	2.0	13.6	0.7	13.8

Signal to Noise Ratio Estimates

By entering all of the design dimensions and governing equations into MATLAB, the sensitivity and SNR can be plotted as a function of a number of parameters. This provides an indication of the most relevant factors to vary as well as optimal values for the design dimensions. Using the behavioral model described above for a beam with two regions of different area moment of inertia, the stress per unit force is computed at

the x-position near the edge of region 2 and the y-position near the edge of the beam (at the center of transducer ribbon, $y = t/2 - t_r/2$), and it is then assumed to be uniform within the transducer ribbon. Six parameters were varied and the overall sensitivity as well as signal to noise ratio were plotted in Figure 27 through Figure 31.

The sensitivity alone is an important parameter, but more important is the signal to noise ratio. Since the silicon material chosen here is heavily doped, the 1/f noise is relatively low and the dominant noise source is thermal noise. The disadvantage to this strategy is that parasitic resistances play a much larger role when the resistance of the individual elements is quite low. After the silicon doping is chosen, the most important design parameters are the beam length (see Figure 29) and the width of the piezoresistive transducer ribbon (see Figure 30). The longer the beam length, the more stress is generated at the base for a particular force. The narrower the transducer ribbon, the higher the stress concentration in the piezoresistive sensing element; but also the higher the resistance of the piezoresistor and so the higher the thermal noise. Any of the parameters that affect the dimensions of the transducer region also affect resistance, and so play a part in the thermal noise. Note that the sensitivity generally decreases as the resistance of the transducer ribbon becomes small, and the sensitivity is limited by a parasitic resistance that has been included in all the calculations (4.7 Ω) based on an estimate of traces' resistances from their geometry.

The overall sensitivity decreases as the silicon resistivity increases due to the dependence of the piezoresistivity constant on doping at high doping levels, but the bridge sensitivity is insensitive to the applied voltage since a ratiometric measurement is

made (see Figure 27 left). The signal to noise ratio increases as the silicon resistivity decreases (both thermal noise and 1/f noise decrease), but eventually the piezoresistivity constant causes sensitivity to decrease so there is an optimal band around 2 mΩ-cm. As the applied voltage increase, SNR increases until 1/f noise dominates (see Figure 27 right).

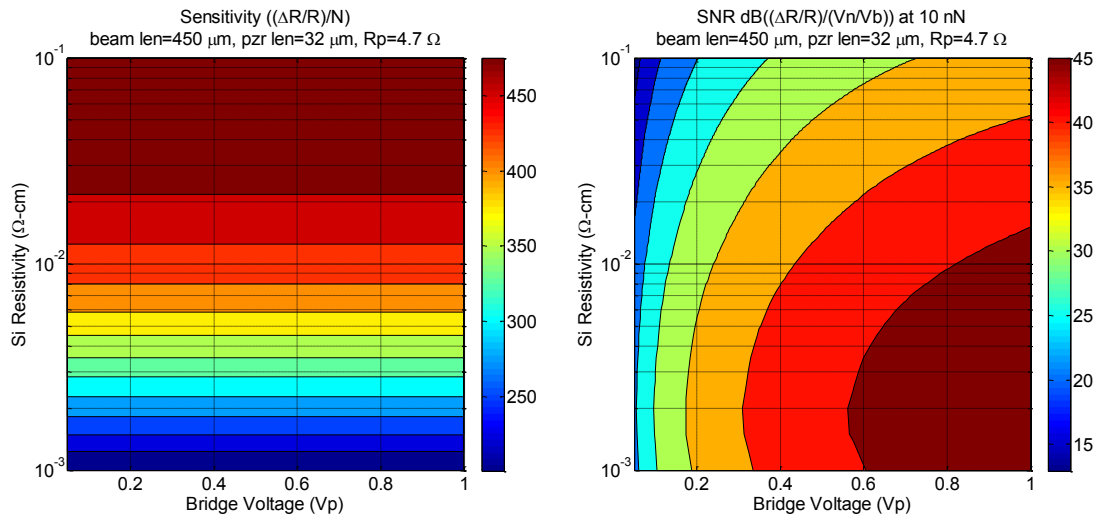


Figure 27: Estimated sensitivity (left) and SNR (right) of the force sensor as a function of applied voltage and silicon resistivity.

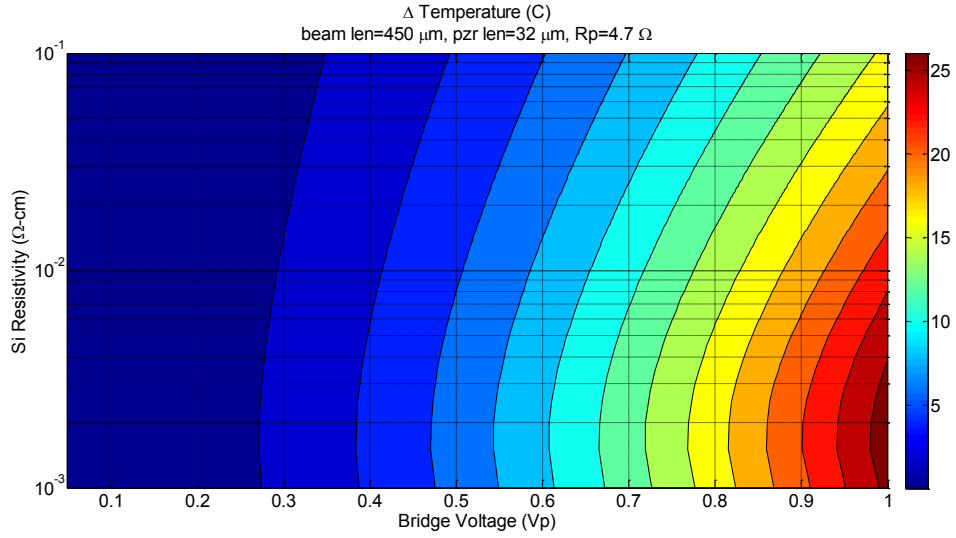


Figure 28: *Estimated maximum temperature rise of the force sensor as a function of applied voltage and silicon resistivity.*

An optimal transducer ribbon length is about 10 to 20 μm for the beam lengths shown, and the cantilever beam should as long as is feasible without succumbing to stiction problems (see Figure 29).

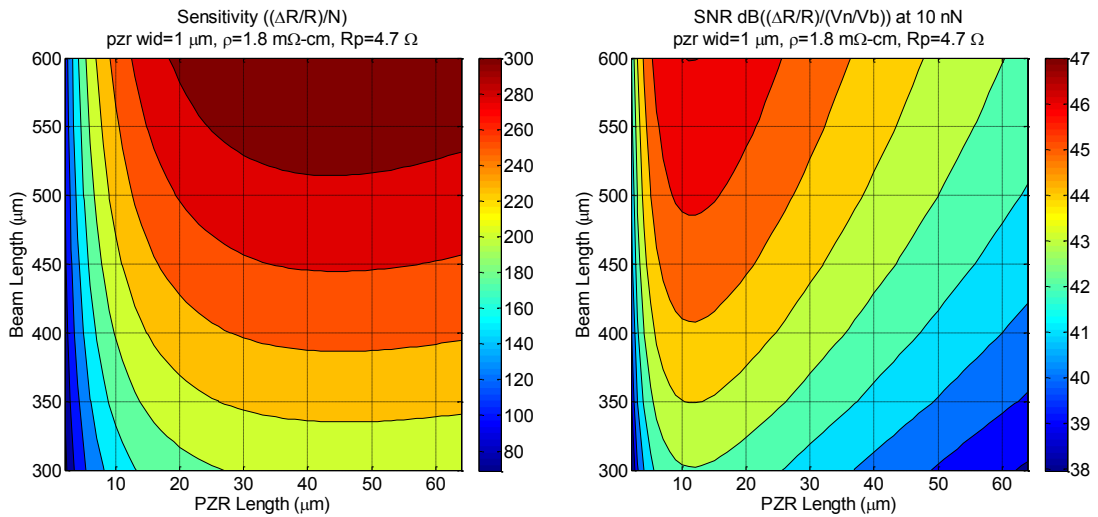


Figure 29: *Estimated sensitivity (left) and SNR (right) of the force sensor as a function of the cantilever beam length and the piezoresistive element length.*

The width of the transducer ribbon should be made as small as possible, and the SNR increases as the length (and hence resistance) decreases, but is limited by the parasitic resistance in the bridge (see Figure 30). However, the transducer ribbon is free-standing so the width needs to be sufficient for a robust structure (transducers less than 1 μm wide typically broke by the end of the processing).

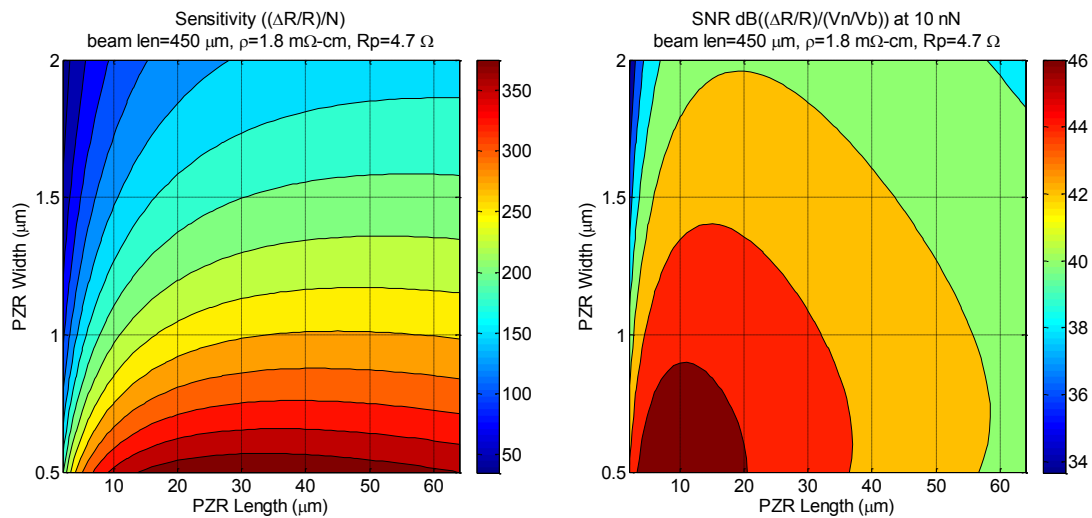


Figure 30: Estimated sensitivity (left) and SNR (right) of the force sensor as a function of the piezoresistive element width and the piezoresistive element length.

The parasitic resistance in the bridge (which is the trace resistance between the transducer ribbon elements) should be minimized since it limits the maximum sensitivity that can be achieved (see Figure 31).

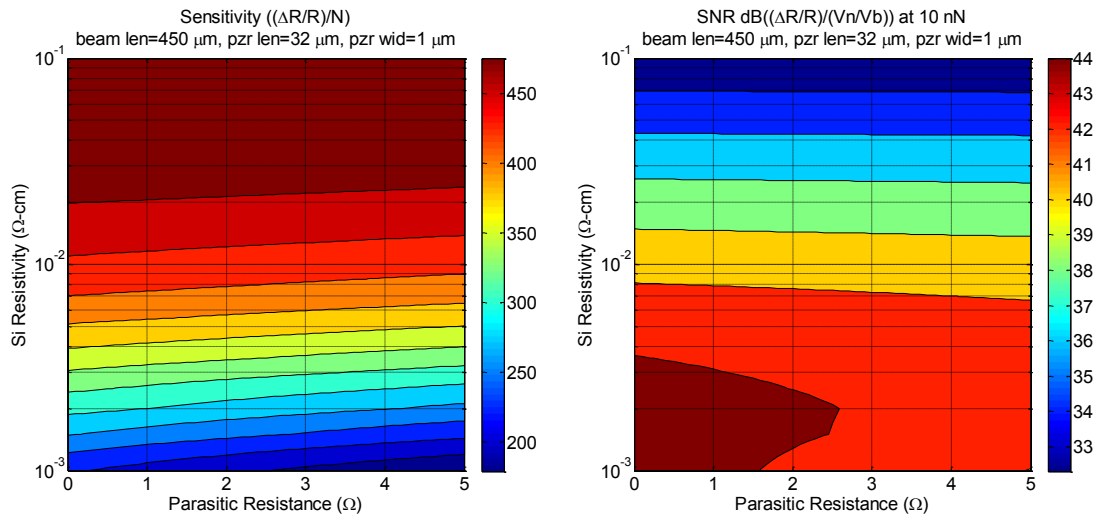


Figure 31: Estimated sensitivity (left) and SNR (right) of the force sensor as a function of parasitic trace resistance and silicon resistivity.

FEA Simulation with CoventorWare

To verify the design, a solid model was created in CoventorWare and analyzed using the built-in MemMech solver using a half-symmetric model made from silicon. The material properties used for the simulation are shown in Table 14, and the silicon <100> plane is aligned along the x-axis.

Table 14: Silicon material properties used in FEA simulation [34].

Parameter		Value	Unit	Common Value
Elastic modulus	E_1	1.657e+005	MPa	165.7 GPa
	E_2	6.390e+004		63.90 GPa
	E_3	7.960e+004		79.60 GPa
Poisson ratio	ν_{12}	2.780e-001		
	ν_{13}	2.780e-001		
	ν_{23}	2.780e-001		
Shear Modulus	G_{12}	7.964e+004	MPa	79.64 GPa
	G_{13}	7.964e+004		
	G_{23}	7.964e+004		
Density	D	2.331e-015	$\text{kg}/\mu\text{m}^3$	
Conductivity	ρ	5.556e+010	$\text{pS}/\mu\text{m}$	
Piezoresistivity	π_{11}	-5.300e-004	MPa^{-1}	
	π_{12}	2.770e-004		
	π_{44}	-7.050e-005		

Note that depending on the options chosen in its internal materials properties database, CoventorWare will *automatically transform the piezoresistive tensor matrix* in order to align the X axis so that it is perpendicular to the wafer flat. This is useful for $\{100\}$ type wafers where the primary flat is the $\{110\}$ plane, since what are referred to as the X and Y axes are at 45 degrees to the wafer flat (see Figure 33). It would be inconvenient use the built-in Layout Editor with everything at 45 degrees. With this in mind, special attention must be paid to properly enter the options in CoventorWare to ensure accurate simulation results.

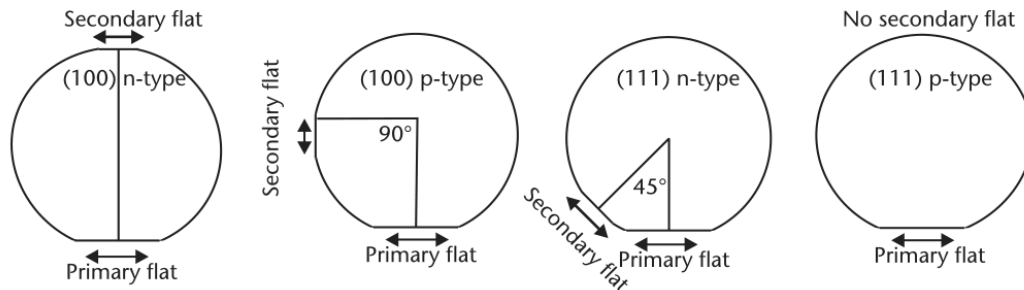


Figure 32: Illustration showing the primary and secondary flats of $\{100\}$ and $\{111\}$ wafers for both n-type and p-type doping (SEMI M1-0302) [35].

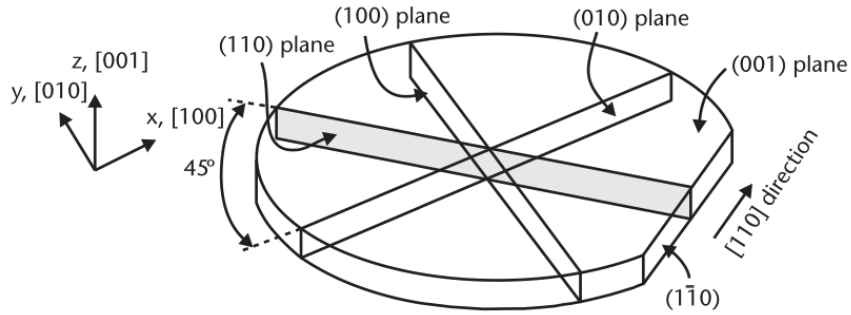


Figure 33: Illustration identifying various crystal planes in a wafer of $\{100\}$ orientation [35].

Summary of stress and displacement

A series of simulations was conducted to determine the resulting stress as two design parameters were varied: the beam length in region 1 and the transducer length in region 2 (see Figure 18). The height of the structure was kept at $10\ \mu\text{m}$ and material properties were not varied. For the mechanics simulations, movement was restricted to the xy-plane to reduce simulation complexity, but for modal / harmonic simulations, the movement was unrestricted. The model size was reduced by simulating a half-symmetric structure.

The resulting stress varied as the design parameters for cantilever beam length and transducer ribbon length varied, but a representative stress distribution is shown below in Figure 34, Figure 36 and Figure 38. Although Mises stress is shown, only the x-direction stress contributes significantly and so Mises is equivalent to x-direction stress (the Mises value is easiest to extract from CoventorWare’s result tables).

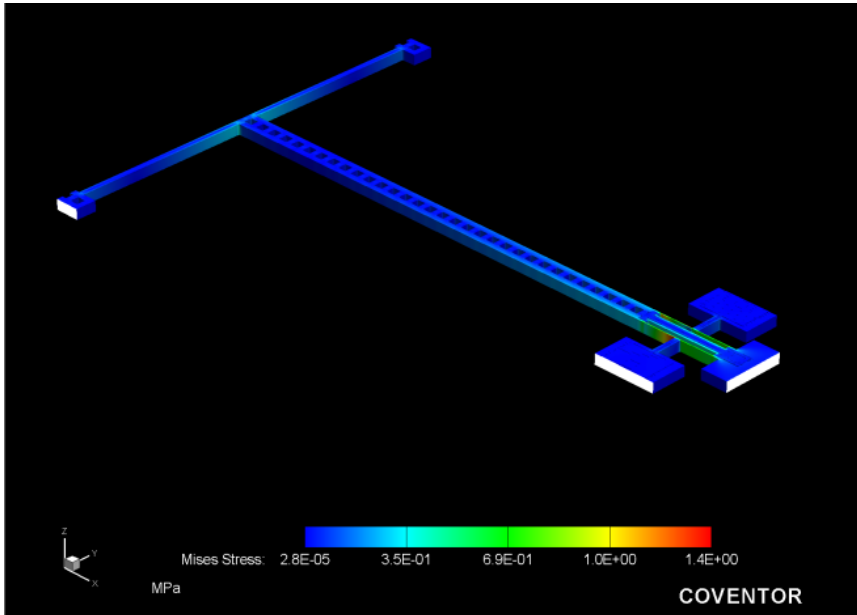


Figure 34: A load of $0.5 \mu\text{N}$ was applied to the front face of the cantilever (labeled in white, left side) which corresponds to $1 \mu\text{N}$ for both halves of the model. The outer faces of the three rectangular blocks at the base of the cantilever are fixed in all directions (labeled in white, right side).

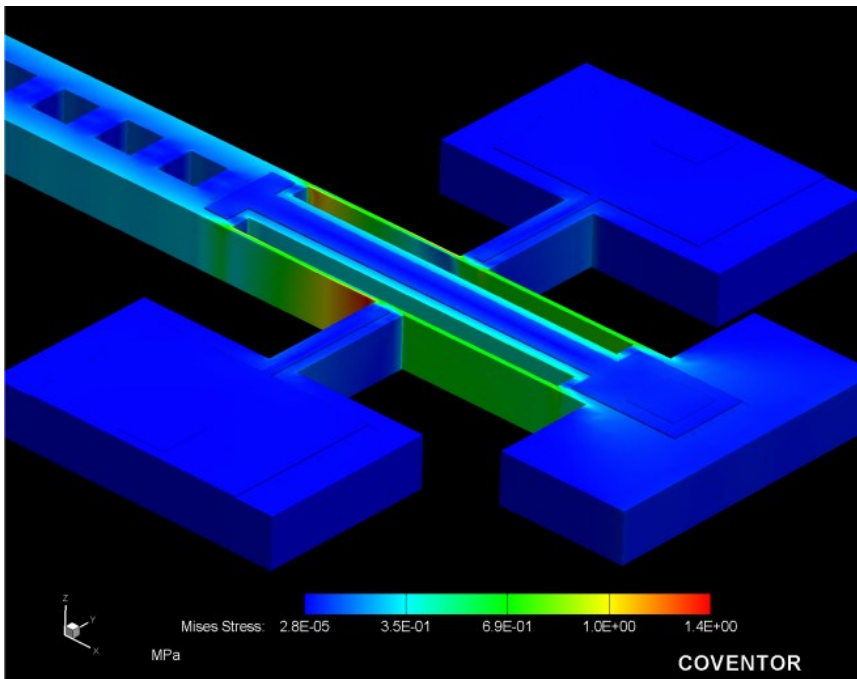


Figure 35: Representative results of stress in the transducer region for $1 \mu\text{N}$ load. The beam length is $450 \mu\text{m}$ and the transducer length is $32 \mu\text{m}$. The height of the structure is $10 \mu\text{m}$, and it is fabricated from highly doped n-type silicon.

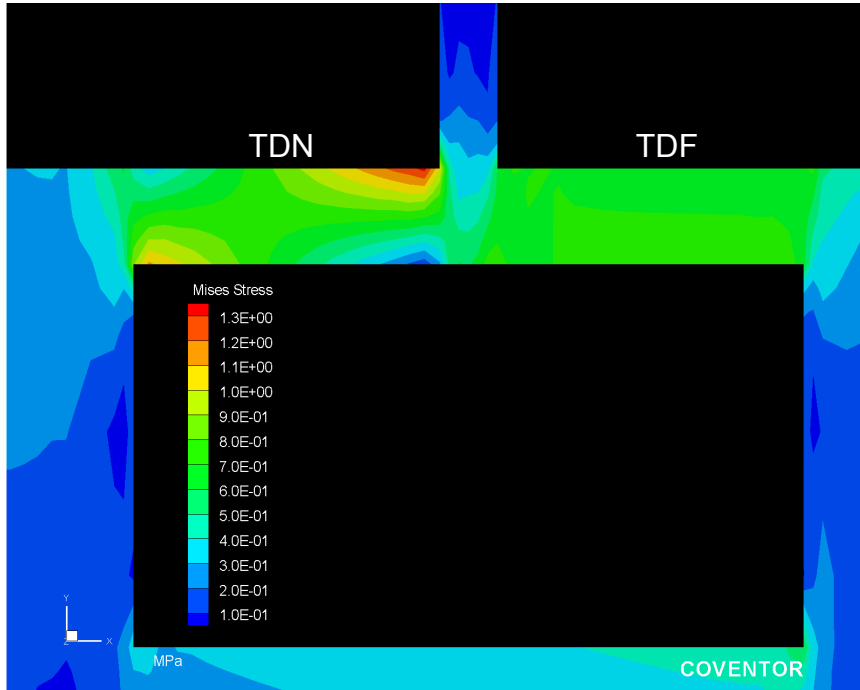


Figure 36: An XY slice through the transducer region of the previous figure. The figure has been exaggerated in the y-direction to show the stress distribution in the 1 μm wide transducer region can be seen.

The results of the series of simulations are tabulated below in Table 15 and Table 16, where the abbreviation TDN refers to stress in the “near” transducer ribbon closer to the plane of symmetry (bottom right in Figure 35), and the abbreviation TDF refers to stress in the “far” transducer ribbon closer to the anchored base (upper left in Figure 35).

Table 15: Parametric simulation results from the MemMech mechanical solver (stress).

Beam Length (μm)	Transducer Length (μm)	TDN ¹ , Stress (MPa)	TDF ² Stress (MPa)	Ave Stress (MPa)
300	16	0.524	0.504	0.514
300	32	0.538	0.510	0.524
300	64	0.559	0.513	0.536
450	16	0.723	0.695	0.709
450	32	0.734	0.696	0.715
450	64	0.747	0.686	0.717
600	16	0.931	0.896	0.913
600	32	0.940	0.892	0.916
600	64	0.947	0.870	0.908

¹TDN: transducer near to center as shown labeled in Figure 36.

²TDF: transducer far from center

Table 16: Parametric simulation results from the MemMech mechanical solver (displacement).

Beam Length (μm)	Transducer Length (μm)	Maximum Displacement (nm)	Spring Stiffness (N/m)
300	16	9.3	107
300	32	13	74.8
300	64	23	43.3
450	16	22	45.8
450	32	29	34.5
450	64	45	22.2
600	16	44	22.7
600	32	55	18.1
600	64	80	12.5

Summary of piezoresistive response

Using the previously computed stress distribution, the change in resistivity was found using CoventorWare’s MemPZR solver. This solver is able to compute the change in resistivity as well as the resulting current density in the model due to the computed stress and applied voltage. A voltage potential of 500 mV was applied to each anchor pad connected to the side beams, and 0 V was applied to the base. The current density distribution is shown below (see Figure 38), as well as the tabulated values for the sensitivity ($\Delta R/R$) (see Table 17).

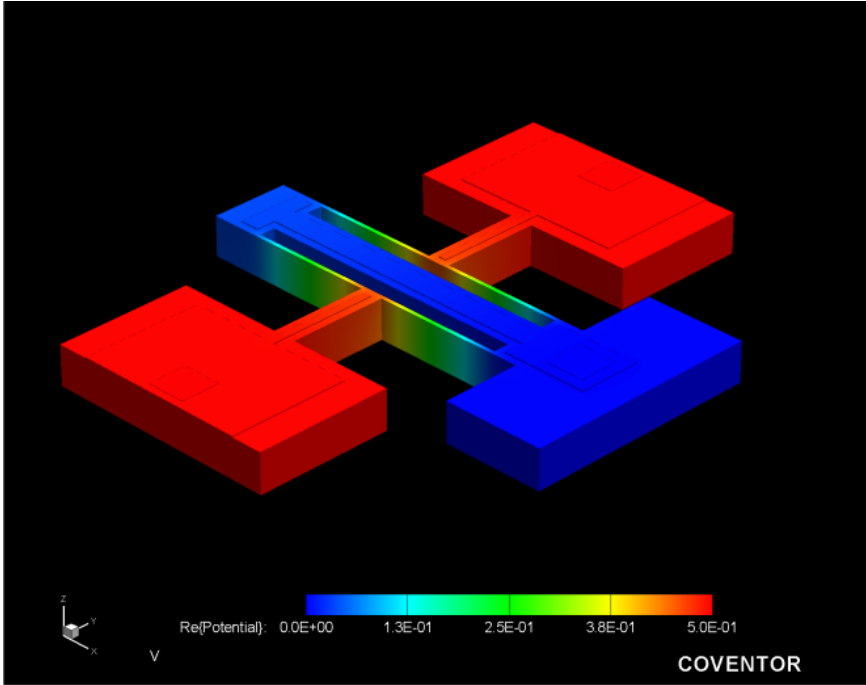


Figure 37: Representative results from the piezoresistive solver showing the applied voltage potential.

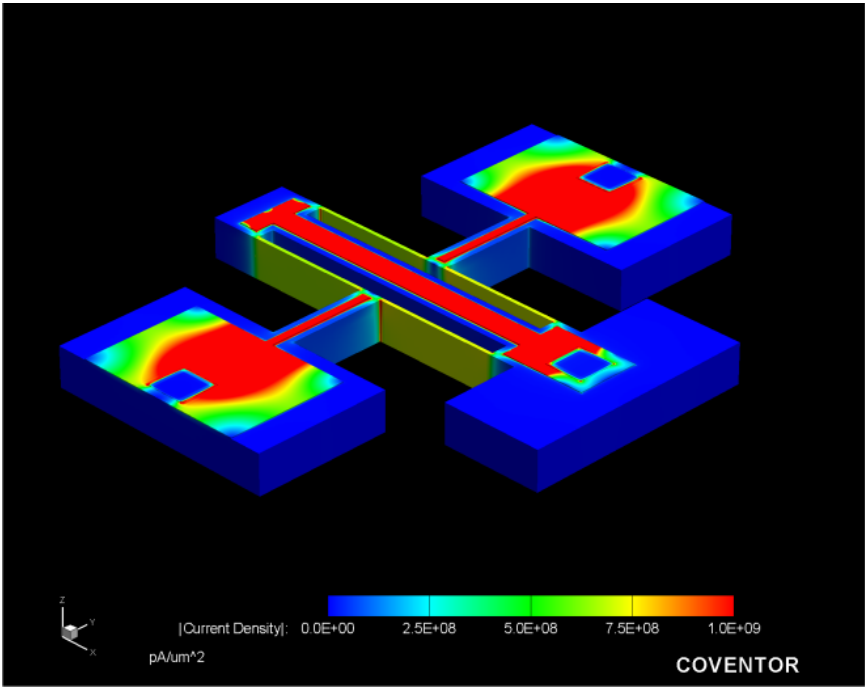


Figure 38: Representative results from the piezoresistive solver showing the resulting current density while under stress.

Table 17: Parametric simulation results from the MemPZR piezoresistive solver.

Beam Length (μm)	Transducer Length (μm)	R (Ω)	ΔR (Ω)	$\Delta R/R$	$(\Delta R/R)/F^*$ $((\Omega/\Omega)/N)$
300	16	21.4	0.004287	0.000176	176
300	32	36.3	0.008511	0.000217	217
300	64	66.1	0.017143	0.000248	248
450	16	21.4	0.005914	0.000242	242
450	32	36.3	0.011606	0.000295	295
450	64	66.1	0.022924	0.000332	332
600	16	21.4	0.007621	0.000312	312
600	32	36.3	0.014868	0.000378	378
600	64	66.1	0.029053	0.000421	421

**Force applied is 1 μN*

Summary of resonant mode

The modal / harmonic option of MemMech in CoventorWare was used to solve for the first three vibration modes since the stiffness of the cantilever beam and its fundamental frequency are related the thermal-mechanical noise of the force sensor (see next section). The modes of movement (see Figure 39) were found to be: (a) beam vibrates in vertical direction (out of plane z-direction), (b) beam vibrates in lateral direction (xy-plane), and (c) beam twists around beam axis (x-axis). Of these, the vibration in the lateral direction is the most relevant since this motion causes compressive and tensile stress in the piezoresistive-transducer region just like a force measurement. These results are tabulated below in Tables 4, 5, and 6.

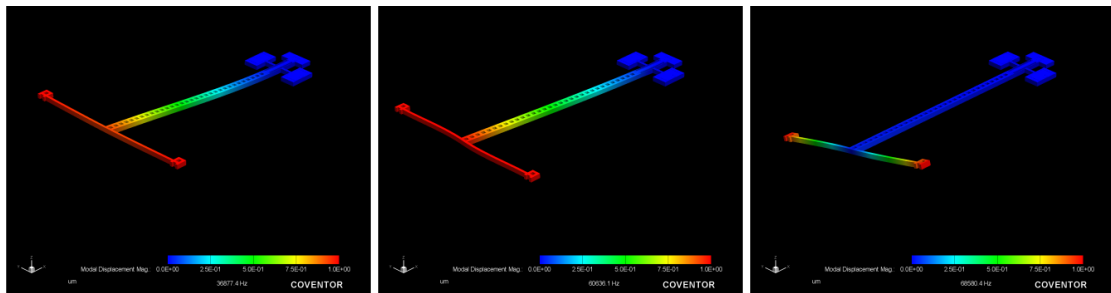


Figure 39: Representative results for the first three modes of vibration where the beam length is 450 μm and the transducer length is 32 μm .

Using harmonic analysis option of MemMech, the quality factor was estimated to be 5. These results were used to estimate the thermal-mechanical noise [13], but this was found to be a small source of noise compared to the other noise sources. Equation 53 shows the thermal mechanical noise (F_{tm}) in units of Newtons/ $\sqrt{\text{Hz}}$ where k is the overall spring constant of the structure, Q is the quality factor, k_B is Boltzmann's constant, f_0 is the resonant frequency, T is the temperature, and B is the measurement bandwidth. The force noise was converted to a voltage noise using the expected sensitivity of the force sensor.

$$F_{tm} = \sqrt{\frac{4kk_BTB}{2\pi f_0}} \quad 53$$

Table 18: Harmonic 1 – Vertical (out of plane) vibration.

		Transducer Length		
		16 μm	32 μm	64 μm
Beam Length	300 μm	63.9 KHz	58.9 KHz	50.5 KHz
	450 μm	39.3 KHz	36.9 KHz	32.7 KHz
	600 μm	25.8 KHz	24.5 KHz	22.3 KHz

Table 19: Harmonic 2 – Lateral (xy plane) vibration.

		Transducer Length		
		16 μm	32 μm	64 μm
Beam Length	300 μm	115.9 KHz	95.0 KHz	70.0 KHz
	450 μm	70.7 KHz	60.6 KHz	47.2 KHz
	600 μm	47.1 KHz	41.3 KHz	33.4 KHz

Table 20: Harmonic 3 – Twist along beam axis vibration.

		Transducer Length		
		16 μm	32 μm	64 μm
Beam Length	300 μm	80.9 KHz	77.7 KHz	72.2 KHz
	450 μm	71.1 KHz	68.6 KHz	64.7 KHz
	600 μm	63.0 KHz	61.5 KHz	58.7 KHz

Sensitivity Characterization

Cantilever Reference Springs

In order to apply a known force to the newly fabricated force sensor so that their output can be calibrated, a spring of known spring constant is needed. In practice, this means that a fixed-free beam of known dimensions and known material needs to be fabricated. Free-standing cantilever beams manufactured using MEMS techniques are available, such as the nanoScience FCL-5 reference spring pack. These springs are relatively stiff and have an accuracy of +50%/-30%.

As an alternative, gold bonding wire (American Fine Wire Corp. 0.001 inch diameter, 99.99% gold with trace beryllium) has been glued onto the ends of tungsten probe tips (American Probe & Technologies 72T-J3/20) (see Figure 40 and Figure 41). Even with uncertainties in measurement of the dimensions, the accuracy is expected to be better than $\pm 30\%$. While assembling the tips, care must be taken to avoid excess glue on the shaft of the gold wire, which will alter the spring constant and also add significant mechanical “noise” to the load/unload measurement. The best method is to place a drop of glue at the end of a tungsten tip bent into a circular loop and then lower the gold bonding wire into the drop of glue. After the glue has dried, the gold wire can be trimmed to length under the microscope by mounting it in a probe station

micromanipulator and using a surgical scissors guided by a jig mounted to the wafer chuck. Repeated attempts are normally needed to get a flat end at the free tip of the gold wire.

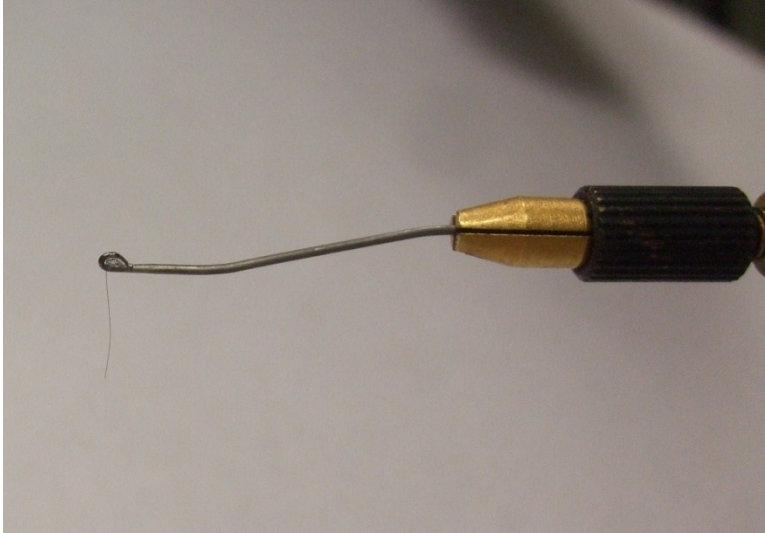


Figure 40: Gold bonding wire attached to a tungsten probe tip which can be mounted in a probe station micromanipulator.

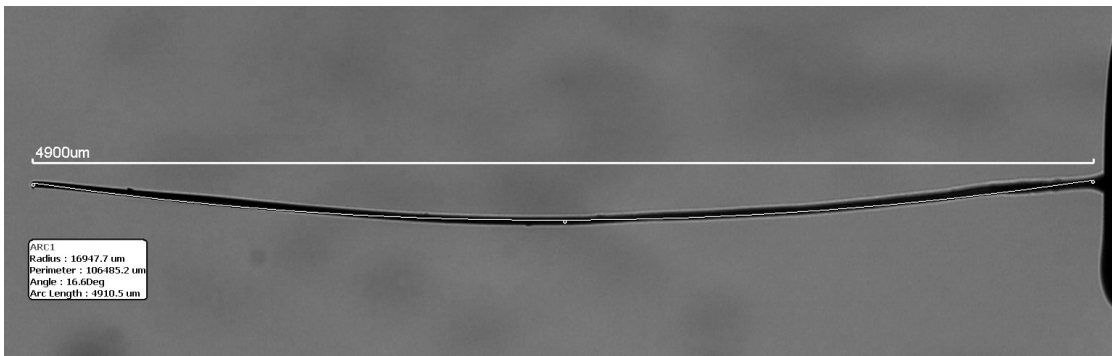


Figure 41: Gold bonding wire cantilever reference of length 4910 μm and width 25 μm.

The cross-section moment of inertia for a fixed-free cantilever beam of cylindrical cross-section is given by equation 54 where r is one-half the diameter of the beam.

$$I_x = \frac{\pi r^4}{4} \quad 54$$

Using linear beam bending theory, the spring constant of the cantilever beam is given by equation 55 where E is the elastic modulus of the material and l is the length of the cantilever beam. The elastic modulus (E) of 79 GPa was used for gold [40].

$$k = 3 \frac{EI_x}{l^3} \quad 55$$

For instance, using the 4910 μm long cantilever, the spring constant is 0.038 N/m which results in a force of 38 nN applied at the tip for every 1 μm the base is moved (or vice-versa). A 0.25 μm error in measurement of the diameter results in an 8% error in the spring constant k , and a 50 μm error in measurement of the length results in a 3% error. Given these uncertainties (4910 μm length $\pm 50 \mu\text{m}$ and 25 μm width $\pm 0.25 \mu\text{m}$) the spring constant is 0.038 ± 0.004 N/m ($0.038 \pm 11\%$ N/m). These expected values have been tabulated (see Table 21) and for comparison the specifications for a commercially available set of reference spring cantilevers (see Table 22).

Table 21: Gold wire cantilever specifications using diameter error $\pm 0.25 \mu\text{m}$ and length error $\pm 50 \mu\text{m}$.

Label	Length (μm)	Diameter (μm)	K (N/m) typical	K (N/m) min	K (N/m) max	K (N/m) min	K (N/m) max
#1	4500	25.0	0.050	0.044	0.056	-12%	+11%
#3	5000	25.0	0.036	0.033	0.041	-11%	+11%
#4	4910	25.0	0.038	0.034	0.043	-11%	+11%
#6	4968	25.0	0.037	0.033	0.041	-11%	+11%
#9	5600	25.0	0.026	0.023	0.029	-11%	+10%
#10	2625	25.0	0.259	0.225	0.297	-14%	+13%

Table 22: nanoScience FCL-5 reference spring cantilever specifications.

Label	K (N/m) typical	K (N/m) min	K (N/m) max	K (N/m) min	K (N/m) max
A	0.12	0.08	0.18	-33%	+50%
B	0.98	0.70	1.50	-29%	+53%
C	12.00	8.00	18.00	-33%	+50%
D	30.00	20.00	45.00	-33%	+50%
E	77.00	49.00	118.00	-36%	+53%

Piezo-Driver for Precise Movement

Integration of a piezo-driver with the micromanipulator body (Süss MicroTec PH120) was accomplished by a custom aluminum clamp that could be bolted onto the base so that the front of a Physik Instrumente (PI) P-216.4S piezo actuator was touching the side of one axis of the micromanipulator (see Figure 42 and Figure 43). Conveniently, two threaded holes are available on each side of the micromanipulator base to attach the clamp made from aluminum U-channel.

The micromanipulator uses a thumb-screw with an internal return spring to move the body on each of three axis defined by ball-bearing rails. There are three thumbscrews for each of the three x-y-z axis. To engage the piezo actuator, the thumbscrew is turned so that the micromanipulator's internal spring forces the body against the piezo actuator, and one lateral axis is then controlled by the piezo actuator.

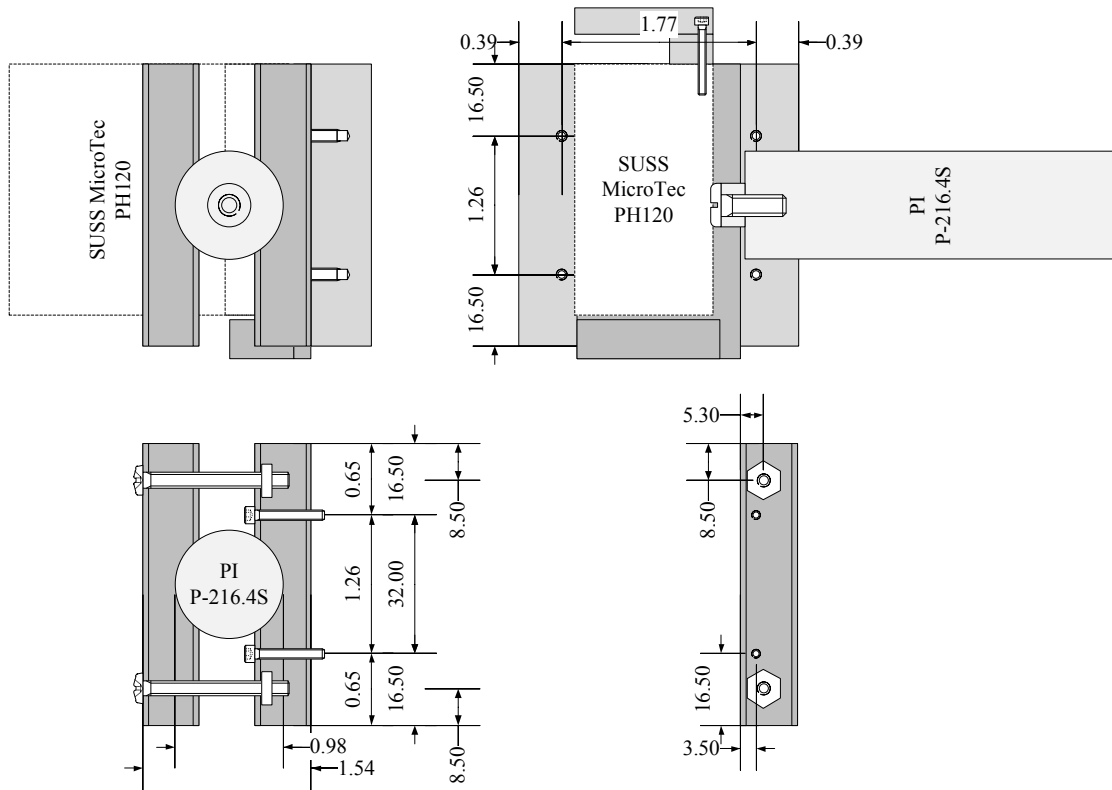


Figure 42: Mounting diagrams for SUSS MicroTec PH120 with Physik Instrument P-216.4S piezo actuator (all measurements in mm).

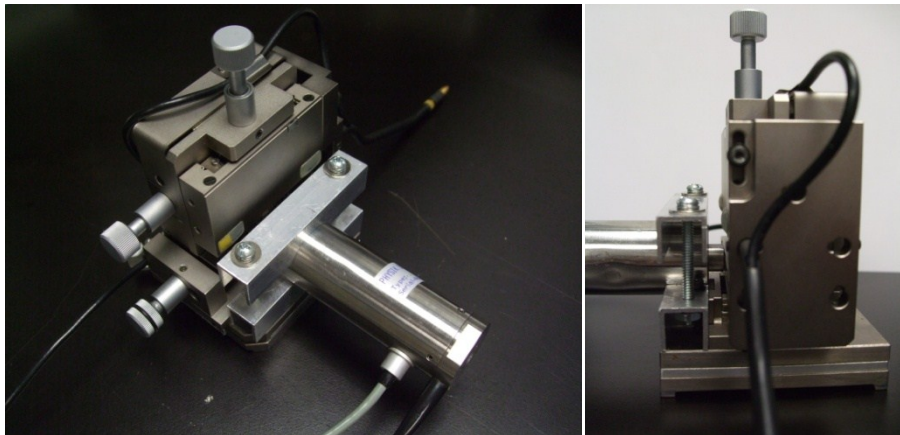


Figure 43: A piezo actuator mounted to the micromanipulator using a machined aluminum clamp.

The analog output voltage from a National Instruments (NI) USB-6009 DAQ module provides 0 V to 5 V to the Physik Instrumente (PI) HVPZT Amplifier E-471.00 (1000 V) control input, and the NI USB-6009 analog input is connected to the HVPZT

Amplifier monitor output. The movement of the micromanipulator can be then controlled from within LabView and the movement calibrated to the probe station microscope. With feedback control enabled (“servo” mode), the monitor indicates exact position with 10 nm precision, but in practice the accuracy of the position is limited by the calibration of the device.

The probe station microscope and imaging software (Motic Image Plus 2.0) has been calibrated to a reference slide provided by the microscope manufacturer (Motic PSM-1000). See Table 23 for calibration numbers.

Table 23: PSM-1000 microscope calibration with Moticam 2300 using 0.5X c-mount.

PSM-1000 Objective	Multiplier*	μm/pixel (x-axis)	μm/pixel (y-axis)
2X	1X	3.348	3.348
2X	2X	1.663	1.663
10X	1X	0.664	0.665
10X	2X	0.333	0.332
20X	1X	0.333	0.334
20X	2X	0.167	0.167

**The PSM-1000 is equipped with a selectable filter ring that contains a 1X UV filter, 1X IR filter, or 2X optical multiplier.*

By recording the movement of the probe tip controlled by the piezo actuator and amplifier coupled with the NI USB-6009 DAQ for known output and input voltages, a calibration table can be made (see Table 24) so that accurate positioning is possible from within LabView. Even with negative feedback control of the piezo stack, the setup needs to be recalibrated periodically.

Table 24: LabView internal calibration of the piezo actuator coupled with NI USB-6009 DAQ.

Input from Monitor		Output to Control	
Max Position (μm)	35.0	Max Voltage (V)	5.000
Voltage at Max (V)	4.536	Position at Max (μm)	36.8
Min Position (μm)	0.0	Min Voltage (V)	0.000
Voltage at Min (V)	0.100	Position at Min (μm)	0.0

The most significant source of calibration error is the uncertainty of the spring constant of the reference spring. Typically, the piezo actuator is moved back and forth by 20 μm during a calibration of a force sensor. Using cantilever reference No. 4 (see Table 21) a ramped loading force of 0 to 770 nN would be applied to the force sensor tip. Uncertainty in the position of 250 nm (much greater than the manufacturer’s specification) would only result in 1% uncertainty in the force loading.

Reference Spring Verification

In order to check the spring stiffness based on dimensions and assumed material properties, the force applied by the cantilever was verified by a calibrated microgram scale analytical balance (Cahn C-30 Microbalance in 0.000 mg range). Two of the cantilevers (one custom gold tip and one tungsten compliant probe tip) were tested by clamping the micromanipulator base (magnetic clamp) to a $\frac{1}{4}$ inch steel box which provided a sturdy base while the cantilever tip was in contact with the microbalance. The piezo-driver attached to the micromanipulator was controlled through the same calibrated LabView software used to test the force sensors, and the position was cycled from 0 to 10 μm , from 0 to 20 μm , and from 0 to 30 μm . The loading rate was 10 $\mu\text{m/s}$ and a measurement was taken after waiting 20 seconds. The process was repeated 10 times at each position for a total of 30 measurements. The spring constant was extracted by converting the recorded mass to a force (using the gravitational constant of 9.8066

m/s²) and dividing by the displacement. The results are summarized in Table 25, and the tabulated measurements can be seen in Appendix VII: Measured Spring Constants. The deviation from the theoretical values was less than 5%.

Table 25: Measured spring stiffness of fine wire beams.

Cantilever Label	No. 5	No. 9
Material	Tungsten	Gold
Elastic Modulus (GPa)	411	79
Length (μm)	5000	5600
Diameter (μm)	25.4	25.0
K (N/m) Theoretical	0.092800	0.027573
K (N/m) Measured	0.089957	0.027029
Deviation (%)	-3.1%	4.5%
N	30	30
SD	0.004386	0.004085

Sensitivity Measurement in LabView

Each device was tested five times with a gold cantilever spring of 0.039 N/m stiffness by ramped loading/unloading at 0.25 μm/s (9.8 nN/sec) which produces 320 force-voltage pairs per test for a total of 1600 data points per device. The probe tip moves a total of 20 μm and one loading step takes 90 seconds with a 10 second wait period between loading and unloading. The LabView control panel for the piezo-driver is shown in Figure 44, and a typical test result is shown in Figure 45. The data is also logged to a text file at 500 ms increments.

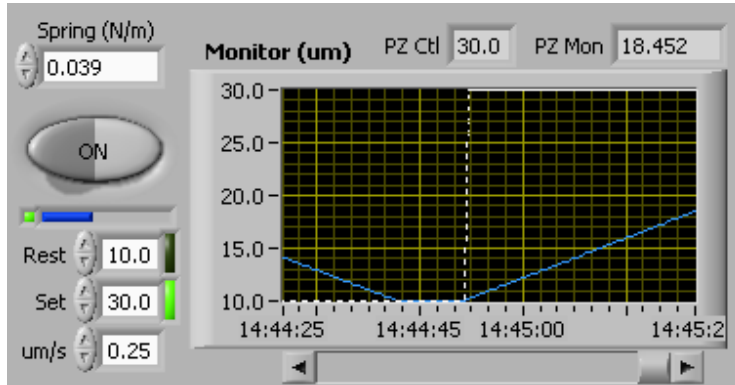


Figure 44: Screenshot from the piezo controller portion of the LabView control panel.

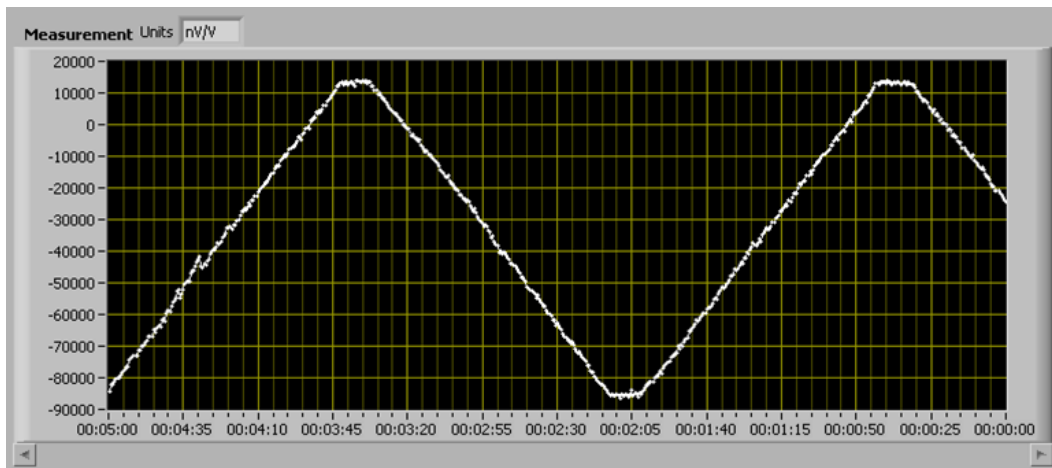


Figure 45: A typical force sensor measurement while it undergoes loading and unloading with a calibration cantilever of known spring constant. Smooth unloading and loading without sudden changes in applied force or excessive noise indicate good mechanical contact.

The sensitivity of the force sensor is derived from the load-unload data by plotting the applied force (N) on the horizontal axis and the measured response (V/V) on the vertical axis. A linear fit is made to the data, and the slope of the fit is equal to the sensitivity (V/V)/N (see Figure 46).

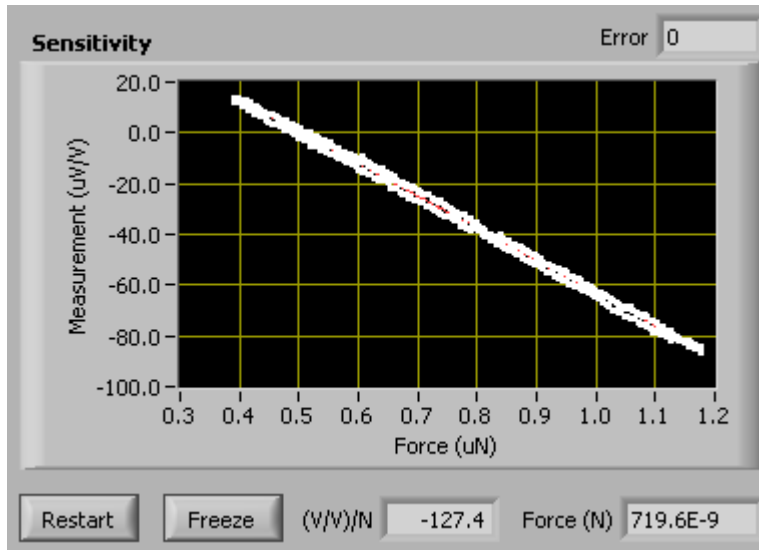


Figure 46: Typical sensitivity plot in LabView showing repeated loading and unloading.

The x-axis (force) is derived from the position given by the piezo-control monitor multiplied by the calibrating cantilever spring constant. The y-axis ($\mu\text{V}/\text{V}$) is directly measured by the inputs to the DAQ hardware. The slope of the line is the sensitivity of the force sensor, and the lack of hysteresis and uniform slope indicates a good quality measurement. A MATLAB script was also used to analyze the logged data and product a linear fit. The calibration process was repeated for each of the various force sensor layouts by testing packaged chips, and the results are tabulated in Table 26.

Table 26: Measured force sensor sensitivity.

Die	Transducer Length (μm)	Beam Length (μm)	Sensitivity ((V/V)/N)
A38	32	450	202
A39	32	450	193
A40	32	450	266
A45	32	450	181
A46	32	450	161
A48	32	450	221
B49	16	300	125
B51	32	300	175
B53	64	300	218
B55	16	450	125
B61	16	600	160
D71	16	450	196
D72	16	450	152
D74	64	450	211
D75	16	600	158
D77	32	600	226
D78	32	600	221
D80	16	450	147
D84	16	600	210

Actual Dimensions and Measured Sensitivity

Deviation from the predicted results was noted, and this deviation was expected to be related to variations in the transducer width. This is the smallest dimension in the layout and most susceptible to processing variations. The width of each beam of each transducer was measured by scanning electron microscopy (see Figure 47 and Figure 48) and the results are tabulated in Appendix VI: Measured Force Sensor Transducer Widths

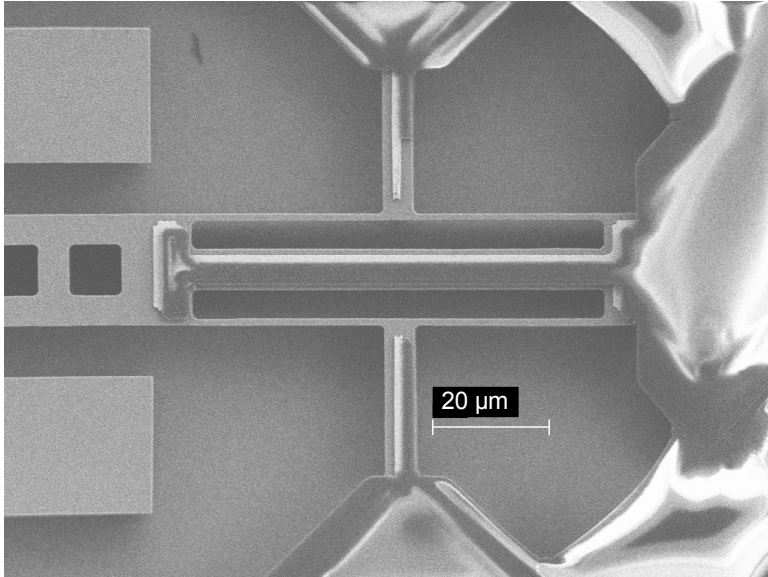


Figure 47: Typical SEM inspection of the force sensor transducer area (Wafer SOI 02, Die A39 - right).

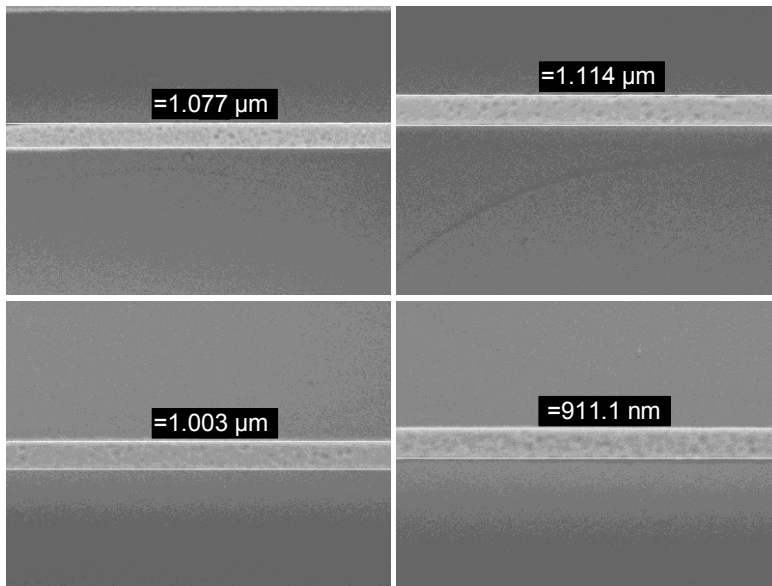


Figure 48: Typical SEM inspection of each of the force sensor transducer beam widths on one side (Wafer SOI 02, Die A39 - right).

Following the measurement of the critical dimensions of the transducer beam widths, the information was used to scale the sensitivity to an equivalent 1.000 μm structure so that it could be compared to the expected sensitivity values (see Table 27).

Table 27: Measured force sensor sensitivity.

Die	TD Length (μm)	TD Width (μm)	Beam Length (μm)	Sensitivity ¹ ((V/V)/N)	Scaled Sensitivity ² ((V/V)/N)
A38	32	1.202	450	202	243
A39	32	1.005	450	193	194
A40	32	1.037	450	266	276
A45	32	1.226	450	181	222
A46	32	1.306	450	161	210
A48	32	0.925	450	221	204
B49	16	0.882	300	125	110
B51	32	0.868	300	175	152
B53	64	0.870	300	218	190
B55	16	1.077	450	125	135
B61	16	1.299	600	160	208
D71	16	0.986	450	196	193
D72	16	1.082	450	152	164
D74	64	1.130	450	211	238
D75	16	1.115	600	158	176
D77	32	1.140	600	226	258
D78	32	1.127	600	221	249
D80	16	1.079	450	147	159
D84	16	1.033	600	210	217

¹The actual measured sensitivity.

²The equivalent sensitivity that the beam would have at exactly 1 μm width.

Conclusion

Finally, the measured sensitivity of the force sensors can be compared to the linear beam bending model and the FEA results. The results for each of the same configuration from Table 27 are averaged together and the results are listed in Table 28.

Table 28: Measured sensitivity of force sensors ((V/V)/N).

Beam Length	Piezoresistive Element Length		
	16 μm	32 μm	64 μm
300 μm	110 (N=1)	152 (N=1)	190 (N=1)
450 μm	163 (N=4)	225 (N=6)	238 (N=1)
600 μm	200 (N=3)	254 (N=2)	*

* not included in fabrication

These same numbers are plotted in Figure 51, and for comparison the model sensitivities (Figure 49, see also Figure 29) and FEA sensitivities (Figure 50) are plotted using the same scale. The CoventorWare FEA seems to have overestimated the sensitivity, but models well the trends related to beam length and piezoresistive transducer length. The estimates from the linear beam bending model are similar to the final results, and this validates the general design methods used for this special kind of force sensor. The lower than expected sensitivity of the fabricated devices is probably due doping variations. The wafers were specified by the manufacturer to be within 1.0 to 5.0 mΩ-cm, and measured at 1.35 mΩ-cm for this wafer (see Appendix I: Layout). Based on the piezoresistivity factor (see Figure 23) a change from 2.0 mΩ-cm to 1.0 mΩ-cm would result in a 22% decrease in sensitivity, so even small variations can have an effect.

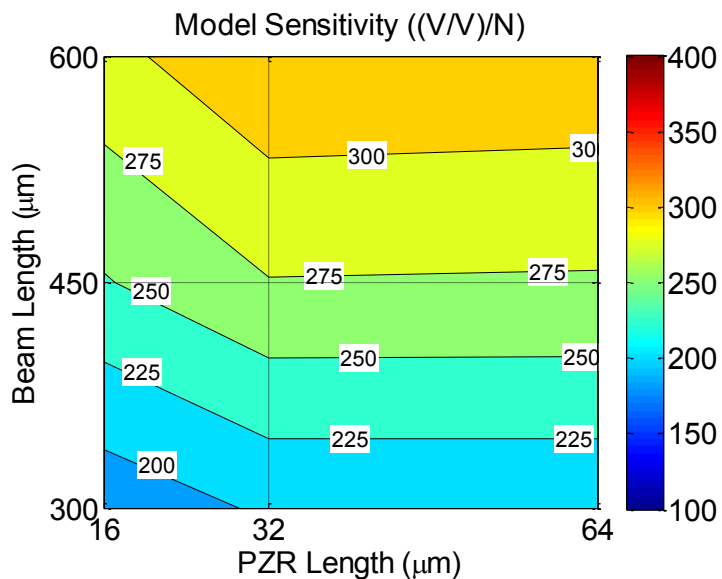


Figure 49: Predicted sensitivity based on beam bending model.

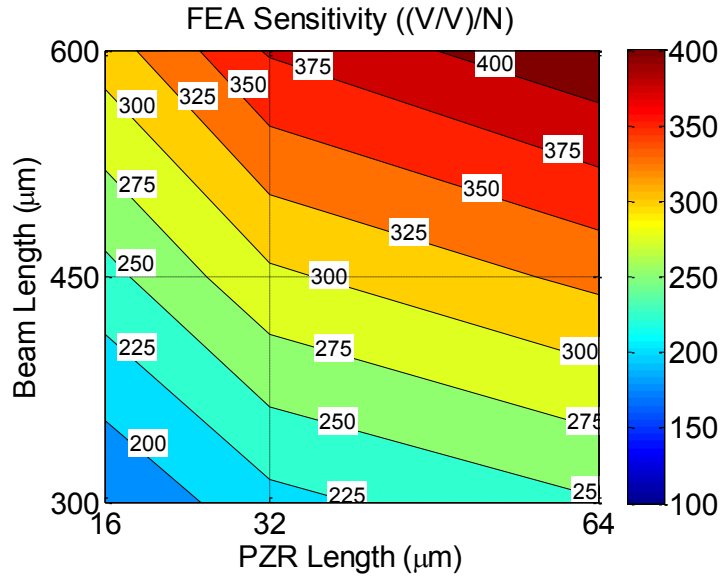


Figure 50: Predicted sensitivity based on FEA simulations.

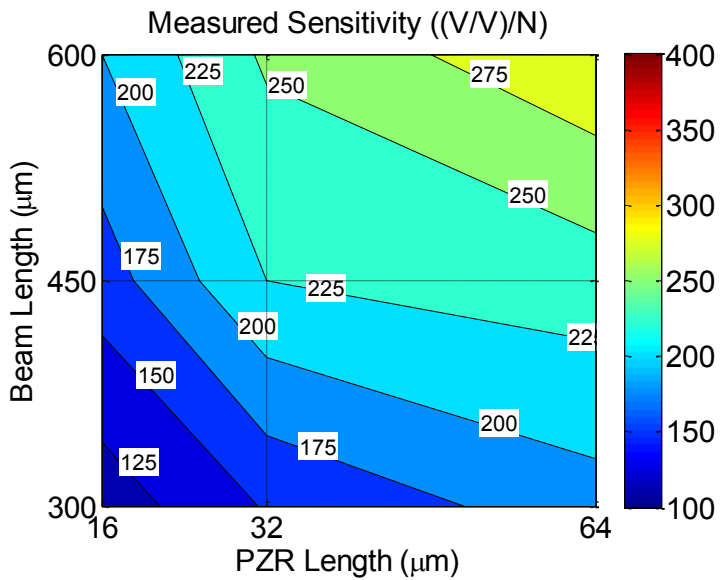


Figure 51: Actual measured sensitivity.

Overall, the performance of the force sensors was very good, and when combined with the supporting electronics, they have the capability of measuring the very small forces involved in cell biomechanics experiments. The results from these experiments are discussed in Chapter 5: Cell Biomechanics.

Chapter 3: Electrostatic Actuator

Principle of Operation

Electrostatic Clamp

An electrostatic attractive force exists between two conductive plates when there is a voltage difference between them. If one of these plates is fixed, and the other is movable and attached to a spring with a stiffness K , a “pull-in” effect occurs when the force between plates increases as the inverse square of the separation while the restoring force of the spring is mostly linear [41]. By starting pull-in at one edge of the electrostatic plates, a zipping motion propagates from the closely separated side to the side that is far apart and clamping between plates can be achieved at a lower voltage than if the separated plates were parallel.

The equation for the restoring force at the end of a cantilever with spring constant k is shown in equation 56.

$$F = kd \tag{56}$$

The spring constant for a beam of rectangular cross section in terms of the width (w), thickness (t) and length (l) is shown in equation 57, where E is the elastic modulus of the material.

$$k = \frac{Ewt^3}{4l^3} \tag{57}$$

The equation for the attractive force between two plates with surface area (A), voltage difference (V) and separation (d) is shown in equation 58, where ϵ is the permittivity of the material between the plates.

$$F = \frac{1}{2} \frac{\epsilon AV^2}{d^2} \quad 58$$

Notice that this design will be independent of the SOI device layer thickness because the electrostatic force and the cantilever spring force both increase linearly with the thickness of the layer.

In order to reduce the pull-in voltage further, one of the electrodes is sometimes made very compliant, so that it can bend towards the other electrode. However, this reduces the maximum available clamping force once the electrode pair has “zipped” shut [41], and the proposed design here uses a relatively stiff moving electrode that is suspended by an S-shaped spring (see Figure 52).



Figure 52: Angled electrostatic clamp which makes use of a small-gap starting zone on the right to reduce the required pull-in voltage.

Discrete Stepped Motion

Motion in a series of discrete steps is implemented through an array of independent electrostatic clamping plates which translate their forward motion to a central shuttle. Each actuator simply clamps shut to the maximum displacement possible when voltage

is applied, as long as the clamping force is greater than the restoring force of the shuttle's suspension beams. Since the entire actuator array and shuttle is defined through a single mask DRIE process on single crystal silicon, the stop positions are highly reliable following fabrication. If the gap between the plates of the electrostatic clamp is $5\ \mu\text{m}$ and the leading edge of the clamp is $2\ \mu\text{m}$ away from the shuttle, then the shuttle will move forward by $3\ \mu\text{m}$ when the electrostatic clamp is closed (see Figure 53, diagram units are in millimeter), which is the spacing between the two contact edges of the fixed electrode and the shuttle. Any displacement can be chosen at design time by adjusting the spacing between these two contact faces. Using an array of clamps around the central shuttle each with different gap spacing, the shuttle can be moved between any one of a set of precise positions.

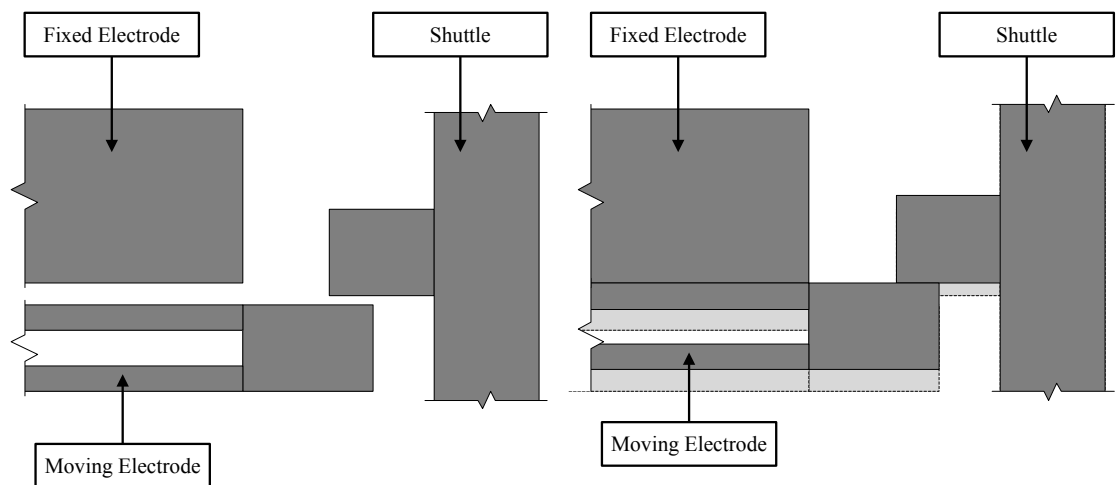


Figure 53: The key components of an electrostatic clamp are shown before actuation (left) and after actuation (right).

Operation in Liquid

Water has a particularly large dielectric constant ($\epsilon_r=75$ at 35°C [42]) which is a great benefit to electrostatic actuators since the attractive force is directly proportional to the

dielectric constant of the media between two plates (see equation 58). Either the force increases when moving from air to water, or the voltage required for actuation decreases for an equivalent force. On the other hand, water has two disadvantages. First, it is much more electrically conductive than air and may short-circuit the voltage across the electrostatic plates. It may also provide unexpected conductive pathways from one part of the chip to another. The temperature of the conductive water will also rise due to Joule heating when there is a current flowing through the water, and due to its high thermal conductivity, transmit that heat to temperature sensitive portions of the chip. Second, it usually contains ions (H^+ and OH^- in pure water, and H^+ , OH^- , Na^+ , Cl^- , HPO_4^{2-} in cell medium) which are attracted to the electrostatic electrodes and weaken their effect through charge screening [36].

FEA Contact Simulation

Material Properties

The same material properties as the piezoresistive sensor design (see Table 29) were used. The insulating layer was modeled as silicon oxide (see Table 30) and the gap was treated as a vacuum.

Table 29: Bulk mechanical properties of silicon for FEA simulation [34].

Silicon Parameter	Value (Common)	Value (CoventorWare)	Options (CoventorWare)
C_{11}	165.7 GPa	1.657e+005 MPa	Elastic-Ortho100
C_{12}	63.9 GPa	6.39e+004 MPa	Elastic-Ortho100
C_{44}	79.6 GPa	7.96e+004 MPa	Elastic-Ortho100
ν_{12}	0.278	2.78e-001	Elastic-Ortho100
ν_{13}	0.278	2.78e-001	Elastic-Ortho100
ν_{23}	0.278	2.78e-001	Elastic-Ortho100
G_{12}	79.64 GPa	7.964e+004 MPa	Elastic-Ortho100
G_{13}	79.64 GPa	7.964e+004 MPa	Elastic-Ortho100
G_{23}	79.64 GPa	7.964e+004 MPa	Elastic-Ortho100

Table 30: Bulk mechanical and electrical properties of silicon dioxide for FEA simulation.

Oxide Parameter	Value (Common)	Value (CoventorWare)
C (stiffness)	70 GPa	7.000e+004 MPa
ν (Poisson ratio)	0.17	1.700e-001
σ (conductivity)	1.00×10^{-15} S/cm	1.000e-007 pS/ μ m

Table 31: Bulk mechanical properties of soft body for FEA simulation.

“Cell” Parameter	Value (Common)	Value (CoventorWare)
C_{soft} (stiffness)	2 KPa	2.000e-003 MPa
C_{hard} (stiffness)	100 KPa	1.000e-002 MPa
ν (Poisson ratio)	0.5	5.000e-001

Simulation Results

In order to determine whether the electrostatic design is feasible, coupled electrostatic-mechanical simulations were performed which included surface contact. These simulation results from the CoventorWare CoSolveEM module indicate that 6 μ m of displacement is possible in air at 50 V using this type of design (Figure 54).

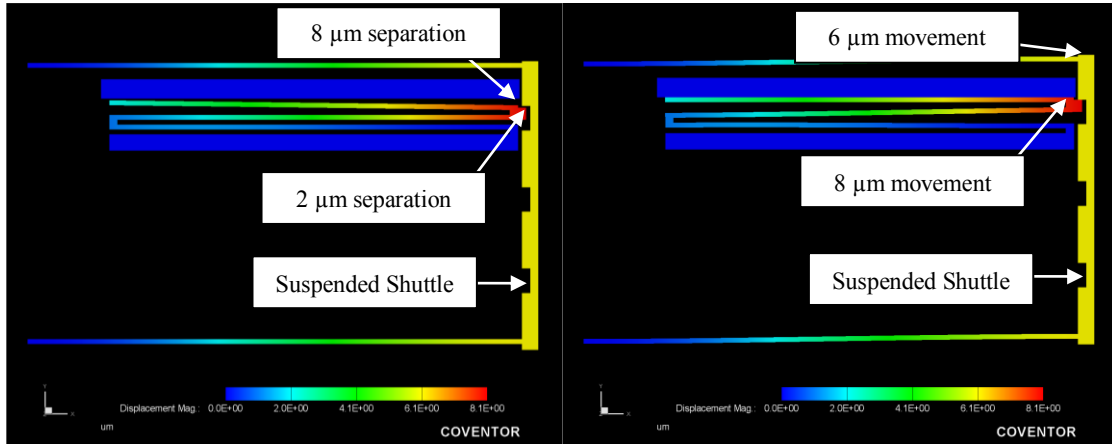


Figure 54: CoSolveEM results of $\frac{1}{2}$ symmetric model at 50V with $6\ \mu\text{m}$ designed displacement shown without geometry scaling (left) and with geometry scaling (right). The electrodes are $500\ \mu\text{m}$ long; the suspension beams supporting the shuttle are $6\ \mu\text{m}$ wide, $10\ \mu\text{m}$ high and $600\ \mu\text{m}$ long; and the shuttle itself is $350\ \mu\text{m}$ long and $40\ \mu\text{m}$ wide.

In addition to the contact-mode simulation for a single voltage, the pull-in voltage based on CoSolveEM trajectory simulations with mechanical contact were performed for 3 designs with various electrode separations (see Table 32). Since the design uses an angled moveable electrode, the actuator separation varies between $2\ \mu\text{m}$ on one side and 4 to $8\ \mu\text{m}$ on the other side. The pull-in voltage can be reduced by increasing the length of the electrode (and thereby reducing the initial angle), but the electrodes are already $500\ \mu\text{m}$ long and the maximum voltage of 43 V is reasonable. In an ideal situation with no parasitic resistances or charge screening, a voltage 75 times less would be necessary if the medium separating the plates is water (ϵ_r of water is 75 at $35\ ^\circ\text{C}$ [42]).

Table 32: Predicted pull-in voltages for various electrode separations.

Actuator Separation	CoSolveEM Pull-In (min ... max)
2 to 4 μm	10.7 V ... 11.0 V
2 to 6 μm	29.4 V ... 29.7 V
2 to 8 μm	42.8 V ... 43.1 V

Layout

In the fabricated design, the gap spacing (G2 in Figure 55) varies between 3 μm and 8 μm , which produces a shuttle movement between 1 μm and 6 μm due to the 2 μm travel distance between the facing edge of the clamp and the contact point on the shuttle (see Figure 57). The design can be easily modified to provide arbitrary displacements by adjusting the separation and increasing the number of actuators in the array.

A diagram of the actuator with labeled dimensions is shown in Figure 55, and the values for these dimensions in the revision 1 and revision 2 designs are listed in Table 33 and Table 34 respectively.

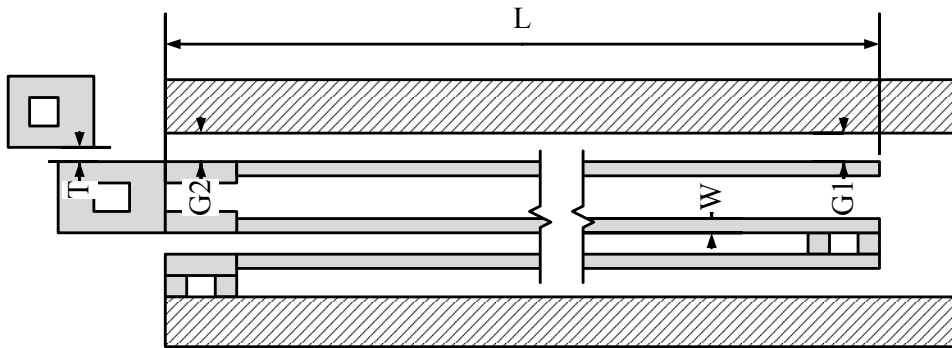


Figure 55: Actuator mechanical diagram with labeled dimensions.

Table 33: Layout parameters of actuator array (revision 1).

Parameter	Value	Description
L	500 μm	Length of plate
b	10 μm	Width of plate (thickness of device layer)
W	4 μm or 6 μm	Width of spring beams
G1	2 μm or 4 μm	Minimum gap between movable plate and contact surface
G2	3 μm to 8 μm (varied on each device)	Maximum gap between movable plate and contact surface
T	2 μm	Gap between movable plate and shuttle

Table 34: Layout parameters of actuator array (revision 2).

Parameter	Value	Description
L	500 μm	Length of plate
b	10 μm	Width of plate (thickness of device layer)
W	4 μm or 6 μm	Width of spring beams
G1	4 μm or 6 μm	Minimum gap between movable plate and contact surface
G2	5 μm to 10 μm (varied on each device)	Maximum gap between movable plate and contact surface
T	2 μm	Gap between movable plate and shuttle

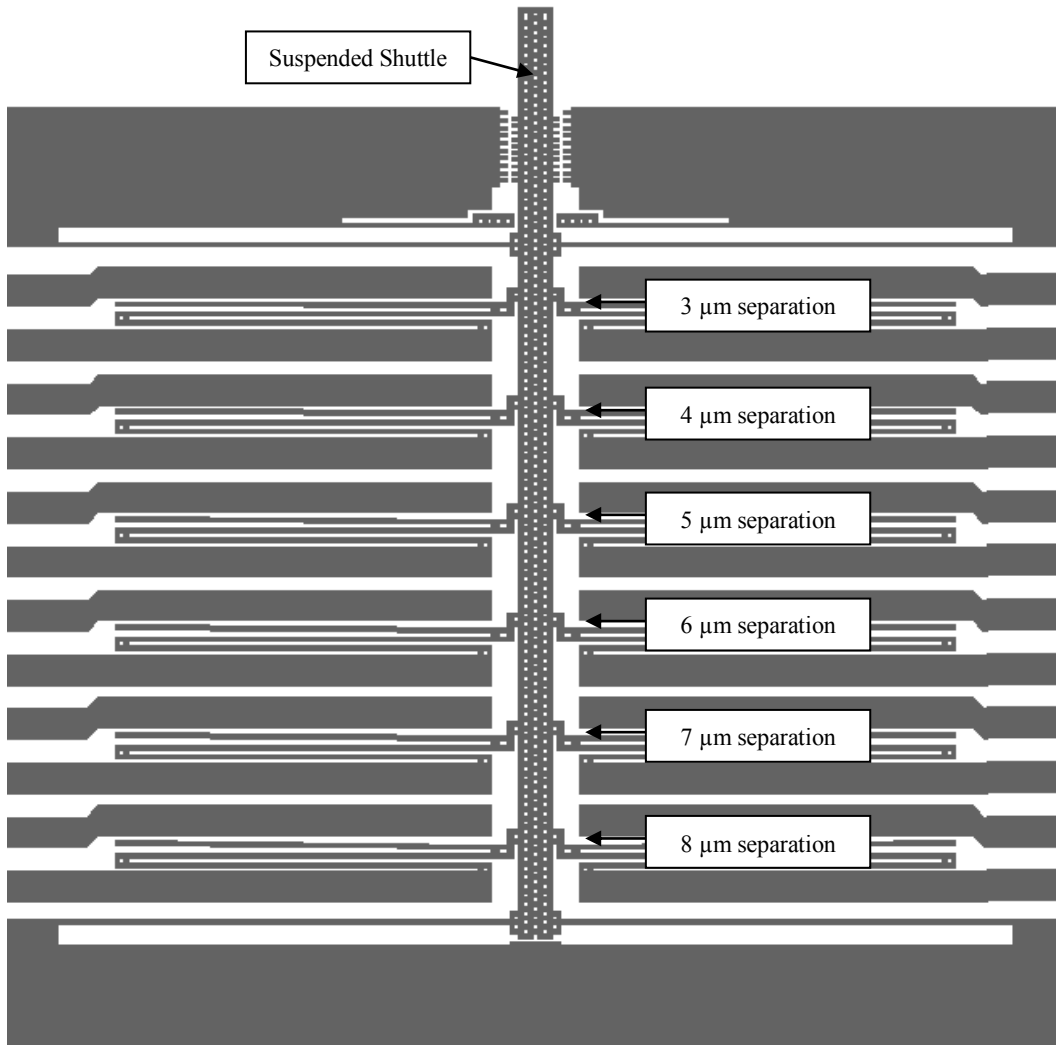


Figure 56: A central shuttle surrounded by an array of electrostatic clamps which translate their forward displacement to the shuttle. The separation of each pair of clamps varies, but the distance to the shuttle is always 2 μm.

Design Revision 1: Complete Encapsulation

Fabrication

The fabrication process is based on bulk micromachining of the 10 μm thick device layer of an SOI wafer. This is followed by a patterned metal layer and an encapsulation layer which electrically isolates conductive structures. Free-standing structures are created by etching the buried oxide layer out from under the device layer. A typical

result is shown in Figure 57. For a detailed discussion of the fabrication process, along with process diagrams, see Appendix I: Layout.

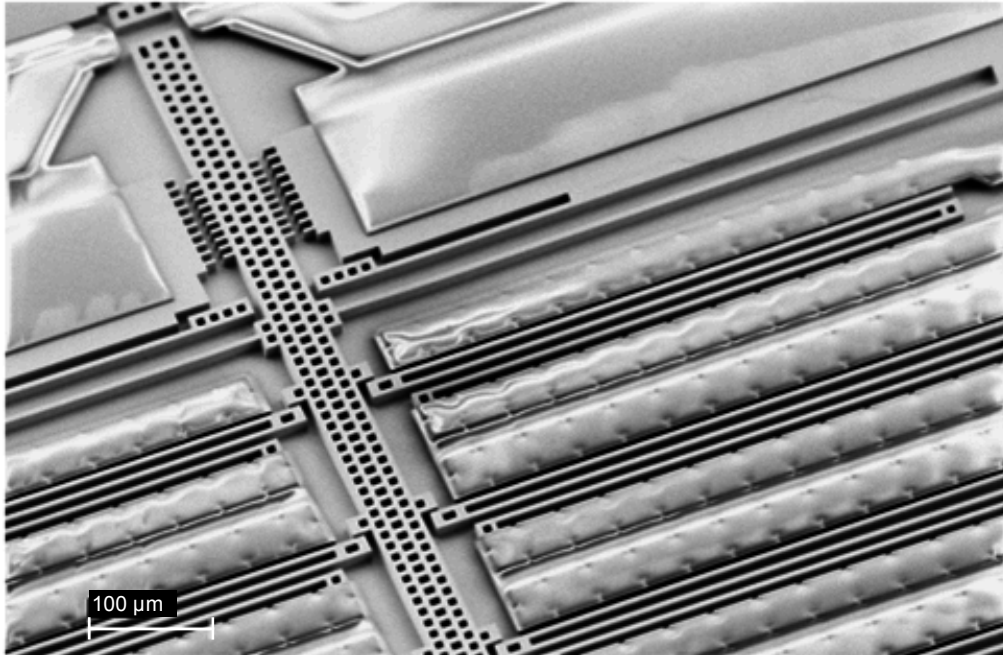


Figure 57: SEM micrograph of central shuttle and surrounding electrostatic actuators. The fixed actuators are encapsulated with AZ 4035 negative photoresist.

Characterization

In order to measure the actuator movement at a particular voltage, a single wafer was mounted on a probe station, and a LabView program controls the input to a MOSFET switch (through a NI PCI-6225 DAQ card) that energizes a particular pair of electrodes. At the same time, the movement of the actuator is captured as a series of time-stamped images, and the forward displacement is extracted using a custom image processing algorithm in MATLAB.

A method of semi-automated position measurement has been developed using MATLAB for the image analysis which allows hundreds of time-stamped images to be rapidly processed. First, a region of interest is defined in the image capture software for

the stack of images (see Figure 58), and movement is recorded as a stack of time-stamped images.

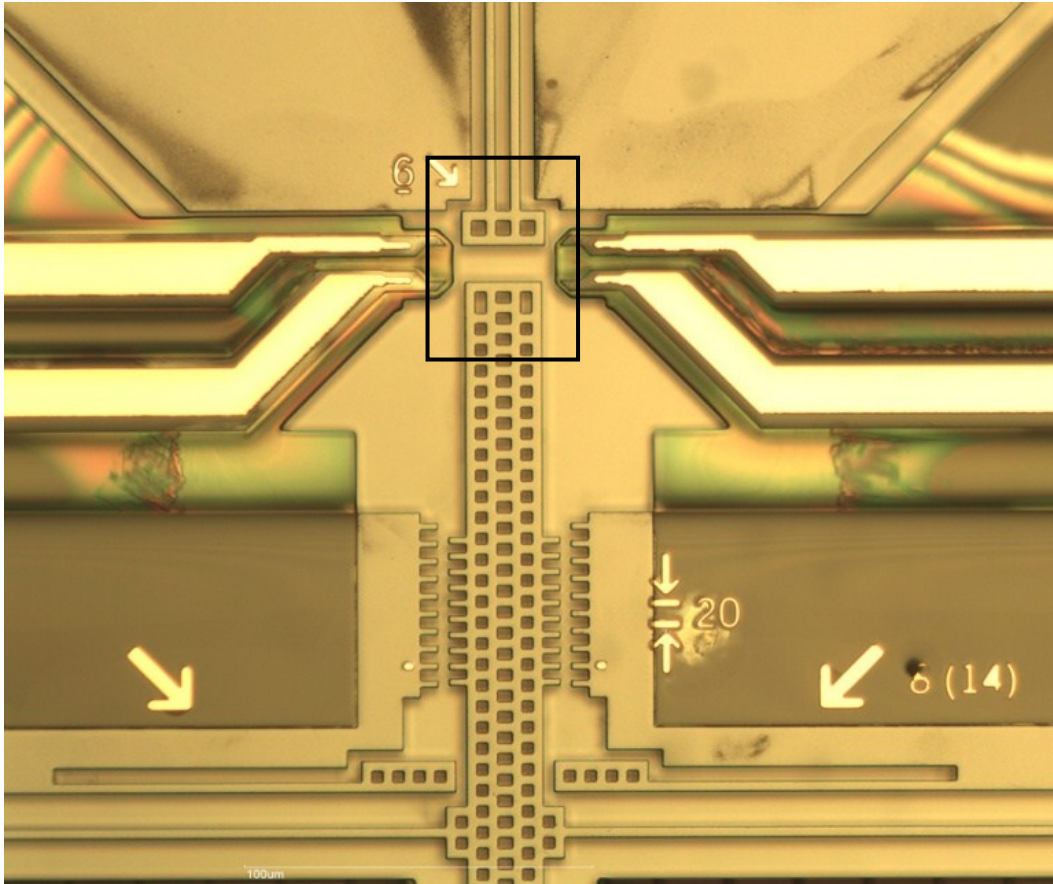


Figure 58: The black box on this image shown the region of interest captured in a series of time-stamped images while the actuators are tested at various voltages.

Next, a smaller area is defined as a parameter to the MATLAB function which sequentially processes the images (see Figure 59). Each line of the image region can be averaged together to form a one-dimensional trace of the brightness, and the dark edges of the two faces can be programmatically found. Finally, these features are converted into a measurement of the gap between them based on the pixel-to-micron scale of the microscope camera.

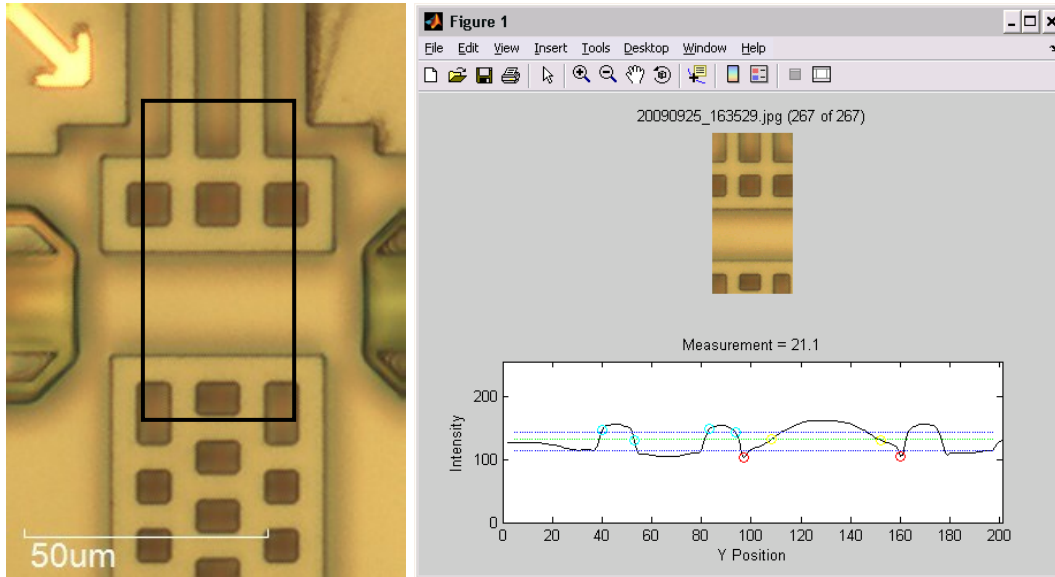


Figure 59: A small region of interest is defined (see top right) where each line of the image region can be averaged together to form a one-dimensional trace of the brightness (see bottom right). The dark edges of the two faces can be programmatically found (see red circles in bottom right).

Results

The initial actuator design used AZ 4035 negative photoresist to separate the two electrodes of each electrostatic clamp to prevent short circuit. The measurement data from MATLAB is combined with data logged from LabView by matching the file timestamps with the data logging timestamps. The result is a chart comparing the displacement to the applied voltage as it is increased (see Figure 60).

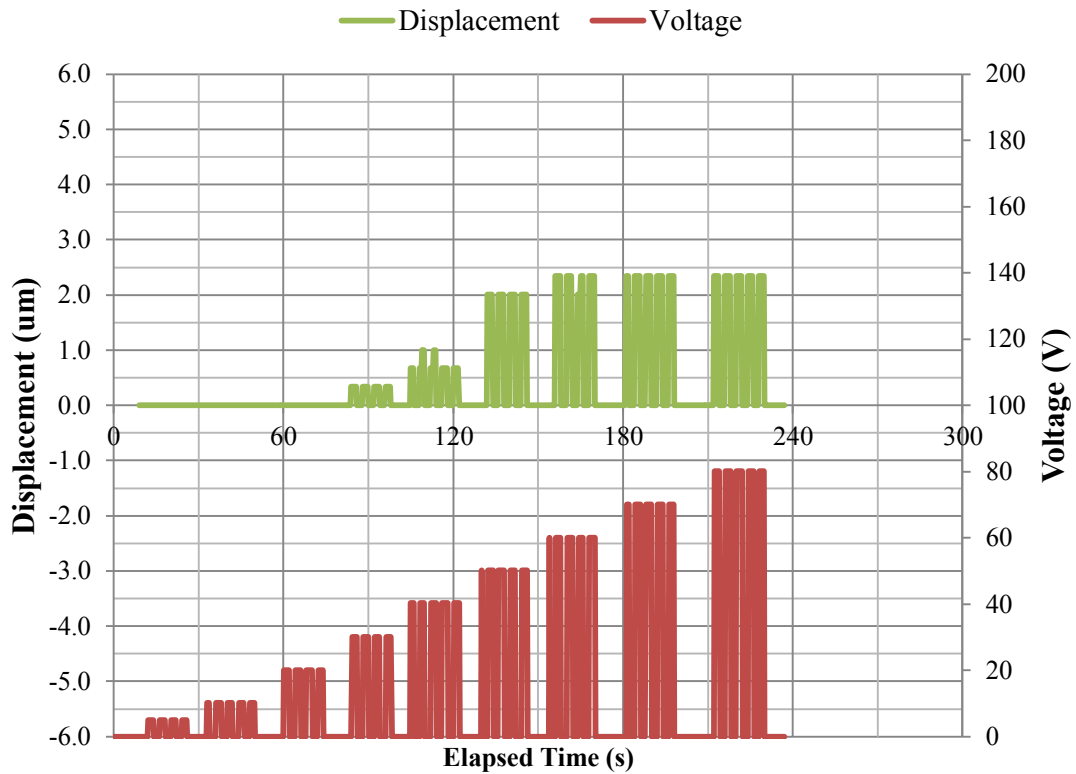


Figure 60: A typical test result showing the behavior of one of the actuator pairs (no. 3). The plates require 60 volts to clamp shut completely, at which point the shuttle moves forward repeatedly by 2.3 μm .

Tests in air of three design variations show that the actuator provides forward motion in 1 μm discrete steps (Figure 61, Figure 62, Figure 63). Linear fit of $y=mx+b$ is shown where $m=1$ is ideal, and $b \neq 0$ is related to alignment offset. Standard deviation is impacted by fabrication defects along the length of the electrostatic plate (particularly in the ISOLATION mask) and measurement error. Deviations from the designed step positions are possibly due to (1) mask misalignment (2) exposure defects (3) fabrication defects. The mask misalignment produces a universal offset, the exposure defects produce a consistent offset in a particular die, and fabrication defects add a random offset to individual electrostatic clamps. In particular, small bumps often formed at the corners of AZ 4035 and caused the position of the clamp to vary.

Nevertheless, for the final application, this actuator needs only to provide displacement in repeatable steps, not necessarily ones specified exactly at design time, so variations from the designed values are not necessarily detrimental as long as the device can be characterized after fabrication.

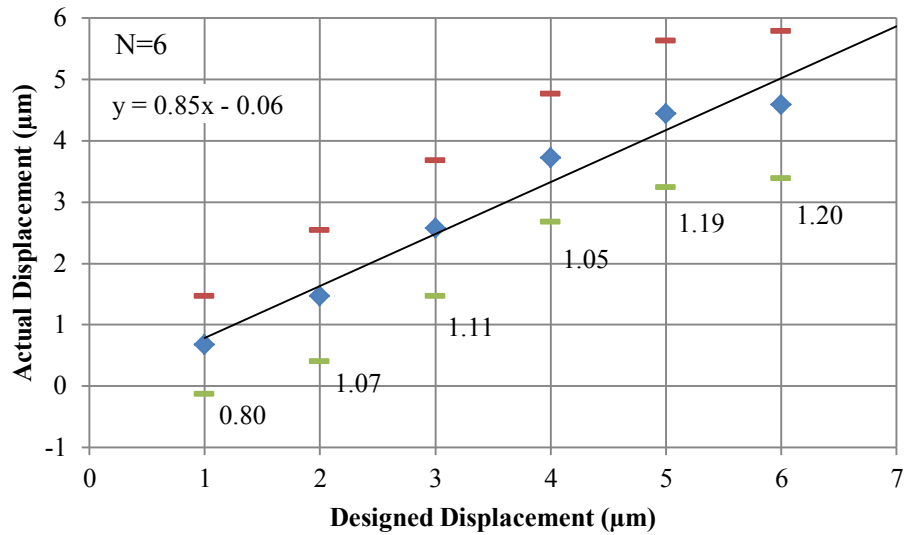


Figure 61: Designed vs. actual displacement for devices having a 4 μm wide moving electrostatic plate and a minimum gap of 2 μm . Error bars indicate standard deviation and the value is shown below each point ($N=6$ devices).

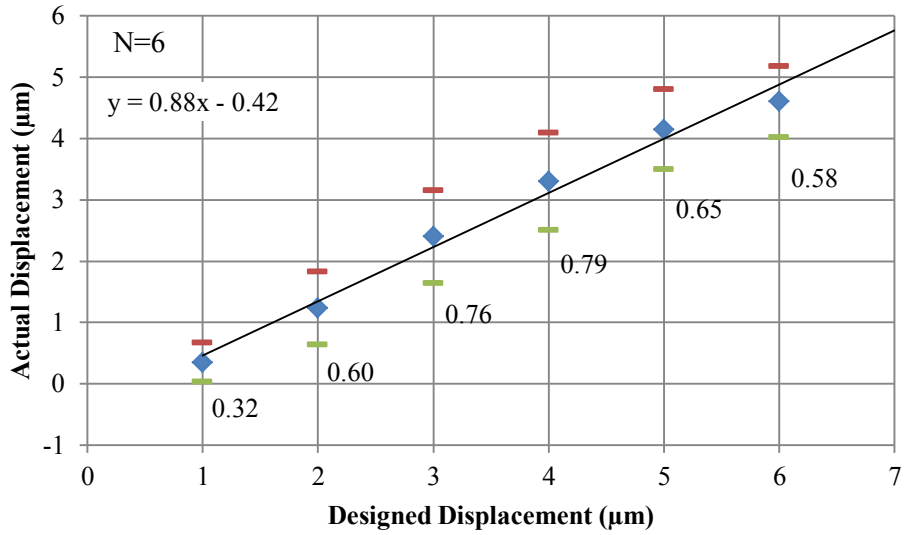


Figure 62: Designed vs. actual displacement for devices having a 6 μm wide moving electrostatic plate and a minimum gap of 2 μm. Error bars indicate standard deviation and the value is shown below each point (N=6 devices).

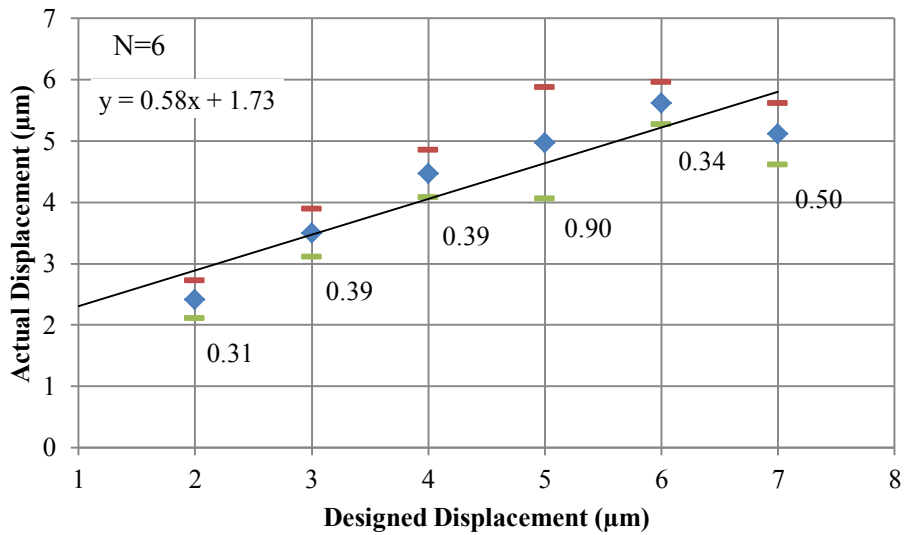


Figure 63: Designed vs. actual displacement for devices having a 6 μm wide moving electrostatic plate and a minimum gap of 4 μm. Error bars indicate standard deviation and the value is shown below each point (N=6 devices). The displacement “droop” at points 6 and 7 are due to incomplete clamping of the actuator pairs at the maximum voltage of 100V DC.

Design Revision 2: Native Oxide

Fabrication

After testing many of the chips with AZ 4035 as the isolation layer, it was found that chips without the protection layer also worked and did not catastrophically fail when clamped. Repeatable motion was observed in water at relatively low voltages and high frequency (2.8 V at 12 MHz). It is suspected that the silicon native oxide provides a sufficient insulating layer so that the conducting silicon electrodes can contact each other without short-circuiting.

A second revision of the ISOLATION mask was made to exploit this observation and the isolation material was switched to SU-8 which has better durability. In the new mask, the ISOLATION layer does not cover the adjacent faces of the silicon electrodes. Dovetail cut-outs exist in the silicon to provide vertical anchor points for the SU-8, and also the cut-outs provide small gaps for fluid flow during actuation which attempt to reduce squeeze-film and stiction effects as the plates are clamped together.

In order to reduce the effects that lithographic variations may have on the final positions of the shuttle, a single mask is used to produce all of the silicon structures so there is no impact from mask alignment errors. In addition, the contact edges of the electrostatic clamp and the shuttle would be over-etched or under-etched in the same direction, thus cancelling out lithographic variations. Over-etching would have an impact on the voltage required for actuation since larger gap spacing would require an increased voltage to clamp shut.

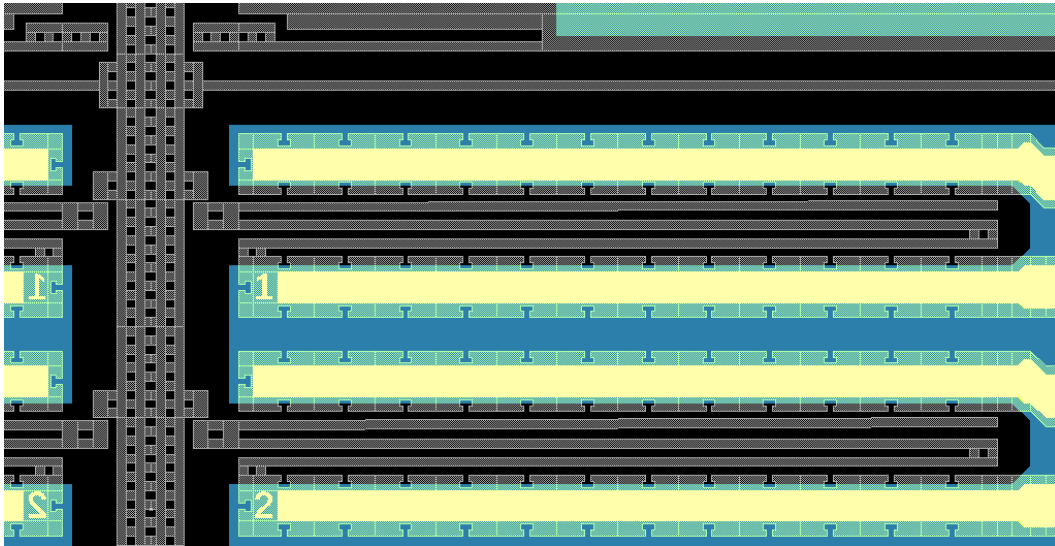


Figure 64: Second generation layout based on 6 μm wide springs. DEVICE layer is gray, METAL layer is yellow, and ISOLATION layer is blue.

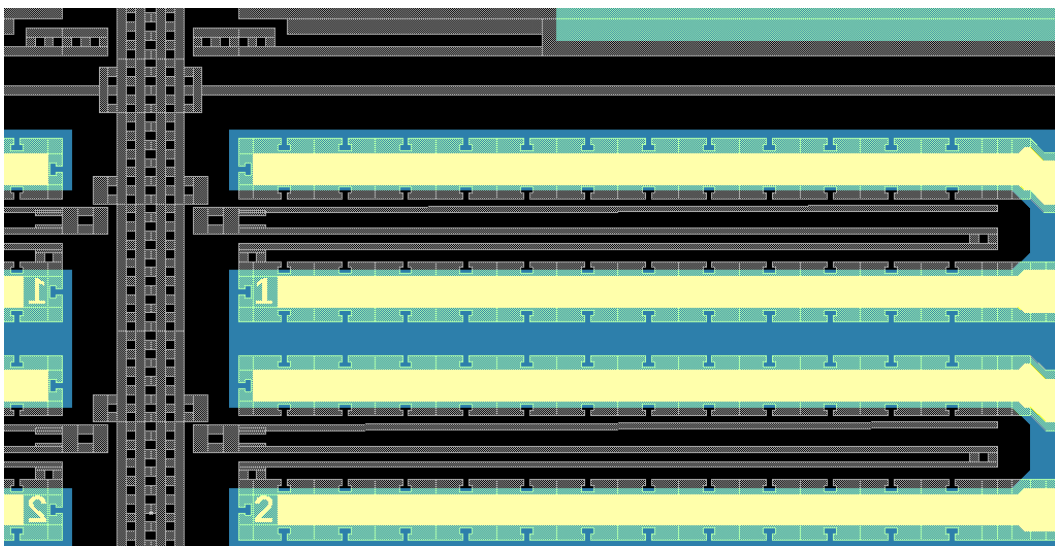


Figure 65: Second generation layout based on 4 μm wide springs. DEVICE layer is gray, METAL layer is yellow, and ISOLATION layer is blue.

Characterization

A “chase” sequence is applied to the actuator pairs in the array, which causes the shuttle to move forward in increments. Each second the actuator moves to a new position, and each second an image is captured at 40X magnification. The displacement is measured from the edge of the sensor to the edge of the shuttle through an automatic feature

extraction algorithm in MATLAB similar to the one used previously, which processes the stack of captured images. See Figure 66 and Figure 67.

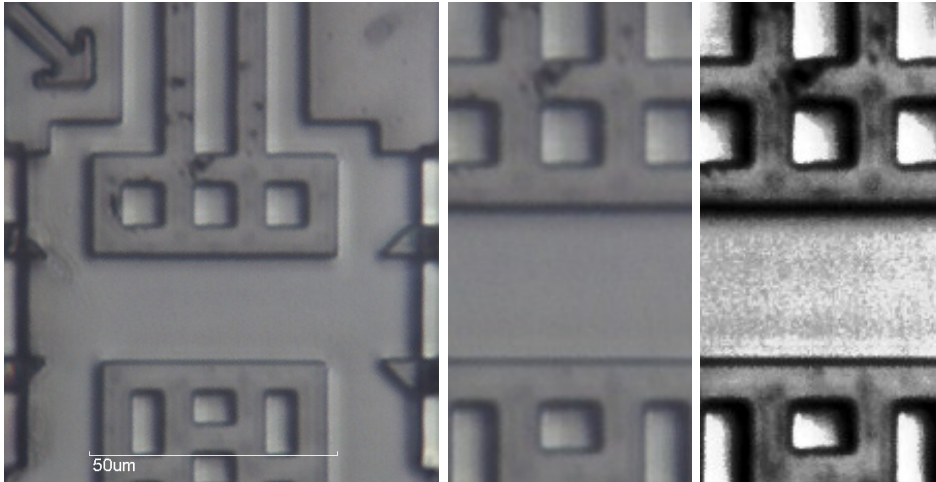


Figure 66: A typical image captured during the actuator test. Each original in the stack (left) is sequentially loaded into MATLAB, and a 200 px by 400 px region of interest is defined (middle). Next, the image is converted to grayscale followed by 8X oversampled and histogram normalized (left).

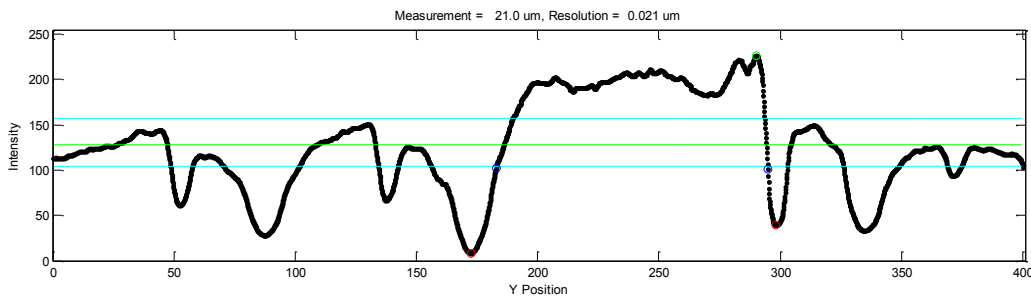


Figure 67: One-dimensional trace obtained by taking the average of the intensity of each row of pixels in the image. The feature extraction finds the edges of gap by looking for the bright area in the middle (green circle), and then finding the local minima (red circles) in the adjacent areas that are below a dark level threshold (blue circles).

The digital resolution is determined by original image resolution, the pixel-to-micron conversion factor and the oversampling. Oversampling makes the sub-pixel measurement more precise, but not necessarily any more accurate than the optical limitations of the original image. In the case of the 40X objective, the calibration is

0.1670 μm / pixel and 8X oversampling makes this 0.021 / μm per data point as shown in Figure 67.

Results

Two devices were tested in water using a driver voltage of 20V V_{pp} (7.1 V_{rms}) at 2Mhz. The first device (Wafer SOI_06 Die B63) is an array of 6 pairs of actuators and they are based on 500 μm long by 6 μm wide plates supported by a 1000 μm long by 6 μm wide folded spring (see Figure 68, see also Figure 64).

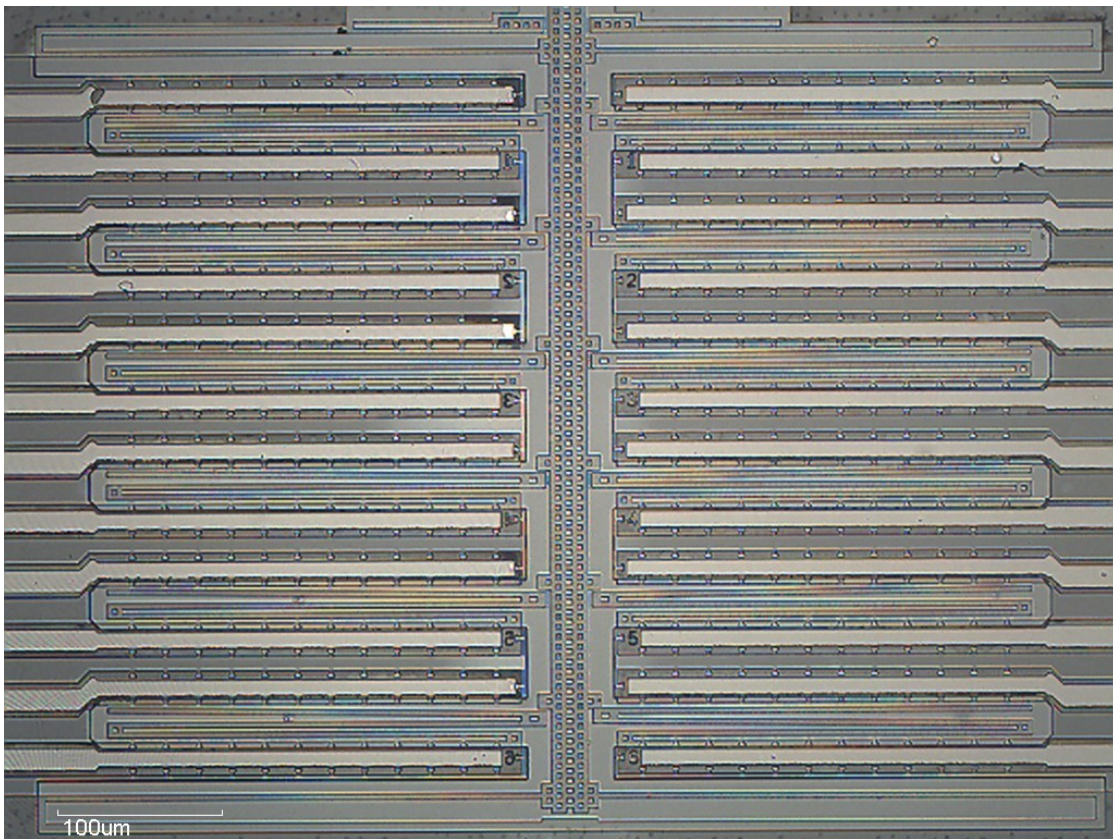


Figure 68: The actuator array on die B63 (Wafer SOI_06), which is based on 6 μm wide springs.

The second device (Wafer SOI_06 Die A06) is an array of 6 pairs of actuators and they are based on 500 μm long by 4 μm wide plates supported by a 1000 μm long by 4 μm wide folded spring (see Figure 69, see also Figure 65).

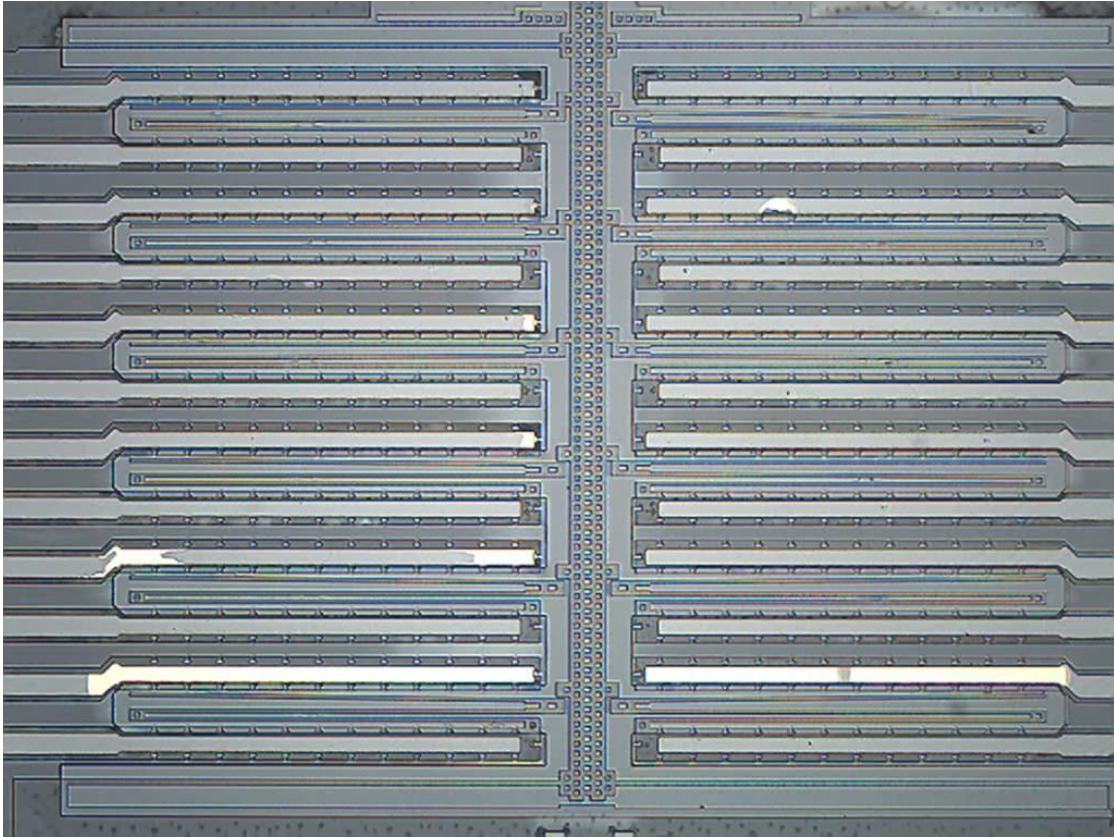


Figure 69: The actuator array of Wafer SOI_06 Die A06, which is based on 4 μm wide springs.

The actuators were left to operate for an extended period while the displacement was recorded optically. The resulting image stack was analyzed using MATLAB and the results are shown for the device with 6 μm wide spring in Figure 70 and for the device with 4 μm wide spring in Figure 71.

Looking at the behavior in Figure 70, the measured displacement lags behind the designed displacement until the 4th stop position (at 6 μm), but after that the actuator is not able to move farther. The springs in this case are too stiff, and the applied voltage is not able to provide enough attractive force. The situation is somewhat better with the more compliant actuators (see Figure 71), but the measured displacement still lags behind the designed displacement. Close inspection reveals that this is due to

incomplete clamping of the moving electrode to the fixed electrode and a small gap often remains at the edge closest to the shuttle. It was noted that one of the two actuators at the 3rd stop position was not functional.

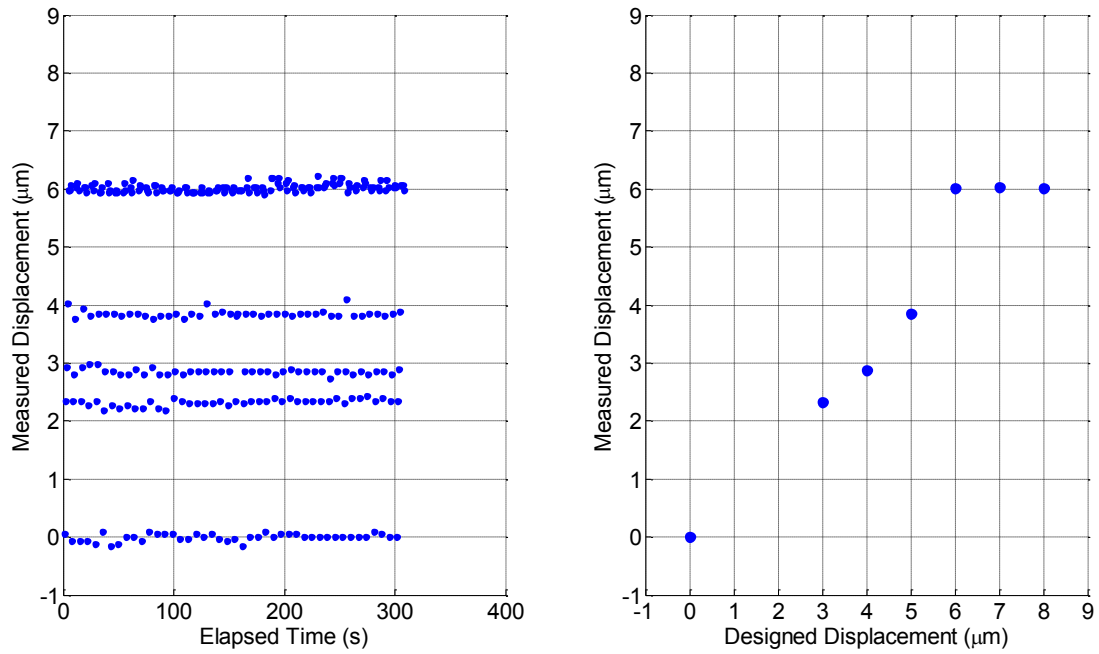


Figure 70: Measured displacement during sequential actuation (left) and the average measured displacement versus designed displacement (right).

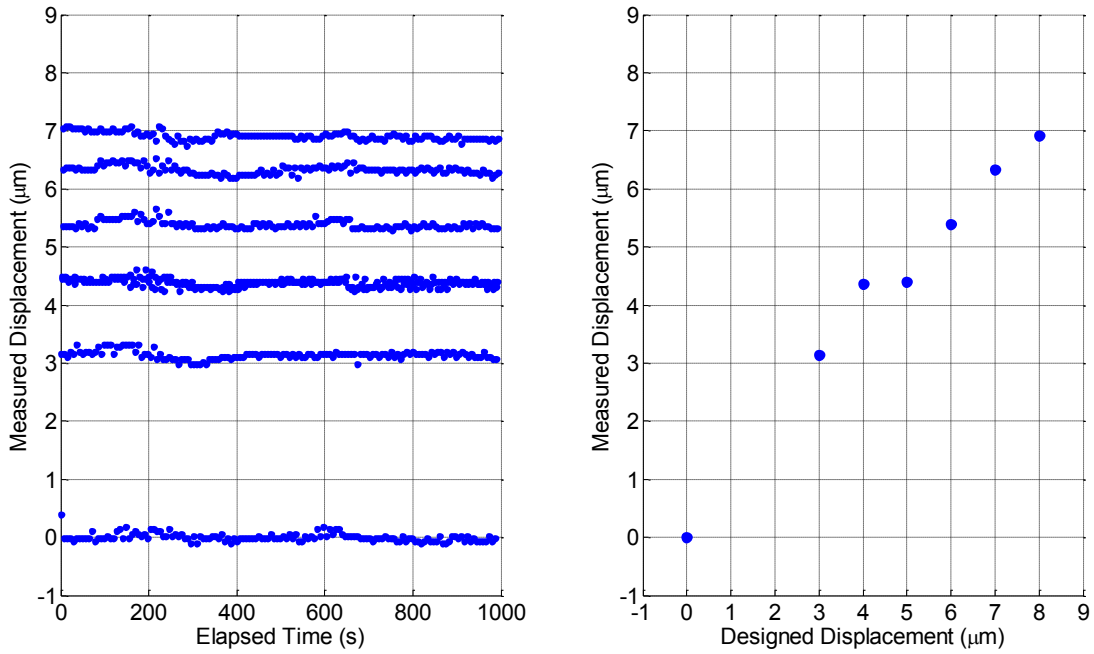


Figure 71: Measured displacement during sequential actuation (left) and the average measured displacement versus designed displacement (right).

Unfortunately, the lack of complete clamping between the electrodes not only affects the position of the actuator shuttle, but also the ability of the actuator to generate precision motion at discrete steps. The statistics of the measured displacements are shown in Table 35 and Table 36. In general, the design with the 4 μm springs performed better since they were able to clamp shut more completely at the given voltage.

Table 35: Statistics of measured displacement (all values in μm).

Position	Average	Standard Deviation	Minimum	Maximum	Range*
0	0.000	0.070	-0.108	0.393	0.501
3	3.140	0.071	2.983	3.317	0.334
4	4.366	0.062	4.235	4.611	0.376
5	4.405	0.060	4.235	4.611	0.376
6	5.390	0.071	5.279	5.655	0.376
7	6.329	0.073	6.198	6.532	0.334
8	6.911	0.068	6.741	7.075	0.334

*Average of Range column is 0.376 μm

Number of samples for each position N=44, Digital resolution = 0.021 μm

Table 36: Statistics of measured displacement (all values in μm).

Position	Average	Standard Deviation	Minimum	Maximum	Range*
0	0.000	0.063	-0.158	0.093	0.251
3	2.324	0.059	2.181	2.432	0.251
4	2.872	0.152	2.724	3.810	1.086
5	3.851	0.064	3.768	4.102	0.334
6	6.012	0.049	5.939	6.106	0.167
7	6.037	0.085	5.939	6.232	0.292
8	6.014	0.075	5.898	6.190	0.292

**Average of Range column is 0.382 μm*

Number of samples for each position N=142, Digital resolution = 0.021

Finally, it should be noted that as the applied voltage increased, stiction between the moving plate and the fixed plate became more likely, and this limited the maximum voltage that could be applied while still allowing the actuators to return to their rest position when the voltage was turned off.

Conclusion

Although repeated actuation in a liquid environment has been demonstrated, three major problems prevent successful integration into the rest of the cell biomechanics test system: (1) variability in displacement, (2) the actuator is functional in water and 10% sucrose, but not in cell media, and (3) interference with the force sensor during actuation.

First, the biggest problem is the variability in the displacement as the actuator is repeatedly tested. For one actuator the average variability was 0.376 μm and for the other it was 0.382 μm , but each discrete position is designed to be 1 μm apart, and this 38% accuracy is not good enough for the cell biomechanics measurements. The cause

of this variability is incomplete clamping of the movable electrostatic plate to the fixed electrode. There are two possible reasons why this may be happening.

One possible reason is that the moveable electrostatic plate is too flexible compared to the stiffness of the suspension beams of the shuttle, so even though the plate clamps shut over the majority of its length, a small gap often develops at the side adjacent to the shuttle and the plates are not fixed completely in their proper position. The other possibility has to do with charge screening, the physics of which has been described in detail for silicon comb drives [36] operating in conductive liquids. A parameter Ω is defined (equation 59) based on geometry and applied voltage where f is the frequency, σ is the conductivity of the media, b is the native oxide thickness, g is the gap between electrostatic plates, and $\epsilon_{ox}\epsilon_0$ is the permittivity of the native oxide. When $\Omega < 1$, the effects of charge screening dominate and preclude electrostatic forces.

$$\Omega \equiv f \frac{\epsilon_{ox}\epsilon_0 g}{\sigma b} \quad 59$$

During the initial design, the region of possible electrostatic actuation was considered based on the limits of charge screening in conductive media (see Figure 72), but the effect of the changing gap distance during clamping was neglected. The critical problem is that as the gap gets smaller, the ionic screening problem gets worse and the electrodes are designed to clamp shut. If equation 59 is rearranged for $\Omega=1$ to find the minimum gap width (g_{min}) where actuation is still possible, the result is equation 60. This function has been plotted in Figure 73 at 2 MHz.

$$g_{min} = \frac{b\sigma}{f\epsilon_{ox}\epsilon_0}$$

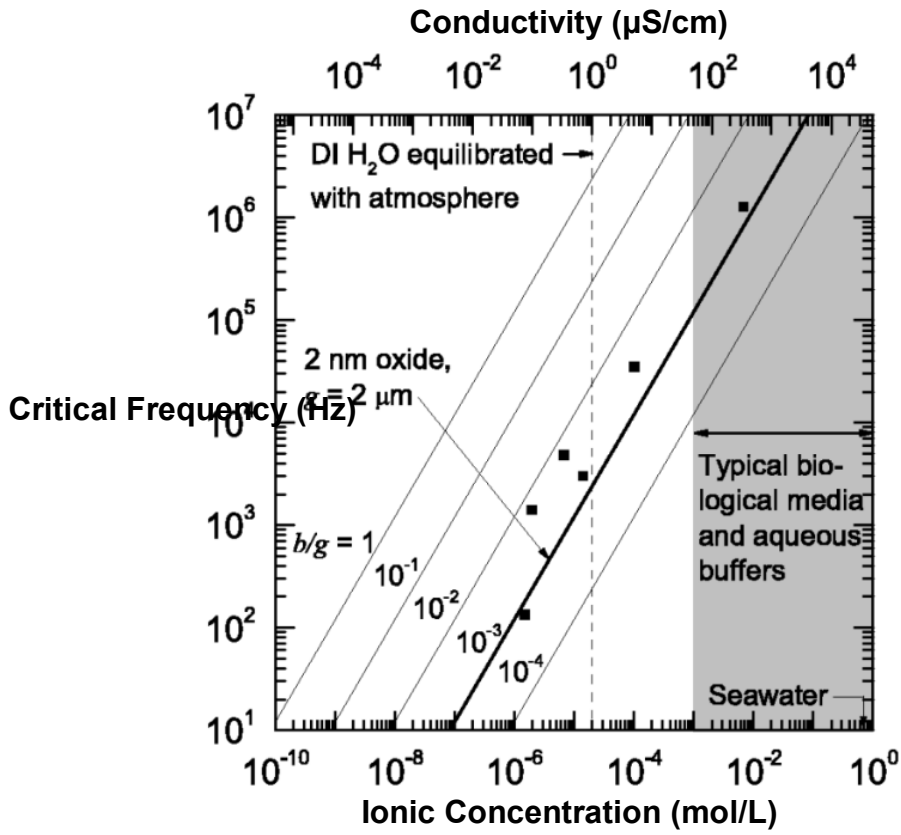


Figure 72: Critical electrostatic actuation frequency at selected values of b/g (directly from [36]).

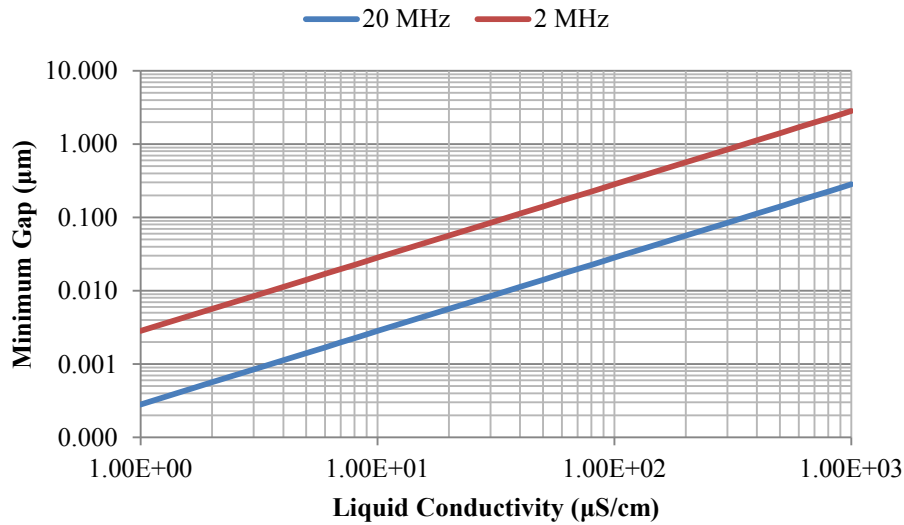


Figure 73: Minimum gap where screening effects do not dominate at 2 MHz and 20 MHz (native oxide thickness $b=2\text{nm}$ and oxide permittivity $\epsilon_{ox}=4$). Conductivity of $1\ \mu\text{S/cm}$ on the left corresponds to very pure water, and $1000\ \mu\text{S/cm}$ on the right corresponds to typical biological media.

The ionic screening effects predict that as long there is ionic media between the two plates as they clamp together, the clamping force will diminish and in short, the pull-in effect will disappear. For very pure water (1 to 10 $\mu\text{S/cm}$), this gap is 3 nm to 28 nm, but for ionic media (1000 $\mu\text{S/cm}$) the gap is 2.8 μm and the clamping actuator would not be able to function in this type of environment based on its current design. Almost no movement was observed in cell media at frequencies from 500 kHz to 5.0 MHz and voltages up to 20 V.

The third problem is interference with the force sensor. It is possible that the high frequency signal (2 MHz) is causing interference directly, but since significant effort has been made to isolate and shield the force sensor electronics. It is more likely that parasitic resistance causes non-uniform on-chip heating which in turn causes an offset in the force-sensing bridge even when there is no force applied. The corresponding

force due to this interference is a few hundred nanonewtons, which swamps out the force that could be measured during cell compression.

Future Work

Based on Figure 73, the gap spacing in future designs must be kept below the range for pull-in to occur, but above the range where ionic screening cancels out the pull-in effect. The design should be changed and mechanical stops added that prevent the moving electrode from being too close to the fixed electrode (labeled with arrows in Figure 74). The moving electrodes on the c-shaped supporting springs are grounded (labeled G in Figure 74), and the anchor wraps around to the adjacent electrode in order to provide a mechanical stop at the same electrical potential.

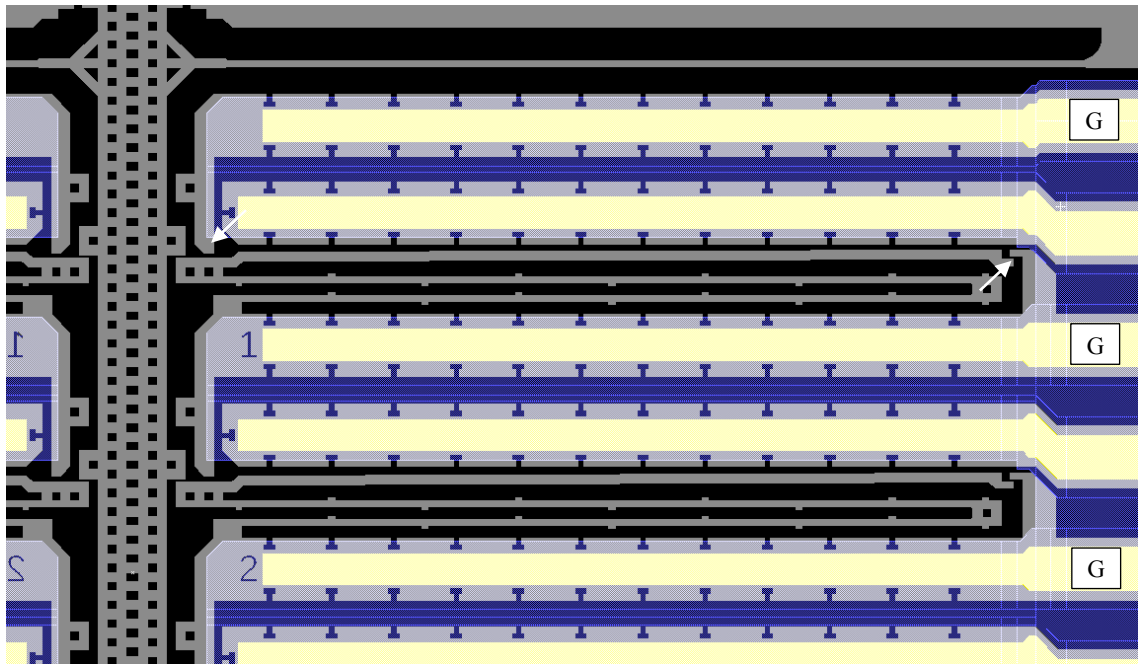


Figure 74: Proposed actuator array which adds mechanical stops in a compact layout.

More detailed diagrams of the mechanical stops next to the shuttle (Figure 75 left) and at the far end (Figure 75 right) show that the moveable electrode can move forward

until it rests 2 μm away from the opposite electrode. With a 2 μm gap, operation in liquids with conductivity up to 600 $\mu\text{S}/\text{cm}$ may be possible at 2 MHz (see Figure 73, above).

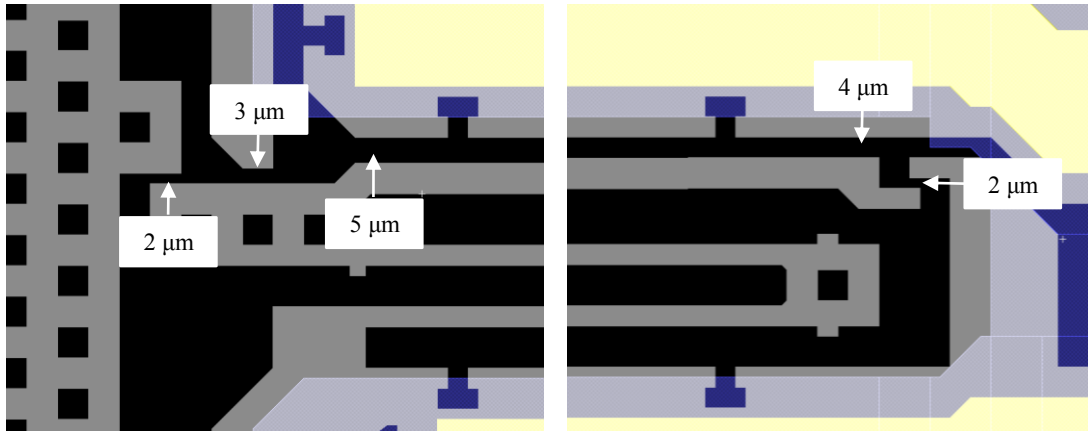


Figure 75: Close-up of mechanical stops which limit the minimum gap to 2 μm while providing 1 μm forward displacement to the moveable shuttle at the left.

Finally, anti-stiction bumps should be added to the narrow beams in the c-shaped supporting springs. Unnecessary right angles at the interface between supporting beams and anchor points should be changed so that they are curved or include 45 degree struts (see Figure 74 top).

Chapter 4: Supporting Electronics

Force Sensor Driver and Preamplifier

The force sensor piezoresistor bridge is driven by a 3125 Hz sinusoidal signal of 200 mV using the Intersil HA5002 (110MHz, High Slew Rate, High Output Current Buffer) as a line driver. Although it is desirable to drive the bridge at higher voltages in order to increase SNR, two factors limit this. First, self-heating produces temperature fluctuations in the bridge which are translated into low frequency interference or measurement drift. Second, fabrication non-uniformities cause the bridge to be slightly unbalanced, and so it produces a small voltage even when no force is applied. This voltage is amplified by 2500X before being sampled by the DAQ which can support only ± 10 V; a nominal preamplifier output of 1 V is reasonable, which means a nominal bridge output voltage of only 400 μ V.

The instrumentation amplifier in this application is similar to a standard three op-amp instrumentation amplifier, but the differential amplifier pair (preamplifier) is followed by a differential analog to digital converter (ADC) input instead of a third op-amp (see Figure 76). This is a standard circuit topology for load cell measurements based on full bridge strain gauges [44]. Often the ADC is next to the preamplifier on the PCB, but in this case a National Instruments (NI) PCI-6225 16-bit DAQ card is used. In Figure 76, *OUT1* and *OUT2* are connected to PCI-6225 Port AI06, and *VB* is connected to PCI-6225 Port AI05. The force sensor bridge is driven by the line driver supplied with a signal from PCI-6225 Port AO01. The force sensor bridge is decoupled from the 2500X low-noise differential preamplifier stage with a 1:25 audio transformer.

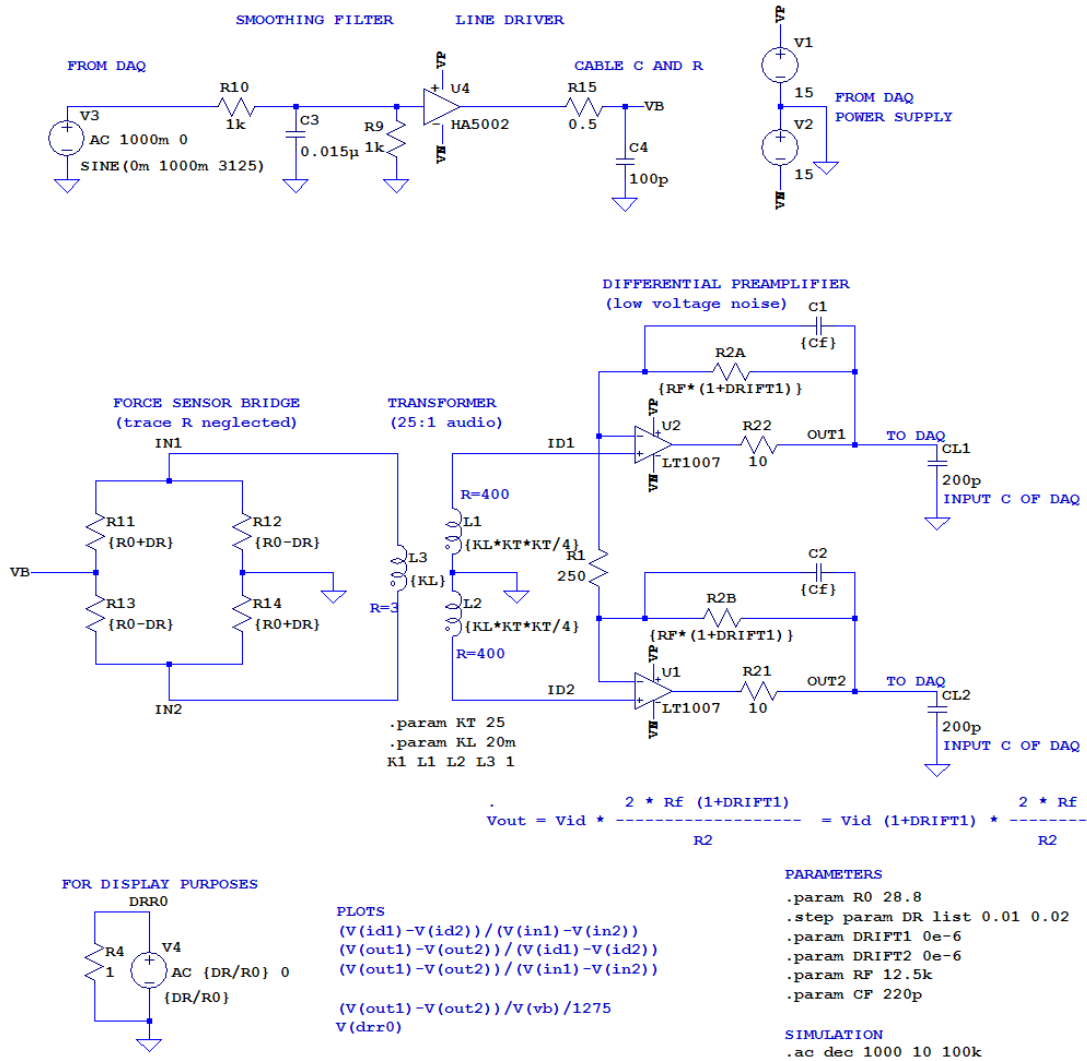


Figure 76: Schematic of force sensor driver and preamplifier circuit.

The differential amplifier acts as a low pass filter, and the front end decoupling transformer acts as a high pass filter. The two combined produce a differential bandpass preamplifier with center frequency of 3750 Hz and gain of 2500 (see Figure 77). The bottom graph in the figure indicates that valid measurements may be made between 1.7 kHz and 5.8 kHz where the difference between the real $\Delta R/R_0$ value (blue) is less than 1% different from the preamplifier output (red). The preamplifier's differential output is then routed off the PCB to the connector box of the ADC. After assembly, the actual

gain of the circuit (measured from the resistance bridge to the ADC terminals) was found to be 2450 at 3125 Hz.

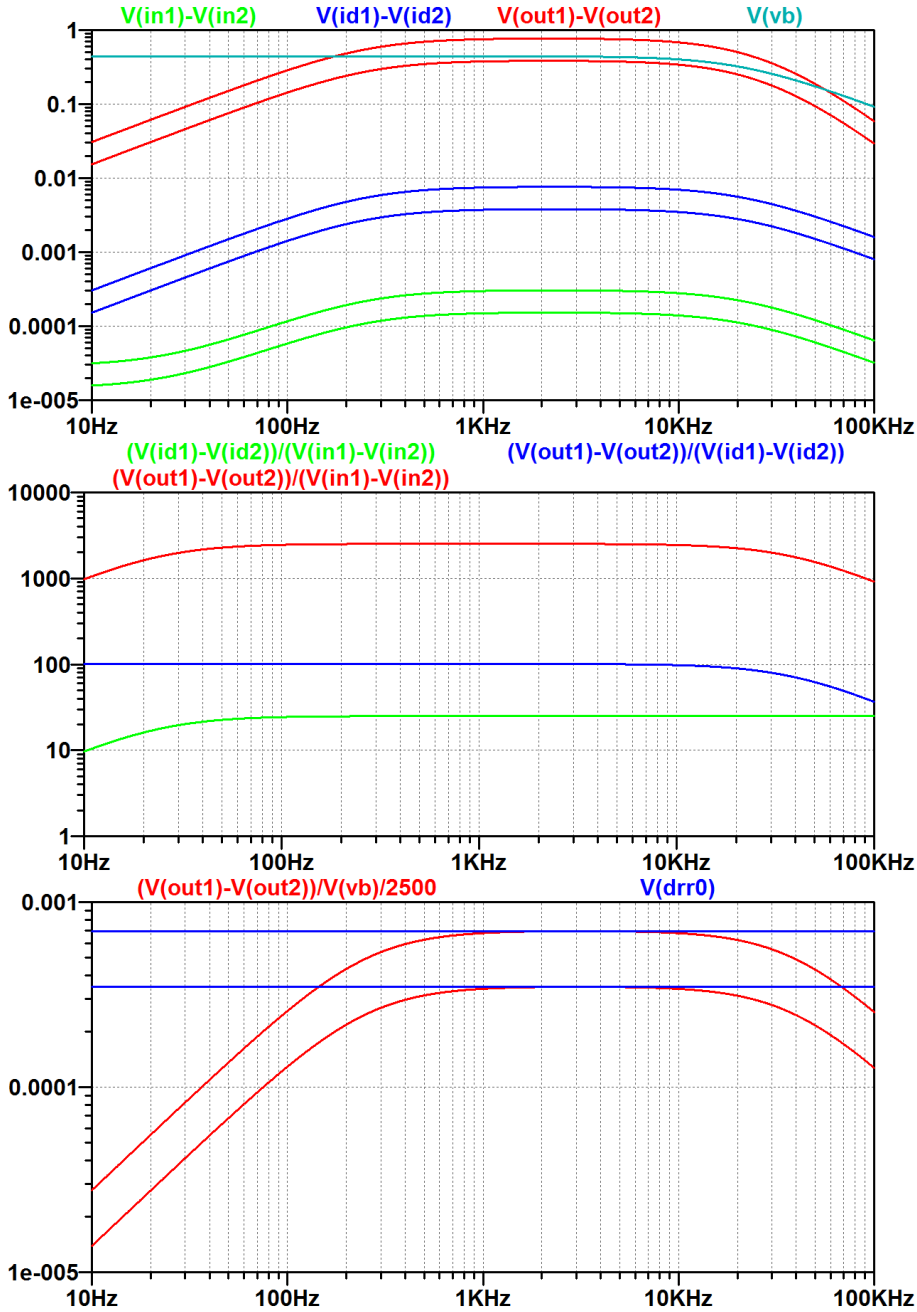


Figure 77: Simulated signal levels (top), signal gains (middle), and the proportional bridge signal which is comparable to $\Delta R/R_0$ (bottom).

To avoid interference from the on-chip heater, the heater duty cycle frequency is set at 200 Hz leading to harmonics at 3000 and 3200 so that 3125 Hz falls between the 15th and 16th harmonics. The actuator drivers operate at 1 MHz to 2 MHz, which is significantly above the carrier frequency and would be filtered by the bandpass preamplifier. After acquisition at a sampling rate of 40 KHz and sample window of 500 ms, the preamplifier signal is then filtered with a 4th order IIR bandpass Butterworth filter in LabView centered on 3125 Hz with passband of 62.5 Hz. This allows most remaining interference to be removed from the carrier signal. The sample window can be decreased to 100 ms at the expense of the noise reduction gained by averaging over a longer window. A low-side lobe window is used as part of the RMS measurement function in LabView to remove sampling glitches at the start and end of the sampling window.

Notes

Op-amp Selection

A number of op-amps were investigated to find the best SNR for the preamplifier. For a preamplifier where the input resistance is a few hundred ohms, the Linear Technology LT1007 provided the best noise performance since it has both low voltage noise, relatively low current noise and precision gain. It was better than the Linear Technology LT1028 low voltage noise op-amp with a BJT front end, and better than the Linear Technology LT1793 low current noise op-amp with JFET front end. Although the LT1028 has exceptionally low voltage noise and is suitable for low impedance sensors (such as magnetic moving coils), it has high power requirements and tends to drift thus

causing low frequency noise when two are paired as a differential amplifier. The LT1793 is more suitable for high impedance sensors which require very low current noise, although it is noted that the LT1793 had very low drift even though the voltage noise was higher than other op-amps tested. High bandwidth versions were also tried (LT1128 and LT1037), but these suffered from high frequency oscillations and proved to be unsuitable particularly because the next stage following the preamplifier is the sample-and-hold capacitor of the ADC. The problems of driving a capacitive load can be mitigated by including a small resistor at the output of the op-amp, but choosing the lower bandwidth LT 1007 produced the best results.

Earlier Version

An earlier version of this board used 800 Hz sinusoidal signal for the AC bridge and 230 Hz heater duty cycle frequency. Capacitive decoupling was used from the bridge to the preamplifier, but it was found that decoupling with a high quality audio transformer provided lower front-end noise.

Measurement with Agilent 34970

Measurement of the bridge was attempted at DC using the Agilent 34970A Multiplexing DMM. This unit has an on-board calibrated current reference for a 4-wire Kelvin measurement of resistance with a 6.5 precision DMM, but this setup can also be used to power a full bridge and measure the voltage offset. To reduce the impact of low frequency noise on the measurement, a chopping strategy was employed where one measurement was made before reversing the bridge current and making a second measurement. This can easily be accomplished through multiplexing relays included on

the breakout board. If the chopping period is sufficiently small, low frequency interference is averaged out, leaving only the signal correlated only with changes in bridge resistance. The resolution of the measurement can be increased by increasing the averaging period, but this leads to a slow sampling rate for each data point and reduces the effectiveness of the chopping strategy. Due to the slow measurement rate (approximately 1 per second) and unsatisfactory signal-to-noise ratio, this strategy was abandoned in favor of an AC driven bridge.

Shielding and Interconnects

The combined circuitry to interface the force sensor with the analog to digital converter was separated between three enclosures with cabling between them, making shielding and grounding difficult, but attention to this issue is very important [45] [46].

The first enclosure was the National Instruments (NI) PCI-6225 board which was mounted in a Dell Dimension E520 computer. A custom shield box made from copper sheet metal was made for the PCI card in order to reduce high frequency interference from other computer components. The second enclosure is the NI SCC-68 connection block through a shielded cable to the PCI-6225 card. The SCC-68 has terminals for all the analog and digital inputs and outputs. It also has an onboard voltage regulator that produces regulated $\pm 15V$ and $+5V$ either from internal power (for limited current) or an external $+5V$ supply. The third enclosure is a custom PCB mounted on the probe station which contains the force sensor preamplifier and other electronics associated with the temperature sensor and actuator switching. A set of two cables connects the DAQ I/O ports from to the NI SCC-68 to the custom PCB; as shown in Figure 78, one cable is

dedicated to low noise analog signals and the other ribbon cable handles everything else. There are separate ground planes for the analog preamplifier and the other electronics which contain digital switching components.

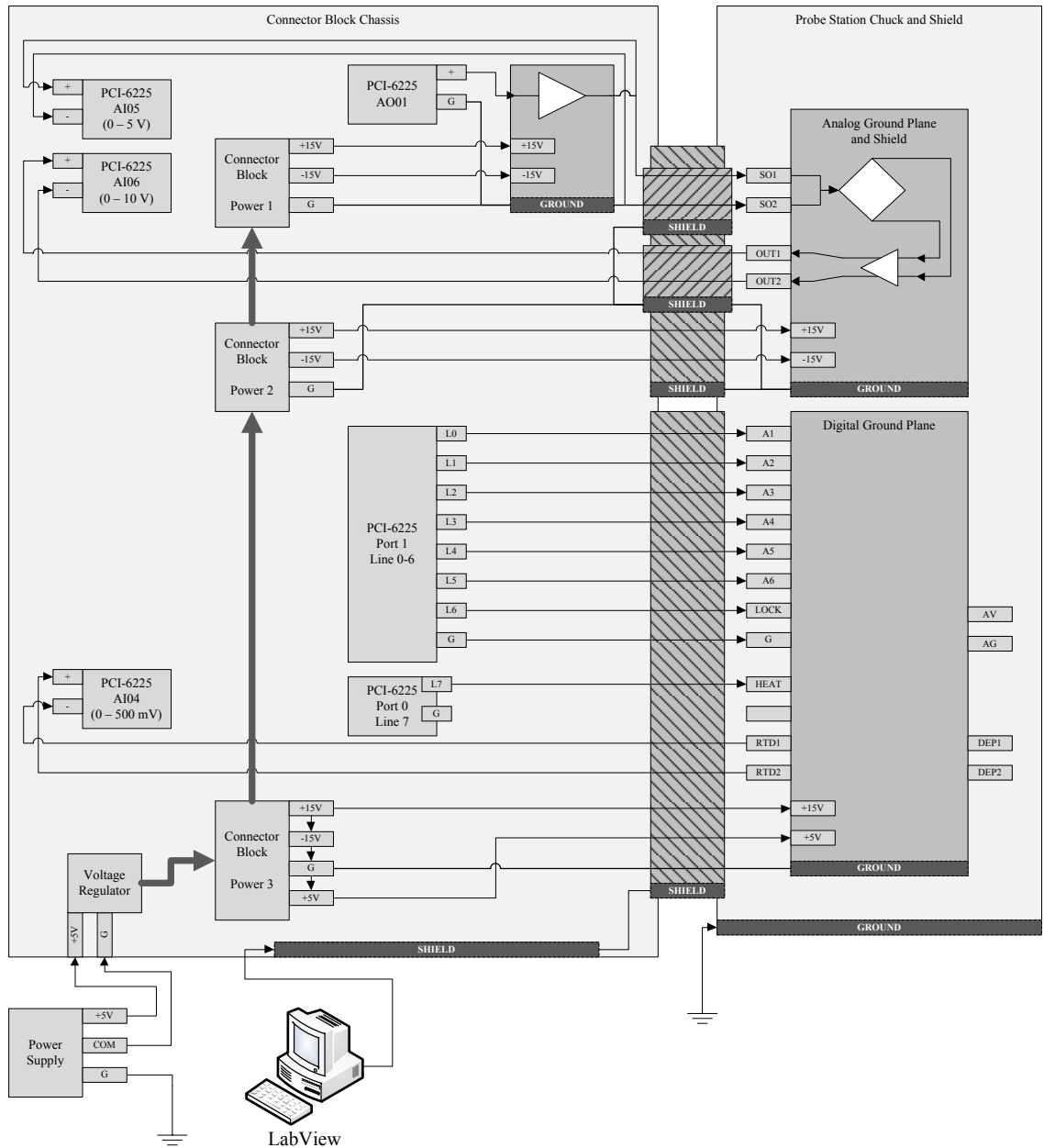


Figure 78: Wiring and Shielding diagram for NI PCI-6225 DAQ break-out box (NI SCC-68) and custom PCB. The six-wire cable for analog signals is IEEE 1394 firewire (double-shielded, 8-inches), and the 14 wire cable for digital signals is a shielded ribbon cable (18-inches).

To mitigate interference problems from ground loops and improper shielding, a single point grounding scheme is used and a single $\pm 15\text{V}$ DC power supply is used to power both the preamplifier electronics and the ADQ breakout board. One exception is the ground to the PCB chassis shield, which is connected to the probe station chuck, and which has an independent path to ground; this shield is not connected elsewhere to prevent a ground loop. Using a single power supply provided better performance than using a ± 18 volt battery supply for the preamplifier electronics since the slowly discharging battery caused strange behavior. Additionally, the bridge is driven with a 3125 Hz sinusoidal signal so that low frequency noise ($1/f$) and 60 Hz interference can be filtered and the force sensor bridge can be capacitively or inductively decoupled from the preamplifier.

All power supply wires were wound through a ferrite RF choke before connection to the PCB, and shielded analog signal cables are fitted with RF chokes at both ends. An IEEE 1394 Firewire cable was found to have an ideal combination of wires and shielding for the analog bridge hookup. This cable has two twisted-pairs with individual foil shielding packed inside a second mesh-plus-foil shield along with two insulated wires. One shielded twisted pair is connected from the line driver to the force sensor bridge. The other shielded twisted pair is connected from the pre-amplifier differential output to the differential ADC input. The cable's outer shield is connected to the breakout board chassis shield.

Once wired up, the SCC-68 connector box was shielded with one layer of 3M Ultraperm 80 cut to fit the exterior, followed by one layer of paper, and finally

aluminum foil connected to the connector block shield terminal; this strategy provided both low frequency and radio-frequency (RF) shielding.

Despite these efforts a few sources of interference produced noticeable problems. The worst culprit was a cellular phone with high speed data capabilities, which caused a significant glitch in the sensor readings whenever the “3G” or “4G” data network was used. A smaller level of interference was noted when cellular phones were connected to the cellular network, but not in use. The only way to remedy this problem was to completely power down cellular phones in the lab while measurements were in progress. Although more difficult to pinpoint, it was suspected that wireless networking on laptop computers also produced interference, but luckily the majority of computers in the laboratory used wired Ethernet for network communication and wireless LAN could be disabled on nearby laptops. Finally, occasional interference was suspected from RF plasma generators which are present in the same building, but this kind of interference was relatively rare and not as severe as the other sources described above.

A 14-wire ribbon cable was used to connect the various digital control signals for the actuator array, as well as the digital control signal for the heater driver, temperature dependent voltage from the RTD, and 15V power to the components..

Actuator Driver

To switch the high frequency voltage to each of the six pairs of actuators, the voltage is controlled through six pull-down transistor. An ON Semiconductor BS107 (200V, N-channel MOSFET transistor) is used to buffer the low power digital IO ports and control the current to a Fairchild Semiconductor 2N5550 (140V, 600mA, 100MHz NPN transistor). Each of the NPN transistors can pull down one of the actuator pairs to ground. When a particular actuator pair in the array is to be energized, the corresponding NPN transistor is turned off. An interlock relay is incorporated on the custom PCB to prevent voltages on the actuators if no control lines are connected.

A circuit representing the driver electronics and two actuators is shown in Figure 79 and Figure 80, and the resulting voltage at the surface of the actuator is simulated in Figure 83 to show the ON-state and OFF-state voltages. The voltage at the NPN transistors before (Figure 81) and after (Figure 82) capacitive coupling to the actuator is also shown. The inductors $L1$ and $L2$ provide a low frequency path to ground in order to prevent small DC voltage offsets from creating an ionic charge screen. In order to simplify the circuitry the transistors ($Q1$ and $Q2$) only operate at positive voltages, and a coupling capacitor ($C1$ and $C2$) removes the DC offset driving the actuator electrode. The capacitor was chosen to be significantly larger than the capacitance of the actuator electrodes.

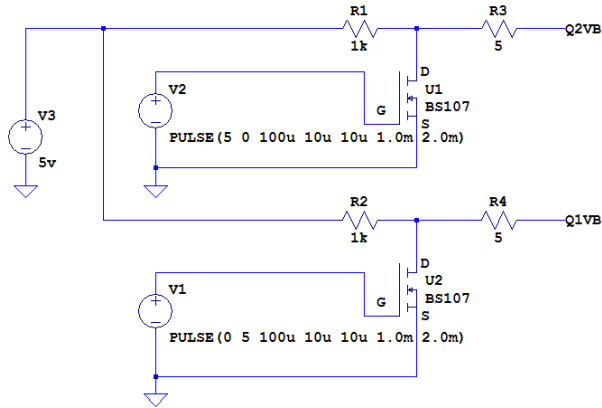


Figure 79: The digital control lines from the ADC are buffered with an N-channel MOSFET transistor before connecting to the actuator control transistors ($Q1$ and $Q2$ below).

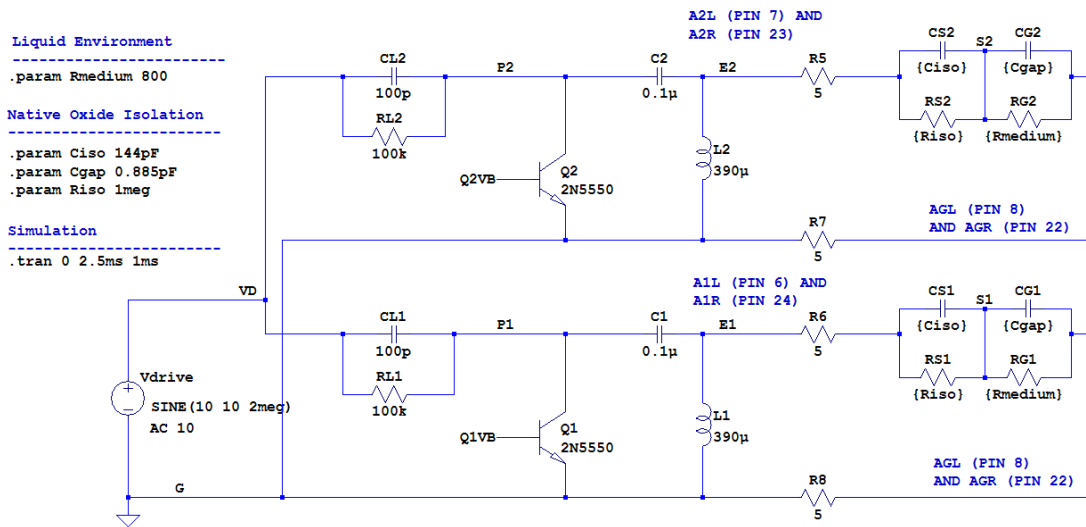


Figure 80: Each actuator pair is driven by a single high frequency voltage source, but the signal to each actuator pair is regulated by a set of NPN pull-down transistors.

In this simulation, the pull-down transistor $Q2$ is on but $Q1$ is off which results in actuator 1 being engaged while the other is not. Each actuator is modeled as having a native oxide layer ($Ciso$ and $Riso$ in the schematic) in series with the electrode gap ($Cgap$ and $Rgap$ in the schematic). The capacitance of the native oxide layer ($Ciso$) was estimated to be 144 pF based on equation 61 using relative permittivity (ϵ_r) of 3.9, a thickness (d) of 1.5 nm and surface area (A) of 500 μm by 10 μm .

$$C = \epsilon_0 \epsilon_r \frac{A}{d}$$

Using the same area, but a relative permittivity of 79 and gap of 4 μm , the capacitance of the gap (C_{gap}) was estimated to be 0.9 pF. If water of resistivity 100 $\text{k}\Omega\text{-cm}$ would fill the gap, then the resistance R_{gap} would be 800 Ω , and the resistance of the native oxide layer (approximate resistivity $1 \times 10^{15} \Omega\text{-cm}$) is over 1 M Ω .

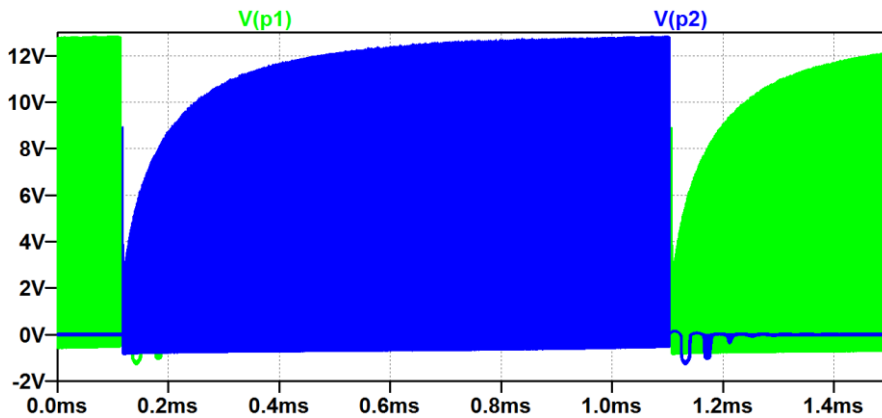


Figure 81: On-state versus off-state comparison of the actuator driver showing the voltage at the transistors Q1 and Q2.

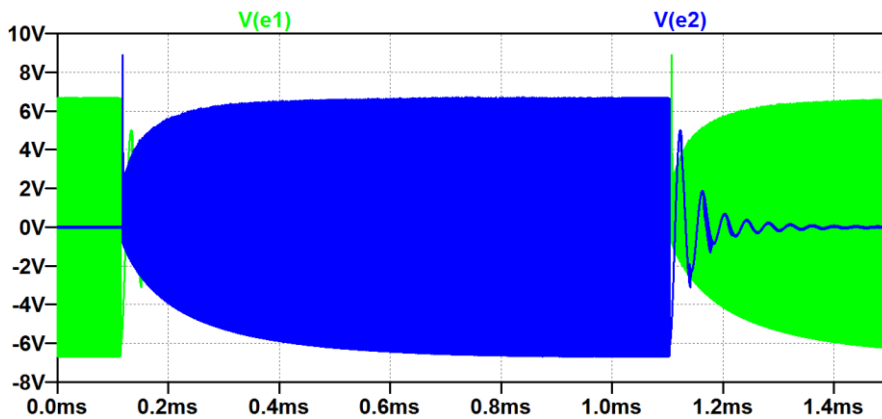


Figure 82: On-state versus off-state comparison of the actuator driver showing the voltage after removing the DC component.

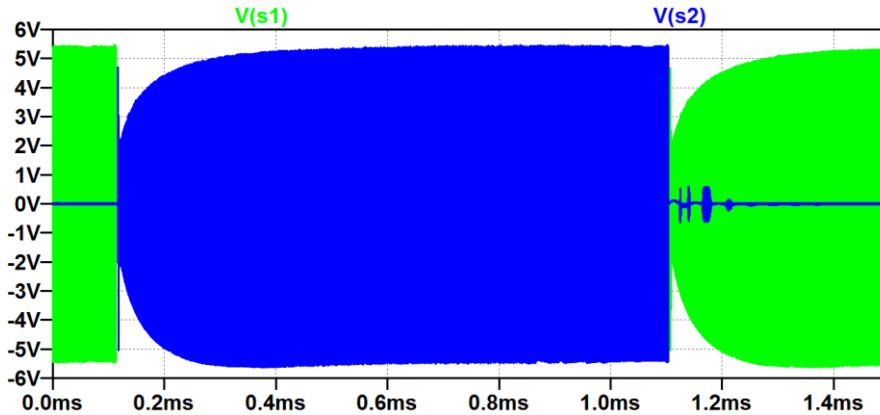


Figure 83: On-state versus off-state comparison of the actuator driver showing the expected voltage at the surface of the electrostatic electrodes.

The simulations show that the actuator driver circuitry effectively switches the voltage to the actuators (2 MHz sinusoidal) within a fraction of a millisecond. An estimate was made of the expected voltage at the surface of the electrode, but parasitic resistances and capacitances between the actuator electrodes may reduce this voltage. A method to test the voltage at the surface of the electrodes while submerged in liquid was not developed.

Temperature Regulation

On-Chip RTD

To find the characteristic temperature dependence of the on-chip RTD, a type K thermocouple probe was clipped onto the back of a packaged chip and the temperature was measured with BK Precision DMM (Test Bench 390A) while the resistance was simultaneously measured with an Agilent 34401 6.5 digit DMM. The chip was allowed to equilibrate at room temperature, moved into a 50 °C oven, and removed back to room temperature 20 minutes later while the temperature and resistance were recorded. The results were plotted (see Figure 84 and Figure 85) and a linear fit was found to the

equation $R = mT + b$, but since the expected behavior of an RTD is $R = R_0(1 + \alpha T)$

then $R_0 = b$ and $\alpha = \frac{m}{R_0}$.

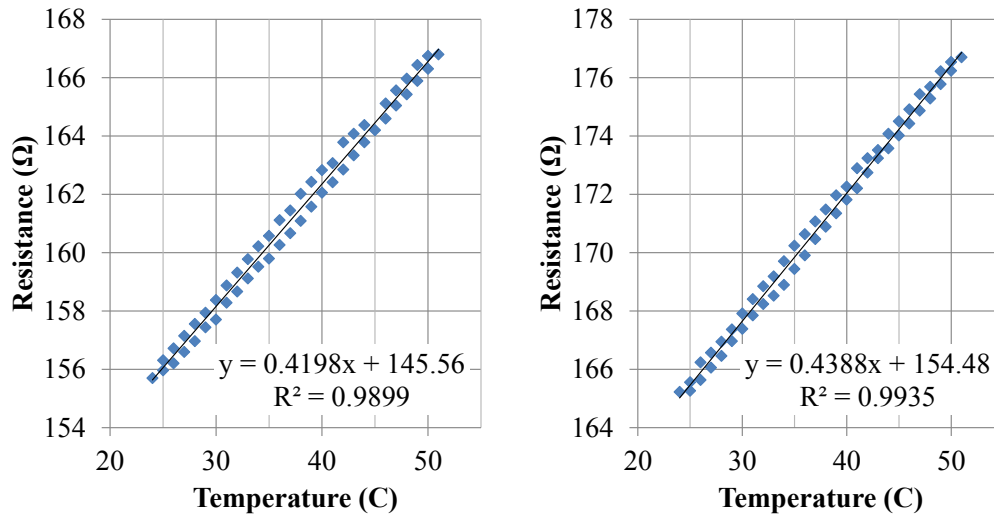


Figure 84: Typical RTD resistance for chips from wafer SOI 02 as a function of temperature. The RTD is made from thin film gold with a chrome adhesion layer.

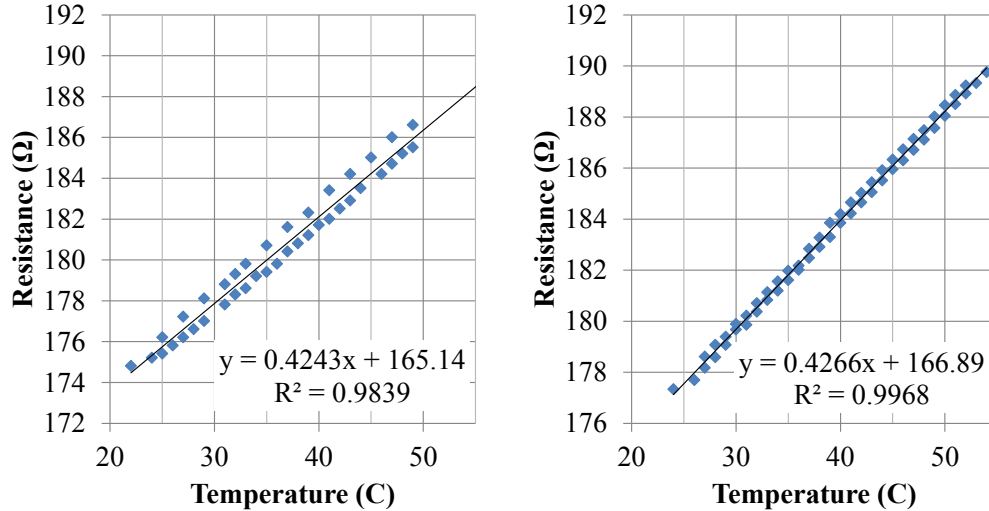


Figure 85: Typical RTD resistance for chips from wafer SOI 06 as a function of temperature. The RTD is made from thin film gold with a chrome adhesion layer.

The temperature coefficient of resistivity (TCR) for chips from wafer SOI 02 was assumed to be 0.002862, and the TCR for chips from wafer SOI 06 was assumed to be 0.002561 (see Table 37). The deviation of the TCR from that of pure gold is due to the

presence of a thin chrome adhesion layer. The TCR of pure gold is 3715 ppm/°C, and the TCR of pure chrome is 5.9 ppm/°C; the expected TCR is the weighted average by thickness as shown in Table 38.

Table 37: Measured RTD parameters.

Wafer	Device	Fitted Slope ($\Omega/^\circ\text{C}$)	Fitted Intercept (Ω)	R0 (Ω)	TCR ($1/^\circ\text{C}$)
SOI 02	A45	0.419835	145.556	145.6	0.002884
SOI 02	D80	0.438792	154.483	154.5	0.002840
SOI 06	A47	0.423626	165.168	165.2	0.002565
SOI 06	D67	0.426592	166.886	166.7	0.002556

Table 38: Gold / Chrome layer thicknesses

Wafer	Cr Layer 1 Thickness	Au Layer Thickness	Cr Layer 2 Thickness	TCR Weighted Average by Thickness
SOI 02	50 nm	200 nm	0 nm*	0.002973 $1/^\circ\text{C}$
SOI 06	50 nm	200 nm	50 nm	0.002479 $1/^\circ\text{C}$

**Second chrome layer not present*

Deviations from the expected temperature coefficient of resistivity are probably due to variations in the thickness of the deposited metals.

Temperature-Compensated Current Source

A temperature compensated current source (Linear Technology LM334) provides 1.438 mA of current to the on-chip RTD, and the resulting voltage drop across the RTD is measured by a differential ADC input. This current source provides accurate current, but is probably the largest source of on-board interference. It causes significant interference on the +5V supply (even with bypass capacitors) when the output load is not sufficiently small ($> 1 \text{ K}\Omega$).

Heater Driver

In order to drive the heater from one of the digital control lines, an ON Semiconductor BS107 (200V, N-channel MOSFET transistor) is used to buffer the low power digital IO ports. Power is supplied from the +15V supply of the PCI-6225 connector block.

LabView Interface

An important part of the experimental setup is the LabView control panel software, which provided instantaneous monitoring and control of the experimental setup as well as data logging and diagnostic information about signal quality. A diagram of the inputs, outputs, and internal processes is shown in Figure 86 and Figure 87. The front display is shown in Figure 88.

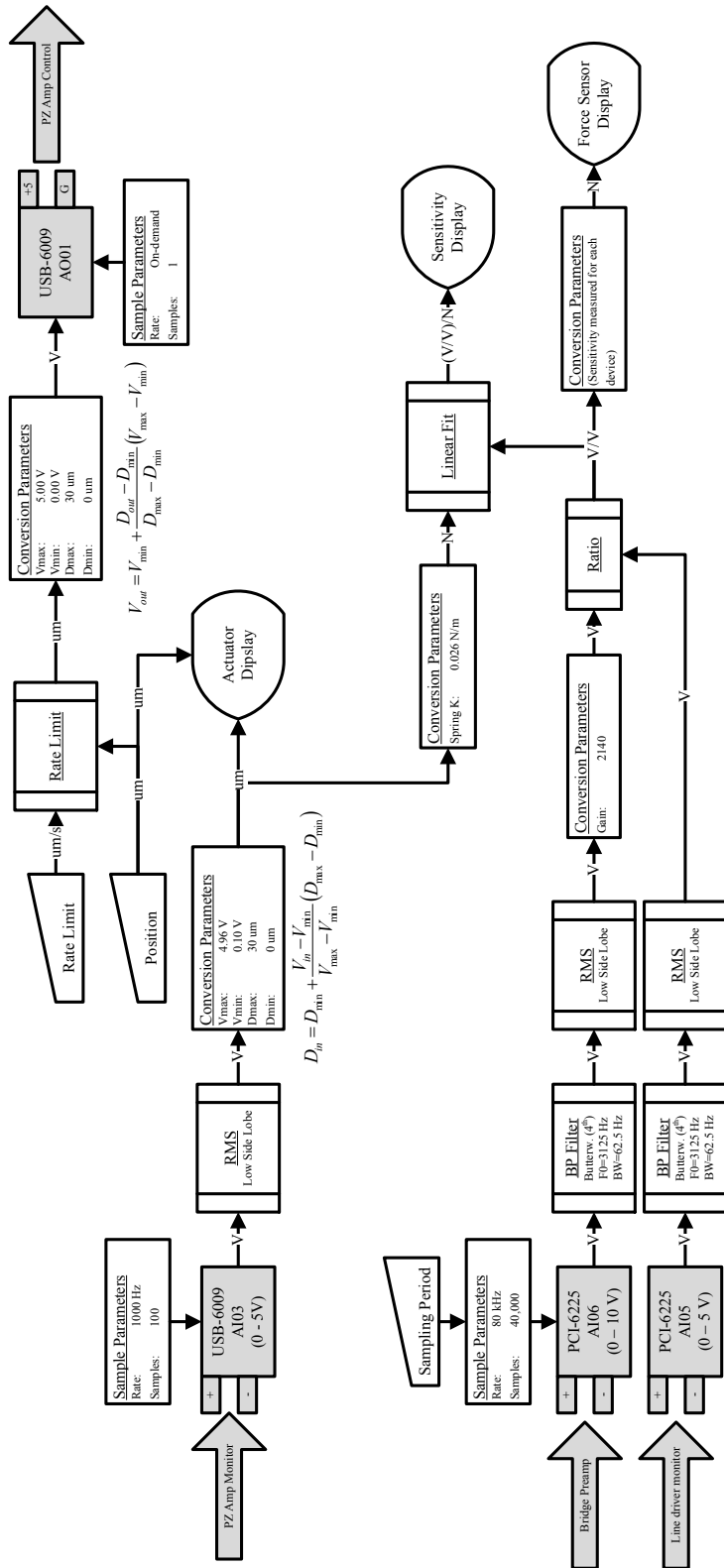


Figure 86: LabView process flow showing inputs, outputs, user display and user input (part 1).

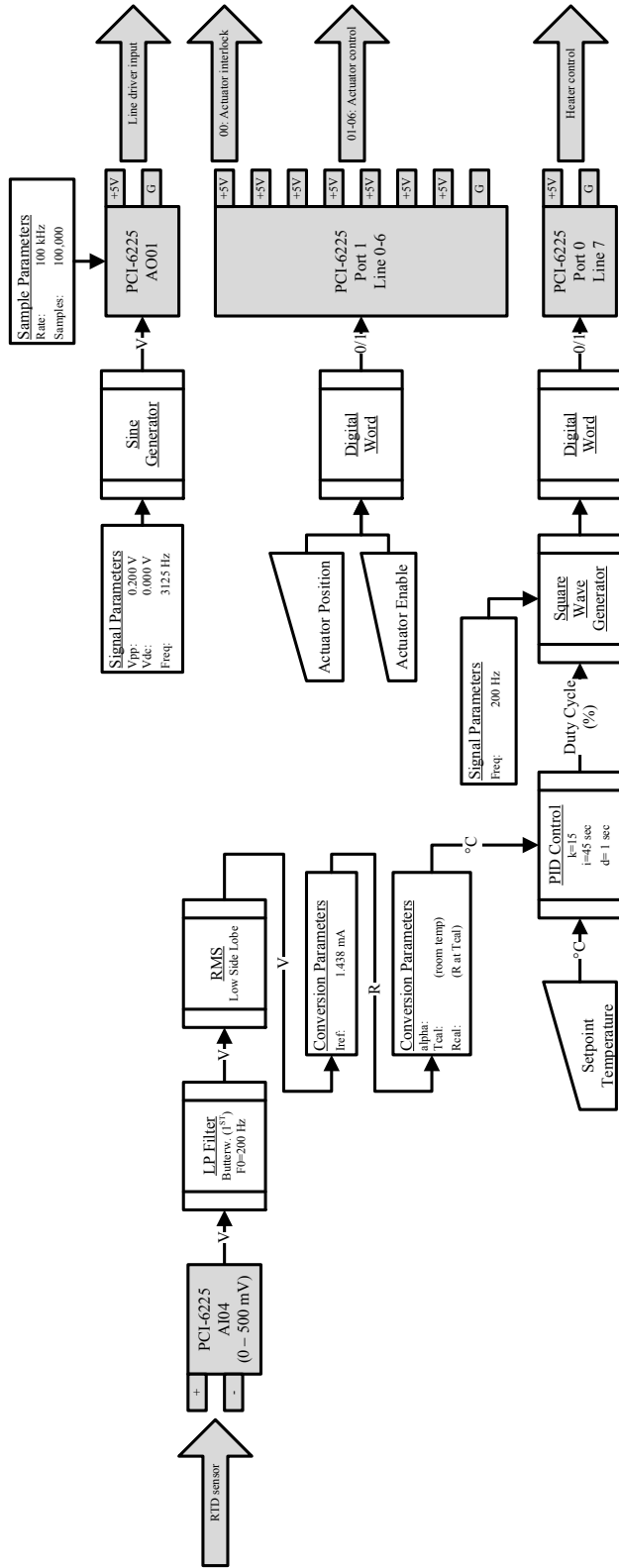


Figure 87: LabView process flow showing inputs, outputs, user display and user input (part 2).

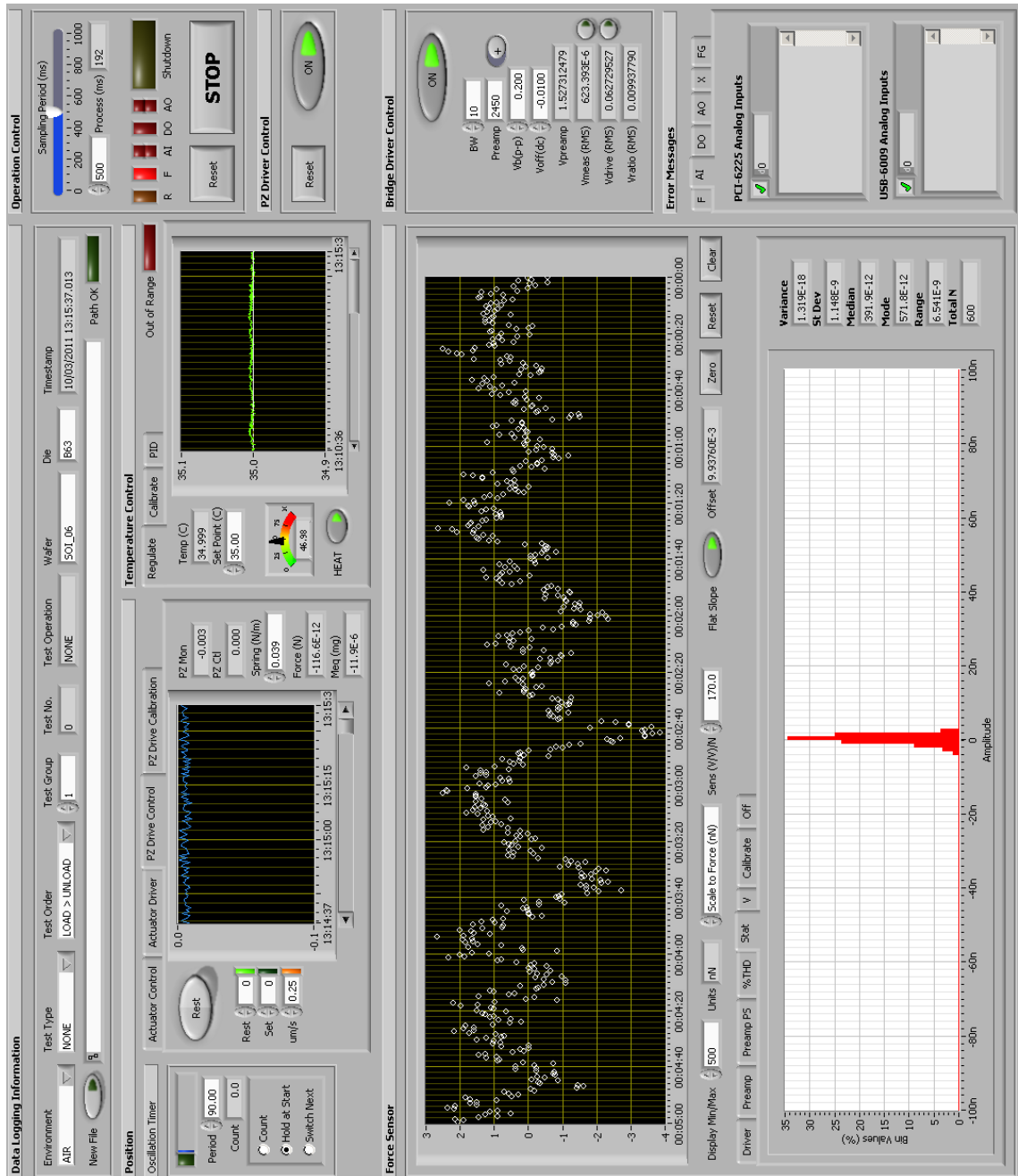


Figure 88: LabView front panel.

Chapter 5: Cell Biomechanics

Model of Cell Behavior

Contact Mechanics

The Hertz contact model, which describes the force versus deformation relationship of two solid objects under pressure, is commonly used in conjunction with experiments involving spherical objects [52]. A number of idealized problems have solutions, such as the indentation of a spherical object into a flat surface, the indentation of a cylindrical punch into a flat surface or the contact of two spheres with different radius. In research work on the behavior of small viscoelastic gel particles under load [51] a model based on the standard linear solid model and Hertz contact mechanics was developed and experimentally verified.

When a mechanical loading force (F) acts along a line that passes through the centers and the contact point of two elastic spheres 1 and 2, the deformation depth (d) under the load can be given by equation 62 [52].

$$\Delta d = \left(\frac{9F^2}{16R^*E^{*2}} \right)^3 \quad 62$$

The relative curvature (R) is defined for the two spheres in contact with radii R_1 and R_2 as given by equation 63.

$$\frac{1}{R} = \frac{1}{R_1} + \frac{1}{R_2} \quad 63$$

The combined strain modulus E^* is given by equation 64 where the Poisson ratio (ν) and Elastic modulus (E) are known for each sphere.

$$\frac{1}{E^*} = \frac{1 - \nu_1^2}{E_1} + \frac{1 - \nu_2^2}{E_2} \quad 64$$

In the case where the sphere is contacting a rigid plane surface, $R_2 \rightarrow \infty$ so that $R = R_1$, and $E_2 \gg E_1$ which results in equation 65.

$$E^* = \frac{E_1}{1 - \nu_1^2} \quad 65$$

The expression for penetration depth is then given by equation 66, or alternately the force by equation 67.

$$\Delta d = \left(\frac{9}{16} \left(\frac{1}{2G} \right)^2 \frac{F^2}{R} \right)^{1/3} \quad 66$$

$$F = \frac{4}{3} \left(\frac{2G}{1} \right) \sqrt{R \Delta d^3} \quad 67$$

But when there is no volume change of the material under compression, the shear stress G is given by equation 68 and equation 66 becomes equation 69.

$$G = \frac{E}{2(1 - \nu^2)} \quad 68$$

$$\Delta d = \left(\frac{9}{16} \frac{F^2}{R} \left(\frac{1 - \nu_1^2}{E} \right)^2 \right)^{1/3} \quad 69$$

This final set of equations (66, 68, and 69) provide the basis for modeling a spherical object under compression, and have been extended [51] to include the viscoelastic properties of the material.

Viscoelastic Model

An ideal viscoelastic material can be represented either as a Maxwell unit (a spring and dashpot in series) in parallel with a second spring suitable for stress relaxation under fixed strain, or as a Kelvin-Voigt unit (a spring and dashpot in parallel) in series with a second spring suitable for modeling creep under fixed stress (see Figure 89).

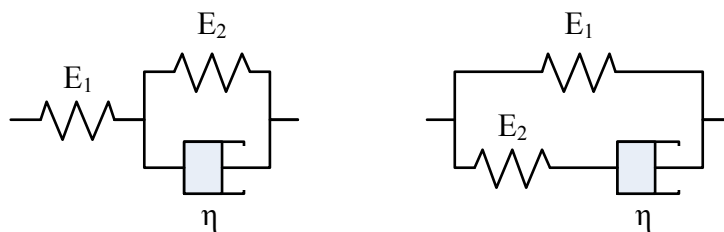


Figure 89: Two models of viscoelastic material: a Kelvin-Voigt unit (spring in parallel with dashpot) in series with a second spring (right) or a Maxwell unit (spring in series with dashpot) in parallel with a second spring (left).

When studying strain relaxation over time, $I(t)$ is defined as the strain relaxation function [51], where $\epsilon(t)$ is strain as a function of time, σ_0 is the fixed applied stress.

$$\epsilon(t) = I(t)\sigma_0 \quad 70$$

Cell biomechanics experiments are typically modeled as a Maxwell unit in parallel $I(t)$ with a second spring [48] (see Figure 89 (left)) since it produces a more convenient stress relaxation equation. The governing equation of stress and strain for this material is shown in 71.

$$\sigma + \frac{\eta}{E_2} \frac{d\sigma}{dt} = E_1 \epsilon + \eta \left(1 + \frac{E_1}{E_2}\right) \frac{d\epsilon}{dt} \quad 71$$

By applying boundary conditions for stress relaxation (fixed strain which is zero before $t=0$ and is equal to ϵ_0 afterwards), the result is equation 72.

$$\sigma + \frac{\eta}{E_2} \frac{d\sigma}{dt} = E_1 \epsilon_0 \quad 72$$

Assume the solution to the stress as a function of time is of the general form shown in equation 73.

$$\sigma(t) = a + ce^{-bt} \quad 73$$

$$\sigma(t) = \begin{cases} \epsilon_0(E_1 + E_2), & t = 0 \\ \epsilon_0(E_1), & t = \infty \end{cases} \quad 74$$

Then the constants a, b and c can be solved using the boundary conditions in equation 74, which results in equation 75, where τ is defined as $\tau = \eta/E_2$.

$$\frac{\sigma(t)}{\epsilon_0} = E_1 + E_2 e^{-(t/\tau)} \quad 75$$

One the other hand, the creep relaxation (where stress is fixed and strain varies as a function of time), is not easy to solve in the manner shown above when using the standard linear solid model (see Figure 89, left). Fortunately, the creep compliance function $I(t)$ for this scenario has already been derived [54] and is shown in equation 76 and equation 77.

$$\frac{\epsilon(t)}{\sigma_0} = C_{crp}(t) = C_g + (C_r - C_g) \left[1 - e^{-(t/\tau_c)} \right] \quad 76$$

$$C_g = \frac{1}{E_1 + E_2}, C_r = \frac{1}{E_1}, \tau_c = \tau \left(\frac{E_1 + E_2}{E_1} \right) \quad 77$$

The creep compliance function can be rewritten as equation 78.

$$I(t) = \left(\frac{1}{E_1 + E_2} \right) + \frac{E_2}{E_1} \left(\frac{1}{E_1 + E_2} \right) \left[1 - e^{-(t/\tau_c)} \right] \quad 78$$

where $\tau_c = \frac{\eta}{E^*}, E^* = \frac{E_1 E_2}{E_1 + E_2}$

The authors studying strain relaxation of viscoelastic gel particles [51], apply the following substitution (equation 79) where the creep compliance function (equation 80) is derived for a Kelvin-Voigt unit in series with a second spring (see Figure 89, right).

$$\frac{1}{2G} = I(t) \quad 79$$

$$I(t) = \frac{1}{E_1} + \frac{1}{E_2} \left(1 - e^{-t/\tau} \right) \text{ where } \tau = \frac{\eta}{E_2} \quad 80$$

This substitution into the contact model results in equation 81 which relates the force (F) and displacement Δd to the material properties of the cell (E_1 , E_2 and η) for the a Kelvin-Voigt type model.

$$F = \frac{4}{3} \left(\frac{1}{\frac{1}{E_1} + \frac{1}{E_2} (1 - e^{-t/\tau})} \right) \sqrt{R} \Delta d^{3/2} \text{ where } \tau = \frac{\eta}{E_2} \quad 81$$

In most cell mechanics literature, the Standard Linear Solid model is used, and substituting the creep compliance function (equation 78) into the contact model (equations 66, 67) results in equation 82.

$$F = \frac{4}{3} \left(\frac{1}{\left(\frac{1}{E_1 + E_2} \right) + \frac{E_2}{E_1} \left(\frac{1}{E_1 + E_2} \right) [1 - e^{-(t/\tau_c)}]} \right) \sqrt{R} \Delta d^{3/2} \quad 82$$

where $\tau_c = \frac{\eta}{E^*}, E^* = \frac{E_1 E_2}{E_1 + E_2}$

Although this model is somewhat cumbersome, the parameters can be fitted to the recorded data using numerical methods just as easily.

Measured Stress Relaxation

Tests with On-chip Actuator

The on-chip actuator array was not capable of compressing the cell while in PBS or cell media, and it causes interference on the force sensor when operating in water or 10% sucrose. Repeated tests were performed with the idea that a baseline behavior of interference could be established without a cell. A measurement based on the difference of the forces from a measurement during actuation with a cell and without a cell, thus revealing the underlying force on just the cell. This method did not provide any useable results, but the test results are shown in Figure 91. The available movement from the actuator was too small – measured at 1.7 μm – and the interference measured on the force sensor was much larger than the expected forces from the cell.

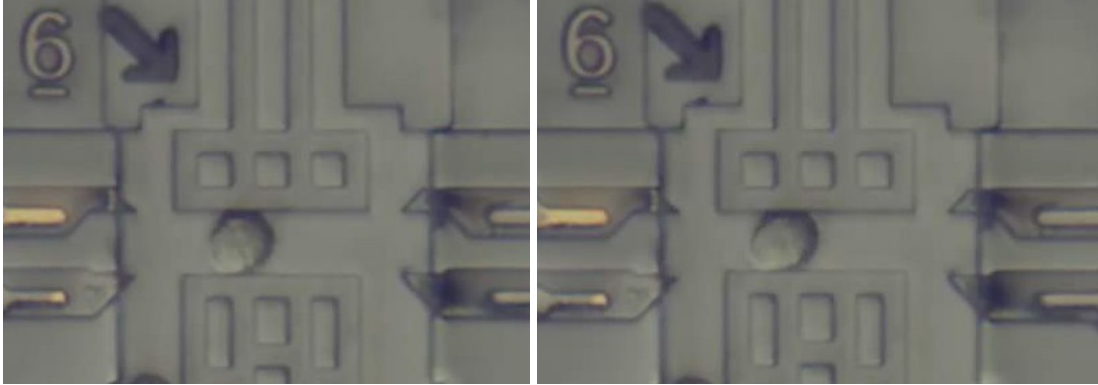


Figure 90: A single MC3T3 cell is compressed by 1.7 μm in 10% sucrose using the on-chip actuator array.

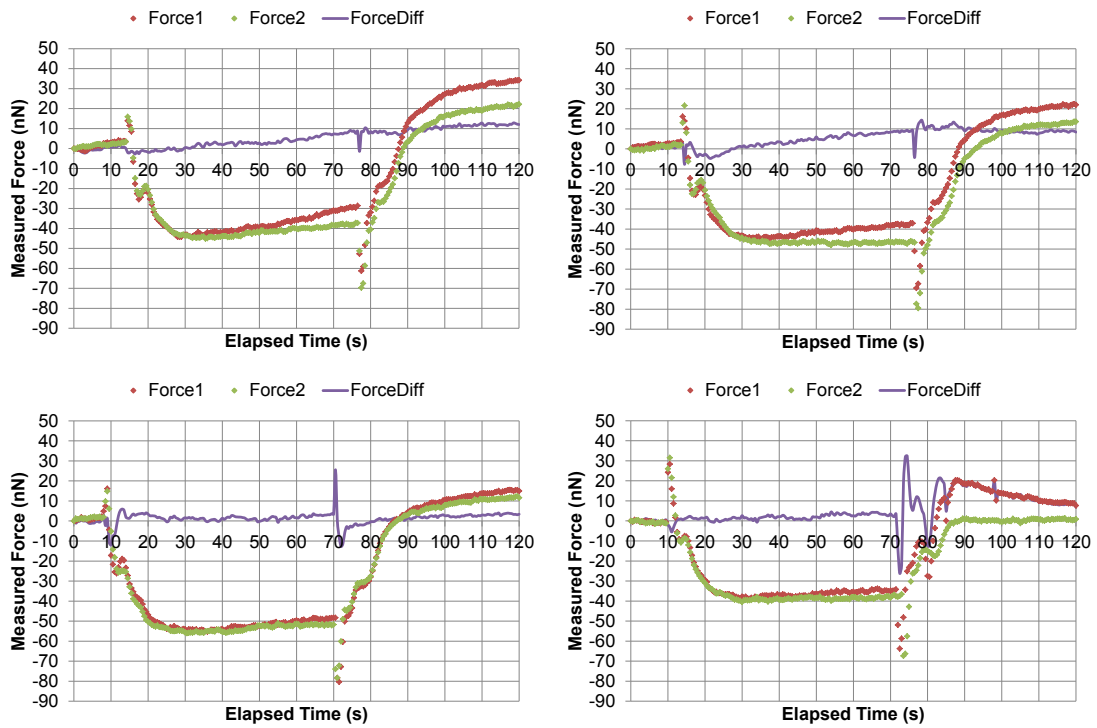


Figure 91: Four compression tests on MC3T3 cells using the on-chip actuator in 10% sucrose. The difference between Force 1 (with cell) and Force 2 (without cell) does not reveal useable measurements of forces on the cell due to the strong interference.

Test with External Piezo-driver

Without the functionality of the actuator array, the central shuttle was moved using a probe tip and piezo-driver controlled through LabView (see Figure 43 above). This

approach was taken so that the force sensor operation could be demonstrated while measuring the forces on cells in cell media.

Each cell is compressed by a fixed amount and the force during the compression (typically 120 seconds) is measured. The compression is also recorded by the microscope camera so the diameter of the cell can be measured for each test. A series of images from a typical compression test is shown in Figure 92.

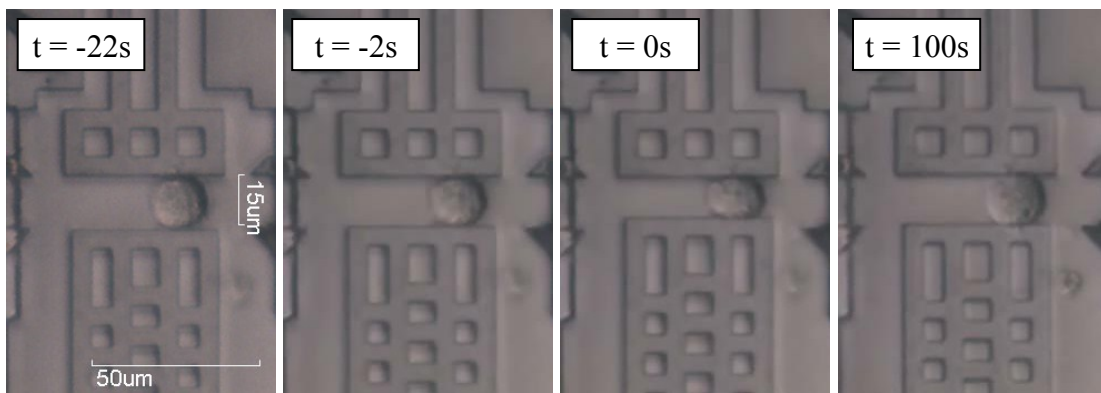


Figure 92: NIH3T3 cell ($16.4\ \mu m$ diameter) compressed by $3.7\ \mu m$ (SOI 06 A47, Number 2, 20110708_122341).

The testing procedure is outlined below in Table 39.

Table 39: Cell Testing Procedure.

Activity	Procedure
Cell Preparation	<ol style="list-style-type: none"> 1. Standard cell culture procedure for NIH3T3 / MC3T3 2. Harvest with trypsin (0.125% solution) and re-suspend in 5 ml cell media 3. Move cells to probe station and store in 36 °C water bath
Device Preparation	<ol style="list-style-type: none"> 1. Mount chip and calibrate RTD to room temperature 2. Wet chip with 70% ethanol to sterilize and prevent bubbles 3. Rinse with DI water for 60 seconds 4. Mount chip and fit outer shielding to probe chuck 5. Wait until temperature regulation is stable at 37 °C 6. Flush chip with cell media 7. Set up probe tip / piezo-driver in contact with shuttle 8. Wait for temperature to stabilize
Software Preparation	<ol style="list-style-type: none"> 1. Set up microscope camera and scale bar 2. Start LabView data logging
Cell Positioning	<ol style="list-style-type: none"> 1. Add suspended cell solution to chip (approximately 20 μL) 2. Wait for cells to settle to bottom 3. Carefully push nearby cell to cell test area 4. Wait for cell to settle to bottom surface (approximately 2 min)
Cell Test	<ol style="list-style-type: none"> 1. Capture pre-compression image 2. Start video 3. Step compression of cell 4. Find new cell and repeat
Step Compression Parameters	<ul style="list-style-type: none"> • Typically 5 μm (25% strain) • 5 μm/s rate limit between positions • 120 second load / 120 second rest

Both NIH3T3 and MC3T3 cells were tested using this method, although only a few cells per session could be successfully tested due to limitations in attracting the cells to the testing area. As the cells settle to the bottom of the dish, they slowly begin to lose their spherical shape and become stickier. With extended contact to the bottom of the chip they try to attach to the surface and grow. Depending on the cell type, tests are not possible more than 1 to 2 hours after harvesting with trypsin.

The F versus Δd data that has been recorded can be numerically fitted to equation 82 using MATLAB's FMINSEARCH, which uses a direct search algorithm to minimize a nonlinear function of several variables. The result is values for the elastic constants

(E_1 and E_2) and the relaxation constant (τ). During the search, the variables are limited to upper and lower bounds as shown in Table 40.

Table 40: Nonlinear fit algorithm upper and lower search bounds.

Parameter	Lower Bound	Upper Bound
E_1 (Pa)	0	1×10^6
E_2 (Pa)	0	1×10^6
τ (sec)	0	1×10^3

The results of the numerous cell compression experiments are listed in Appendix VIII: NIH3T3 Test Data and Appendix IX: MC3T3 Test Data. As well as the raw data, the fitted parameters are also tabulated for all the tests. Many of the cells exhibited the characteristic viscoelastic behavior that was expected. However, a number of tests produced no discernible visco-elastic response and the measured forces were much smaller, but the reason behind this is unclear. The details of the time-varying response may simply be buried in the low-frequency background noise of the force measurement.

In order to estimate the repeatability of the measurements, an experiment was performed where the same cell was repeatedly compressed by the same amount for a shorter duration of 10 seconds with a 10 second rest period. The NIH3T3 cell diameter was $15.1 \mu\text{m}$ and it was compressed by $4.7 \mu\text{m}$ (31%). The data can be seen in the appendix and the recorded data was fit to a purely linear elastic model (see equation 69). A summary is shown in Table 41 which gives an estimate for the standard deviation under the best measurement conditions.

Table 41: Summary of a single repeated cell compression.

Statistic	E (Pa)
Mean	82
Standard Deviation	6.9
Count (N)	5

NIH3T3 and MC3T3 Comparison

In order to begin the investigation of possible mechanical biomarkers, a comparison of the mechanical properties of NIH3T3 (immortalized mouse fibroblast line) cells and MC3T3 (immortalized mouse osteoblast line) cells is made by plotting the extracted parameters to look for distinguishable sets of data. The mean values of the elastic modulus for NIH3T3 cells and MC3T3 cells are summarized in Table 42. Although the standard deviations are large, they are comparable to other microplate compression experiments on fibroblasts cells [49].

Table 42: Summary of measured NIH3T3 and MC3T3 elastic modulus.

Statistic	NIH3T3 E (Pa)	MC3T3 E (Pa)
Mean	210.5	273.8
Standard Deviation	140.7	152.0
Count (N)	17	9

At this sample size, the bulk elastic modulus cannot be used as a characteristic mechanical property to separate the two types of cells (see Figure 93).

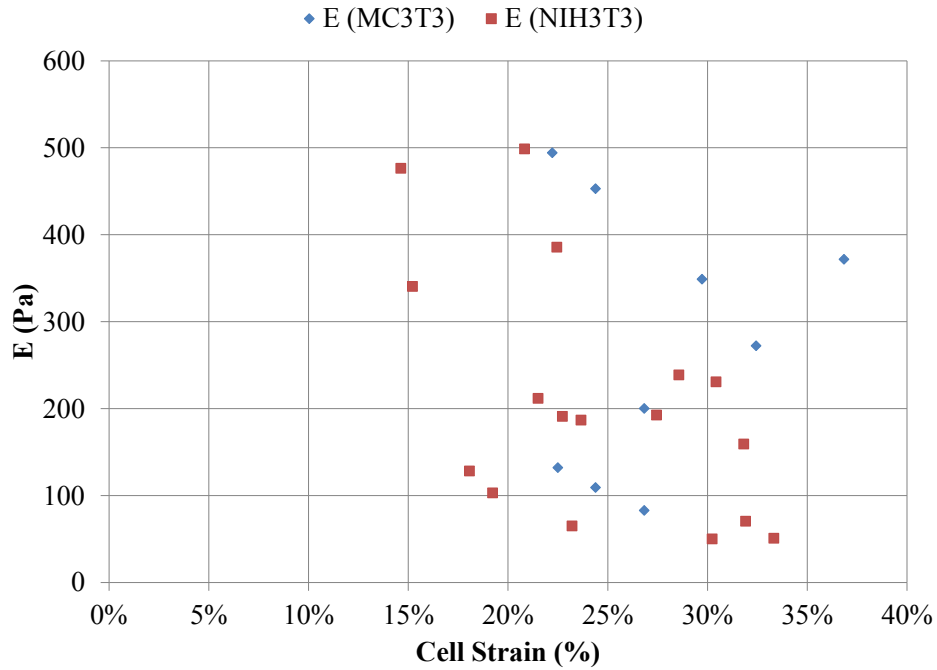


Figure 93: Bulk elastic modulus (E) of NIH3T3 and MC3T3 cells derived by fit to a purely elastic contact model.

Many of the cells tested did not have a discernible viscoelastic response, and those measurements have been removed from the data set of viscoelastic parameters. The mean values for the viscoelastic parameters of NIH3T3 cells are summarized in Table 43, but a comparable table for MC3T3 cells is not available due to the small sample size.

Table 43: Measured values for mouse fibroblast (NIH3T3) mechanical properties.

Statistic	E_1 (Pa)	E_2 (Pa)	η (Pa-S)
Mean	171.6	491.5	12.5×10^3
Standard Deviation	119.5	246.2	13.6×10^3
Count (N)	9	9	9

Although the standard deviation in the results for the viscoelastic parameters are similar to other reported results (see summary Table 44 [49]), the average value of the elastic constants E_1 and E_2 are much lower. These reported values were chosen since they were

performed using microplate compression which is similar to the compression technique in this research, and fibroblast cells were also studied. The difference in values may be because the cells are from two different animals, or because the applied strain was much larger (approximately 60% on 10 μm diameter cells) than performed in these experiments (approximately 25% on 16 μm diameter cells). There may also be differences in cell preparation which may impact the mechanical properties of the interior of the cells.

Table 44: Reported results for avian chick fibroblast mechanical properties [49].

Statistic	E_1 (Pa)	E_2 (Pa)	η (Pa-S)
Mean	960	510	1.3×10^4
Standard Deviation	199*	194*	†
Count (N)	11	11	11

* converted from 95% confidence interval to standard deviation ($MEAN \pm 1.96 \times SD$)

† value not reported, but stated to range from 1×10^3 to 1×10^5 Pa-s

The next four figures, which plot E_1 (Figure 94), E_2 (Figure 95), viscosity (Figure 96) and relaxation constant (Figure 97), are similar in nature to the plot of bulk elastic modulus (Figure 93) in that none of these parameters offer a definitive way to separate the NIH3T3 cells from the MC3T3 cells. The analysis also suffers from the lack of reliable information from the MC3T3 cells since the measured forces were small (near the noise floor of the force sensor) and therefore did not produce a good quality fit to the model. This results in only two useable measurements for the MC3T3 cells.

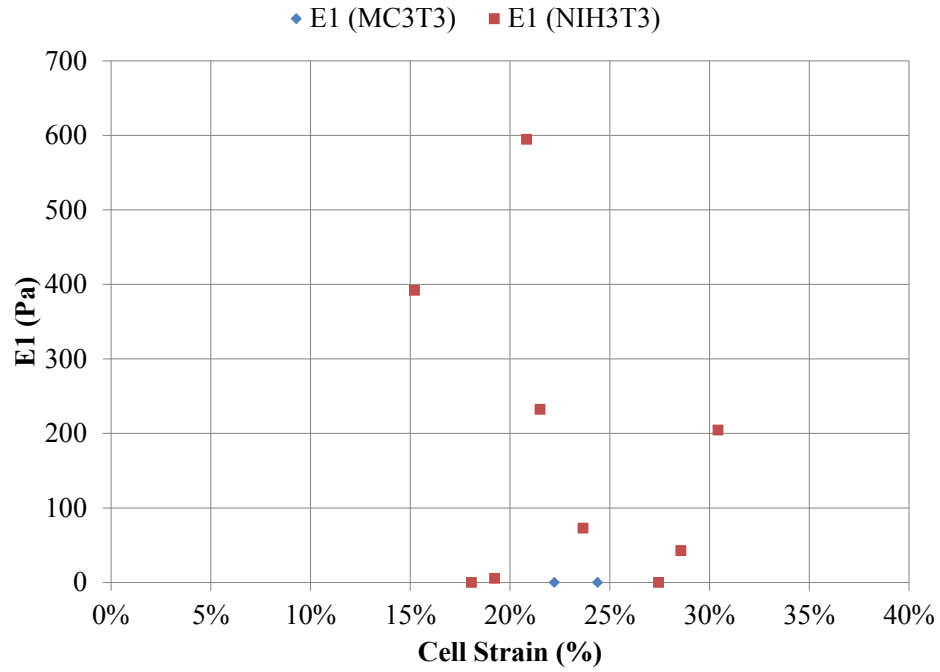


Figure 94: Equilibrium elastic modulus (E_1) of NIH3T3 and MC3T3 cells derived by fit to a viscoelastic (SLS) contact model.

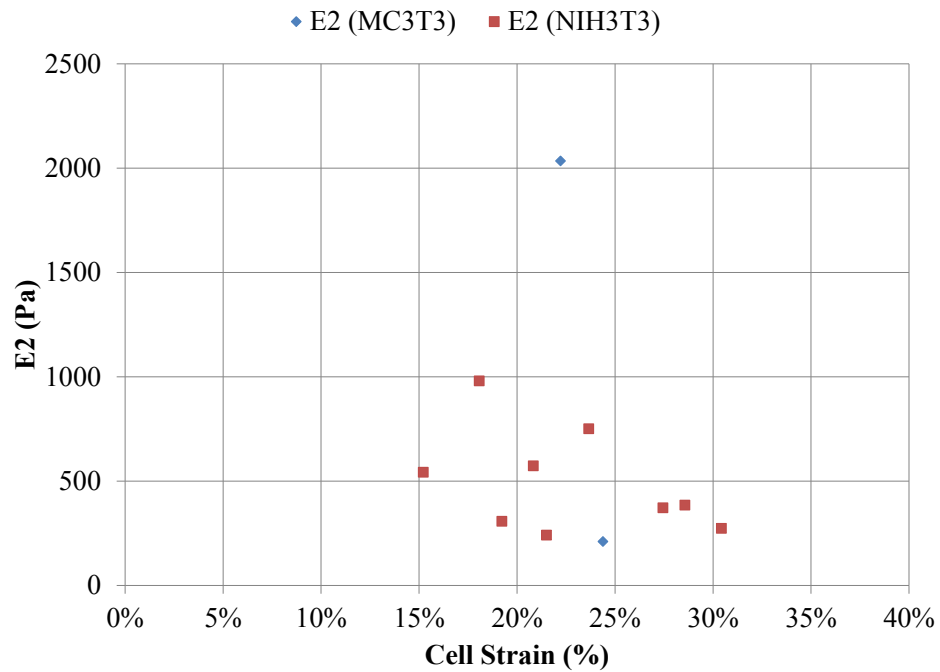


Figure 95: Elastic modulus (E_2) of NIH3T3 and MC3T3 cells derived by fit to a viscoelastic (SLS) contact model.

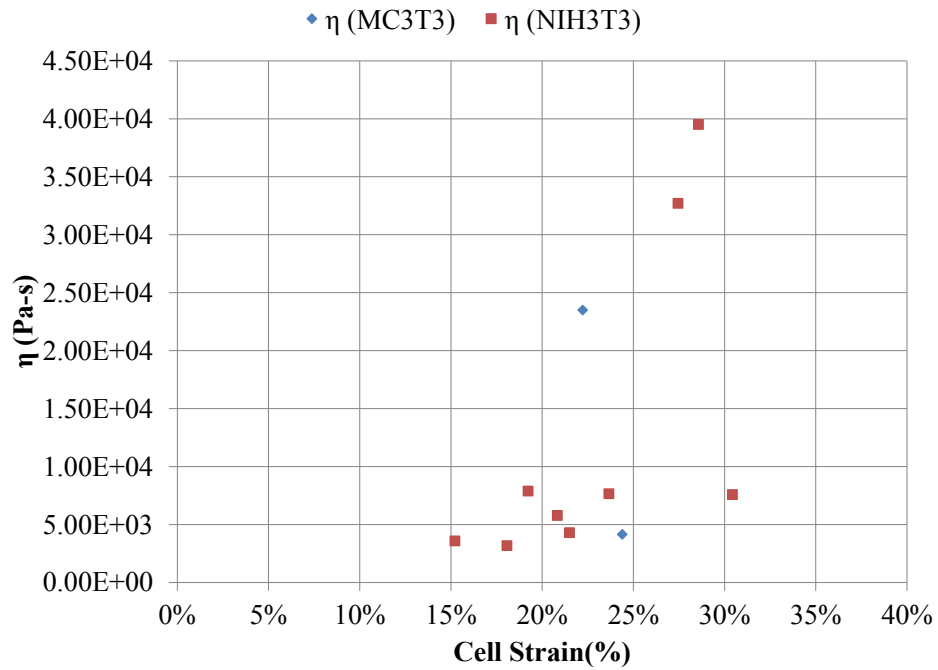


Figure 96: Viscosity (η) of NIH3T3 and MC3T3 cells derived by fit to a viscoelastic (SLS) contact model.

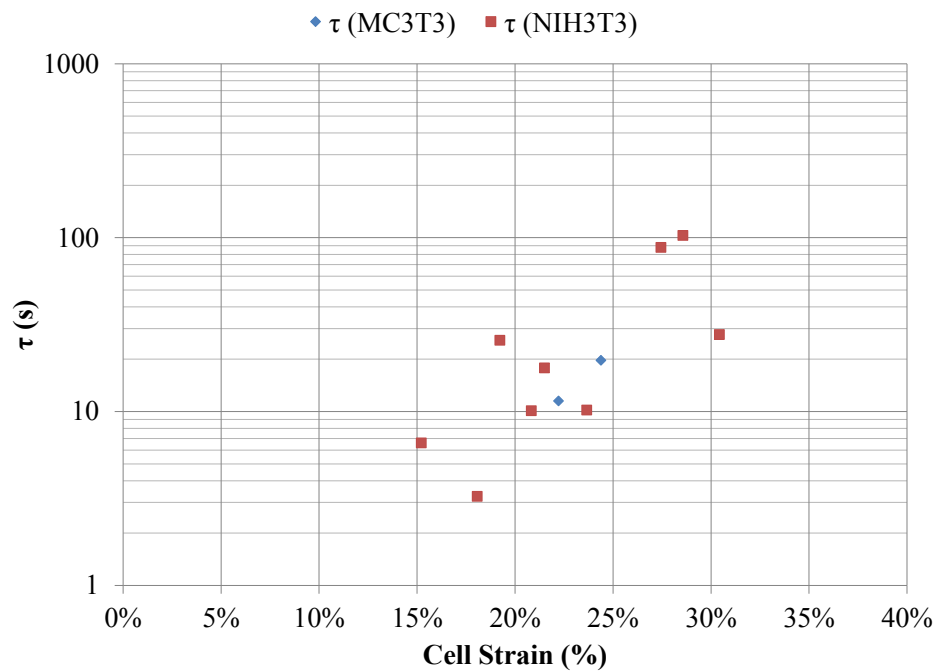


Figure 97: Relaxation time (τ) of NIH3T3 and MC3T3 cells derived by fit to a viscoelastic (SLS) contact model.

There is a significant amount of variation in the data and the values of the mechanical properties of NIH3T3 and MC3T3 cells overlap. Without much larger sample sizes, a mechanical biomarker which differentiates the two types of cells is not visible. Many of the MC3T3 cells exhibited limited viscoelastic behavior, which could be because they are not very viscous, or because the value of E_2 is very small.

Conclusion

The objective of this research was to establish the technology to measure the mechanical properties of biological cells. Although the on-chip actuator array did not perform well (particularly due to interference with the force sensor), the force sensor and associated electronics exceeded expectations. Even with these force sensing capabilities, the forces measured for certain cells was smaller than anticipated based on background literature research, and further refinement of the design will be needed to test suspended MC3T3 cells and accurately measure their mechanical properties. Improvement of the actuator array will be complex, due to the ionic screening that is present when the electrostatic clamps are open, but which changes in an unknown way as the gap between the electrostatic clamps closes. Technical improvements combined with a better cell-positioning system (possibly involving microfluidics) may one day allow high-throughput screening of cells based on their mechanical properties using a BioMEMS platform similar to this one.

Bibliography

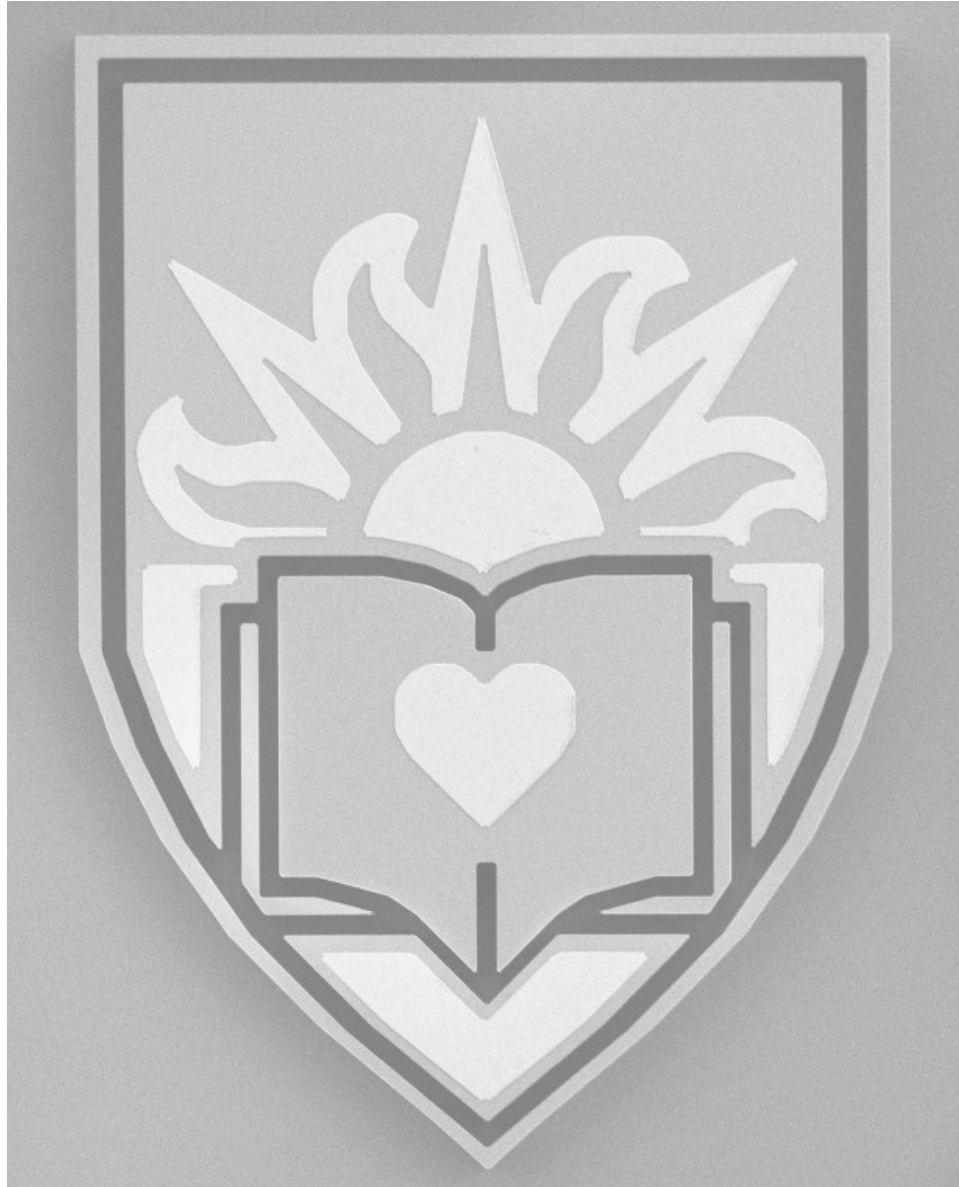
- [1] P.J. Ehrlich, L.E. Lanyon. "Mechanical Strain and Bone Cell Function: A Review." *Osteoporosis International*, vol. 13, no. 9, pp. 688-700, 2002. doi: [10.1007/s001980200095](https://doi.org/10.1007/s001980200095).
- [2] National Cancer Institute. "Structure of Bone Tissue." Internet: training.seer.cancer.gov/anatomy/skeletal/tissue.html, [Sep. 19, 2011].
- [3] Henry Gray. *Anatomy of the Human Body*, 20th ed. Philadelphia, PA: Lea & Febiger, 1918. Available: www.bartleby.com/107/illus77.html, [Sep. 19, 2011].
- [4] William F. Ganong. *Review of Medical Physiology*, 17th ed. Norwalk, CT: Appleton & Lange, 1995, pp. 352-356.
- [5] G. D'Ippolito, P.C. Schiller, C. Ricordi, B.A. Roos, G.A. Howard. "Age-Related Osteogenic Potential of Mesenchymal Stromal Stem Cells from Human Vertebral Bone Marrow." *Journal of Bone and Mineral Research*, vol. 14, no. 7, pp. 1115-1122, 1999. doi: [10.1359/jbmr.1999.14.7.1115](https://doi.org/10.1359/jbmr.1999.14.7.1115).
- [6] C.L. Korecki, C.K. Kuo, R.S. Tuan, J.C. Iatridis. "Intervertebral Disk Cell Response to Dynamic Compression Is Age and Frequency Dependent." *Journal of Orthopedic Research*, vol. 6, no. 27, pp. 800-806, Jun. 2009. doi: [10.1002/jor.20814](https://doi.org/10.1002/jor.20814).
- [7] D. B. Burr, A.G. Robling, C.H. Turner. "Effects of biomechanical stress on bones in animals." *Bone*, vol. 30, no. 5, pp. 781-786, 2002. doi: [10.1016/S8756-3282\(02\)00707-X](https://doi.org/10.1016/S8756-3282(02)00707-X).
- [8] R.L. Duncan, C.H. Turner. "Mechanotransduction and the Functional Response of Bone to Mechanical Strain." *Calcified Tissue International*, vol. 57, pp. 344-358, 1995. doi: [10.1007/BF00302070](https://doi.org/10.1007/BF00302070).
- [9] J. You, C.E. Yellowley, H.J. Donahue, Y. Zhang, Q. Chen, C.R. Jacobs. "Substrate Deformation Levels Associated With Routine Physical Activity Are Less Stimulatory to Bone Cells Relative to Loading-Induced Oscillatory Fluid Flow." *Journal of Biomechanical Engineering*, vol. 122, no. 4, pp. 387-394, 2000. doi: [10.1115/1.1287161](https://doi.org/10.1115/1.1287161).
- [10] Wenyue Zhang. "Design, Modeling, Fabrication and Characterization of an MEMS System for Measuring the Mechanical Compliance of a Biological Cell." Ph.D. Dissertation, Lehigh University, 2007.
- [11] J.C. Doll, S. Park, B.L. Pruitt. "Design optimization of piezoresistive cantilevers for force sensing in air and water." *Journal of Applied Physics*, vol. 106, no. 6, pp. 064310, 2009. doi: [10.1063/1.3224965](https://doi.org/10.1063/1.3224965).
- [12] Jonah A. Harley, Thomas W. Kenny. "1/f Noise Considerations for the Design and Process Optimization of Piezoresistive Cantilevers." *Journal of Microelectromechanical Systems*, vol. 9, no. 2, pp. 226-235, 2000. doi: [10.1109/84.846703](https://doi.org/10.1109/84.846703).
- [13] T.B. Gabrielson. "Mechanical-thermal noise in micromachined acoustic and vibration sensors." *IEEE Transactions on Electron Devices*, vol. 40, pp. 903-909, 1993. doi: [10.1109/16.210197](https://doi.org/10.1109/16.210197).
- [14] A. Partridge, J.K. Reynolds, B.W. Chui, E.M. Chow, A.M. Fitzgerald, L. Zhang, N.I. Maluf. "A high-performance planar piezoresistive accelerometer." *Journal*

- of *Microelectromechanical Systems*, vol. 9, no. 1, pp 58-66, 2000. doi: [10.1109/84.825778](https://doi.org/10.1109/84.825778).
- [15] L. Sun, J. Wang, W. Rong, X. Li, H. Bao. "A silicon integrated micro nano-positioning XY-stage for nano-manipulation." *Journal of Micromechanics and Microengineering*, vol. 18, pp. 125004 (9pp), 2008. doi: [10.1088/0960-1317/18/12/125004](https://doi.org/10.1088/0960-1317/18/12/125004).
- [16] E.J. Eklund, A.M. Shkel. "Single-mask fabrication of high-G piezoresistive accelerometers with extended temperature range." *Journal of Micromechanics and Microengineering*, vol. 17, pp. 730–736, 2007. doi: [10.1088/0960-1317/17/4/009](https://doi.org/10.1088/0960-1317/17/4/009).
- [17] T. L. Waterfall, K. B. Teichert, B. D. Jensen. "A Model for Predicting the Piezoresistive Effect in Microflexures Experiencing Bending and Tension Loads." *Journal of Microelectromechanical Systems*, vol. 17, no. 1, pp. 1204-1209, 2008. doi: [10.1109/JMEMS.2007.911874](https://doi.org/10.1109/JMEMS.2007.911874).
- [18] M. Gnerlich, S.F. Perry, S. Tatic-Lucic. "A Submersible Piezoresistive MEMS Lateral Force Sensor for Cellular Biomechanics Applications." *Proceedings of the 16th International Conference on Solid-State Sensors, Actuators and Microsystems*, Beijing, 5-9 Jun. 2011, pp. 2207-2210. doi: [10.1109/TRANSDUCERS.2011.5969365](https://doi.org/10.1109/TRANSDUCERS.2011.5969365).
- [19] James M. Gere, Stephen P. Timoshenko. *Mechanics of Materials*. PWS Publishing Company, 1997.
- [20] American Wood Council. "DESIGN AID No. 6: Beam Design Formulas with Shear and Moment Diagrams." Internet: www.awc.org/pdf/DA6-BeamFormulas.pdf, 2007.
- [21] Chang Liu. *Foundations of MEMS*. New Jersey: Prentice Hall, 2005, pp. 213.
- [22] C.S. Smith. "Piezoresistance effect in germanium and silicon." *Physical Review*, vol. 94, pp. 42-49, 1954. doi: [10.1103/PhysRev.94.42](https://doi.org/10.1103/PhysRev.94.42).
- [23] O.N. Tufte, E.L. Stelzer. "Piezoresistive Properties of Heavily Doped N Silicon." *Physical Review*, vol. 133, no. 6A, pp A1705-A1716, 1964. doi: [10.1103/PhysRev.133.A1705](https://doi.org/10.1103/PhysRev.133.A1705).
- [24] X. Yu, J. Thaysen, O. Hansen, A. Boisen. "Optimization of sensitivity and noise in piezoresistive cantilevers." *Journal of Applied Physics*, vol. 92, no. 10, pp. 6296-6301, 2002. doi: [10.1063/1.1493660](https://doi.org/10.1063/1.1493660).
- [25] H. Nyquist. "Thermal Agitation of Electric Charge in Conductors." *Physical Review*, vol. 32, pp. 110-113, 1928. doi: [10.1103/PhysRev.32.110](https://doi.org/10.1103/PhysRev.32.110).
- [26] J.B. Johnson, "Thermal Agitation of Electricity in Conductors." *Physical Review*, vol. 32, pp. 97-109, 1928. doi: [10.1103/PhysRev.32.97](https://doi.org/10.1103/PhysRev.32.97).
- [27] F.N. Hooge. "1/f Noise is no Surface Effect." *Physics Letters A*, vol. 29, no. 3, pp. 139-140, 1969. doi: [10.1016/0375-9601\(69\)90076-0](https://doi.org/10.1016/0375-9601(69)90076-0).
- [28] W. Schottky, "Über spontane Stromschwankungen in verschiedenen Elektrizitätsleitern." *Annalen der Physik*. vol. 57, no. 23, pp. 541-567, 1918. doi: [10.1002/andp.19183622304](https://doi.org/10.1002/andp.19183622304).
- [29] P.J. Mohr, B.N. Taylor, D.B. Newell. "CODATA Recommended Values of the Fundamental Physical Constants: 2006." *Reviews of Modern Physics*, vol. 80, pp. 633, 2008. doi: [10.1103/RevModPhys.80.633](https://doi.org/10.1103/RevModPhys.80.633).

- [30] A. Mohammed, W. Moussa, E. Lou. "High Sensitivity MEMS Strain Sensor Design and Simulation." *Sensors*, vol. 8, pp. 2642-2661, 2008. doi: [10.3390/s8042642](https://doi.org/10.3390/s8042642).
- [31] W.R. Thurber, R.L. Mattis, Y.M. Liu, J.J. Filliben. "Resistivity-Dopant Density Relationship for Phosphorus-Doped Silicon." *Journal of the Electrochemical Society*, vol. 127, pp. 1807-1812, 1980. doi: [10.1149/1.2130006](https://doi.org/10.1149/1.2130006).
- [32] Solecon Laboratories, Inc. "Solecon Labs Technical Note: Converting Resistivity to Carrier Concentration." Internet: www.solecon.com/pdf/converting_resistivity_to_carrier_concentration_graph_si_ge.pdf.
- [33] Y. Qiu, R. Liao, X. Zhang. "Real-Time Monitoring Primary Cardiomyocyte Adhesion Based on Electrochemical Impedance Spectroscopy and Electrical Cell-Substrate Impedance Sensing." *Analytical Chemistry*, vol. 80, pp. 990-996, 2008. doi: [10.1021/ac701745c](https://doi.org/10.1021/ac701745c).
- [34] M. A. Hopcroft, W. D. Nix, and T. W. Kenny. "What is the Young's Modulus of Silicon?" *Journal of Microelectromechanical Systems*, vol. 19, pp. 229-238, 2010. doi: [10.1109/JMEMS.2009.2039697](https://doi.org/10.1109/JMEMS.2009.2039697).
- [35] Nadim Maluf, Kirt Williams. *An Introduction to Microelectromechanical Systems Engineering*, 2nd ed. Boston: Artech House, 2000.
- [36] T. Sounart, T. Michalske, K. Zavadil. "Frequency-Dependent Electrostatic Actuation in Microfluidic MEMS." *Journal of Microelectromechanical Systems*, vol. 14, no. 1, pp. 125-133, 2005. doi: [10.1109/JMEMS.2004.839006](https://doi.org/10.1109/JMEMS.2004.839006).
- [37] V. Mukundan, B. Pruitt. "MEMS Electrostatic Actuation in Conducting Biological Media." *Journal of Microelectromechanical Systems*, vol. 18, no. 2, pp. 405-413, 2009. doi: [10.1109/JMEMS.2009.2013398](https://doi.org/10.1109/JMEMS.2009.2013398).
- [38] J. Li, M.P. Brenner, T. Christen, M.S. Kotilainen, J.H. Lang, A.H. Slocum. "Deep-Reactive Ion-Etched Compliant Starting Zone Electrostatic Zipping Actuators." *Journal of Microelectromechanical Systems*, vol. 14, no. 6, pp. 1283-1297, 2005. doi: [10.1109/JMEMS.2005.851842](https://doi.org/10.1109/JMEMS.2005.851842).
- [39] N. Golay, A. Masse, Y. Pétremand, W. Noell, J.-F. Manceau, N.F. de Rooij. "Scalable Cascaded Snap-In Actuators For Large-Stroke Displacements." *Solid-State Sensors, Actuators and Microsystems Conference, 2009*, Denver, CO (USA), 21-25 Jun. 2009, pp. 1754-1757. doi: [10.1109/SENSOR.2009.5285742](https://doi.org/10.1109/SENSOR.2009.5285742).
- [40] C. Dresbach, M. Mittag, M. Petzold. "Elastic Properties of Bonding Wires." *Electronic System Integration Technology Conference (ESTC)*, Berlin (DE), 13-16 Sep. 2010, pp. 1-4. doi: [10.1109/ESTC.2010.5642992](https://doi.org/10.1109/ESTC.2010.5642992).
- [41] M.P. Brenner, J.H. Lang, J. Li, A.H. Slocum, "Optimum Design of an Electrostatic Zipper Actuator." *Technical Proceedings of the 2004 NSTI Nanotechnology Conference*, vol. 2, 2004, pp. 371-374.
- [42] M. Uematsu, E.U. Franck. "Static Dielectric Constant of Water and Steam." *Journal of Physical and Chemical Reference Data*, vol. 9, no. 4, 1980, pp. 1291-1306. doi: [10.1063/1.555632](https://doi.org/10.1063/1.555632).
- [43] R. Legtenberg, J. Gilbert, S.D. Senturia, M. Elwenspoek. "Electrostatic Curved Electrode Actuators." *Journal of Microelectromechanical Systems*, vol. 6, no. 3, pp. 257-265, 1997. doi: [10.1109/84.623115](https://doi.org/10.1109/84.623115).

- [44] Mark Thoren. “Linear Technology Application Note 96: Delta Sigma ADC Bridge Measurement Techniques.” Internet: www.linear.com/docs/6637.
- [45] Alan Rich. “Analog Devices Application Note 347: Shielding and Guarding.” Internet: www.analog.com/static/imported-files/application_notes/41727248AN_347.pdf.
- [46] Ralph Morrison. *Grounding and Shielding Techniques in Instrumentation*, John Wiley & Sons, New York, 1967.
- [47] E. Darling, M. Topel, S. Zauscher, T. Vail, F. Guilak. “Viscoelastic properties of human mesenchymally-derived stem cells and primary osteoblasts, chondrocytes, and adipocytes.” *Journal of Biomechanics*, vol. 41, pp. 454–464, 2008. doi: [10.1016/j.jbiomech.2007.06.019](https://doi.org/10.1016/j.jbiomech.2007.06.019).
- [48] E. Peeters, C. Oomens, C. Bouten, D. Bader, F. Baaijens. “Viscoelastic Properties of Single Cells Under Compression.” *Journal of Biomechanical Engineering*, vol. 127, pp. 237-243, 2005. doi: [10.1115/1.1865198](https://doi.org/10.1115/1.1865198).
- [49] O. Thoumine, A. Ott. “Time scale dependent viscoelastic and contractile regimes in fibroblasts probed by microplate manipulation.” *Journal of Cell Science*, vol. 110, pp. 2109-2116, 1997.
- [50] Yuan-cheng Fung. *Biomechanics: Mechanical Properties of Living Tissues*, 2nd ed. Springer, New York, 1993.
- [51] W.M. Lu, K.L. Tunga, S.M. Hunga, J.S. Shiaua, K.J. Hwang. “Compression of deformable gel particles.” *Powder Technology*, vol. 116, pp. 1-12, 2001. doi: [10.1016/S0032-5910\(00\)00357-0](https://doi.org/10.1016/S0032-5910(00)00357-0).
- [52] Stephen P. Timoshenko, James N. Goodier, *Theory of Elasticity*, 3rd ed. McGraw-Hill Publishing Company, New York, USA, 1970, pp. 409-414.
- [53] Kenneth L. Johnson, *Contact Mechanics*. Cambridge University Press, New York, 1985.
- [54] David Roylance, “Engineering Viscoelasticity” in *Mechanics of Materials*. John Wiley & Sons, New York, 1996.
- [55] Süss MicroTek. “Alignment Mark and Dimension with Vernier Scale” Internet: snf.stanford.edu/Process/Masks/AlgnMkVernier.pdf [Sept. 19, 2011].
- [56] S. Greek, F. Ericson, S. Johansson, M. Fürtsch, A. Rump. “Mechanical characterization of thick polysilicon films: Young’s modulus and fracture strength evaluated with microstructures.” *Journal of Micromechanics and Microengineering*, vol. 9, pp. 245–251, 1999. doi: [10.1088/0960-1317/9/3/305](https://doi.org/10.1088/0960-1317/9/3/305).
- [57] S. Pamidighantam, R. Puers, K. Baert, H. Tilmans. “Pull-in voltage analysis of electrostatically actuated beam structures with fixed–fixed and fixed–free end conditions.” *Journal of Micromechanics and Microengineering*, vol. 12, pp. 458-464, 2002. doi: [10.1088/0960-1317/12/4/319](https://doi.org/10.1088/0960-1317/12/4/319).

Appendices



Lehigh University logo fabricated at Sherman Fairchild Center from 10 μm thick silicon etched by DRIE and subsequently patterned with 200 nm thick gold. The shield is 172 μm wide by 240 μm tall.

Appendix I: Layout

Design Rules

The fabrication limitations (design rules) for this process were determined by a series of experiments using standard silicon test wafers and similar materials, before the masks were designed.

- Silicon Layer (DEVICE)
 - Minimum Line Width: 1 μm
This limitation is set by the patterning resolution of OCG 825 with the Süss-Microtek MJB3 contact aligner in high-performance vacuum mode, combined with the Adixen AMS-100 I-Speeder DRIE etching machine.
 - Free-standing structures must not have interiors more than 8 μm away from any edge to allow the buried oxide etch to release them. Wider free-standing structures should contain a series of etch holes to facilitate release.
 - Anchored structures should have interiors at least 10 μm away from all edges to prevent the buried oxide etch from releasing them.
- Metal Layer (METAL)
 - METAL should be 2 μm inside the DEVICE layer.
This limitation is set by the ability of the lift-off resist (AZ nLOF 2070) to conform to the edges of the 10 μm high silicon structures.
 - Minimum line width: 2 μm
 - Minimum line spacing: 6 μm (due to lift-off resist undercut)
- Isolation Layer (ISOLATION)
 - ISOLATION can be patterned both inside DEVICE features (top of device) and outside (surface of handle)
 - Minimum line width on top of device: 2 μm
 - Minimum line spacing: 4 μm (due to SU-8 resolution)

Resolution Tests of DRIE Silicon

OCG-825 Test Recipe

1. Dehydrate at 120°C for 20 minutes
2. Vapor prime in a sealed box with HMDS and Xylene in a dish

3. Spin-coat OCG-825 at 5000 RPM for 40 seconds
4. Soft bake
 - a. Convection oven 95° C for 30 min
 - b. Rehydrate at room temperature for 15 min
5. Align and expose 2.0 seconds at 25 mW/cm²
6. Develop
 - a. 60 seconds in OCG 809 developer 50% dilution
 - b. Rinse in DI water
 - c. Blow dry with nitrogen

The resolution test results are shown in Figure 98 and the average deviations are listed in Table 45.

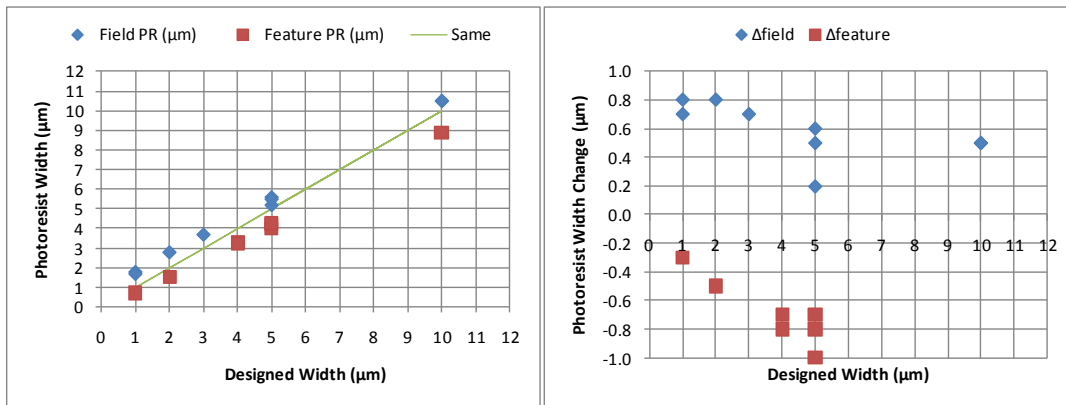


Figure 98: OCG 825 photoresist (positive) resolution characterization showing slightly narrower lines and wider trenches than present on the mask.

Table 45: Summary of deviation from feature and field in OCG 825

	Δ field	Δ feature
Average (µm)	0.59	-0.73
SD	0.19	0.24
N	9	9

The photoresist is present on the wafer for features and acts as etch mask layer (which is not etched and forms ridges). The field areas become bare silicon (which is etched and forms trenches). Following DRIE (LOWROUGHNESS recipe) the ridges and trenches

were measured by SEM and the results are shown in Figure 99 and summarized in Table 46.

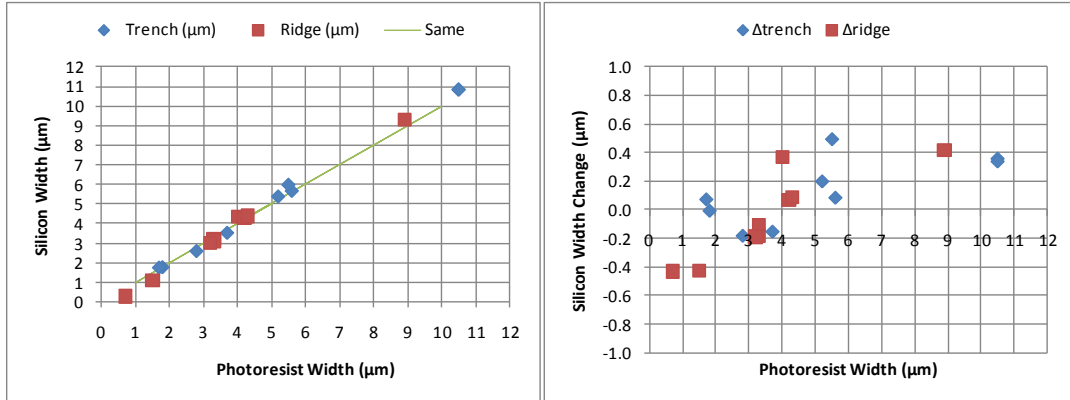


Figure 99: DRIE resolution characterization showing very little change in size (features become ridges, and field becomes trenches) during the 10 minute etching.

Table 46: Summary of etching deviation from photoresist mask.

	Δ trench	Δ ridge
Average (µm)	0.13	-0.04
SD	0.23	0.31
N	9	9

The final silicon structures are expected to be approximately 0.75 µm smaller than the designed features on the mask, or an over-etch of 0.38 µm in each direction. This was originally seen to be a benefit since 1 µm lines could become very narrow, approaching 0.25 µm; narrower beams in the transducer region result in increased force sensor sensitivity (see Chapter 2: Piezoresistive Force Sensor). However, suspended beams this thin became very fragile and often did not survive subsequent fabrication steps (see Appendix II: Fabrication).

The alignment of METAL and ISOLATION layers to the silicon device layer is reliably ± 2 µm (see Figure 131). This is achieved through a special alignment mark which

integrates a set of vertical and horizontal Vernier scales for direct measurement of misalignment during mask alignment (see Figure 105).

Mask Layout

Index of Devices

A position index of all of the dies on the wafer is shown in Figure 100. The dimensions of all features that were varied are listed in Table 47 for revision 1 and Table 48 for revision 2.

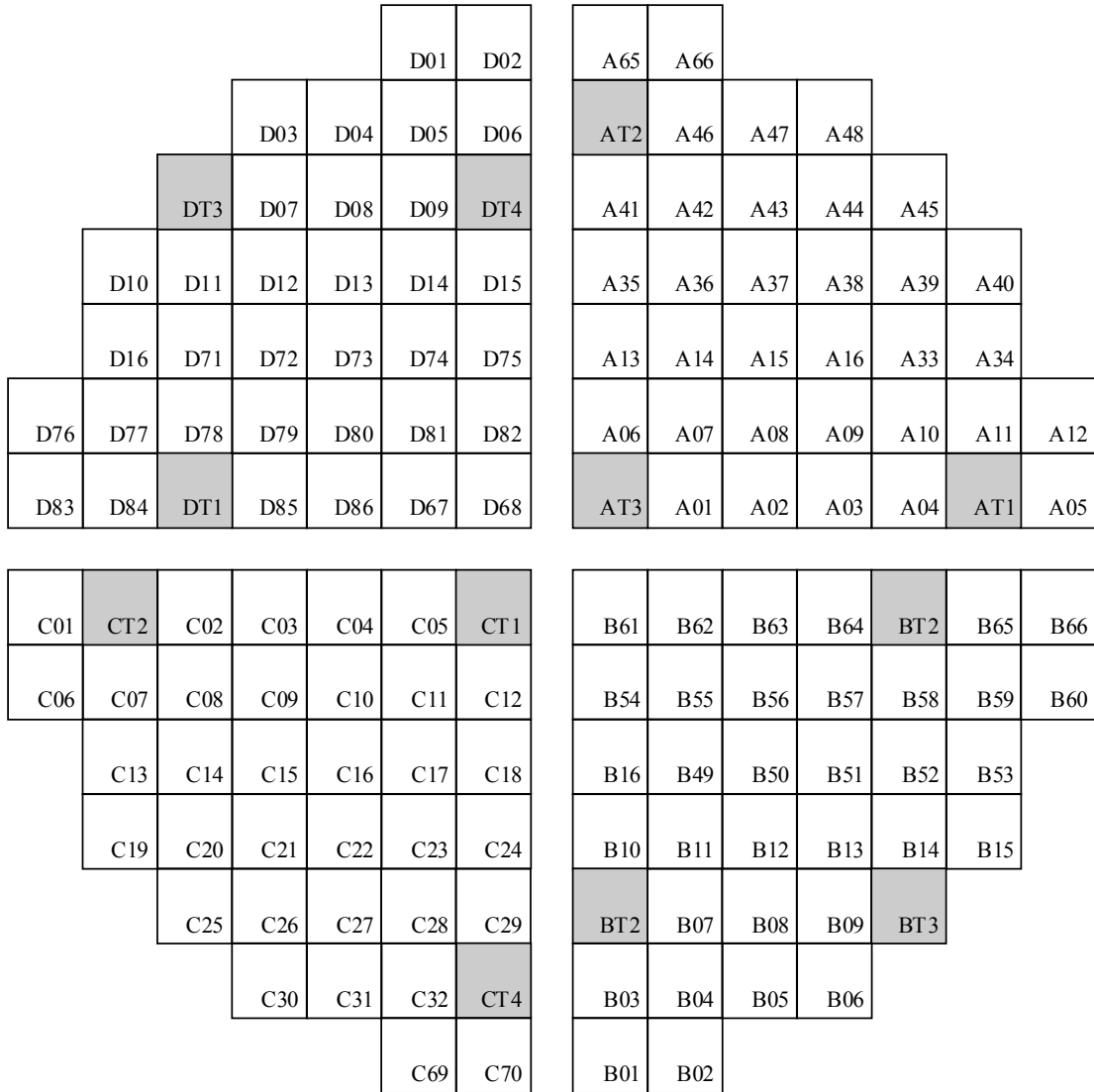


Figure 100: The location of each numbered die on the wafer. Each die number is unique to a particular design, but some are duplicated across the 4 quadrants (A,B,C,D).

Table 47: Design parameters of all devices dies (revision 1).

Quadrant	Die ID	Count	Force Sensor Dimensions ¹	Sensor-Actuator Gap	Actuator Dimensions ²	Description
ABCD	01-06	24	B450 L32 W01	20	W4 / G2	1 st choice
ABCD	07-12	24	B450 L32 W01	15	W4 / G2	1 st choice
ABCD	13-16	16	B450 L32 W01	10	W4 / G2	1 st choice
A	33-36	4	B450 L32 W01	20	W6 / G2	3 rd choice
A	37-40	4	B450 L32 W02	20	W6 / G2	3 rd choice
A	41-44	4	B450 L32 W01	15	W6 / G2	3 rd choice
A	45-48	4	B450 L32 W02	15	W6 / G2	3 rd choice
B	49-64	16	All variations	20	W6 / G2	Validation
C	17-18	2	B450 L16 W01	20	W4 / G2	2 nd choice
C	19-20	2	B450 L64 W01	20	W4 / G2	2 nd choice
C	21-22	2	B600 L16 W01	20	W4 / G2	2 nd choice
C	23-24	2	B600 L32 W01	20	W4 / G2	2 nd choice
C	25-26	2	B450 L16 W01	15	W4 / G2	2 nd choice
C	27-28	2	B450 L64 W01	15	W4 / G2	2 nd choice
C	29-30	2	B600 L16 W01	15	W4 / G2	2 nd choice
C	31-32	2	B600 L32 W01	15	W4 / G2	2 nd choice
D	71-72	2	B450 L16 W02	20	W6 / G4	2 nd choice
D	73-74	2	B450 L64 W02	20	W6 / G4	2 nd choice
D	75-76	2	B600 L16 W02	20	W6 / G4	2 nd choice
D	77-78	2	B600 L32 W02	20	W6 / G4	2 nd choice
D	79-80	2	B450 L16 W02	15	W6 / G4	2 nd choice
D	81-82	2	B450 L64 W02	15	W6 / G4	2 nd choice
D	83-84	2	B600 L16 W02	15	W6 / G4	2 nd choice
D	85-86	2	B600 L32 W02	15	W6 / G4	2 nd choice
AB	65	2	B450 L32 W01	02	W4 / G2	Diagnostic
AB	66	2	B600 L32 W01	02	W4 / G2	Diagnostic
D	67	1	B450 L32 W02	02	W6 / G2	Diagnostic
D	68	1	B600 L32 W02	02	W6 / G2	Diagnostic
C	69	1	B450 L32 W02	02	W6 / G4	Diagnostic
C	70	1	B600 L32 W02	02	W6 / G4	Diagnostic

¹ B=beam length (μm), L=transducer length (μm), W=transducer width (μm)

² W=beam width (μm), G=actuator gap (μm)

Table 48: Design parameters of all devices dies (revision 2).

Quadrant	Die ID	Count	Force Sensor Dimensions ¹	Sensor-Actuator Gap	Actuator Dimensions ²	Description
ABCD	01-05	20	B450 L32 W01	20	W4 / G2	1 st choice
ABCD	06	4	B450 L32 W01 ISO	20	W4 / G2	Insulated TD
ABCD	07-11	20	B450 L32 W01	15	W4 / G2	1 st choice
ABCD	12	4	B450 L32 W01 ISO	15	W4 / G2	Insulated TD
ABCD	13-15	12	B450 L32 W01	10	W4 / G2	1 st choice
ABCD	16	4	B450 L32 W01 ISO	10	W4 / G2	Insulated TD
A	33-36	4	B450 L32 W01	20	W6 / G2	3 rd choice
A	37-39	3	B450 L32 W02	20	W6 / G2	3 rd choice
A	40	1	B450 L32 W02 ISO	20	W6 / G2	Insulated TD
A	41-43	3	B450 L32 W01	15	W6 / G2	3 rd choice
A	44	1	B450 L32 W01 ISO	15	W6 / G2	Insulated TD
A	45-47	3	B450 L32 W02	15	W6 / G2	3 rd choice
A	48	1	B450 L32 W02 ISO	15	W6 / G2	Insulated TD
B	49-64	16	All variations	20	W6 / G2	Validation
C	17-18	2	B450 L16 W01	20	W4 / G2	2 nd choice
C	19-20	2	B450 L64 W01	20	W4 / G2	2 nd choice
C	21-22	2	B600 L16 W01	20	W4 / G2	2 nd choice
C	23-24	2	B600 L32 W01	20	W4 / G2	2 nd choice
C	25-26	2	B450 L16 W01	15	W4 / G2	2 nd choice
C	27-28	2	B450 L64 W01	15	W4 / G2	2 nd choice
C	29-30	2	B600 L16 W01	15	W4 / G2	2 nd choice
C	31-32	2	B600 L32 W01	15	W4 / G2	2 nd choice
D	71-72	2	B450 L16 W02	20	W6 / G4	2 nd choice
D	73-74	2	B450 L64 W02	20	W6 / G4	2 nd choice
D	75-76	2	B600 L16 W02	20	W6 / G4	2 nd choice
D	77-78	2	B600 L32 W02	20	W6 / G4	2 nd choice
D	79-80	2	B450 L16 W02	15	W6 / G4	2 nd choice
D	81-82	2	B450 L64 W02	15	W6 / G4	2 nd choice
D	83-84	2	B600 L16 W02	15	W6 / G4	2 nd choice
D	85-86	2	B600 L32 W02	15	W6 / G4	2 nd choice
AB	65	2	B450 L32 W01	02	W4 / G2	Diagnostic
AB	66	2	B600 L32 W01	02	W4 / G2	Diagnostic
D	67	1	B450 L32 W02	02	W6 / G2	Diagnostic
D	68	1	B600 L32 W02	02	W6 / G2	Diagnostic
C	69	1	B450 L32 W02	02	W6 / G4	Diagnostic
C	70	1	B600 L32 W02	02	W6 / G4	Diagnostic

¹ B=beam length (μm), L=transducer length (μm), W=transducer width (μm)

² W=beam width (μm), G=actuator gap (μm)

Masks

Snapshots of the 4-inch masks are shown below (enlarged) in Figure 101 (DEVICE), Figure 102 (METAL), Figure 103 (ISOLATION revision 1) and Figure 104 (ISOLATION revision 2).

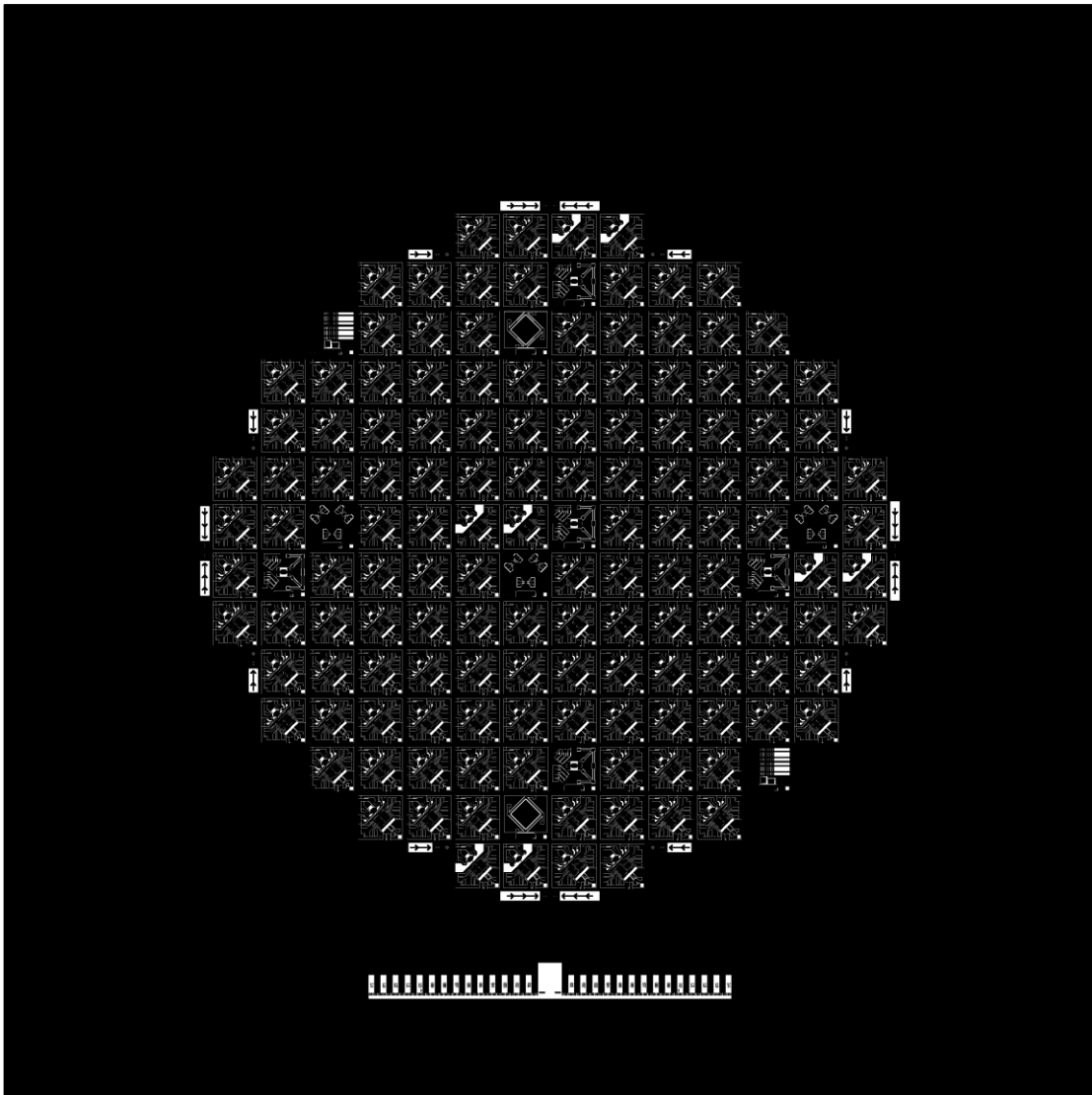


Figure 101: DEVICE mask (same for revision 1 and revision 2) layout for 3-inch wafer (4-inch quartz AR chrome mask). Wafer flat alignment mark is visible at the bottom.

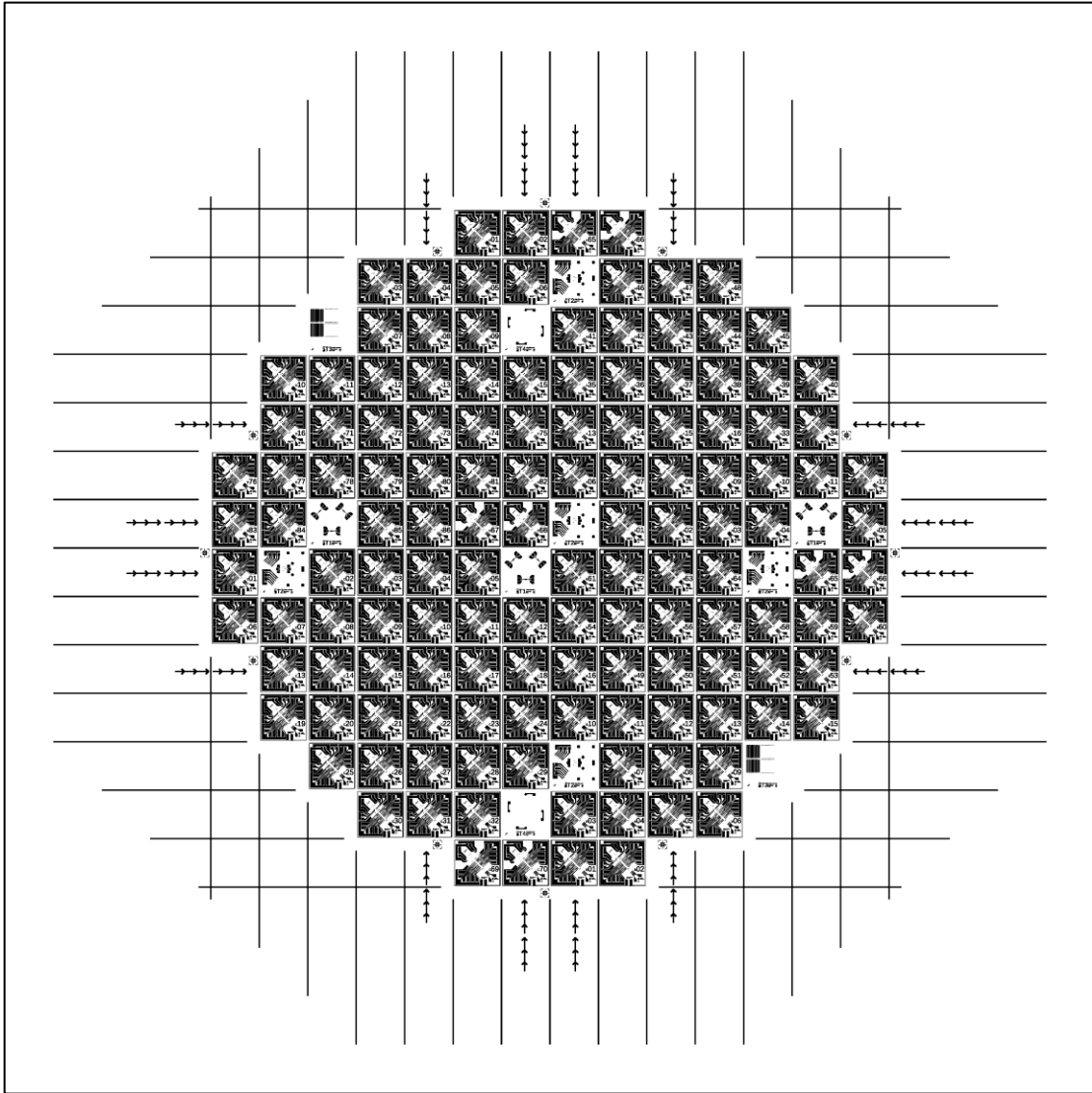


Figure 102: METAL mask (same for revision 1 and revision 2) layout for 3-inch wafer (4-inch quartz AR chrome mask).

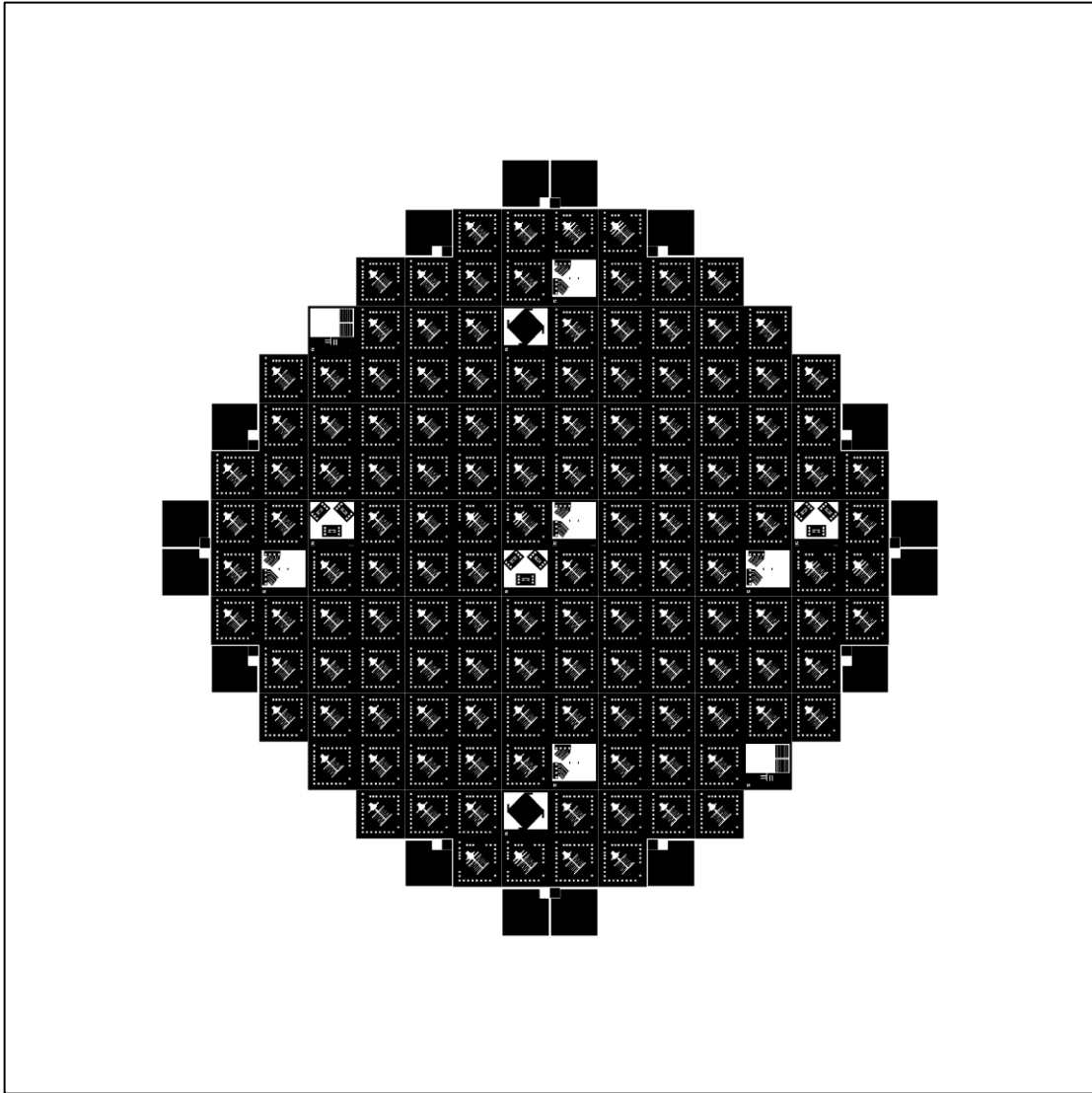


Figure 103: ISOLATION mask (revision 1) layout for 3-inch wafer (4-inch quartz AR chrome mask)

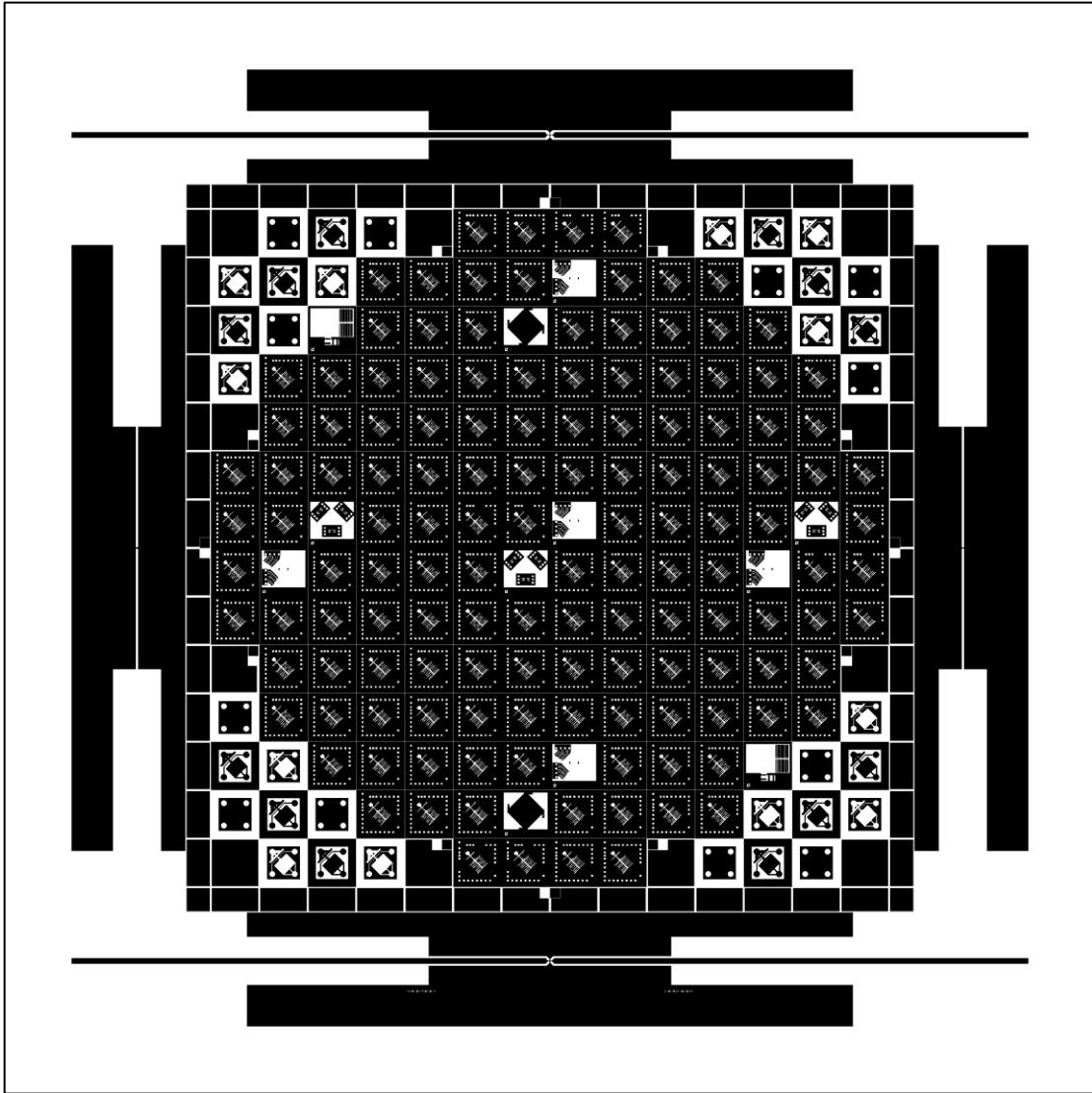


Figure 104: ISOLATION mask (revision 2) layout for 3-inch wafer (4-inch quartz AR chrome mask).

Alignment Marks

Precision alignment marks contain both the complementary cross and two additional features: (1) a set of horizontal and vertical Vernier scales allow the user to identify misalignment and correct it before exposure, and (2) a “window blind” pattern that dims and brightens as the bars in the mask overlap the trenches in the wafer (this is particularly useful for rotational alignment).

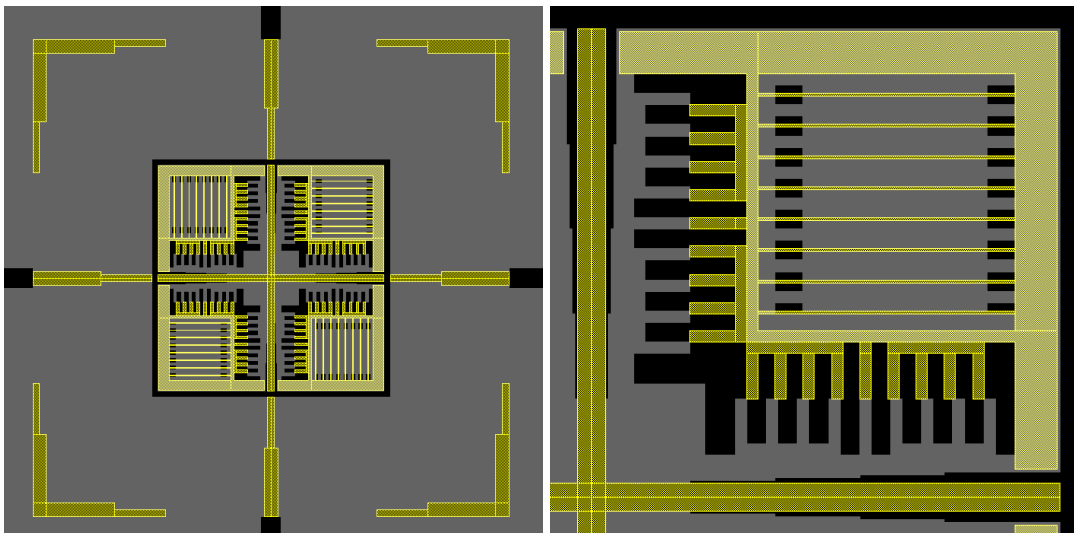


Figure 105: Precision alignment marks are positioned at the edges of the wafer.

A similar inverted cross with associated Vernier scales is available as a standardized alignment mark (see Figure 106) for 0.5 μm alignment resolution [55].

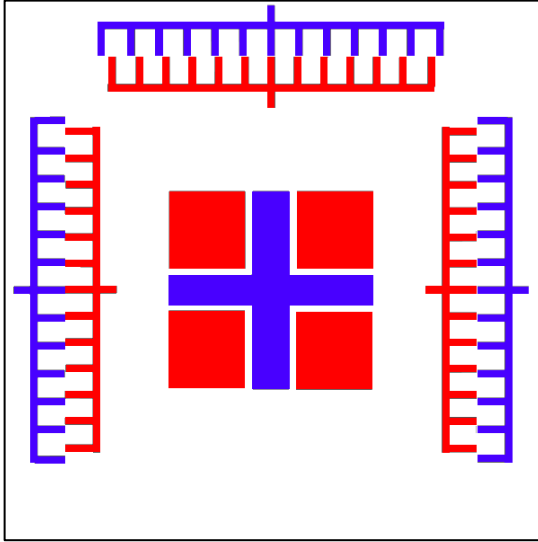


Figure 106: Precision alignment mark that includes an inverted cross and Vernier scales [55].

Typical Device Layout

The typical layout for a device is shown in Figure 107, where the first device layer and metal layers are visible. The layout is shown again in Figure 108 which also has the isolation layer visible. Each device measures 4 mm by 4 mm.

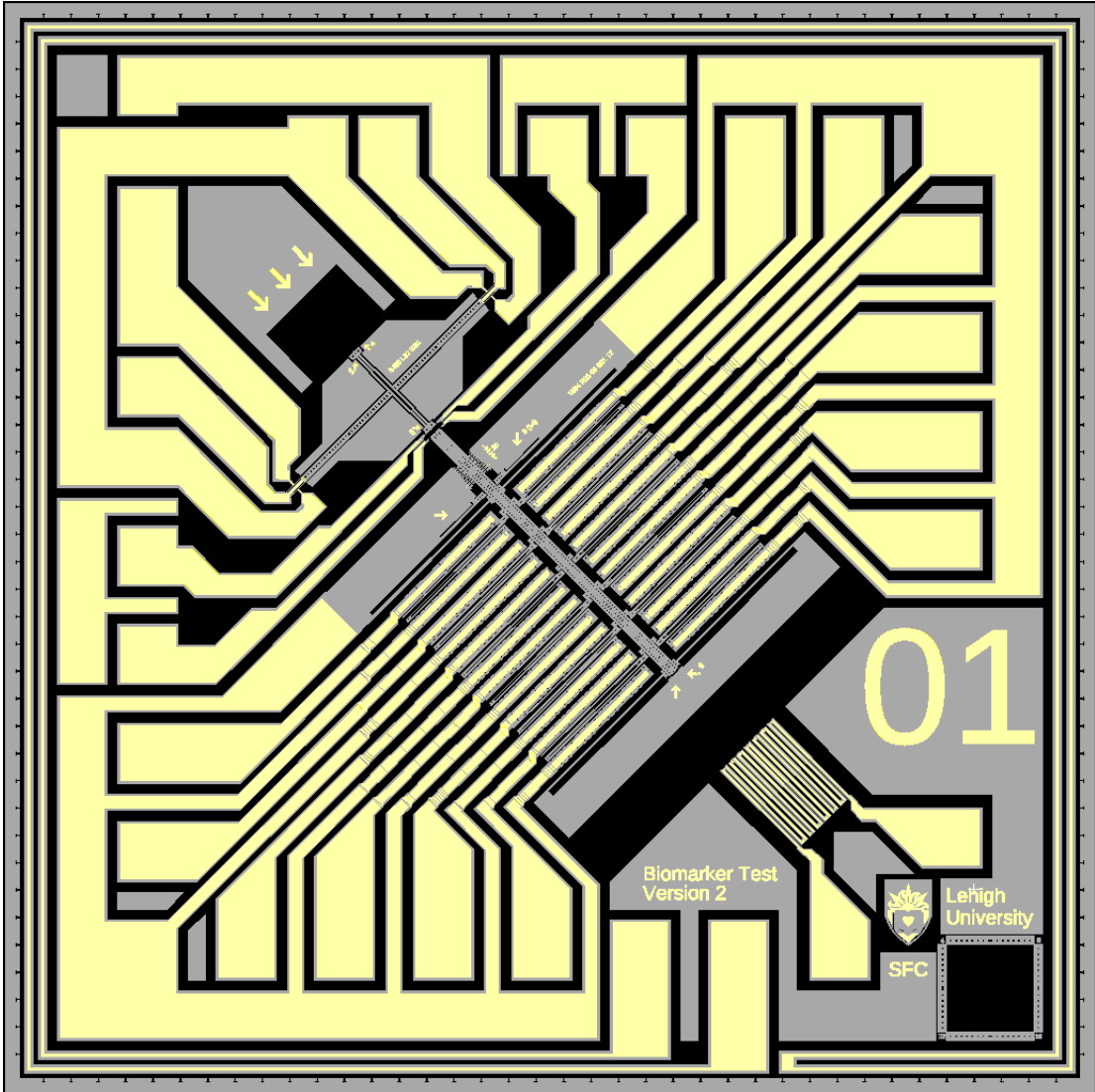
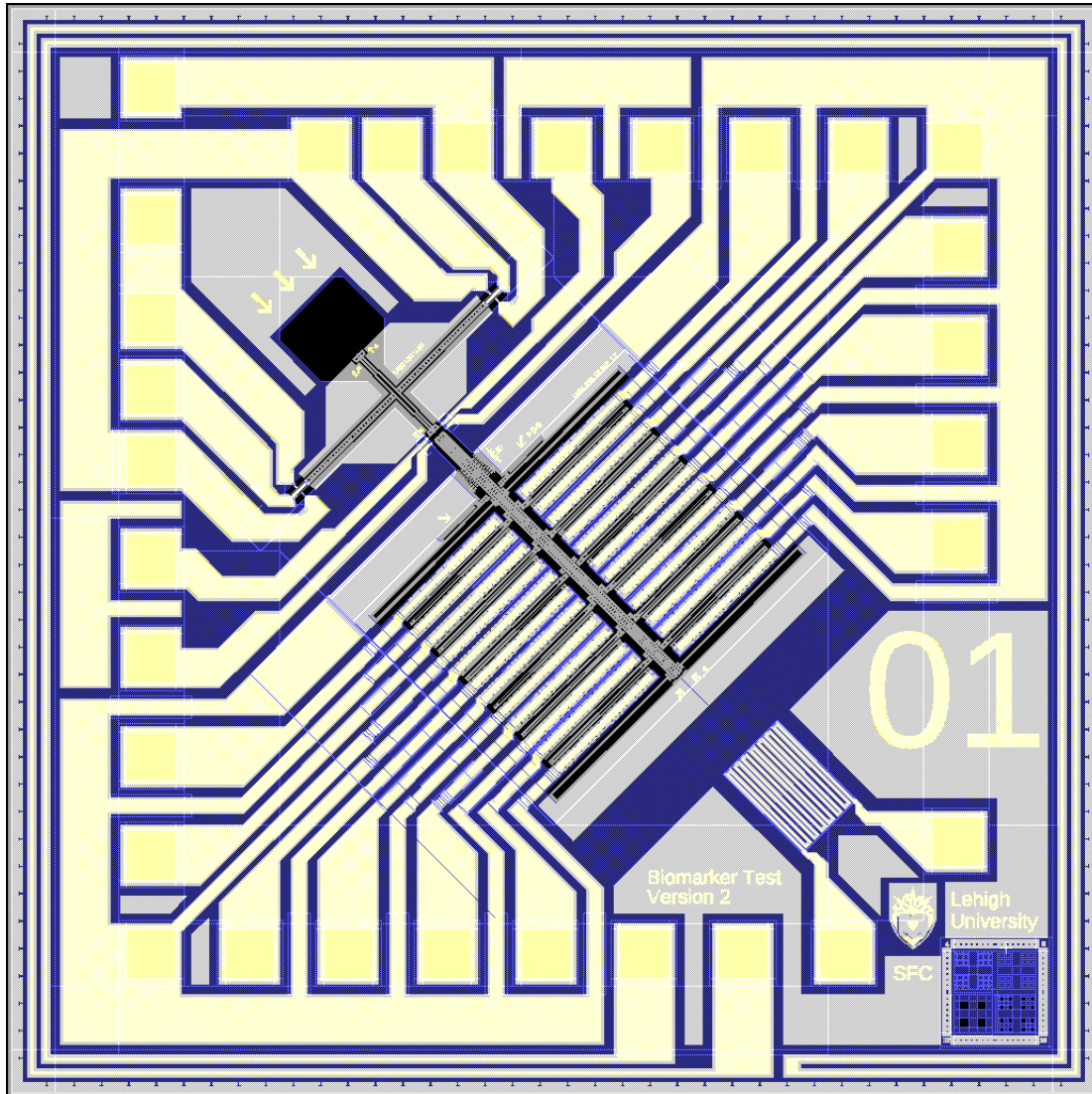


Figure 107: Typical layout showing DEVICE layer in grey and METAL layer in yellow.



*Figure 108: Typical device die layout showing **DEVICE** layer in grey, **METAL** layer in yellow, and **ISOLATION** layer in blue.*

An oxide etch test structure was included in the lower right of the chip, but this structure was no satisfactory due to the different lateral etch rate at the ISOLATION-to-BOX layer interface from the DEVICE-to-BOX layer interface. The BHF wet etch travels much faster at the photoresist interface than the silicon interface.

Test Dies

See also Device Test Results section below.

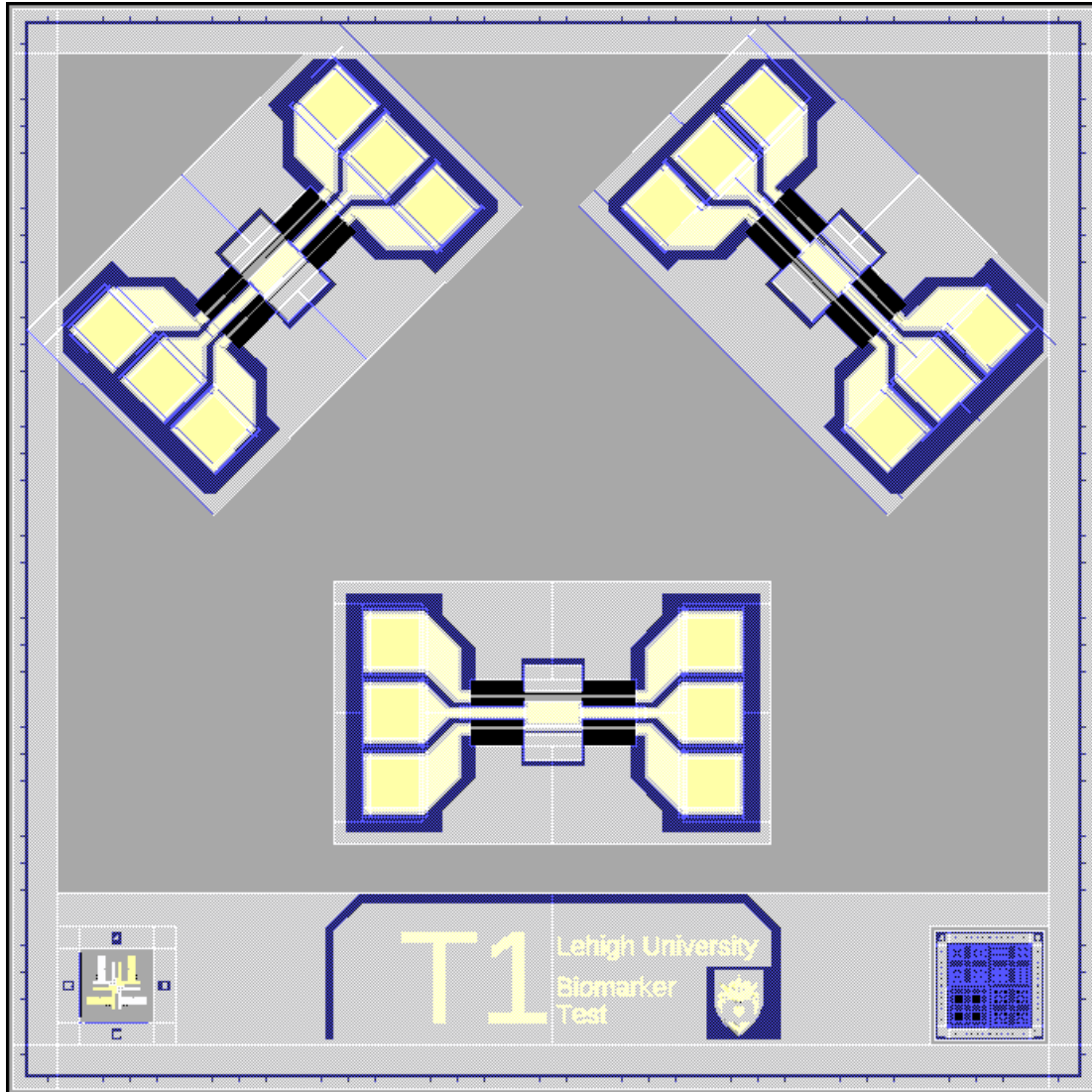


Figure 109: Test Die #1 for piezoresistive constant which was based on beam stretching induced by an electrostatic clamp.

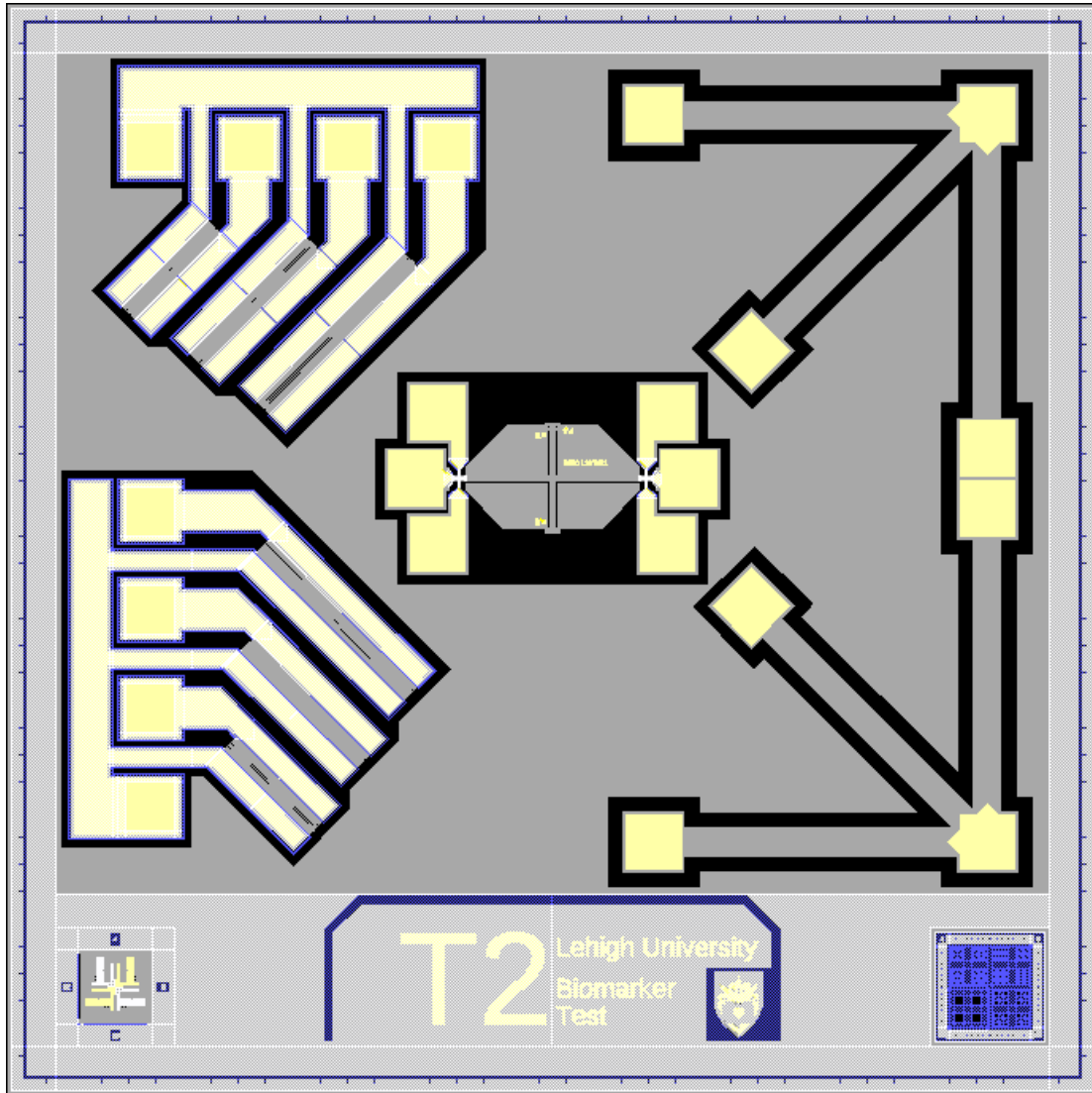


Figure 110: Test Die #2 for bulk resistivity (right), critical dimensions (center) and silicon elastic modulus (left) [56].

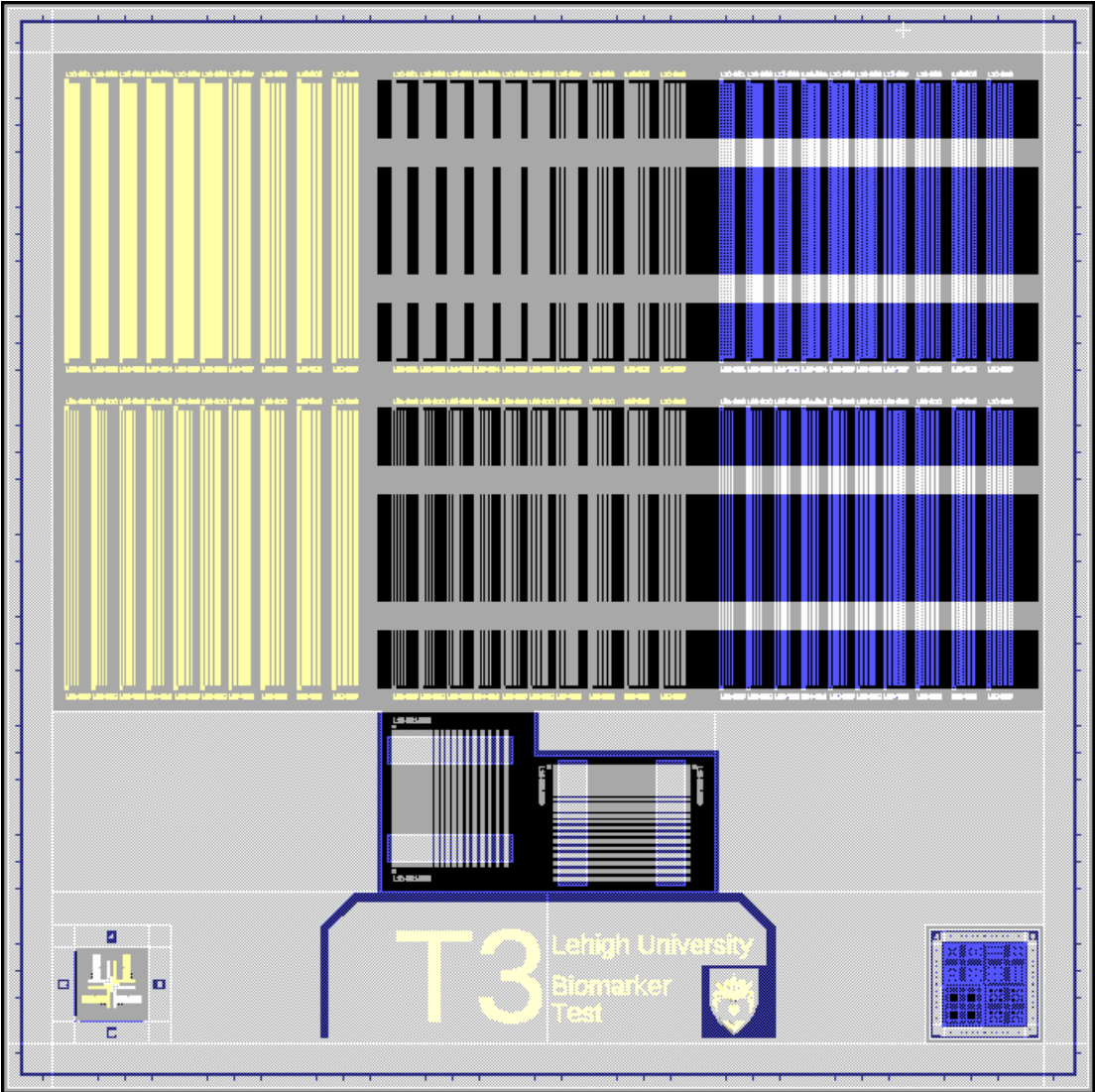


Figure 111: Test die #3 for resolution (line & spacing).

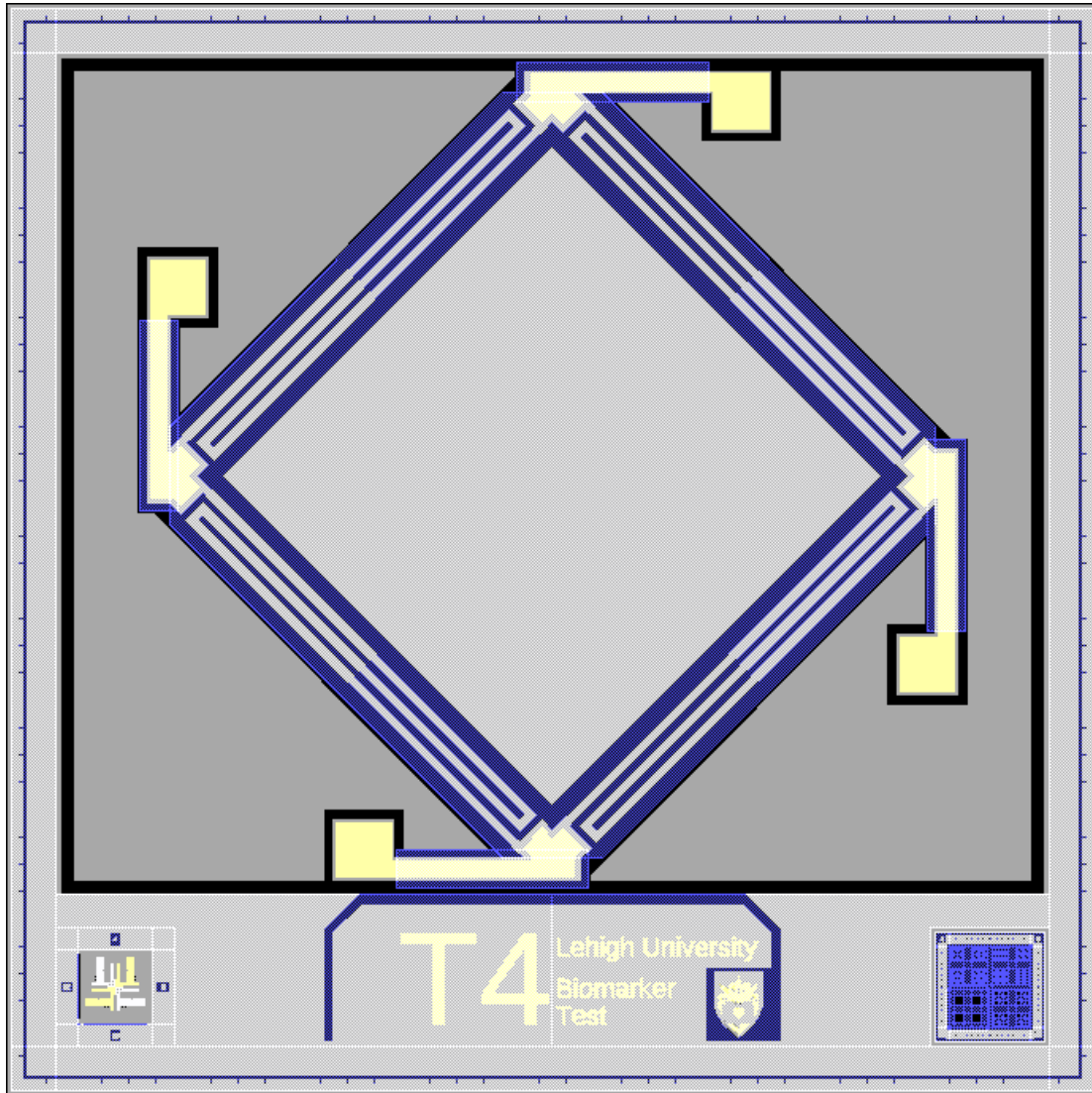


Figure 112: Test die #4 containing a piezoresistive full bridge.

Appendix II: Fabrication

The fabrication process (see Table 50 and Table 57) is based on SOI wafers (Ultrasil Corp. see Table 49) that are n-type doped by to a conductivity of between 1 and 5 m Ω -cm. The actual resistivity after fabrication was measured to be between 1.3 and 2.5 m Ω -cm. The detailed fabrication process developed for the Sherman Fairchild Laboratory clean room is listed in the following appendices but summarized in the following sections.

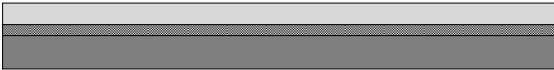

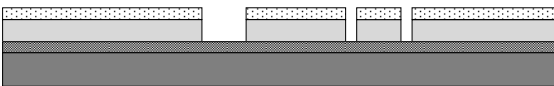

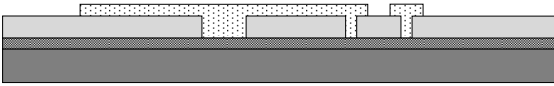
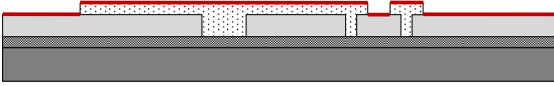
Table 49: Silicon-on-insulator (SOI) wafer specifications.

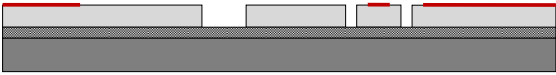
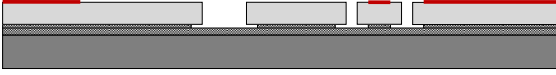
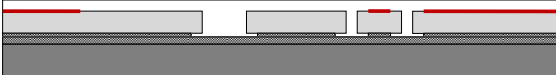
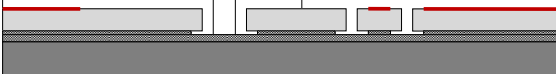

Specification	Value
Manufacturer	Ultrasil Corporation
Lot #	UD-7567 / UH-7573
Type	N / PH
Orientation	(1-0-0)
Diameter	76.2 \pm 0.1 mm
Quantity	10
Device Thickness	10 \pm 0.5 μ m
Device Resistivity	0.001 – 0.005 Ω -cm
Handle Thickness	500 \pm 10 μ m
Handle Resistivity	1-10 Ω -cm
Buried Oxide	ON D
Buried Oxide Thickness	2 μ m \pm 5%
Date Manufactured	June 11, 2009

Revision 1

Fabrication Process Flow

Table 50: Fabrication process flow (revision 1).

Cross Section	Description
	SOI wafer (10 μm device layer / 2 μm buried oxide)
	Photoresist mask for DRIE etch (DEVICE mask)
	DRIE etch of device layer to stop at buried oxide layer (Bosch process)
	Mask layer removal using photoresist stripper
	Photoresist mask for lift-off (METAL mask)
	E-beam metal deposition (50 nm chrome / 200 nm gold)

Cross Section	Description
	Lift-off using photoresist stripper
	Wet etch of oxide (pre-etch to develop undercut)
	Negative tone resist (AZ N4035) spin-on
	UV exposure and development to form electrical isolation (ISOLATION mask) followed by an extended UV flood exposure and hard bake
	Wet etch of oxide to release free standing silicon device structures

Encapsulation Material Tests

SU-8 Tests

A number of tests were performed with SU-8 in order to use it as an encapsulating material which could fill exactly half of a 4 μm wide trench, but ultimately the right combination of process parameters could not be found. Although high-resolution results for narrow trenches in SU-8 have been reported, consistent results along the entire length of 500 μm trenches could not be achieved.

The test recipe for SU-8 was as follows:

1. Dehydrate at 120°C for 20 minutes
2. Vapor prime in a sealed box with HMDS and Xylene in a dish
3. Spin-coat SU-8 3010 at 3000 RPM for 60 seconds
4. Soft bake
 - a. Place wafer on an aluminum disk (4-inch diameter, 2 mm thickness)
 - b. 1 minute on 70°C hotplate
 - c. 2 minutes on 95°C hotplate
 - d. 1 minute on 70°C hotplate
 - e. Let cool 10 minutes on benchtop
 - f. Remove wafer from disk
5. Align and expose 12 seconds at 25 mW/cm² using manufacturer recommended Omega Optical PL-360-LP filter
6. Post-exposure bake
 - a. Same as soft bake
7. Develop
 - a. 60 seconds in Microchem SU-8 developer
 - b. Blow dry with nitrogen
 - c. Rinse 10 seconds in fresh Microchem SU-8 developer
 - d. Spin at 1500 RPM to dry

A number of problems were observed while trying to optimize the SU-8 resolution while maintaining good adhesion. In the discussion below, the above recipe was used unless specified otherwise. The best results were achieved by generally following the manufacturer's recommendations.

First, if Omega Optical PL-360-LP filter is not used, the top of the structures are overexposed and the bottom is underexposed. The sidewalls are sloping inward and structures are not completely encapsulated (see Figure 113).

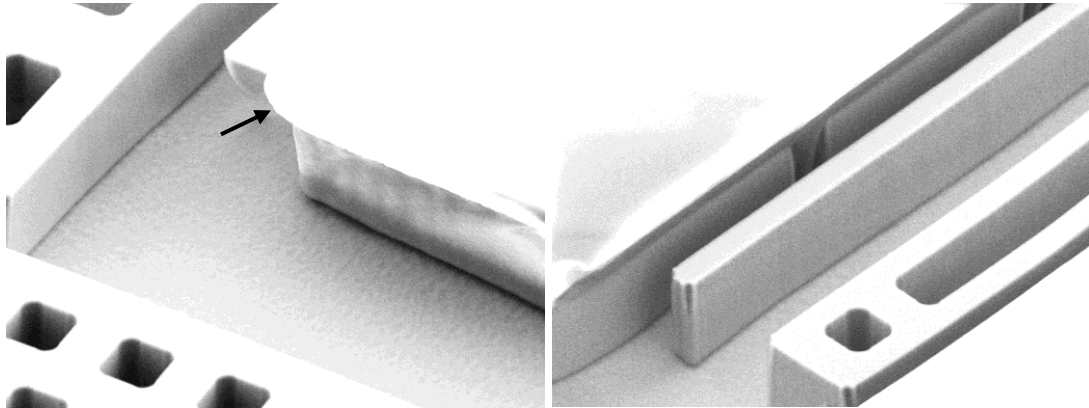


Figure 113: SU-8 3010 T-Topping with 16 second dose (left) 8 second dose (right).

Second, residue that looks like cobwebs is often present in narrow trenches (see Figure 114).

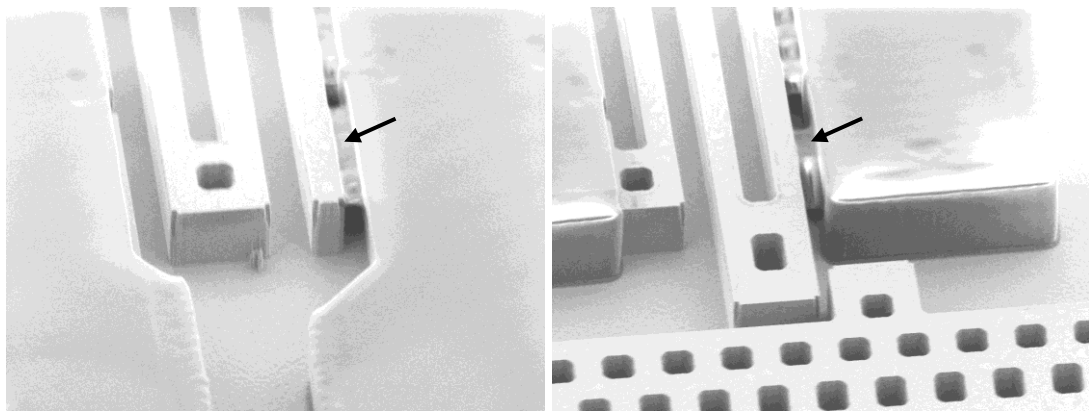


Figure 114: SU-8 3010 (16 sec dose / 1 min develop) where "cobwebs" are visible in narrow trenches at standard development time.

Various attempts were made to modify the development time but the results were not satisfactory (see Figure 115 and Figure 116).

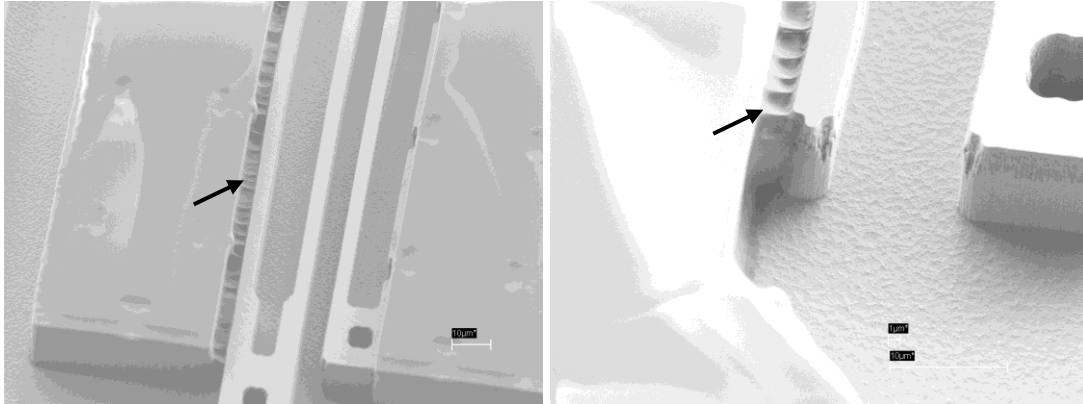


Figure 115: SU-8 3010 (16 sec dose / 5 min develop) where longer development time does not improve resolution.

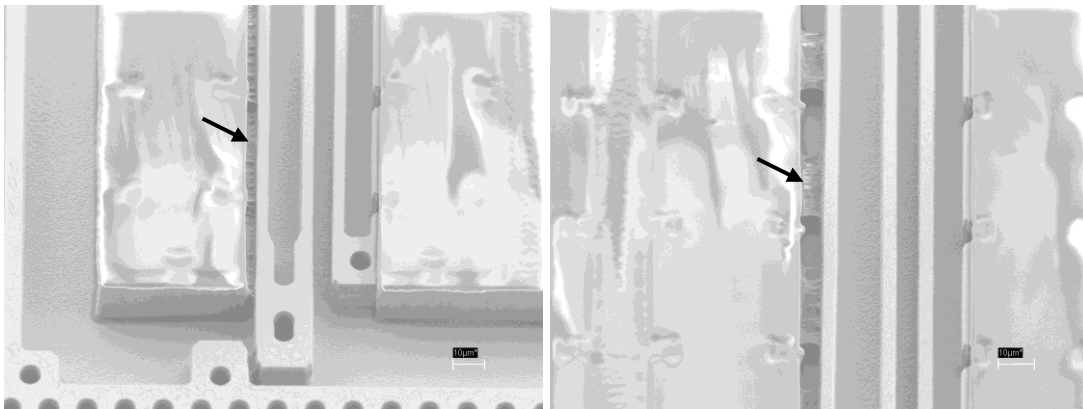


Figure 116: SU-8 3010 (16 sec dose / 15 min develop) where longer development removes more material but does not eliminate “cobweb” effect.

At very long development times, certain test structures were found to have delaminated and fallen on top of an adjacent line pattern. After the extended development, they were fused together (see Figure 117).

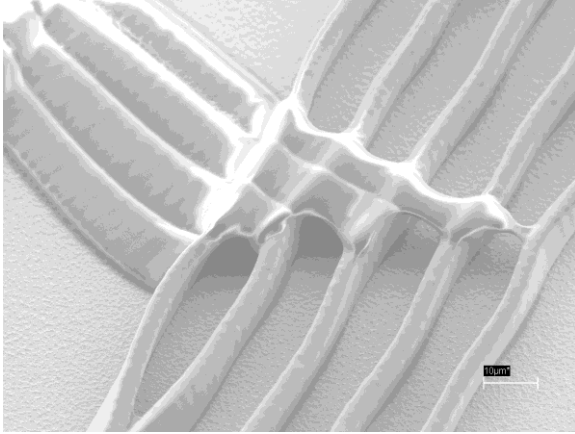


Figure 117: SU-8 3010 (16 sec dose / 15 min develop) where a set of four SU-8 lines have fused together.

SU-8 3000 series resist was also compared to the 2000 series at various exposure doses but the results were similarly unsatisfactory (Figure 118 and Figure 119).

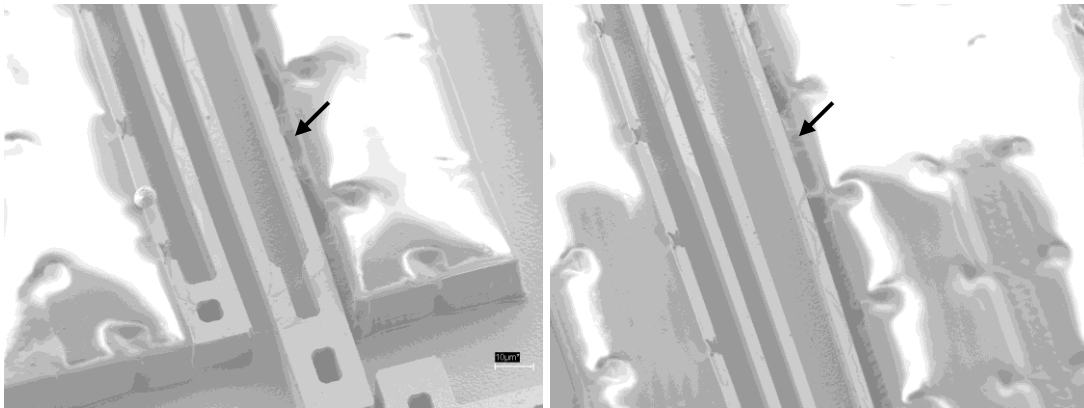


Figure 118: SU-8 2015 (8 sec dose / 1 min develop) formulation has similar resolution limitations as SU-8 3010.

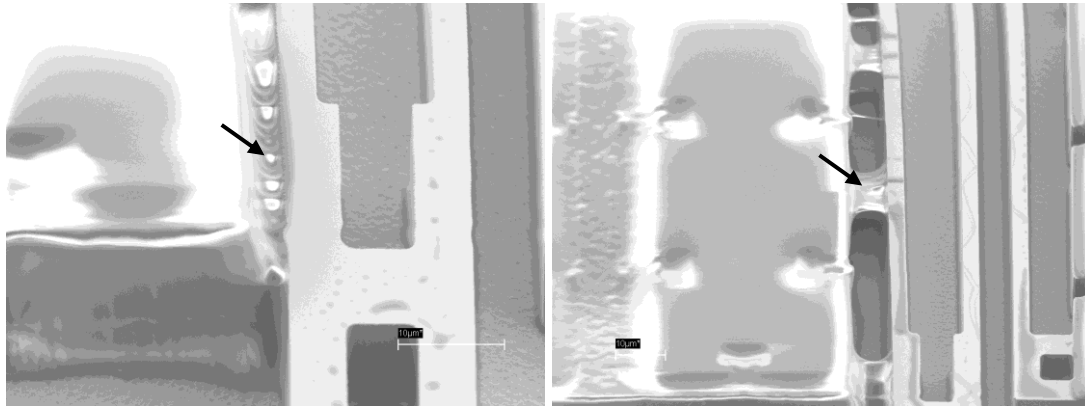


Figure 119: *SU-8 2015 (12 sec dose / 1 min develop) formulation has similar resolution limitations as SU-8 3010.*

Finally, the original SU-8 formulation was used, which had slightly better resolution, even though the final results were still not satisfactory for this application (Figure 120).

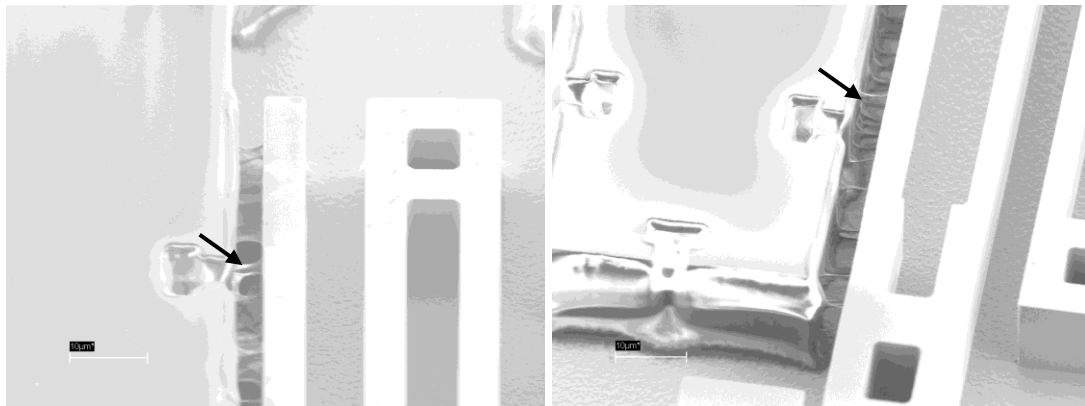


Figure 120: *SU-8 2 (12 sec dose / 1 min develop) formulation has similar resolution limitations as SU-8 3010.*

AZ n4035 Tests

Due to insufficient resolution of SU-8, AZ 4035 negative tone resist was explored as a replacement. It was found to offer superior resolution and adhesion. It was able to encapsulate 10 μm tall structures, while filling half (2 μm) of 4 μm trenches. It also adhered well to gold and was able to stand up to the following buffered HF wet etch without loss of adhesion. After testing at various doses (see Figure 121 and Figure 122),

the final exposure dose chosen for the process was 8.0 seconds. The complete recipe can be found in the following appendix.

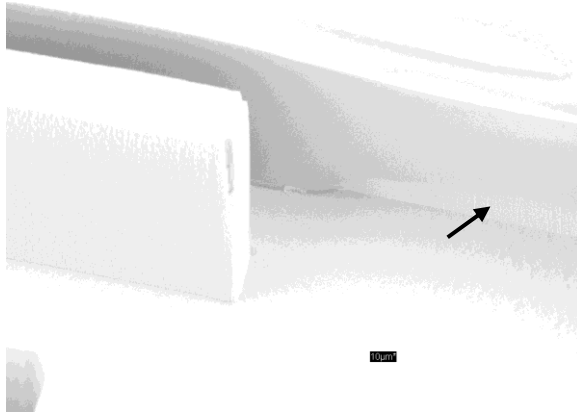


Figure 121: AZ n4035 with 6 second exposure was found to have clear trenches but negative sidewalls which left the bottom of encapsulated structures exposed.

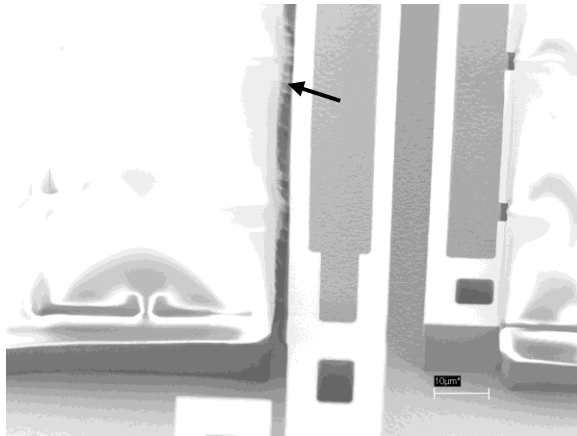


Figure 122: AZ n4035 with 10 second exposure was found to have straight sidewalls but residue left in trenches.

Fabrication Results

In order to ensure that the encapsulation material was able to grip around the edges of the raised silicon structures and maintain good adhesion, an oxide pre-etch step was performed after DEVICE and METAL patterning (see Figure 123), before the ISOLATION layer patterning. Figure 123 also shows the typical sidewall shape of the silicon DEVICE layer after DRIE.



Figure 123: Silicon block after DRIE, metal and oxide pre-etch with 5:1 BHF for 10 min.

DRIE and Metal Deposition

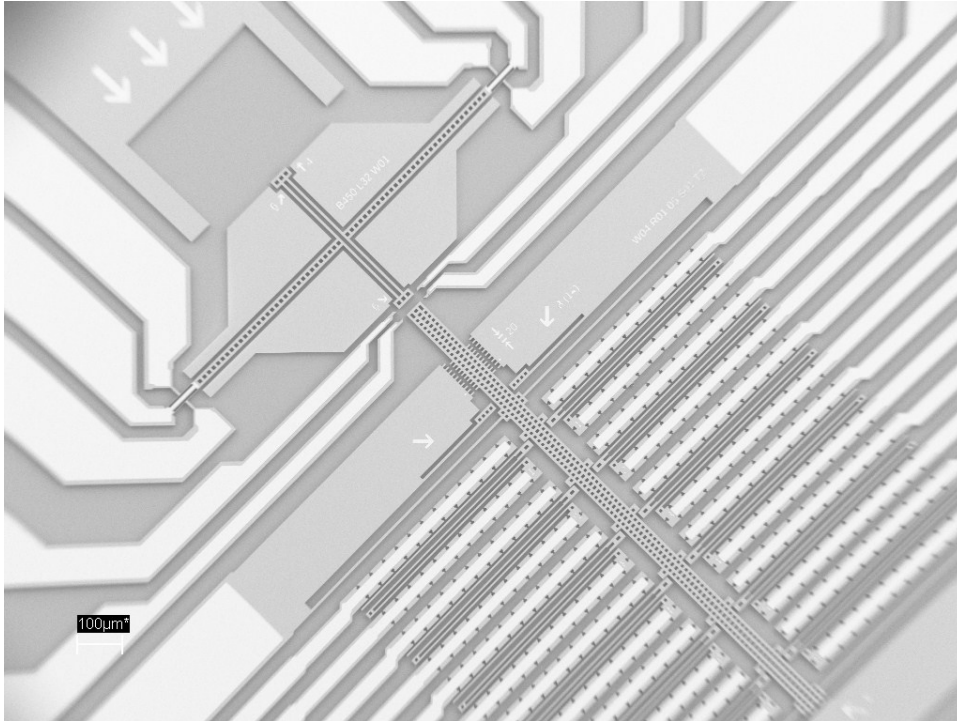


Figure 124: Device wafer (SOI) showing unreleased structures after bulk silicon etch and Cr/Au metal lift-off.

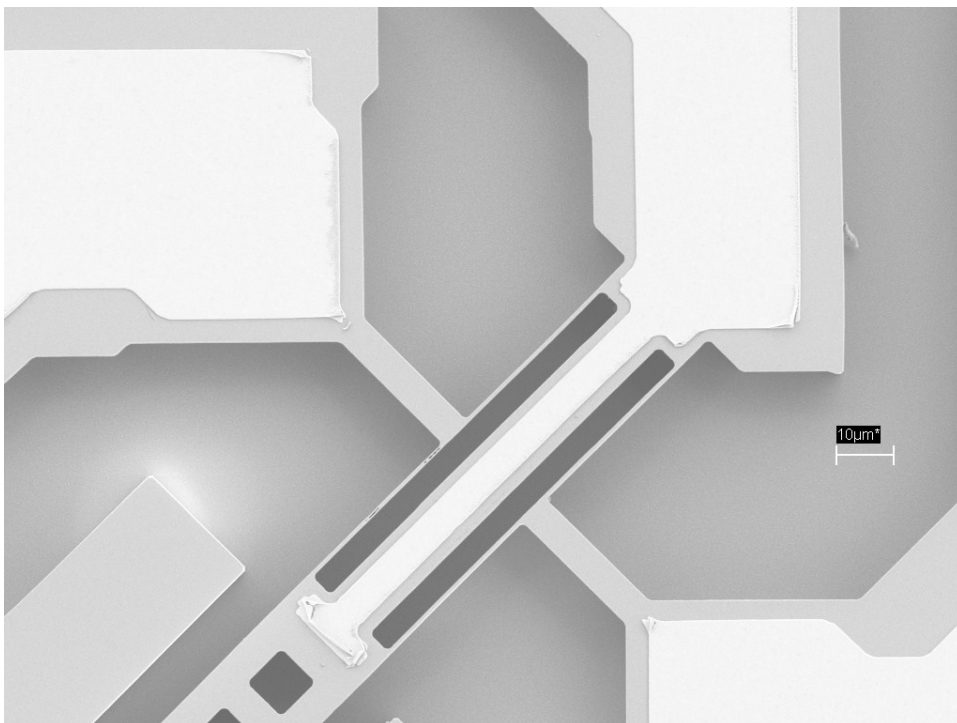


Figure 125: Close-up showing transducer region of the force sensor; the thin transducer beams are 0.6 μm wide (left).

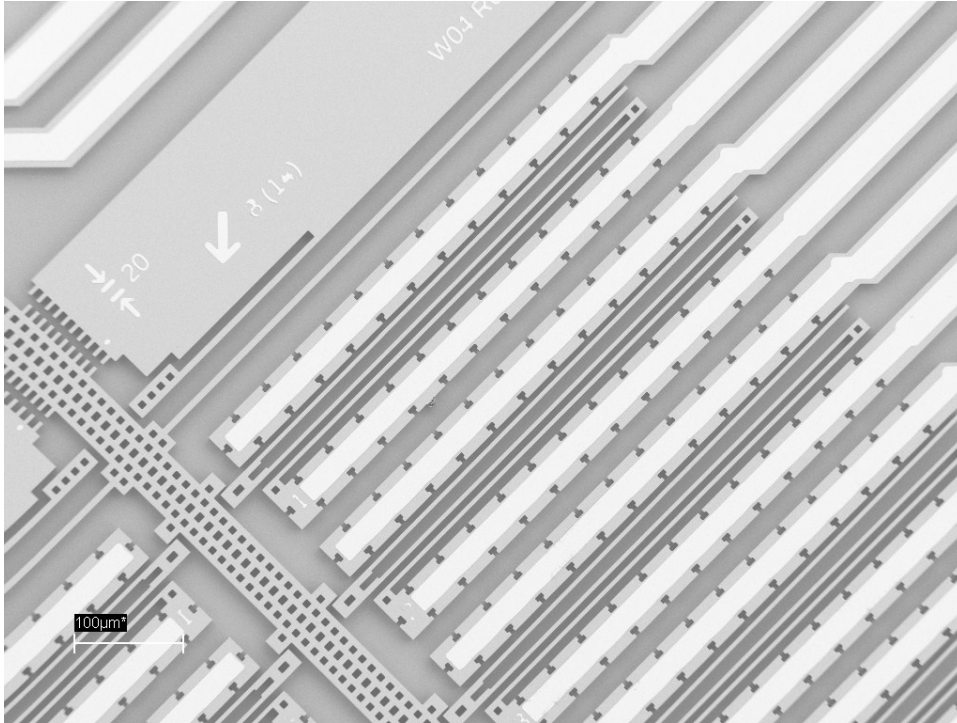


Figure 126: Close-up of actuator array region before encapsulation showing zip-mode electrostatic actuators and central shuttle (right).

Pre-Release

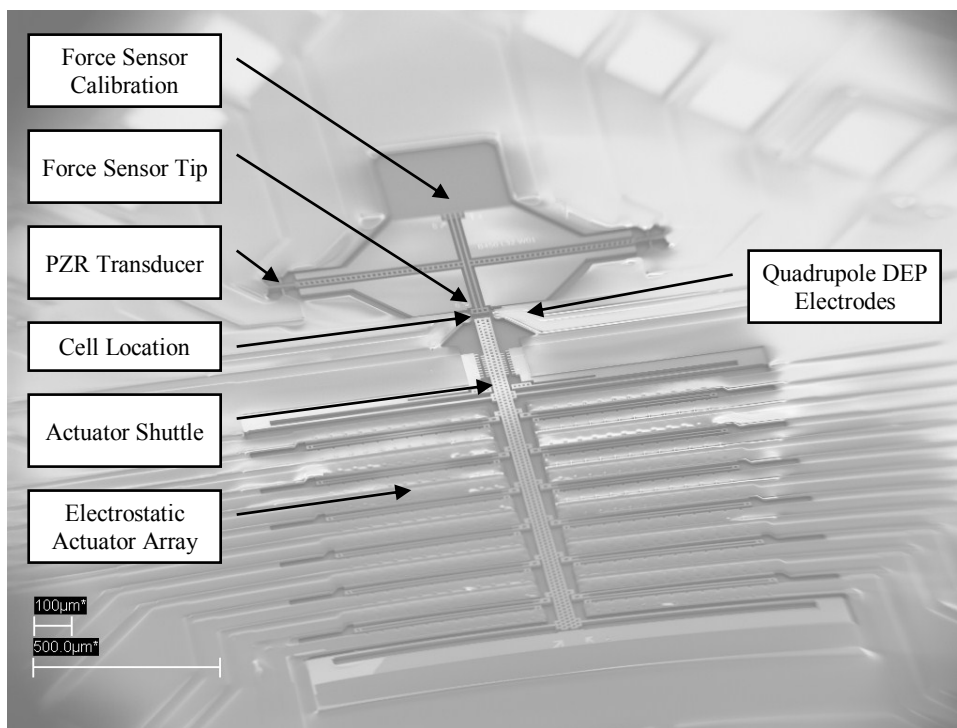


Figure 127: A typical chip from wafer SOI 01.



Figure 128: Typical results from the actuator region on wafer SOI_01.

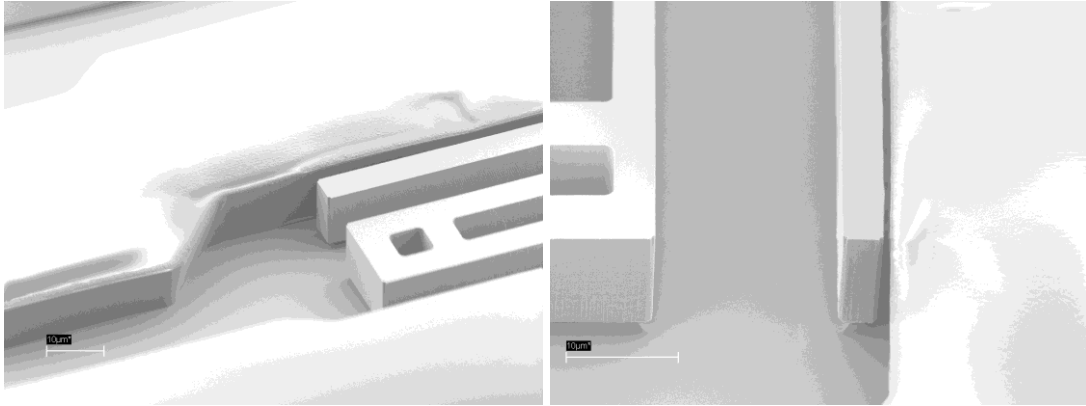


Figure 129: Actuator region from wafer SOI_01 showing straight sidewalls and clear trenches. An 8 second exposure was found to be optimal. Partially etched buried oxide layer is shown beneath the silicon device layer structures.

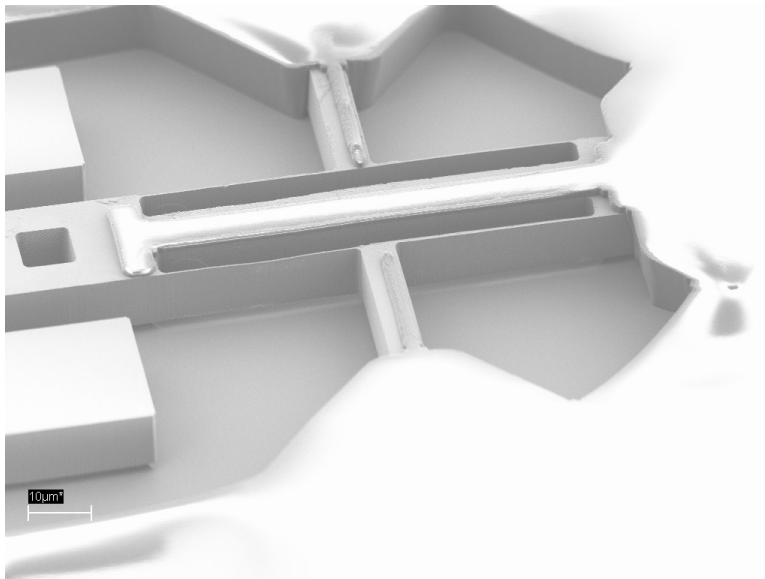


Figure 130: SOI_01 transducer region.

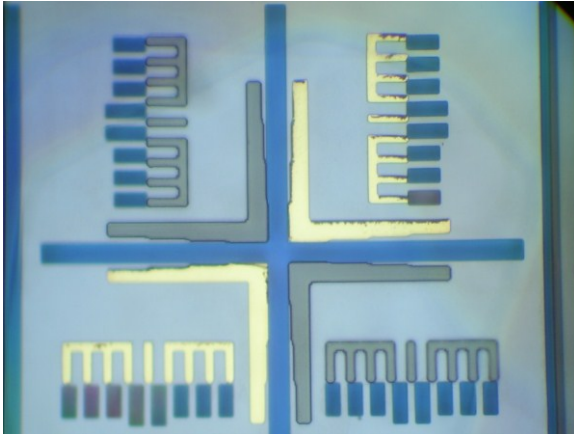


Figure 131: *SOI_01 Alignment mark with 1 μm Vernier scales. Alignment to within 1 μm between all layers was achieved.*

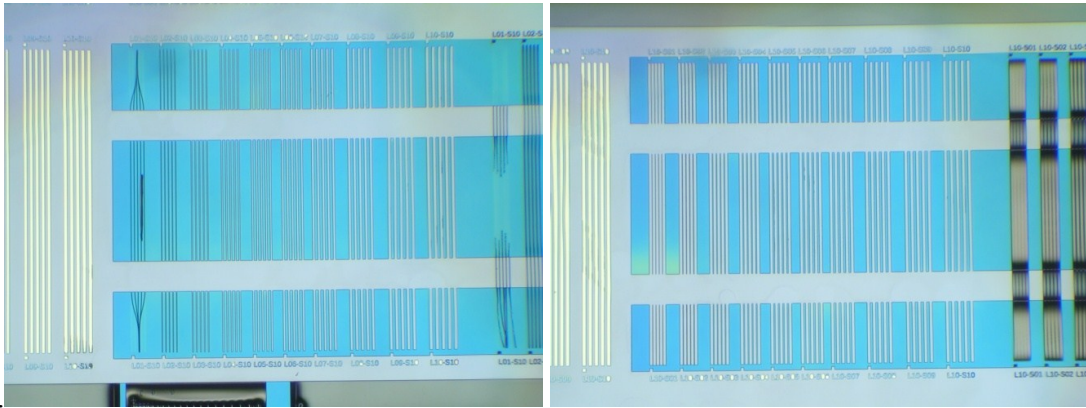


Figure 132: *SOI_01 DEVICE Layer line (left) and spacing (right) test structures.*

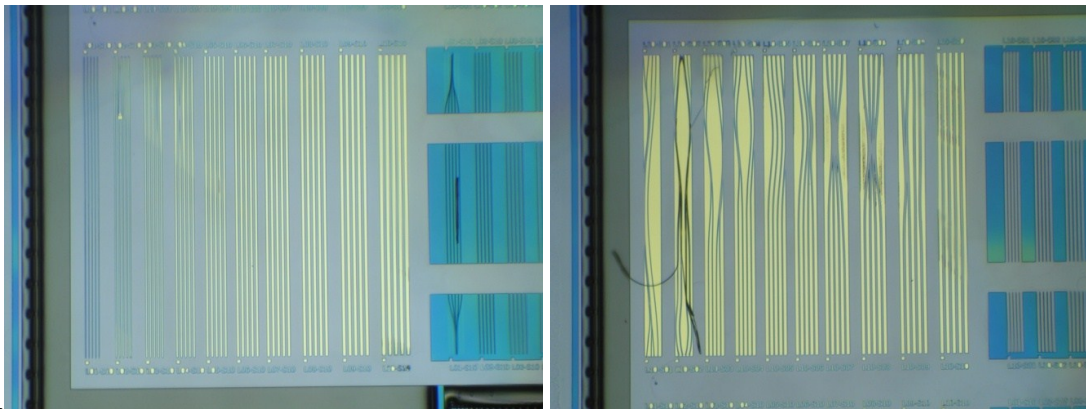


Figure 133: *SOI_01 METAL Layer line (left) and spacing (right) test structures.*

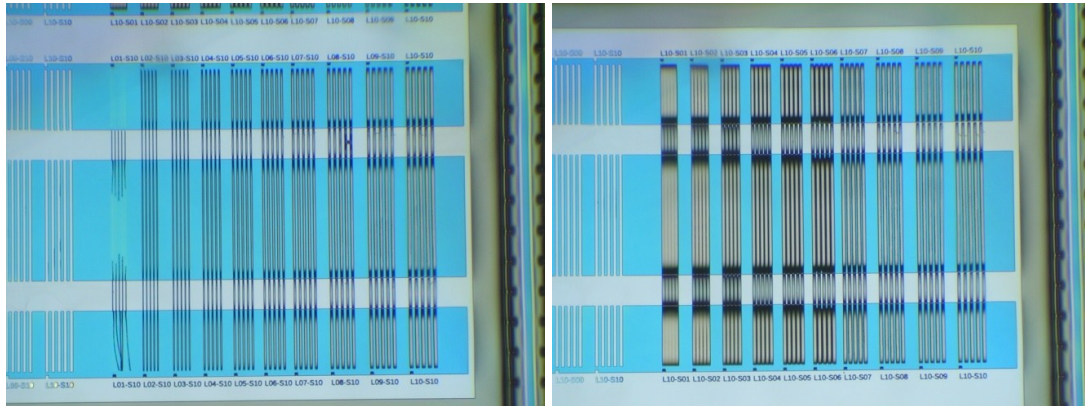


Figure 134: SOI_01 ISOLATION Layer line (left) and spacing (right) test structures.

Final Release

A typical device die following the last release step is shown in Figure 135.

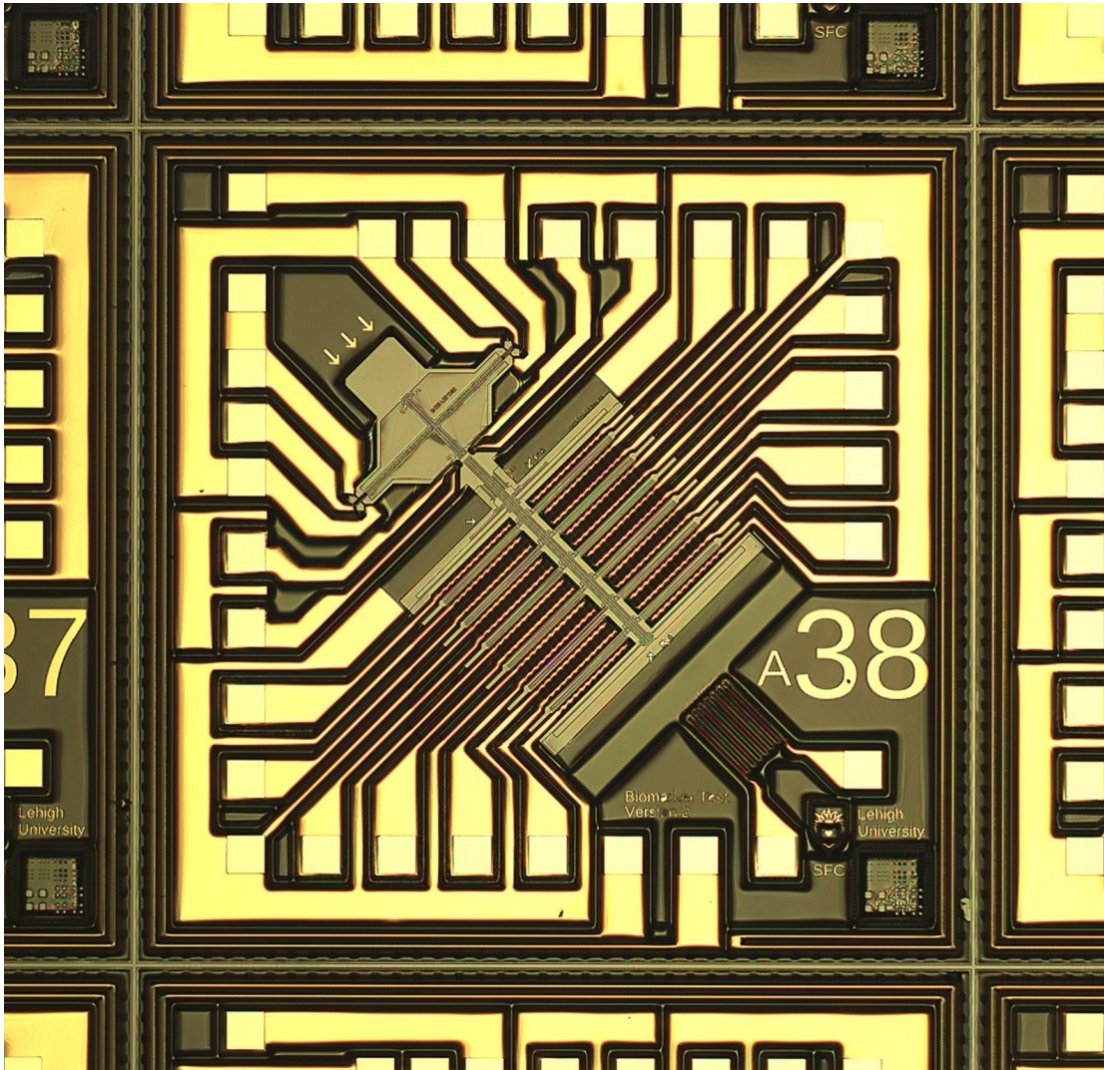


Figure 135: A typical device die following the last release step, but before wafer dicing.

Limitations

An important limitation of the process is over-etch of the very narrow structures in the force sensor. Although narrow transducers improve sensitivity, over-etch causes device failure when they become too narrow as shown in Figure 136. Damage at tops of the transducers is most likely due to fluid flow during fabrication following the first etching step.

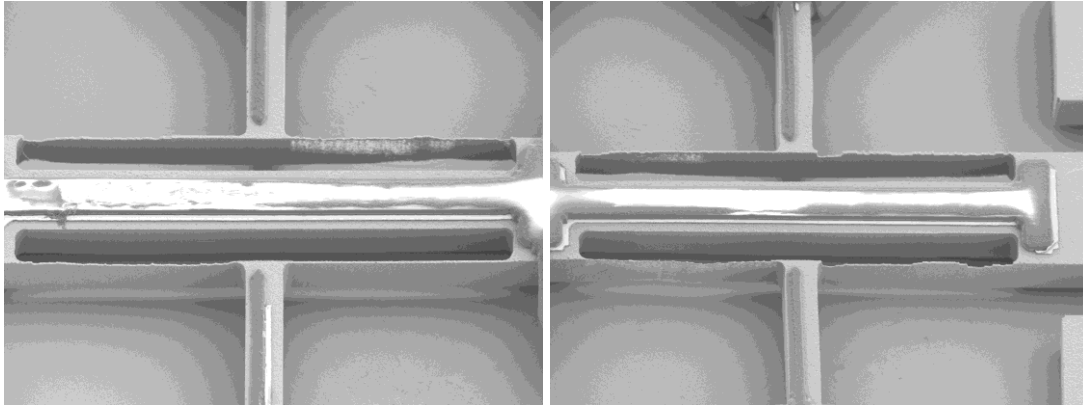


Figure 136: Over-etch on wafer SOI 02, Die A08 transducer region (1 μm mask width) following final release step.

A hairline crack is visible in an over-etched 1 μm beam (see Figure 137 from wafer SOI 02, Die A08) but 2 μm beams do not suffer from is problem. The result of this crack is a large bridge offset, and large amounts of low frequency noise since the contact resistance in the crack may “sense” all kinds of extraneous vibration and changes in environmental parameters.

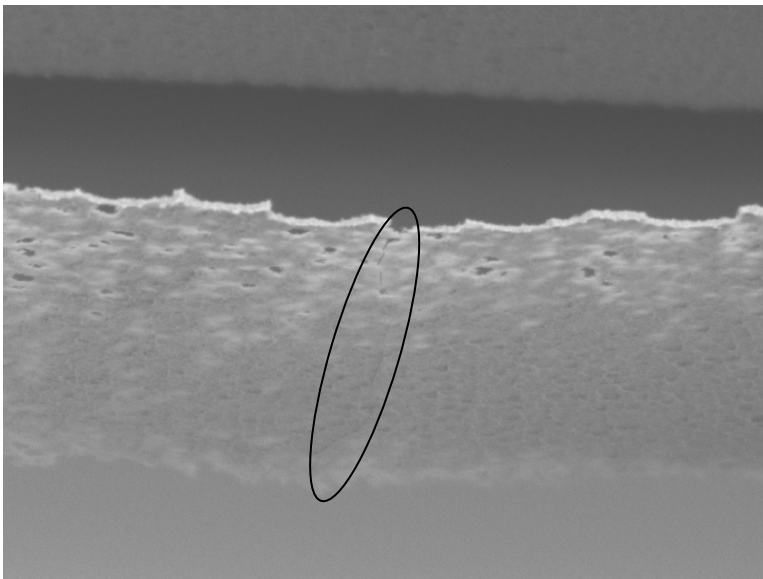


Figure 137: A hairline crack is visible in an over-etched 1 μm beam, but 2 μm beams do not suffer from is problem.

Although they had superior resolution, it must be noted that chips fabricated with AZ n4035 negative photoresist as the encapsulation material did not show the same stability as that expected from SU-8. Packaged chips from this batch started to go bad after about 1 year with significant cracking and delamination occurring which prevented operation of the chips in liquid.

Packaging

The first step following fabrication was dicing into individual dies. This was accomplished with a Tempress Model 602 wafer dicing saw using a 0.003 inch (76 μm) wide blade. The results can be seen in Figure 138.

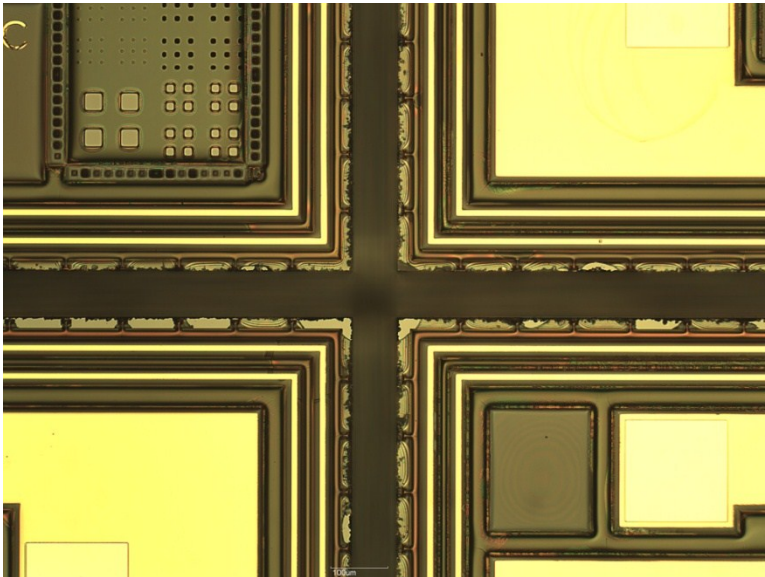


Figure 138: Following dicing with 0.003 inch (76 μm) blade. The wafer was then manually broken into individual chips with a pair of tweezers.

After dicing and separation, the chips are optically inspected for defects, and the resistances of the heater loop and resistance temperature detector are checked on a probe station (SUSS MicroTec PM5) with a digital multimeter (Agilent 34401A). Undamaged chips are then packaged by gluing them into a 28-bin empty cavity dual-

inline-package (Spectrum Semi P/N CSB02804 for revision 1 and Spectrum Semi P/N CSB02806 for revision 2) with silver-filled conductive epoxy paste (see Figure 139).

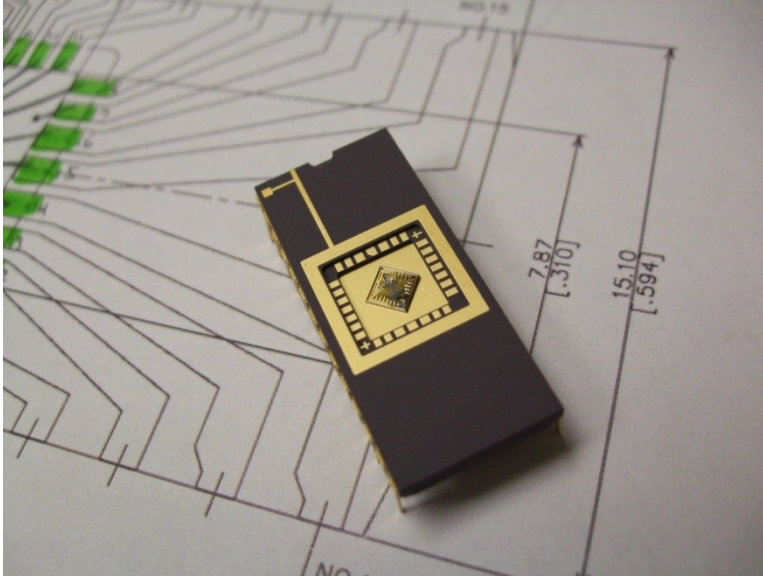


Figure 139: Each chip is mounted in a 28-pin empty cavity dual-inline-package (DIP).

After the epoxy has set, the headers of the DIP and the pads of the chip are connected together with a wedge bonder (Tempress Model 1100 with CoorsTek 2G30-2030 bonding wedge) and gold bonding wire (American Fine Wire Corp. 0.001 inch diameter, 99.99% gold with trace beryllium). The bonding diagram is shown in Figure 140 and a description of each pin assignment is listed in Table 51 (the pad layout is the same for both revision 1 and revision 2 and the chips are pin compatible).

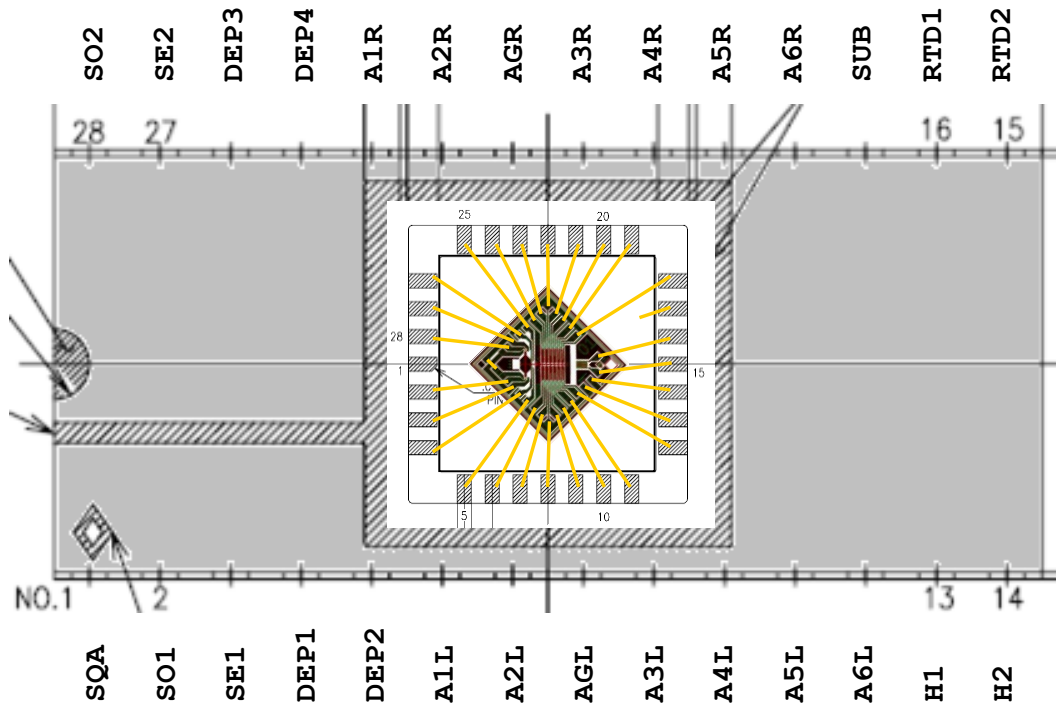


Figure 140: Wire bonding diagram for the chip in a 28-pin DIP.

Table 51: Description of DIP pin assignment.

Label	Description
SO1 / SO2	driver connection to the force sensor bridge
SE1 / SE2	force sensor bridge offset voltage
DEP0 – DEP4	connections to the four triangular DEP electrodes
SUB / SQA	connections to device substrate and a ring surrounding the DIP cavity
A1L – A6L / A1R – A6R	left and right side connections to the actuator array
RTD1 / RTD2	resistance temperature detector (thin film gold layer is used which provides good linearity)
H1 / H2	heater loop around the edge of the chip (15 V heats the packaged chip to about 40°C at room temperature)

After wirebonding, the chips were encapsulated under a microscope and using the probe station and micromanipulators (see Figure 141). A blunt needle was filled with Dow-Corning Sylgard 184 (silicone elastomer) and used to encapsulate each chip. Special care was taken to only apply the encapsulation material to the outer edges of the chip

covering the wirebonds while leaving the center open. This is difficult because Sylgard 184 is self-leveling, so after a small amount was dispensed the chip was repeatedly baked at 15 minutes at 65°C to cure it. This method was improved somewhat in revision 2 below.

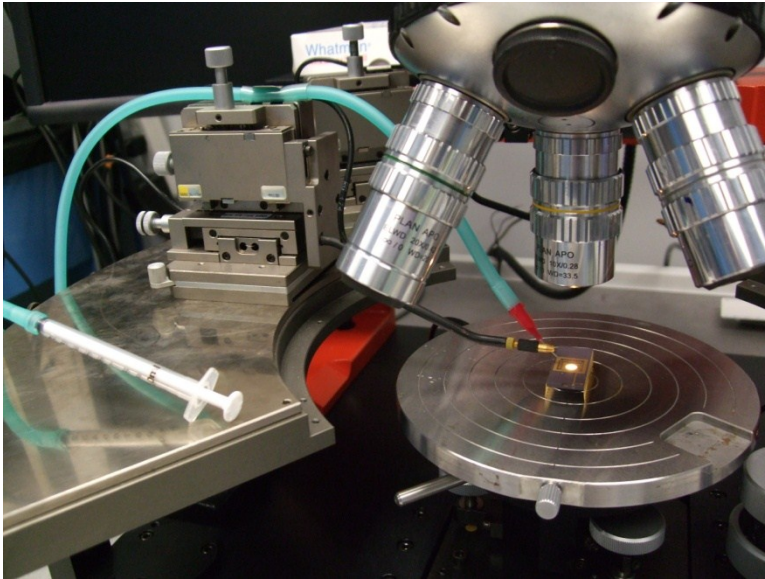


Figure 141: A blunt needle was filled with Dow-Corning Sylgard 184 (silicone elastomer) and used to encapsulate each chip.

After encapsulation, a polystyrene dish (Corning 430165 35mm cell culture dish) with a circular cutout is mounted on top to contain the cell media and cells (see Figure 142). A punch was made from one-half inch aluminum tube that could be connected to a soldering iron and easily remove the circular cutout. Extra material is removed from the dish by sanding the top and bottom surfaces flat.

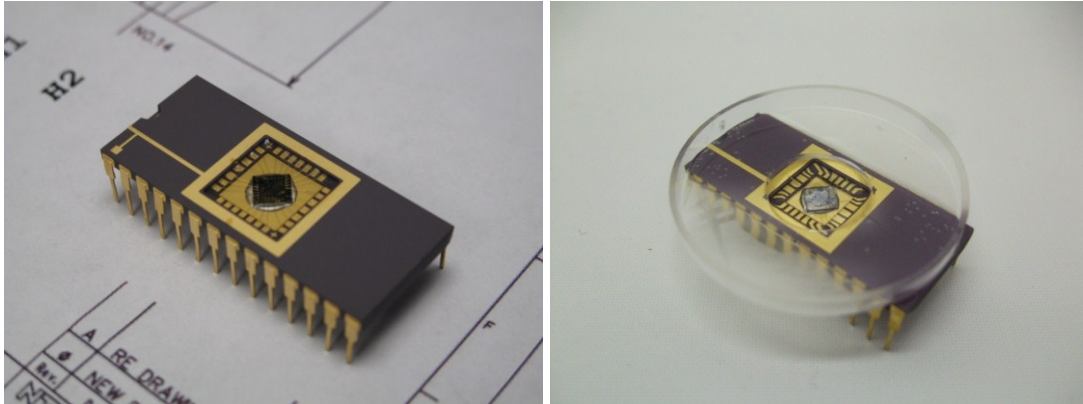


Figure 142: A typical 28-pin DIP following PDMS encapsulation and final packaging.

Device Test Results

Silicon Device Layer Resistivity

The resistance of a conductive rectangular block of material with cross section area wt , length l and resistivity ρ is given by equation 83.

$$R = \rho \frac{l}{wt} \quad 83$$

Resistivity can be measured from resistance if the width (w), thickness (t) and length (l) are known (see equation 84).

$$\rho = R \frac{wt}{l} \quad 84$$

A resistivity test structure was included in each wafer and it is shown on the right side of Die T2 (see Figure 143). Resistance was measured with an Agilent 34401A 6.5 digit multimeter. Each pad is separated by a uniform bar of silicon of width of 100 μm , thickness of 10 μm , and length of 1000 μm . These dimensions were chosen so that $\rho=R$ in units of $\Omega\text{-}\mu\text{m}$.

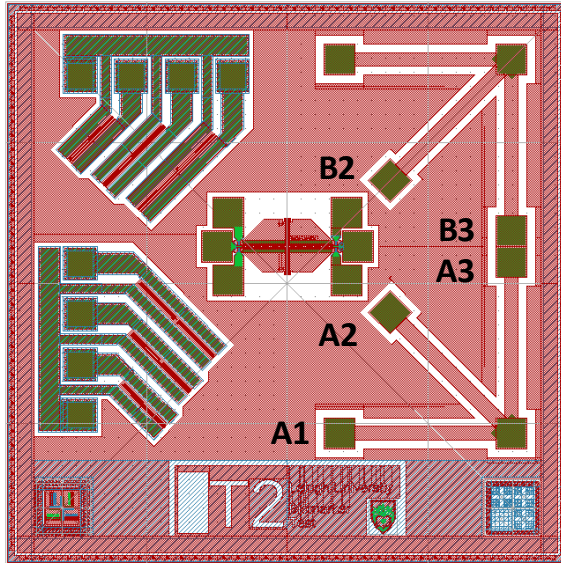


Figure 143: Die T2 which contains a resistivity test structure on the right side.

The results for measurement of Die AT2 from wafer SOI_02 are shown in Table 52, and the average resistivity is 1.35 mΩ-cm (N=6, SD=0.004).

Table 52: Wafer SOI_02 resistivity measurement using AT2 test die.

Group*	Position	R (Ω)	ρ (Ω-μm)	ρ (mΩ-cm)
A	1	14.93	13.43	1.343
A	2	15.00	13.50	1.350
A	3	15.01	13.51	1.351
B	3	15.11	13.53	1.353
B	2	15.11	13.53	1.353
B	1	15.07	13.49	1.349

*Contact resistance for group A was 1.50 Ω and contact resistance for group B was 1.58 Ω.

The manufacturer's resistivity for the wafers was specified as 1 mΩ-cm to 5 mΩ-cm (see Table 49).

Silicon Device Layer Elastic Modulus

The elastic modulus of a material can be extracted from a test structure designed to snap shut as the voltage is increased [56]. The pull-in voltage (or collapse voltage V_{coll}) for a fixed plate and a spring is given by equation 85.

$$V_{coll} = \sqrt{\frac{8w^3d^3}{27El^3l_{el}\epsilon}} \quad 85$$

Where w is the width of the spring, d is the gap between the plate and the spring, l is the total length of the spring, l_{el} is the effective electrode length (overlapping region between the fixed electrode and the spring), E is the elastic modulus of the spring material, and ϵ is the permittivity of the material in the gap. The spring and the electrode are both assumed to have the same vertical height. The equation can be rearranged to express E in terms of V_{coll} and the other parameters (see equation 86).

$$E = \frac{27V_{coll}^2l^3l_{el}\epsilon}{8w^3d^3} \quad 86$$

Once the voltage reaches the level of V_{coll} , movement of the spring is rapid and the structure clamps shut. This change can be observed while testing the structure on a probe station. The test structure included on the wafer (see Figure 144) was adapted directly from elastic modulus test structures for polysilicon [A-1]. The label “parallel” in the figure indicates parallel to the direction of the majority of free-standing beams on the rest of the wafer and “normal” is oriented perpendicular to those. Note that the assumed thickness of the device layer has no impact on the elastic modulus measurement.

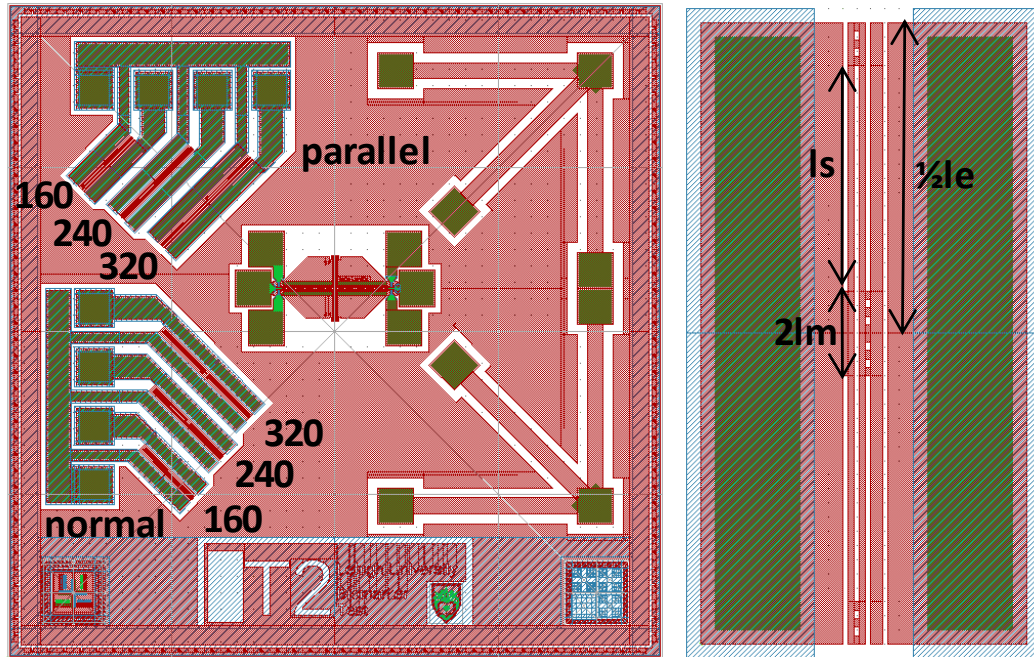


Figure 144: Die T2 which contains resistivity test structure on the left side as well as test structures for elastic modulus. A close up of one of the spring-and-plate elastic modulus test structures is shown on the right.

The assumed parameters are listed in Table 55 and adjusted from the mask dimensions with an over-etch of $0.35 \mu\text{m}$ based on measurements of the spring width (t). The dimensions of the test structures were measured by SEM inspection (LEO 1550 VP) and tabulated in Table 53 and Table 54. There was as much as $0.2 \mu\text{m}$ variation in width (t) of the springs along their length.

Table 53: Measured dimensions for DIE AT2 ($l_s=160 \mu\text{m}$).

Variable	Measured Value	Unit	Description
T	3.27	μm	spring width
D	4.85	μm	gap width
l_s	160.9	μm	spring length
l_{m1}	30.3	μm	spring mount length (outer)
l_{m2}	29.9	μm	spring mount length (center)
$\frac{1}{2}l_e$	220.7	μm	effective electrode length

Table 54: Measured dimensions for DIE AT2 ($l_s=240 \mu\text{m}$).

Variable	Measured Value	Unit	Description
T	3.31	μm	spring width
D	4.73	μm	gap width
l_s	242.6	μm	spring length
l_{m1}	30.7	μm	spring mount length
l_{m2}	30.2	μm	spring mount length
$\frac{1}{2}l_e$	303.5	μm	effective electrode length

Table 55: Parameters for elastic modulus measurement.

Variable	Value	Value with Offset	Unit	Description
offset	0.35	N/A	μm	photolithography over-etch in each direction
t	4.00	3.30	μm	spring thickness (in direction of movement)
w	10.00	10.00	μm	spring width (perpendicular to movement)
l_s	160, 240, or 320	160.35, 240.35, or 320.35	μm	spring length
l_m	30.0	29.65	μm	spring mount length
d	4.0	4.70	μm	electrode gap
ϵ	8.85E-12	N/A	F/m	permittivity of free space

Unfortunately, there is approximately a 5% change in E per $0.1 \mu\text{m}$ variation in gap distance (d in Table 55), so minor variations in photolithography have a large impact on the measured elastic modulus (E). The inaccuracy of this method due to the process variations exceeds the expected variation in material properties. The results for measurement of Die AT2 from wafer SOI_02 are shown in Table 56, and the average E is 95.7 GPa ($N=6$, $SD=5.5$) the expected E was 130 GPa [34].

Table 56: Wafer SOI_01 silicon elastic modulus (E) measurement using AT2 test die.

Direction	l_{s1} (μm)	V_{coll} (V) expected	V_{coll} (V) measured	E (GPa)
Parallel	160.4	93.3	80.9	94.8
Parallel	240.4	43.5	39.3	102.9
Parallel	320.4	25.1	22.5	101.2
Normal	160.4	93.3	78.0	88.2
Normal	240.4	43.5	37.2	92.4
Normal	320.4	25.1	21.7	94.4

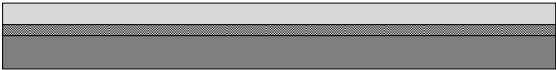

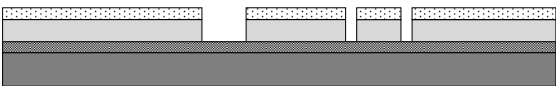

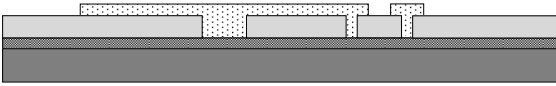
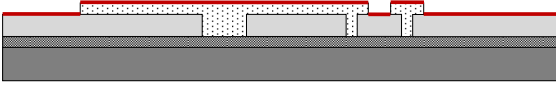
The elastic modulus of the silicon device layer has no impact on the sensitivity of the force sensors (see Chapter 2: Piezoresistive Force Sensor) but does affect the expected behavior of the electrostatic clamps (see Chapter 3: Electrostatic Actuator).


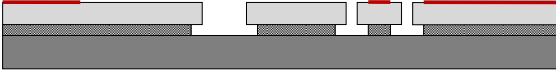
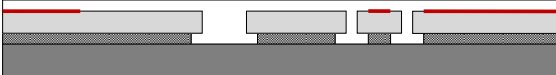
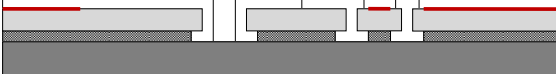
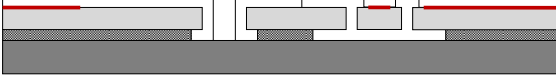
The most likely source of the discrepancy between the measured and expected elastic modulus is inaccuracy in the pull-in voltage model. The equation used for V_{coll} and E would be much more complex and would lead to significantly different values of E when electrode configuration, residual stress, non-linear stiffening, charge redistribution and electric field fringe effects are considered [57].

Revision 2

Fabrication Process Flow

Table 57: Fabrication process flow (revision 2).

Cross Section	Description
	SOI wafer (10 μm device layer / 2 μm buried oxide)
	Photoresist mask for DRIE etch (DEVICE mask)
	DRIE etch of device layer to stop at buried oxide layer (Bosch process)
	Mask layer removal using photoresist stripper
	Photoresist mask for lift-off (METAL mask)
	E-beam metal deposition (50 nm chrome / 200 nm gold / 50 nm chrome)

Cross Section	Description
	Lift-off using photoresist stripper
	Wet etch of oxide (etch through BOX to HANDLE)
	Encapsulation (SU-8) spin-on
	UV exposure and development to form electrical isolation (ISOLATION mask) followed by an extended UV flood exposure and hard bake
	Wet etch of oxide to release free standing silicon device structures

Fabrication Results

Since the ISOLATION layer no longer needs to fill the narrow trenches separating the moving electrostatic actuator plate from the stationary one, SU-8 was used as the encapsulation material due to its superior chemical stability. Typical results are shown in Figure 145 and Figure 146.

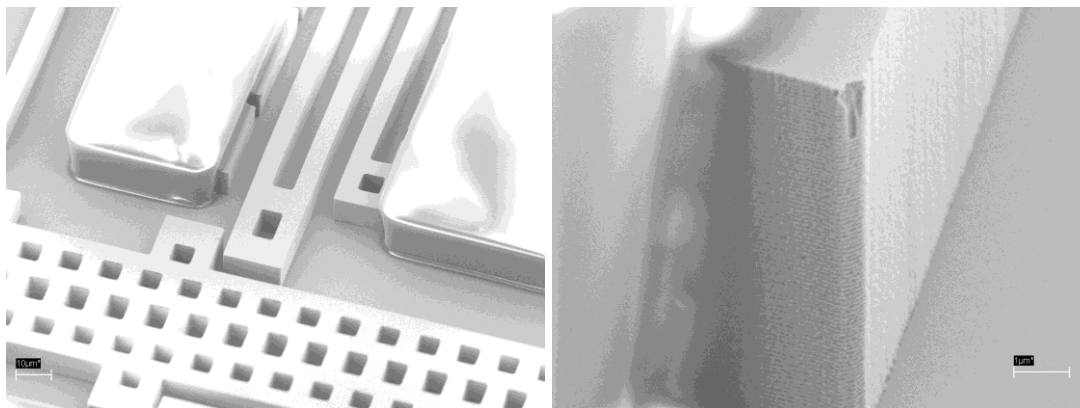


Figure 145: Corner of silicon actuator with SU-8 encapsulation showing DRIE scallops and typical sidewall profile.



Figure 146: Structures to be free-standing are not encapsulated (such as this electrostatic actuator) while everything else is encapsulated in SU-8.

Packaging

In order to encapsulate the chips following wirebonding, an improved method was developed. The chip was mounted in a ZIF socket connected to the supporting electronics, and heated to 40°C using the on-chip heater (see Figure 147). Furthermore, the ratio of the PDMS curing agent (Dow Corning Sylgard 184) was doubled in order to facilitate more rapid curing as the dispensed PDMS contacted the warm areas of the chip. This technique helped prevent the PDMS from getting into the center of the chip

since it would begin to gel as soon as it contacted the heater loop which surrounds the edge of the chip (see Figure 148).

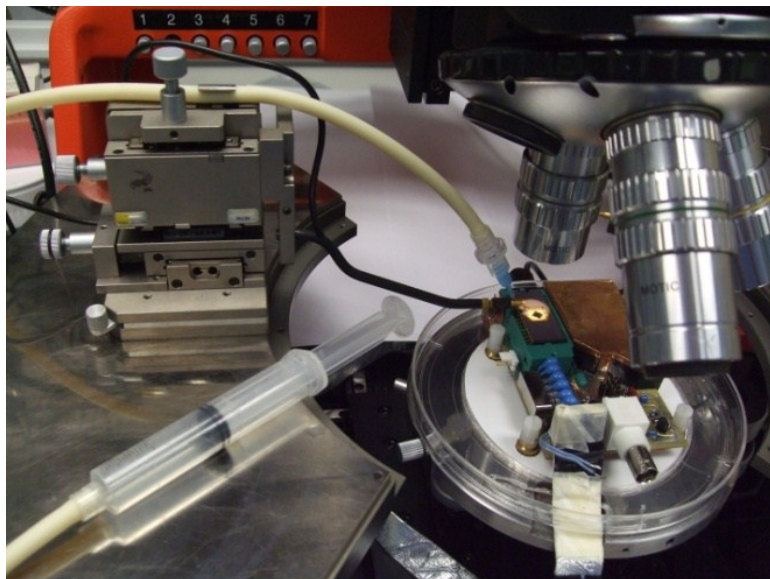


Figure 147: PDMS was carefully placed on the chip while it was heated using the on-chip heater.

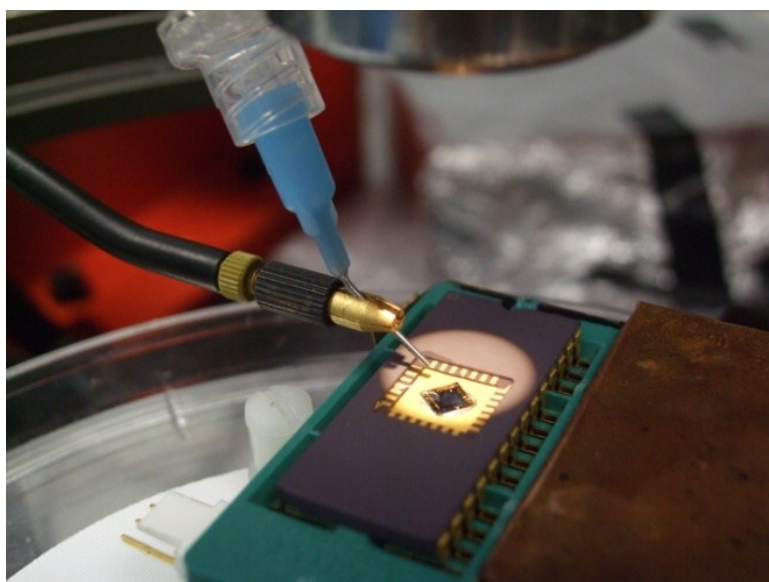


Figure 148: On-chip heating helped cure the PDMS more rapidly as it neared the center of the chip.

The final result of the packaging is shown in Figure 149, after a dish created from a polypropylene ring (cut from a 5 ml centrifuge tube with a hot knife and sanded flat)

was mounted on top of the chip with PDMS and cured in a 50 °C oven (Blue M Electric Co. Stabil-Therm C-3991-Q).



Figure 149: A completed chip with PDMS encapsulation and polypropylene dish.

Device Test Results

The results for measurement of Die AT2 from wafer SOI_06 are shown in Table 58, and the average resistivity is 1.34 mΩ-cm (N=6, SD=0.012). Almost the same method of measurement was used as Revision 1, except that this time the chip was wirebonded before testing.

Table 58: Wafer SOI_06 resistivity measurement using AT2 test die.

Group*	Position	R (Ω)	ρ (Ω-μm)	ρ (mΩ-cm)
A	1	15.05	13.20	1.320
A	2	15.12	13.27	1.327
A	3	15.33	13.48	1.348
B	3	15.21	13.36	1.336
B	2	15.22	13.37	1.337
B	1	15.37	13.52	1.352

**This chip was wirebonded and the pad resistance from A3 to B3 was 1.85 Ω.*

Equipment and Materials

A complete list of the materials used in the fabrication and packaging of the devices is shown in Table 60 below.

Table 59: Materials listing.

Manufacturer	Model	Description
FujiFilm Electronic Materials	OCG 825	Positive photoresist
Arch Chemicals	OCG 809	Developer for OCG 825
Baker	PRS-3000	Photoresist stripper
AZ Electronic Materials	nLOF 2070	Negative lift-off resist
AZ Electronic Materials	MIF 300	Developer for nLOF 2070
AZ Electronic Materials	400T Stripper	Photoresist stripper
Rohm Haas Electronic Materials	Microposit Remover 1165	Photoresist stripper
MicroChem	SU-8 3010	Photopatternable epoxy
MicroChem	SU-8 Developer	Developer for SU-8
Dow Corning	Sylgard 184	Packaging silicone (PDMS)

A complete list of the equipment used in the fabrication and testing of the devices is shown in Table 60 below.

Table 60: Equipment listing.

Manufacturer	Model	Description
National Appliance Co.	Model 5831	Oven for soft bake
Fisher	Model 215F	Oven for hardbake or dehydration bake
Blue M Electric Company	Stabil-Therm C-3991-Q	PDMS packaging bake
Corning	PC-520	Hotplate for general use
Fisher Scientific	Isotemp 11-800-495HP	Hotplate for SU-8 step 1 (65°C)
Thermolyne	HP-11515B	Hotplate for SU-8 step 2 (95°C)
PTC Instruments	572CM Spot Check	Calibrated thermometer
Raytek	MT6	Infrared thermometer
Karl Suss	MJB3	High performance contact aligner
Omega Optical	PL-360-LP	UV filter for SU-8
Indel Systems	Electron Beam Evaporator	Thin film metal deposition
Tempress	Model 602	Dicing saw
Tempress	Model 1100	Ultrasonic wedge bonder
Technics West Inc.	PEII-A Plasma System	Reactive ion etching (RIE)
Adixen	AMS 100 I-Speeder	Deep reactive ion etching (DRIE)
LEO	1550 VP	Scanning electron microscope (SEM)
Tencor	alpha-step 200	Contact profilometer
Nikon	Optiphot	Microscope
Nikon	BP Plan 5,10,40,100	Microscope objectives
SUSS MicroTec AG	PM5	Probe station
Motic	PSM-1000	Microscope
Motic	PLAN APO ELWD 2,10,20	Microscope objectives
Motic	Moticam 2300	Microscope camera
SUSS MicroTec AG	PH120	Micromanipulator
BK Precision	Test Bench 390A	Digital multimeter
Agilent Technologies	34401A	6 ½ digit multimeter
Agilent Technologies	34970A	Data acquisition/Switch unit
Agilent Technologies	33521A	Signal generator
Agilent Technologies	DSO1024A	Oscilloscope
Kenwood	PR18-5	Power supply (5V)
R.S.R.	PW-3033	Power supply (±30V)
National Instruments	PCI-6225	16-bit DAQ card
National Instruments	SCC-68	DAQ breakout box for NI PCI-6225
National Instruments	USB-6009	14-bit DAQ module
Physik Instrumente	E-471.00	HVPZT power amplifier
Physik Instrumente	P-216.4S	Piezo actuator
Dell	Dimension E520	PC with LabView 8.5 and Motic software

Appendix III: Fabrication Process #1

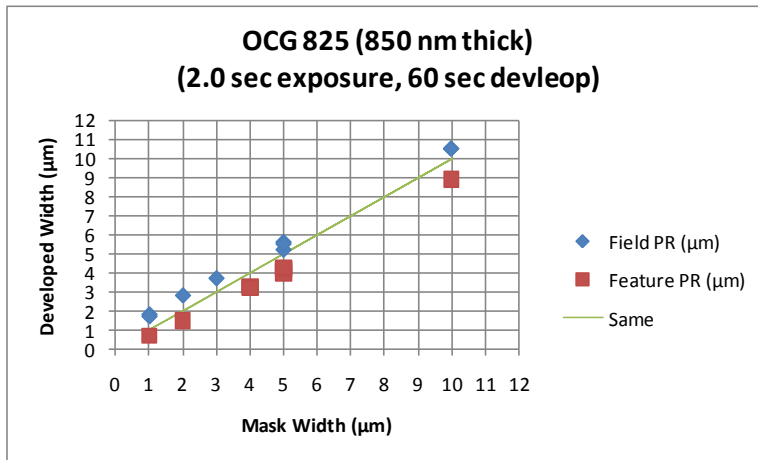
Starting Materials

1. 3 inch SOI wafers
 - a. 2 μm buried oxide layer / 10 μm device layer
 - b. Device resistivity 0.001 – 0.005 $\Omega\text{-cm}$

Device Layer Photoresist Patterning (DEVICE mask)

1. Dehydration
 - a. 120 °C in convection oven for 20 min
2. Vapor prime
 - a. Process immediately after dehydration bake
 - b. 10 min. in priming box with HMDS:Xylene in 1:1 ratio in the glass dish
 - c. Use approximately 12 drops of each, total
3. Spin-coat positive tone photoresist
 - a. OCG 825 (20 cs) target thickness 0.8 μm
5000 RPM, 40 sec, low acceleration setting, acceleration = 40
4. Softbake
 - a. Convection oven 95° C for 30 min
Place wafer cassette upright so wafers are lying flat during bake
 - b. Rehydrate at room temperature for 15 min by leaving cassette on benchtop (relative humidity is typically 35%)
5. Mask Exposure
 - a. Warm up the Karl Suss MJB3 contact aligner UV lamp by performing two 10 sec. exposures with no wafer
 - b. Load Biomarker Test project DEVICE mask
Position mask with primary flat alignment mark on the right
 - c. Carefully adjust height setting
 - d. Align primary flat line to the corresponding mask alignment mark on wafer
 - e. Expose each wafer for 1.40 sec @ 25 mW/cm²
6. Develop
 - a. OCG 809 Developer and DI water solution in 1:1 mix
 - b. Submerge for 60 sec and agitate
7. Rinse & dry
 - a. Rinse in DI water 5 times
 - b. Blow dry with nitrogen
8. Inspection

- a. CD 1 μm lines should be visible as 0.8 to 0.6 μm lines
- b. If failure, strip and repeat PR deposition.



Deep Reactive Ion Etching

1. LOWROUGHNESS Process using AMS 100 (should already be programmed)
This process lasts about 5 min and etches about 12 μm deep, but etch will stop on buried oxide layer at 10 μm .
2. Strip
 - a. 30 min in Baker PRS 3000 (standard 2-bath method)
 - b. Rinse in DI water 5 times
 - c. Blow dry with nitrogen

Metal Layer Photoresist Patterning (METAL mask)

1. Warm up the hotplate to 110° C
2. Dehydration
 - a. 120 °C in convection oven for 20 min
3. Vapor prime
 - a. Process immediately after dehydration bake
 - b. 10 min. in priming box with HMDS:Xylene in 1:1 ratio in the glass dish
 - c. Use approximately 12 drops of each, total
4. Spin-coat negative tone lift-off photoresist
 - a. AZ nLOF 2070 target thickness 2 to 5 μm coverage over 10 μm ridge / trench
5000 RPM, 60 sec, low acceleration setting, acceleration = 0
5. Softbake
 - a. Verify temperature with spot-check thermometer ($\pm 2^\circ\text{C}$)
 - b. Hot-plate 110° C for 60 seconds exactly

- c. Let cool 5 min
- 6. Mask Exposure
 - a. Warm up UV lamp by performing two 10 sec. exposures with no wafer
 - b. Load Biomarker Test project METAL mask
Position mask with METAL text on top (i.e. away from you when mask is loaded)
 - c. Carefully adjust height setting
 - d. Align to the corresponding mask alignment mark on wafer
 - e. Expose each wafer for 3.20 sec @ 25 mW/cm²
- 7. Post Exposure Bake
 - a. Hot-plate 110° C for 60 seconds exactly
- 8. Develop
 - a. AZ 300 MIF developer full strength
 - b. Submerge for 2 minutes and agitate with gentle swirling motion
- 9. Rinse & dry
 - a. Rinse in DI water 5 times
 - b. Blow dry with nitrogen
- 10. Inspection (optical microscope)
 - a. CD 2 μm lines should be visible as 1 to 3 μm lines on top of ridges
Corners of ridges should be covered with photoresist
 - b. If failure, strip in AZ 400T and repeat photoresist patterning.

Metallization and Lift-Off

- 1. Using e-beam evaporator for total thickness of 250 nm
500 Å (50 nm, 0.050 μm) Chrome
2000 Å (200 nm, 0.200 μm) Gold
- 2. Lift-off
 - a. 4 hours in AZ 400 T stripper (3.5 hours in first bath, 30 min in second bath)
Note that Baker PRS 3000 stripper is incompatible with AZ nLOF 2070.
 - b. Rinse in DI water 5 times
 - c. Do not let dry and rinse thoroughly with IPA squeeze bottle

Device Undercut

Use appropriate caution and labware with HF / BHF.

- 1. Use BHF 5:1 mix (5 parts of 40% NH₄F to 1 part 49% HF) by volume
Etch rate of oxide is approximately 100 to 120 nm / min.

2. Typically 100 ml NH₄F and 20 ml HF is mixed, in a 600 ml polyethylene beaker
 - a. Submerge wafer for 10 minutes
 - b. Small bubbles of hydrogen will form on the surface of the wafer
 - c. At this point, the smallest structures will be partially released.
3. Rinse in DI water 5 times
4. Blow dry (gently) with nitrogen

Insulation Layer Photoresist Patterning (ISOLATION mask)

1. Warm up the hotplate to 110° C
2. Dehydration
 - a. 120 °C in convection oven for 20 min
3. Vapor prime
 - a. Process immediately after dehydration bake
 - b. 10 min. in priming box with HMDS:Xylene in 1:1 ratio in the glass dish
 - c. Use approximately 12 drops of each, total
4. Spin-coat negative tone photoresist
 - a. AZ n4035 target thickness 1 to 2 μm coverage over 10 μm ridge / trench
1500 RPM, 40 sec, low acceleration setting, acceleration = 60
 - b. Edge bead removal with Acetone squeeze bottle at 700 RPM (30 sec)
5. Softbake
 - a. Verify temperature with spot-check thermometer (±2° C)
 - b. Hot-plate 110° C for 60 seconds exactly
 - c. Let cool 5 min
6. Mask Exposure
 - a. Warm up UV lamp by performing two 10 sec. exposures with no wafer
 - b. Load Biomarker Test project ISOLATION mask
Position mask with ISOLATION text on top (i.e. away from you when mask is loaded)
 - c. Carefully adjust height setting
 - d. Align to the corresponding mask alignment mark on wafer
Use HP mode to ensure straight sidewalls.
 - e. Expose each wafer for 8.00 sec @ 25 mW/cm²
7. Post Exposure Bake
 - a. Hot-plate 110° C for 20 seconds exactly
8. Develop
 - a. AZ 300 MIF developer full strength
 - b. Submerge for 3 minutes and gently swirl
9. Rinse & dry
 - a. Rinse in DI water 5 times

- b. Blow dry with nitrogen (gently)
- 10. Inspection (optical microscope)
 - a. The trenches between the actuator electrodes should be ½ filled with photoresist with no residue.
 - b. If failure, strip in AZ 400T and repeat photoresist patterning.
- 11. Inspection (SEM)
 - a. The photoresist covering the electrodes should and have straight sidewalls, and completely cover the silicon down to the bottom. Check the fixed electrode next to the end of the moving electrode.
 - b. If failure, strip in AZ 400T and repeat photoresist patterning.
- 12. Resist hardening
 - a. Flood expose each wafer five times for 8 seconds at 25 mW/cm² with a 60 second wait between exposures
 - b. Hard bake the resist on hot-plate 110° C for 2 minutes
Note: resist should be capable of standing up to water, BHF and IPA at this point, however it will be damaged by acetone.

Device Release

Use appropriate caution and labware with HF / BHF.

1. Use BHF 5:1 mix (5 parts of 40% NH₄F to 1 part 49% HF) by volume
Etch rate of oxide is approximately 100 to 120 nm / min.
2. Typically 100 ml NH₄F and 20 ml HF is mixed, in a 600 ml polyethylene beaker
 - a. Submerge wafer for 60 to 70 minutes
Alternately, submerge the wafer for 10 minutes at a time for a total of 60 to 70 minutes and rinse between etches
 - b. Small bubbles of hydrogen will form on the surface of the wafer
 - c. At this point, all structures are fully released.
3. Rinse in DI water 5 times
4. Do not dry. Let wafer sit in plenty of DI water for 2 hours in order for all HF to diffuse out of undercut regions
5. Blow dry (very gently) with nitrogen

Protection Layer & Wafer Dicing

1. Dehydration
 - a. 120 °C in convection oven for 20 min
2. Vapor prime
 - a. Process immediately after dehydration bake
 - b. 10 min. in priming box with HMDS:Xylene in 1:1 ratio in the glass dish

- c. Use approximately 12 drops of each, total
3. Spin-coat positive tone photoresist as protective layer
 - a. AZ 9260 target thickness 5 μm coverage over 10 μm ridge / trench
3000 RPM, 60 sec, low acceleration setting, acceleration = 20
 - b. Edge bead removal with Acetone squeeze bottle at 1000 RPM (30 sec)
4. Softbake
 - a. Convection oven 95° C for 15 min
 - b. Let cool / rehydrate 15 min
5. Flood Exposure
 - a. Warm up UV lamp by performing two 10 sec. exposures with no wafer
 - b. Flood expose each wafer three times for 10 seconds at 25 mW/cm² with a 60 second wait between exposures
Note: nitrogen bubbles will form in resist if single dose is too high
6. Wafer Dicing
 - a. Cut the wafer using 100 μm saw blade and use 4.000 mm for X-axis and Y-axis index
7. Remove resist
 - a. Puddle develop for 6 minutes in AZ 400K 1:4 mix with DI water
 - b. **Carefully** handle wafer during rinsing, it will easily break along dicing lines
8. Free individual dies
 - a. Gently break wafer along dicing lines
 - b. For smaller pieces, grasp group of dies along edges using two tweezers
 - c. Gently pull tweezers opposite directions and bend. Dies should break apart easily.

Appendix IV: Fabrication Process #2

Starting Materials

1. 3 inch SOI wafers
 - a. 2 μm buried oxide layer / 10 μm device layer
 - b. Device resistivity 0.001 – 0.005 $\Omega\text{-cm}$

Device Layer Photoresist Patterning (DEVICE mask)

1. Dehydration
 - a. 120 °C in convection oven for 20 min
2. Vapor prime
 - a. Process immediately after dehydration bake
 - b. 10 min. in priming box with HMDS:Xylene in 1:1 ratio in the glass dish
 - c. Use approximately 12 drops of each, total
3. Spin-coat positive tone photoresist
 - a. OCG 825 (20 cs) target thickness 0.8 μm
5000 RPM, 40 sec, low acceleration setting, acceleration = 40
4. Softbake
 - a. Convection oven 95° C for 30 min
Place wafer cassette upright so wafers are lying flat during bake
 - b. Rehydrate at room temperature for 15 min
5. Mask Exposure
 - a. Warm up UV lamp by performing two 10 sec. exposures with no wafer
 - b. Load Biomarker Test project DEVICE mask
Position mask with primary flat alignment mark on the right
 - c. Carefully adjust height setting
 - d. Align primary flat line to the corresponding mask alignment mark on wafer
 - e. Expose each wafer for 1.40 sec @ 25 mW/cm²
6. Develop
 - a. OCG 809 Developer and DI water solution in 1:1 mix
(old developer mix results in underdeveloped ragged edges)
 - b. Submerge for 60 sec and agitate
7. Rinse & dry
 - a. Rinse in DI water 5 times
 - b. Blow dry with nitrogen
8. Inspection
 - a. CD 1 μm lines should be visible as 0.8 to 0.6 μm lines

- b. If failure, strip and repeat PR deposition.
9. Solvent removal
 - a. To remove solvent from patterned resist, no hard bake is necessary. Just wait overnight.

Deep Reactive Ion Etching

1. LOWROUGHNESS Process using Adixen AMS-100 I-Speeder (should already be programmed)
This process lasts about 5 min and etches about 12 μm deep, but etch will stop on buried oxide layer at 10 μm .
2. Dry strip oxygen plasma
(this step effectively removes hardened photoresist which is not soluble in the wet strip)
 - a. 50 sccm oxygen, 300 mT, 300 W for 5 minutes
3. Wet strip
 - a. 30 min in Baker PRS 3000 (standard 2-bath method)
 - b. Rinse in DI water 5 times
 - c. Blow dry with nitrogen
4. Inspect
 - a. If there is residue remaining after wet strip, repeat oxygen plasma clean and wet strip until there is no residue

Native Oxide Removal

Use appropriate caution and labware with HF / BHF.

1. Dilute HF approximately 50:1 mix by volume
(Typically mixed in a 600 ml polyethylene beaker with 600 ml water and small amount of HF)
2. Repeatedly dunk wafer until water zips off the back indicating that native oxide is removed
3. Rinse in DI water 5 times
(failure to rinse completely may cause problems in the next photolithography step)
4. Blow dry (gently) with nitrogen

Metal Layer Photoresist Patterning (METAL mask)

1. Warm up the hotplate to 110° C
2. Dehydration
 - a. 120 °C in convection oven for 20 min

3. Vapor prime
 - a. Process immediately after dehydration bake
 - b. 10 min. in priming box with HMDS:Xylene in 1:1 ratio in the glass dish
 - c. Use approximately 12 drops of each, total
4. Spin-coat negative tone lift-off photoresist
 - a. AZ nLOF 2070 target thickness 2 to 5 μm coverage over 10 μm ridge / trench
4000 RPM, 60 sec, low acceleration setting, acceleration = 0
5. Softbake
 - a. Verify temperature with spot-check thermometer ($\pm 2^\circ\text{C}$)
 - b. Hot-plate 110°C for 60 seconds exactly
 - c. Let cool 5 min
6. Mask Exposure
 - a. Warm up UV lamp by performing two 10 sec. exposures with no wafer
 - b. Load Biomarker Test project METAL mask
Position mask with METAL text on top (i.e. away from you when mask is loaded)
 - c. Carefully adjust height setting
(Good contact is important to properly develop sidewalls)
 - d. Align to the corresponding mask alignment mark on wafer
 - e. Expose each wafer for 3.20 sec @ 25 mW/cm^2
7. Post Exposure Bake
 - a. Hot-plate 110°C for 60 seconds exactly
 - b. Let cool 5 min
8. Develop
 - a. AZ 300 MIF developer full strength
 - b. Submerge for 2 minutes and agitate with gentle swirling motion
9. Rinse & dry
 - a. Rinse in DI water 5 times
 - b. Blow dry with nitrogen
10. Inspection (optical microscope)
 - a. CD 2 μm lines should be visible as 1 to 3 μm lines on top of ridges
Corners of ridges should be covered with photoresist
 - b. If failure, strip in Shipley Microposit Remover 1165 and repeat photoresist patterning.

Metallization and Lift-Off

1. Using e-beam evaporator:
500 \AA (50 nm, 0.050 μm) Chrome

2000 Å (200 nm, 0.200 μm) Gold

100 Å (10 nm, 0.010 μm) Chrome

(Note: titanium cannot be substituted for chrome due to HF release step)

2. Lift-off

- a. Load wafers into cassette upside down, and leave a slot open between them.

Also load a blank wafer in the bottom which serves to protect the surface of the wafer above it from strong fluid flow during agitation and rinsing.

- b. 2 hours in heated Shipley Microposit Remover 1165
(1 hour in first bath, 1 hour in second bath)

Note that positive resist strippers are incompatible with AZ nLOF 2070.

- c. Rinse in DI water 5 times
- d. Carefully blow dry with nitrogen

3. Residue removal

(AZ nLOF 2070 produces reliable undercut, but may leave some residue after stripping)

- a. 50 sccm oxygen, 300 mT, 300 W for 3 minutes

Oxide Pre-release Etch

Use appropriate caution and labware with HF / BHF.

This vapor HF etching technique is based on:

Y. Fukuta, H. Fujita, H. Toshiyoshi. "Vapor Hydrofluoric Acid Sacrificial Release Technique for Micro Electro Mechanical Systems Using Labware." *Japanese Journal of Applied Physics*. Vol. 42, Pt. 1, No. 6A, pp. 3690–3694, 2003.

1. Prepare "wafer lid"

- a. Using circular cutouts made from Bytac (PTFE/vinyl) surface protective film,
sandwich the wafer between two layers
- b. The back side will be completely covered,
and the front side will be exposed through the circular window

2. Add approximately 5-10 ml of 50% HF to the bottom of a 600 ml polyethylene beaker

3. Place the "wafer lid" on top of the beaker

4. Heat the back side of the wafer using a halogen or incandescent light

- a. The backside is maintained at approximately 55 °C
- b. The wafer side is approximately 40 °C

- c. Temperature of the wafer affects the etch rate:
 - too low: etch rate is fast but non-uniform / condensation forms on wafer
 - too high: etch rate is slow / no condensation on wafer
- 5. Wait approximately 20 minutes for 2 μm of buried oxide to be etched through
Note that some small structures are now released and are very fragile
- 6. Rinse **carefully** in DI water 5 times
(failure to rinse completely may cause problems in the next photolithography step)
- 7. Blow dry **gently** with nitrogen

Insulation Layer Photoresist Patterning (ISOLATION2 mask)

Areas must be free from oxide and native oxide in order for SU-8 to adhere to substrate.

1. Warm two hotplates: one hotplate to 100° C, one hotplate to 70° C
2. Dehydration
 - a. 120 °C in convection oven for 20 min
3. Spin-coat negative tone photopatternable epoxy
 - a. SU-8 3010 target thickness 1 to 2 μm coverage over 10 μm ridge / trench
3000 RPM, 60 sec, low acceleration setting, acceleration = 0
 - b. Edge bead removal with Acetone squeeze bottle at 700 RPM (30 sec)
4. Softbake
 - a. Verify temperature with spot-check thermometer ($\pm 2^\circ\text{C}$)
 - b. Place wafer on 4-inch diameter, 2mm thick aluminum block
 - c. Hot-plate 70° C for 60 seconds
 - d. Hot-plate 100° C for 60 seconds
 - e. Hot-plate 70° C for 60 seconds
 - f. Let cool 4 min
5. Mask Exposure
 - a. Warm up UV lamp by performing two 10 sec. exposures with no wafer
 - b. Load Biomarker Test project ISOLATION2 mask
Position mask with ISOLATION2 text on top (i.e. away from you when mask is loaded)
 - c. Carefully adjust height setting
 - d. Align to the corresponding mask alignment mark on wafer
Use HP mode to ensure straight sidewalls.
Note that alignment is critical at this step for functional actuators.
 - e. Using dedicated UV filter for SU8,
expose each wafer for 18.00 sec @ 25 mW/cm²
6. Post Exposure Bake

- a. Place wafer on 4-inch diameter, 2mm thick aluminum block
 - b. Hot-plate 70° C for 60 seconds
 - c. Hot-plate 100° C for 60 seconds
 - d. Hot-plate 70° C for 60 seconds
 - e. Let cool 4 min
7. Develop
 - a. SU-8 Developer full strength
Typically, use 200 ml in 2000 ml beaker
 - b. Submerge for 60 seconds and gently swirl
 8. Dry
 - a. Gently blow dry with nitrogen pointed at the center of the wafer
 - b. DO NOT rinse in DI water
 9. Rinse & spin
 - a. Place wafer on spin-coater
 - b. Using small pipette cover wafer with a puddle of fresh SU-8 developer, and wait 10 seconds.
 - c. Spin at 1500 RPM for 60 seconds to dry
 10. Inspection (optical microscope)
 - a. The trenches between the actuator electrodes should be clear with no residue.
The vias for etch release should also be clear of residue.
 - b. If failure, SU-8 can be slowly stripped with oxygen plasma RIE as long as it has not been hardbaked.

Clean & Harden

1. 30 second oxygen plasma descum in RIE
50 sccm oxygen, 300W power, 300 mT pressure
2. Hardbake 120 °C dehydration oven for 15 minutes

Protection Layer & Wafer Dicing

1. Dehydration
 - a. 120 °C in convection oven for 20 min
2. Vapor prime
 - a. Process immediately after dehydration bake
 - b. 10 min. in priming box with HMDS:Xylene in 1:1 ratio in the glass dish
 - c. Use approximately 12 drops of each, total
3. Spin-coat positive tone photoresist as protective layer
 - a. AZ 9260 target thickness 5 μm coverage over 10 μm ridge / trench
3000 RPM, 60 sec, low acceleration setting, acceleration = 20

4. Softbake
 - a. Convection oven 95° C for 15 min
 - b. Let cool / rehydrate 15 min
(AZ 9260 may require much longer rehydration times if humidity is low)
5. Flood Exposure
 - a. Warm up UV lamp by performing two 10 sec. exposures with no wafer
 - b. Flood expose each wafer three times for 10 seconds at 25 mW/cm² with a 60 second wait between exposures
Note: nitrogen bubbles will form in resist if single dose is too high
6. Wafer Dicing
 - a. Cut the wafer using 100 µm saw blade and use 4.000 mm for X-axis and Y-axis index
7. Remove resist
 - a. Puddle develop for 6-10 minutes in AZ 400K 1:4 mix with DI water
 - b. **Carefully** handle wafer during rinsing, it will easily break along dicing lines

Device Release

Use appropriate caution and labware with HF / BHF.

1. Prepare “wafer lid”
 - a. Using circular cutouts made from Bytac (PTFE/vinyl) surface protective film,
sandwich the wafer between two layers
 - b. The back side will be completely covered,
and the front side will be exposed through the circular window
2. Add approximately 5-10 ml of 50% HF to the bottom of a 600 ml polyethylene beaker
3. Place the “wafer lid” on top of the beaker
4. Heat the back side of the wafer using a halogen or incandescent light
 - a. The backside is maintained at approximately 55 °C
 - b. The wafer side is approximately 40 °C
 - c. Temperature affects etch rate:
too low: etch rate is fast but non-uniform / condensation forms on wafer
too high: etch rate is slow / no condensation on wafer
5. Wait approximately 60 minutes for 8 µm of undercut to release silicon structures
6. Rinse **carefully** in DI water
7. Rinse **carefully** with IPA
8. Blow dry **gently** with nitrogen

Prepare for Packaging

1. Free individual dies
 - a. Gently break wafer along dicing lines
 - b. For smaller pieces, grasp group of dies along edges using two tweezers
 - c. Gently pull tweezers opposite directions and bend. Dies should break apart easily.
2. Clean and dry
 - a. Rinse individual die thoroughly with IPA (avoid squirting bubbles with squeeze bottle which can cause damage)
 - b. Immediately blow dry with nitrogen vertically down on the center of the die.
If the die is clean, this usually causes the released structures to spring up into their free-standing positions.
 - c. Repeated rinses & blow dry may be necessary
Device sticking is usually due to residue

Addendum: Descum

1. 15 second oxygen plasma treatment in RIE: 50 sccm oxygen, 300W power, approx. 100 mT pressure

Addendum: Dry Strip

1. 5 minute oxygen plasma treatment in RIE: 50 sccm oxygen, 300W power, approx. 300 mT pressure

Appendix V: Fabrication Process – DRIE Configuration

Adixen AMS-100 I-Speeder

STEP 1: 10 D 8MBAR (Thermalization)

Process Time

Start
Unlimited Duration
Wafer temp: 10° C

SH Options

He Pressure: 8E0 mbar

STEP 2: TEMPO 30S 8MBAR (Temporization)

Process Time

Duration: 30 sec

SH Options

He Pressure: 8E0 mbar

STEP 3: LOWROUGHNESS (Process)

Gas

Ramp: none
Pulsed:

	Inactive (sccm)	Active (sccm)	Priority	Duration (sec)
SF6 (1000)	0	200	2	2
C4F8 (400)	0	150	1	1

Power / Pressure

Source Gen. Load: 700 Tune: 790
 SH Gen 1 SH Gen 2
Priority: Regulation Node

Position / Power

	Pressure (mbar)	Position (%)	Source (W)	SH (W)	Power High (W)	Time High (ms)	Power Low (W)	Time Low (ms)
C4F8	-	100	1500	-	80	10	0	90
SF6	-	100	1500	-	-	-	-	-

Process Time

Duration: 5 min, 0 sec

Stop on process time

EPD

Maintain plasma

SH Options

He Pressure: 8E0 mbar

SH Position: 200.0 mm

Etch Rate Characterization

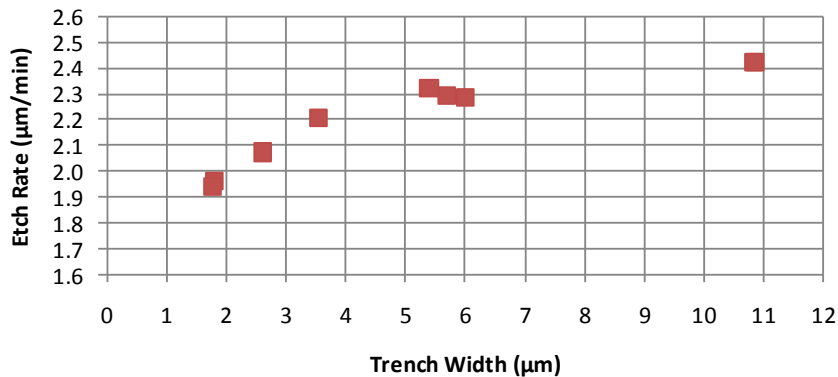


Figure 150: Etch rate on a <100> silicon wafer as a function of trench width. OCG 825 photoresist was used as an etch mask with the LOWROUGHNESS process described above.

Appendix VI: Measured Force Sensor Transducer Widths

All measurements made with a LEO 1550 VP scanning electron microscope (SEM).

Table 61: Measured force sensor transducer widths (left side).

Die	TD-Left-1 (nm)	TD-Left-2 (nm)	TD-Left-3 (nm)	TD-Left-4 (nm)	Ave-Left (nm)
A38	1374	1057	1189	1115	1184
A39	1126	927	940	940	983
A40	1136	979	984	928	1007
A45	1181	1270	1277	1362	1273
A46	1409	1273	1345	1248	1319
A48	893	710	1060	934	899
B49	869	983	782	972	901
B51	852	944	842	809	862
B53	853	768	971	963	889
B55	1190	1043	1104	1093	1108
B59	916	968	953	973	952
B61	1361	1292	1243	1322	1305
B63	1064	1140	1087	1218	1127
D71	980	902	914	1177	994
D72	1097	998	1096	1181	1093
D74	1117	1064	1012	1209	1101
D75	1112	1110	1043	1251	1129
D77	1081	1150	1195	1177	1151
D78	1100	982	1223	950	1064
D80	1102	1050	1130	1176	1115
D83	658	665	688	608	655
D84	998	984	965	1253	1050

Table 62: Measured force sensor transducer widths (right side).

Die	TD-Right-1 (nm)	TD-Right-2 (nm)	TD-Right-3 (nm)	TD-Right-4 (nm)	Ave-Right (nm)
A38	1305	1178	1115	1279	1219
A39	1077	1114	911	1003	1026
A40	1062	1000	1170	1037	1067
A45	1204	1080	1339	1096	1180
A46	1236	1334	1272	1333	1294
A48	896	921	878	1108	951
B49	918	865	968	696	862
B51	953	896	810	839	875
B53	872	710	880	946	852
B55	1077	1064	975	1067	1046
B59	1060	934	830	1076	975
B61	1368	1315	1164	1326	1293
B63	1211	1124	1153	1097	1146
D71	1102	922	985	902	978
D72	1115	1042	1049	1075	1070
D74	1191	1156	1205	1084	1159
D75	1186	1024	1178	1018	1102
D77	1171	1093	1233	1020	1129
D78	1272	1193	1275	1022	1191
D80	1098	1012	1015	1047	1043
D83	484	-	-	-	484
D84	1108	915	1068	975	1017

Table 63: Measured force sensor transducer widths (summary).

Die	Average (nm)	Range (nm)	SD (nm)	MAX (nm)	MIN (nm)
A38	1202	317	108.9	1374	1057
A39	1005	215	88.7	1126	911
A40	1037	242	82.4	1170	928
A45	1226	282	104.6	1362	1080
A46	1306	173	58.7	1409	1236
A48	925	398	120.7	1108	710
B49	882	287	101.5	983	696
B51	868	144	56.5	953	809
B53	870	261	93.4	971	710
B55	1077	216	60.6	1190	975
B59	964	246	78.5	1076	830
B61	1299	204	67.1	1368	1164
B63	1137	154	55.9	1218	1064
D71	986	276	102.4	1177	902
D72	1082	183	55.0	1181	998
D74	1130	197	72.5	1209	1012
D75	1115	233	84.9	1251	1018
D77	1140	213	69.9	1233	1020
D78	1127	325	131.2	1275	950
D80	1079	164	57.8	1176	1012
D83	621	204	81.8	688	484
D84	1033	338	107.4	1253	915

Appendix VII: Measured Spring Constants

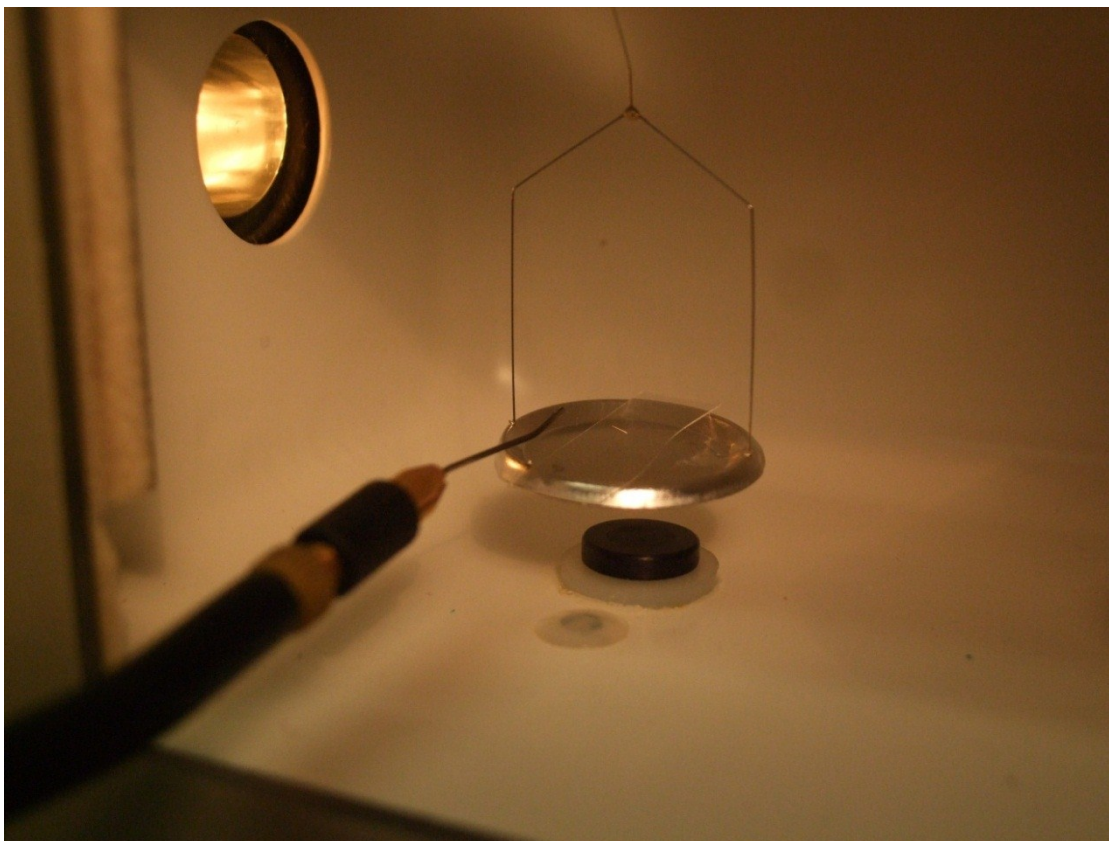


Figure 151: The spring constant of a specially prepared fine gold wire is verified using a CAHN C-30 microbalance in 0.000 mg range setting.

Table 64: Measured weights for reference cantilever No. 5 at various positions.

No. 5		Weight (mg)								
Position (μm)	1	2	3	4	5	6	7	8	9	10
0	0.051	0.060	0.052	0.053	0.041	0.044	0.045	0.058	0.054	0.046
10	0.141	0.147	0.144	0.145	0.139	0.136	0.141	0.142	0.142	0.149
0	-0.107	-0.098	-0.103	-0.113	-0.098	-0.106	-0.101	-0.117	-0.106	-0.112
20	0.063	0.078	0.075	0.082	0.079	0.081	0.077	0.085	0.080	0.078
0	-0.011	-0.017	-0.016	-0.012	-0.011	-0.014	-0.011	-0.012	-0.015	-0.010
30	0.268	0.262	0.265	0.260	0.268	0.267	0.255	0.265	0.264	0.243

Table 65: Measured forces (converted from above) for reference cantilever No. 5 at various positions.

No. 5		Force (μN)									
Position (μm)	1	2	3	4	5	6	7	8	9	10	
0	0.500	0.588	0.510	0.520	0.402	0.431	0.441	0.569	0.530	0.451	
10	1.383	1.442	1.412	1.422	1.363	1.334	1.383	1.393	1.393	1.461	
0	-1.049	-0.961	-1.010	-1.108	-0.961	-1.039	-0.990	-1.147	-1.039	-1.098	
20	0.618	0.765	0.735	0.804	0.775	0.794	0.755	0.834	0.785	0.765	
0	-0.108	-0.167	-0.157	-0.118	-0.108	-0.137	-0.108	-0.118	-0.147	-0.098	
30	2.628	2.569	2.599	2.550	2.628	2.618	2.501	2.599	2.589	2.383	

Table 66: Measured weights for reference cantilever No. 9 at various positions.

No. 9		Weight (mg)									
Position (μm)	1	2	3	4	5	6	7	8	9	10	
0	0.039	0.048	0.037	0.043	0.035	0.042	0.044	0.042	0.045	0.040	
10	0.075	0.065	0.061	0.075	0.069	0.073	0.068	0.069	0.072	0.061	
0	0.041	0.040	0.048	0.045	0.044	0.048	0.032	0.044	0.050	0.049	
20	0.085	0.097	0.105	0.095	0.105	0.092	0.102	0.094	0.103	0.105	
0	0.001	-0.002	0.001	-0.004	-0.003	0.002	-0.002	-0.001	0.001	0.003	
30	0.086	0.075	0.082	0.088	0.085	0.082	0.088	0.092	0.081	0.090	

Table 67: Measured forces (converted from above) for reference cantilever No. 9 at various positions.

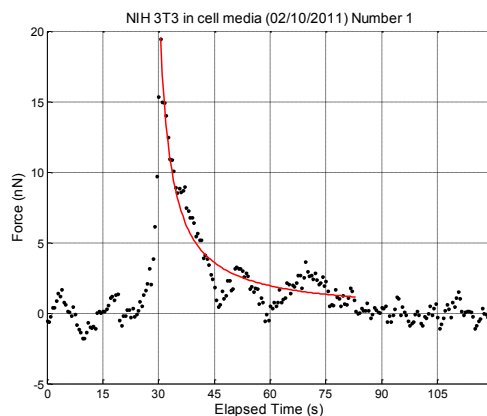
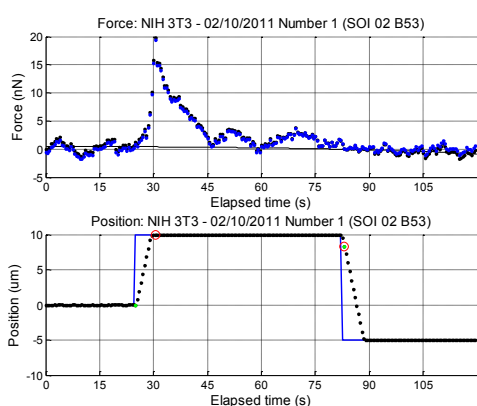
No. 9		Force (μN)									
Position (μm)	1	2	3	4	5	6	7	8	9	10	
0	0.382	0.471	0.363	0.422	0.343	0.412	0.431	0.412	0.441	0.392	
10	0.735	0.637	0.598	0.735	0.677	0.716	0.667	0.677	0.706	0.598	
0	0.402	0.392	0.471	0.441	0.431	0.471	0.314	0.431	0.490	0.481	
20	0.834	0.951	1.030	0.932	1.030	0.902	1.000	0.922	1.010	1.030	
0	0.010	-0.020	0.010	-0.039	-0.029	0.020	-0.020	-0.010	0.010	0.029	
30	0.843	0.735	0.804	0.863	0.834	0.804	0.863	0.902	0.794	0.883	

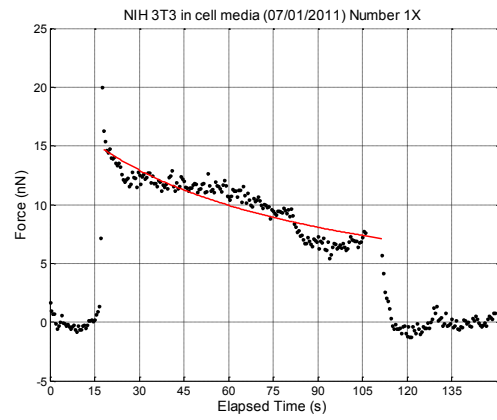
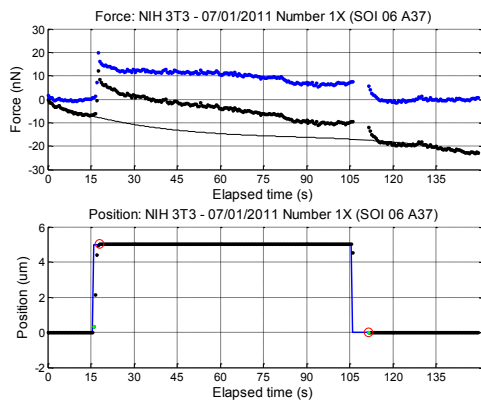
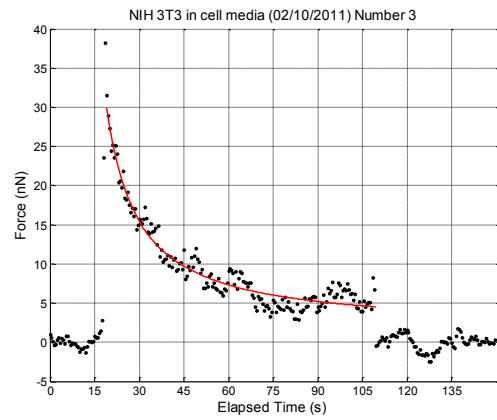
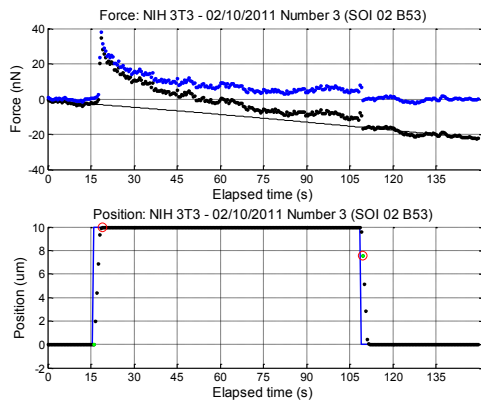
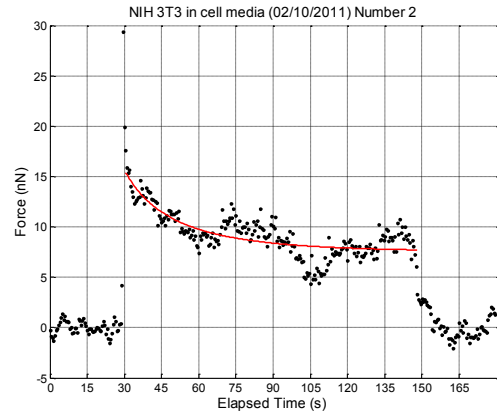
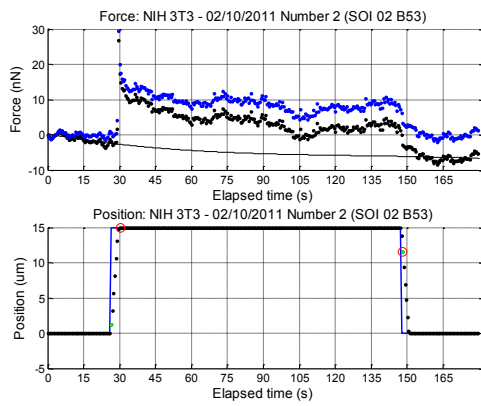
Appendix VIII: NIH3T3 Test Data

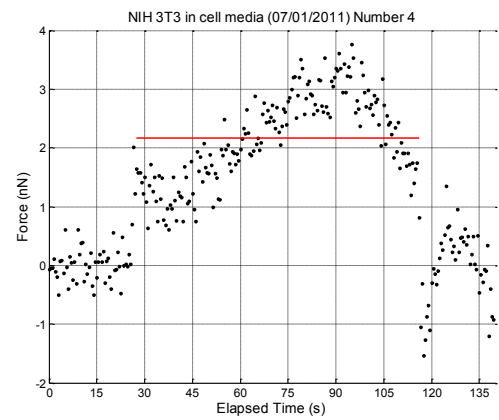
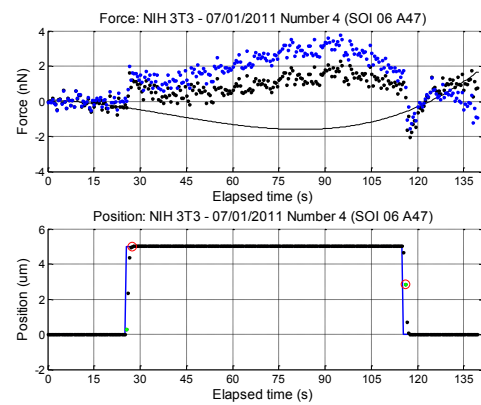
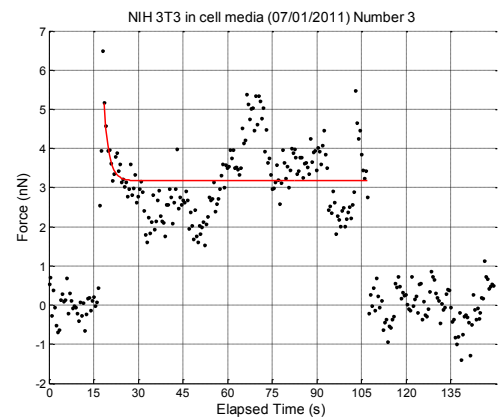
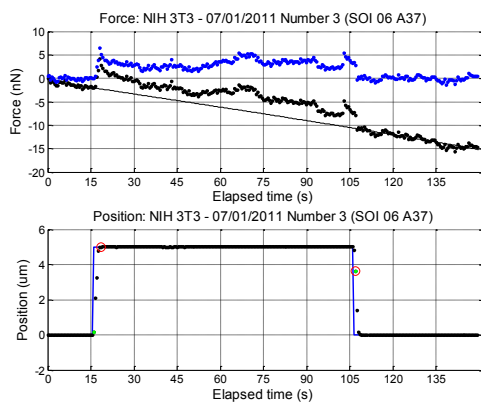
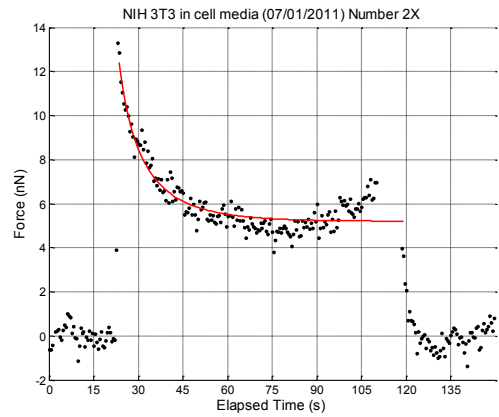
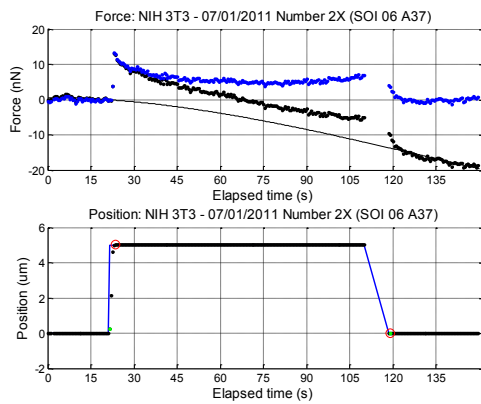
Raw Data and Model Fit Figures

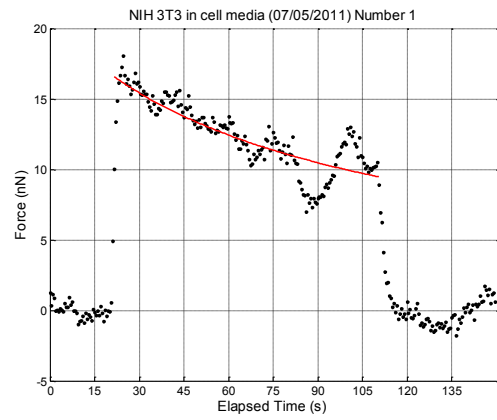
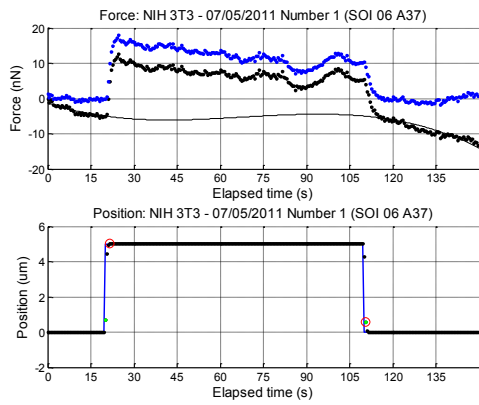
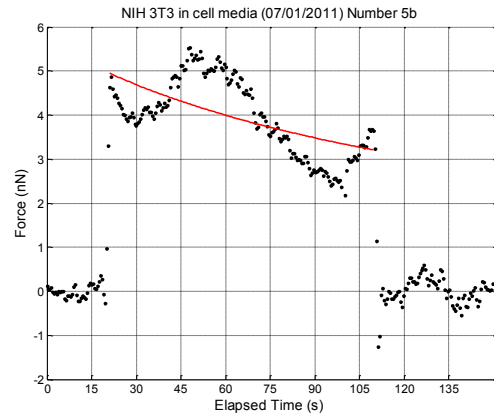
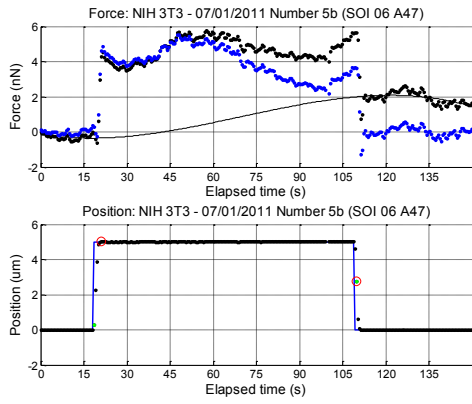
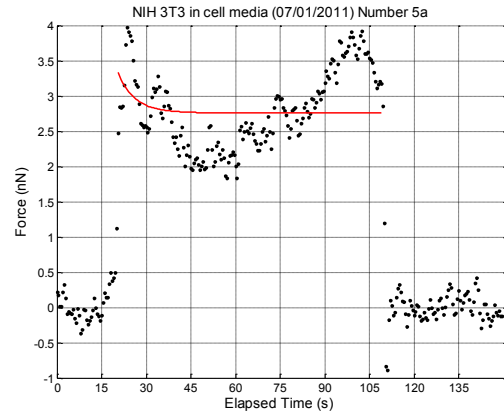
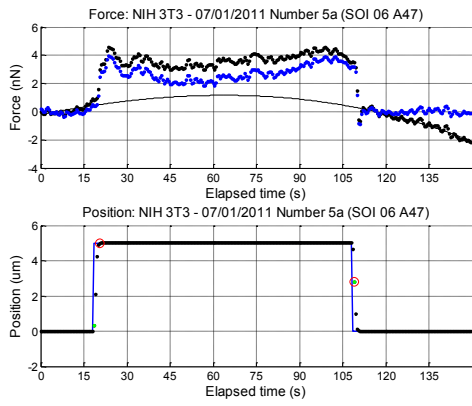
Measurements tagged with letters (e.g. Number 1A, 1B) indicated multiple measurements on the same cell.

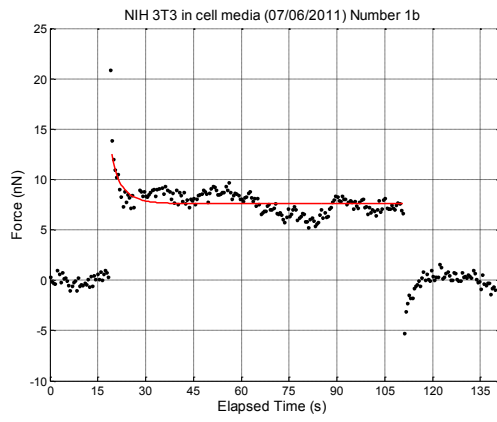
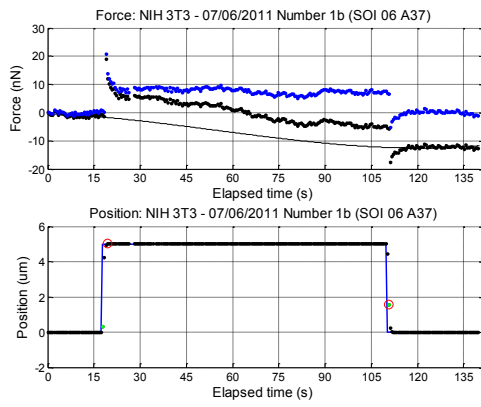
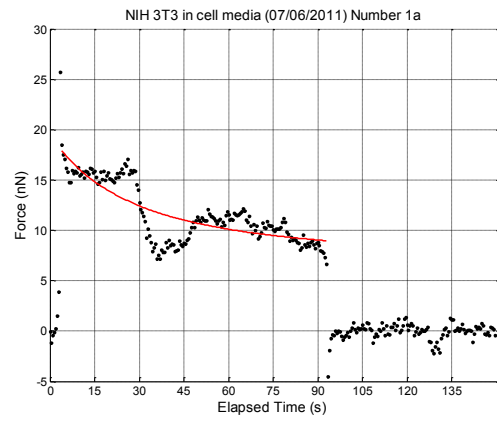
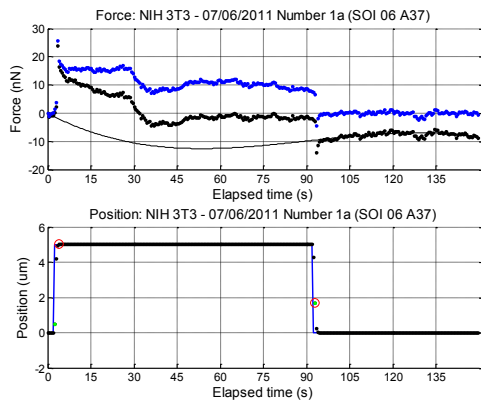
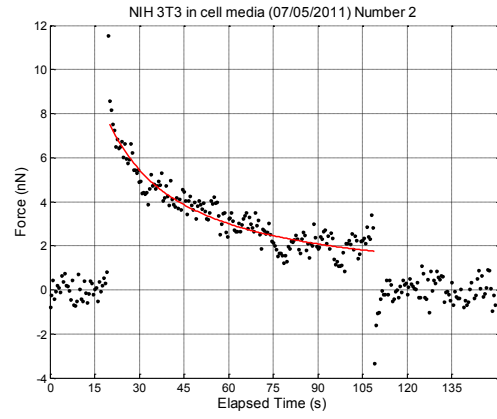
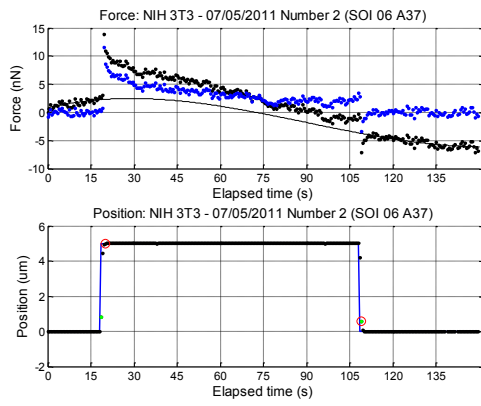
In the tests results below, the left-hand figures show a chart split into two parts: the measured force (top) and the recorded position of the shuttle (bottom). The black dots show the data as recorded, the black line shows the trend line, and the blue dots show the data after the parabolic trend has been removed in order that the regions before and after the test appear flat. The right-hand figures show the force data with low frequency drift removed (this is the same as the blue plot on the left), and overlaid is the visco-elastic model fit (red) (see equation 82 above).

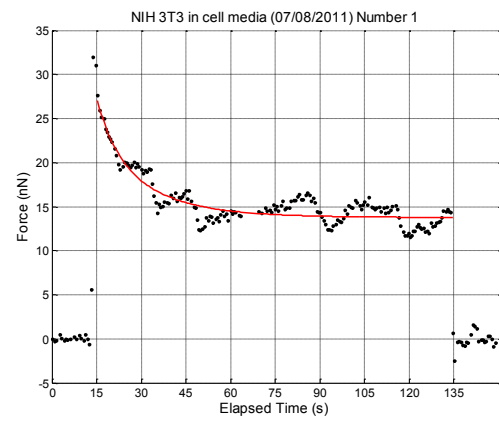
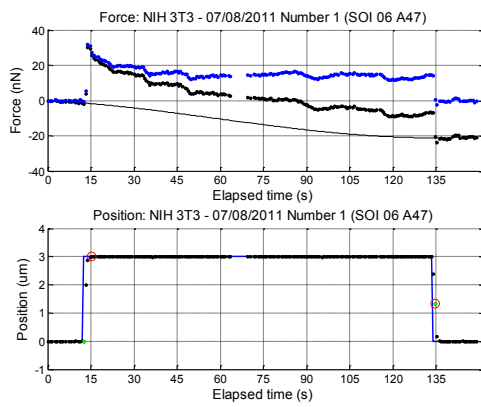
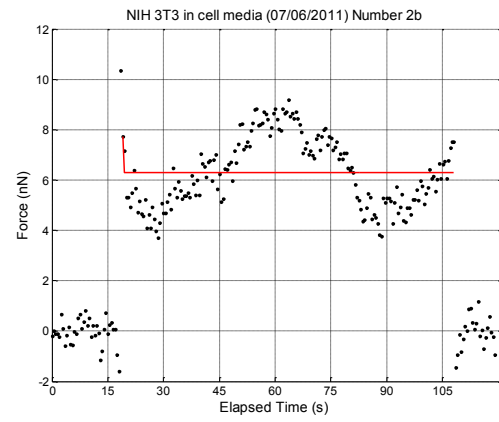
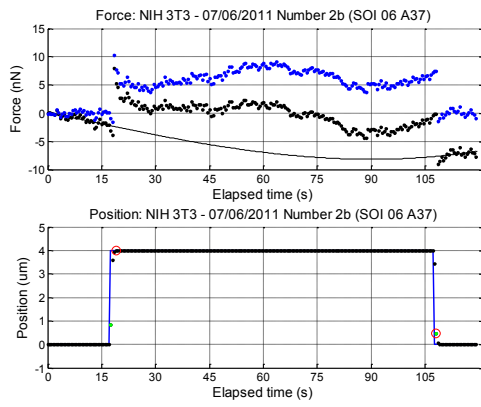
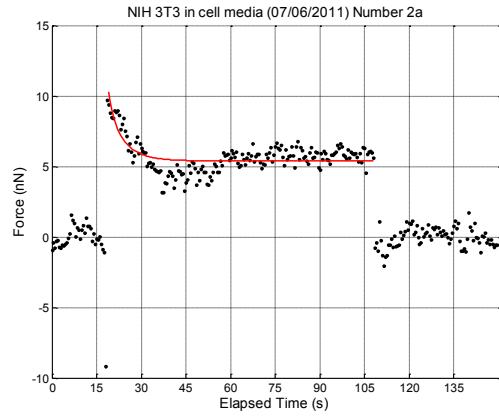
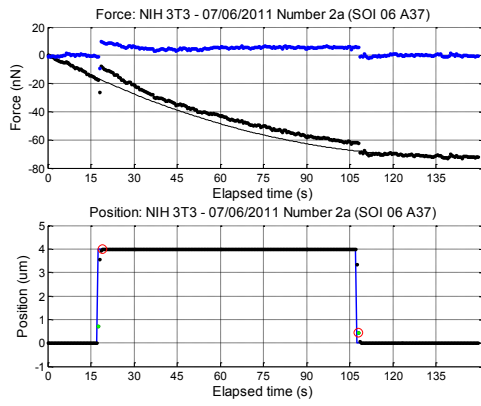


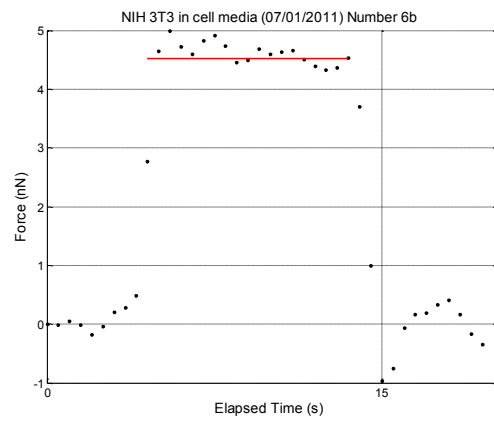
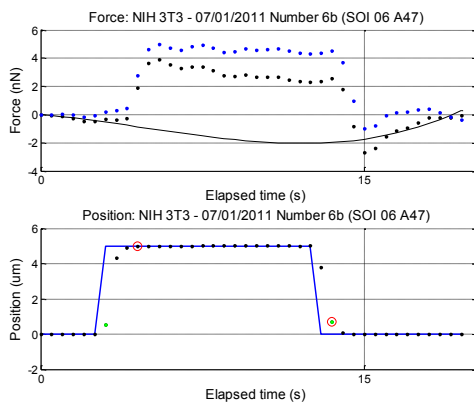
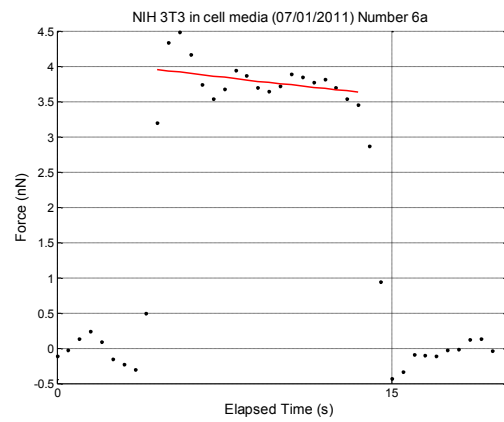
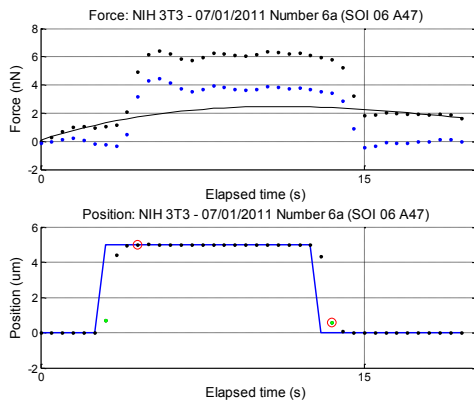
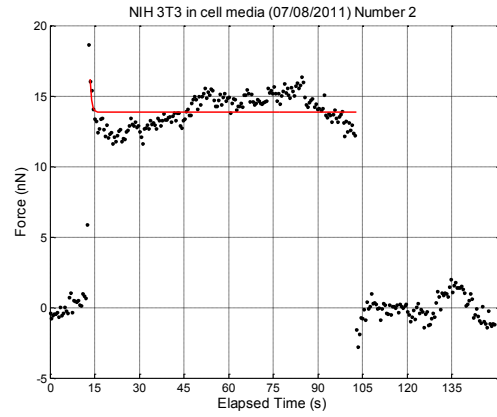
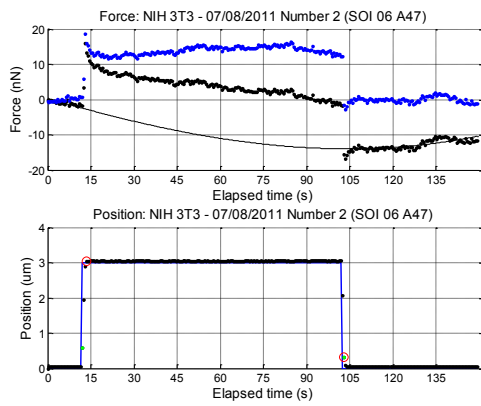


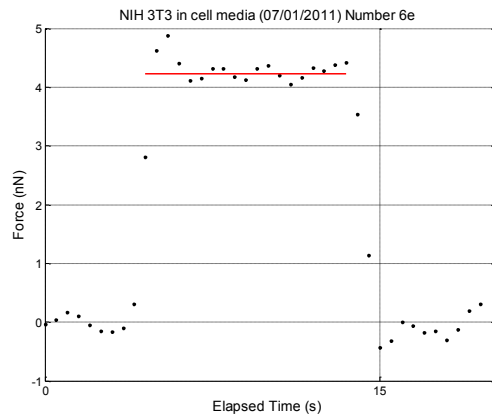
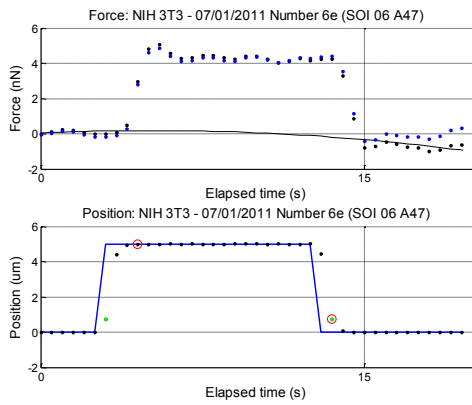
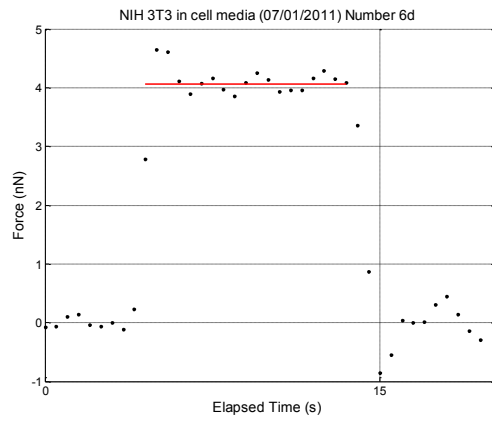
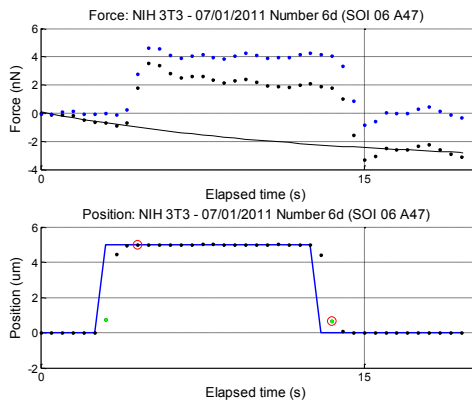
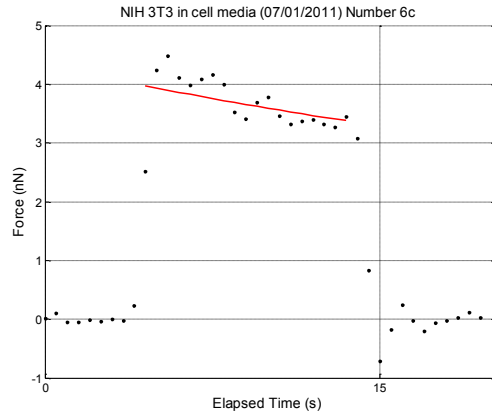
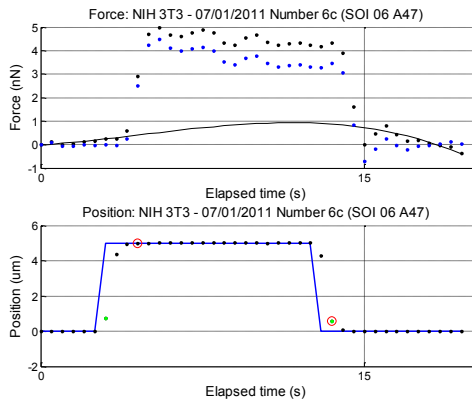












Tabulated Model Fit Parameters

Measurements tagged with letters (e.g. Number 1a, 1b) indicated multiple measurements on the same cell.

The one-pixel resolution for optical measurements is $0.335 \mu\text{m} / \text{px}$.

Table 68: NIH3T3 fit to pure elastic model.

Device	Timestamp	Diameter (μm)	ΔD (μm)	E (Pa)	Tag
SOI 06 A47	20110701_160027	15.067	4.687	76.5	Number 6A
SOI 06 A47	20110701_160027	15.067	4.687	91.3	Number 6B
SOI 06 A47	20110701_160027	15.067	4.687	74.0	Number 6C
SOI 06 A47	20110701_160027	15.067	4.687	82.0	Number 6D
SOI 06 A47	20110701_160027	15.067	4.687	85.5	Number 6E
Average				81.9	
Std. Dev.				6.9	
Count (N)				5	

Table 69: NIH3T3 fit to pure elastic model.

Device	Timestamp	Diameter (μm)	AD (μm)	E (Pa)	Tag
SOI 02 B53	20110210_185900	16.600	3.000	128.1	Number 1
SOI 02 B53	00000000_000000	18.600	4.000	211.7	Number 2
SOI 02 B53	20110210_192600	18.300	4.330	186.8	Number 3
SOI 06 A37	20110701_171305	17.076	4.687	192.6	Number 1X
SOI 06 A37	20110701_171305	15.402	2.344	340.4	Number 2X
SOI 06 A37	20110701_172641	18.750	4.353	64.9	Number 3
SOI 06 A47	20110701_155137	14.397	4.353	50.0	Number 4
SOI 06 A47	20110701_155137	15.067	5.022	50.9	Number 5A
SOI 06 A47	20110701_155137	15.737	5.022	70.4	Number 5B
SOI 06 A37	20110705_185423	16.406	4.687	238.6	Number 1
SOI 06 A37	20110705_190502	17.411	3.348	103.0	Number 2
SOI 06 A37	20110706_163333	15.402	4.687	230.8	Number 1A
SOI 06 A37	20110706_163333	14.732	4.687	159.2	Number 1B
SOI 06 A37	20110706_165802	14.732	3.348	190.9	Number 2A
SOI 06 A37	20110706_165802	13.728	2.009	476.4	Number 2B
SOI 06 A47	20110708_120808	16.071	3.348	498.7	Number 1
SOI 06 A47	20110708_122341	16.406	3.683	385.7	Number 2
Average				210.5	
Std. Dev.				140.7	
Count (N)					17

Table 70: NIH3T3 fit to standard linear solid model.

Device	Timestamp	Diameter (μm)	ΔD (μm)	E_1 (Pa)	E_2 (Pa)	Viscosity (Pa-s)	Tau (s)	R^2	Tag
SOI 02 B53	20110210_185900	16.600	3.000	0.0	979.6	3.18E+03	3.25	85.9%	Number 1
SOI 02 B53	00000000_000000	18.600	4.000	232.4	240.9	4.29E+03	17.8	62.8%	Number 2
SOI 02 B53	20110210_192600	18.300	4.330	72.8	750.6	7.65E+03	10.2	93.6%	Number 3
SOI 06 A37	20110701_171305	17.076	4.687	0.0	371.9	3.27E+04	87.9	74.8%	Number 1X
SOI 06 A37	20110701_171305	15.402	2.344	391.9	542.5	3.58E+03	6.59	83.6%	Number 2X
SOI 06 A37	20110701_172641	18.750	4.353	85.5	53.5	65.4	1.22	5.2%	Number 3
SOI 06 A47	20110701_155137	14.397	4.353	66.6	0.0	2.37E-06	1.95	0.0%	Number 4
SOI 06 A47	20110701_155137	15.067	5.022	67.0	13.9	72.5	5.22	3.1%	Number 5A
SOI 06 A47	20110701_155137	15.737	5.022	0.0	117.5	1.93E+04	164	32.3%	Number 5B
SOI 06 A37	20110705_185423	16.406	4.687	42.7	384.9	3.95E+04	103	69.4%	Number 1
SOI 06 A37	20110705_190502	17.411	3.348	5.5	306.8	7.89E+03	25.7	84.3%	Number 2
SOI 06 A37	20110706_163333	15.402	4.687	204.4	273.1	7.58E+03	27.7	64.4%	Number 1A
SOI 06 A37	20110706_163333	14.732	4.687	206.9	135.2	360	2.66	34.2%	Number 1B
SOI 06 A37	20110706_165802	14.732	3.348	242.9	220.8	731	3.31	44.6%	Number 2A
SOI 06 A37	20110706_165802	13.728	2.009	634.4	143.6	3.42	0.0238	0.6%	Number 2B
SOI 06 A47	20110708_120808	16.071	3.348	594.6	572.9	5.77E+03	10.1	75.4%	Number 1
SOI 06 A47	20110708_122341	16.406	3.683	513.5	87.0	39.5	0.454	1.4%	Number 2
Average				171.6*	491.5*	12460*	32.5*		
Std. Dev.				207.7*	246.2*	13625*	36.8*		
Count (N)				9*	9*	9*	9*		

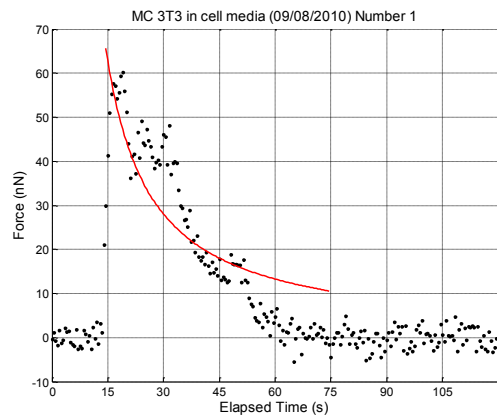
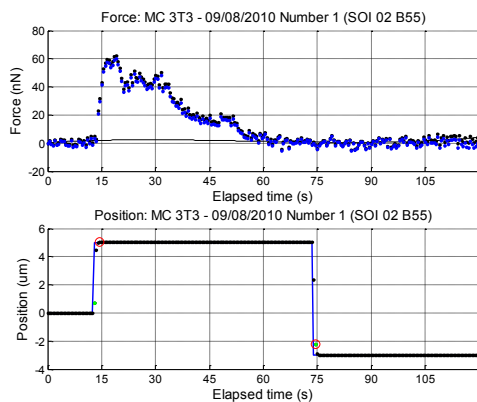
*Excluding values for R^2 values below 50%

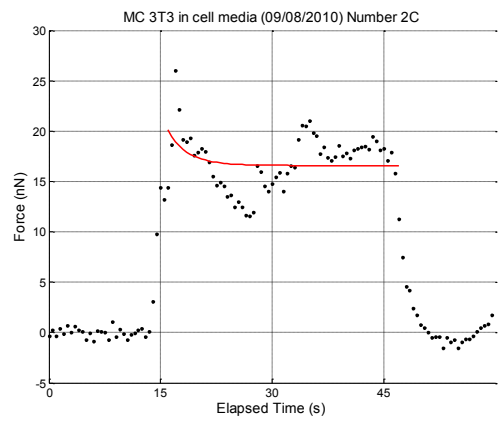
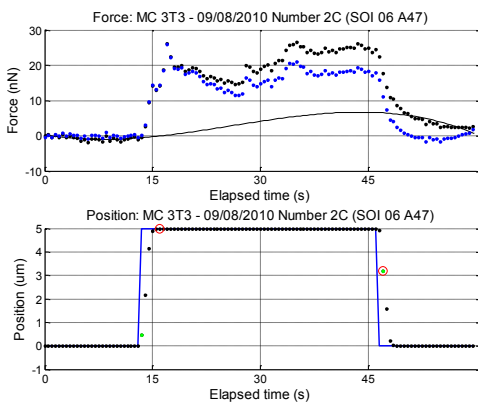
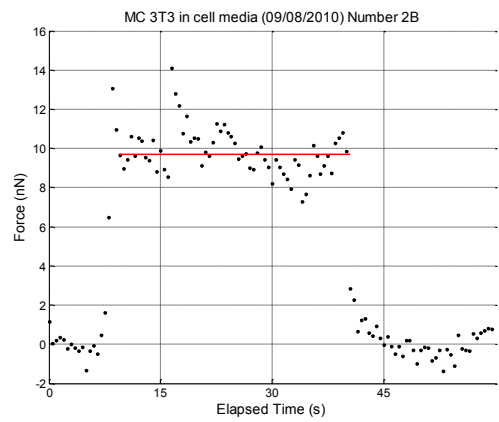
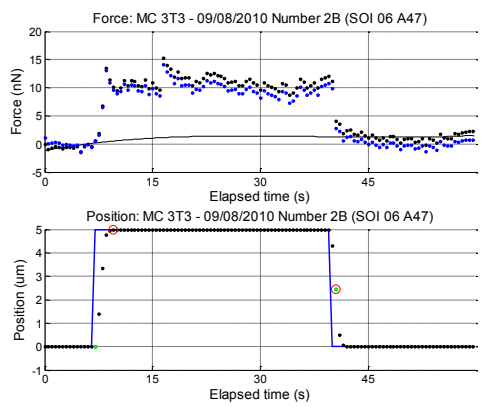
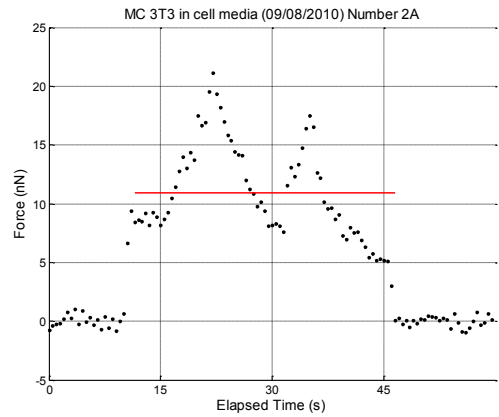
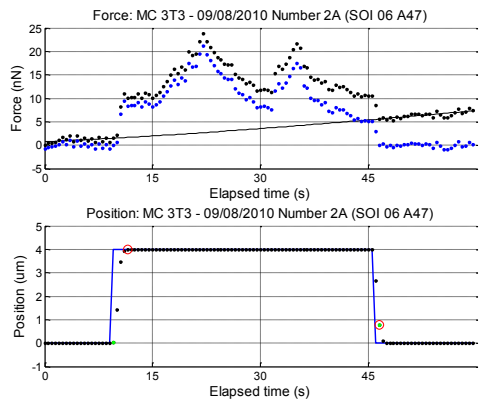
Appendix IX: MC3T3 Test Data

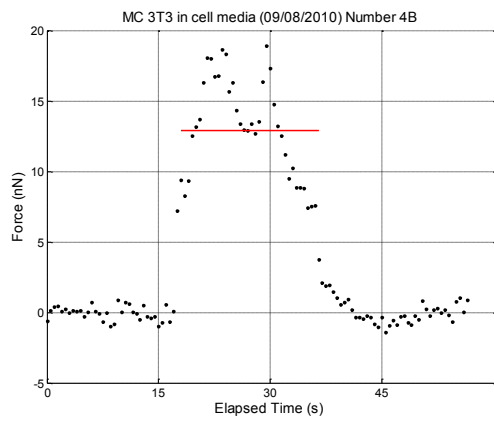
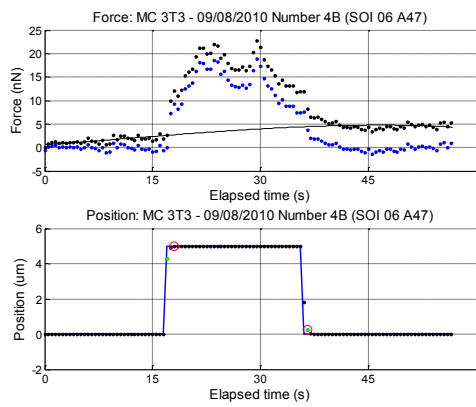
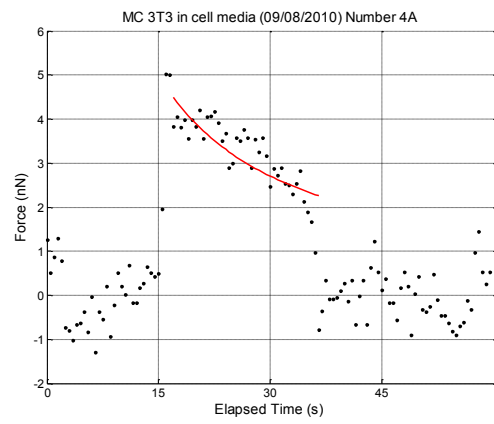
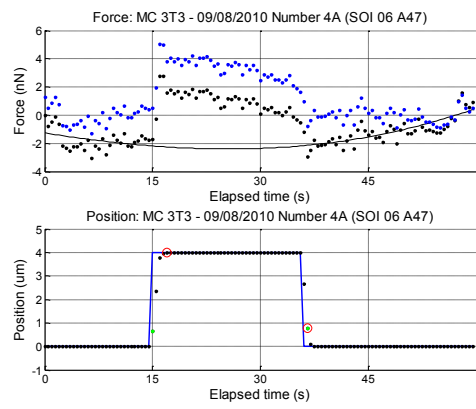
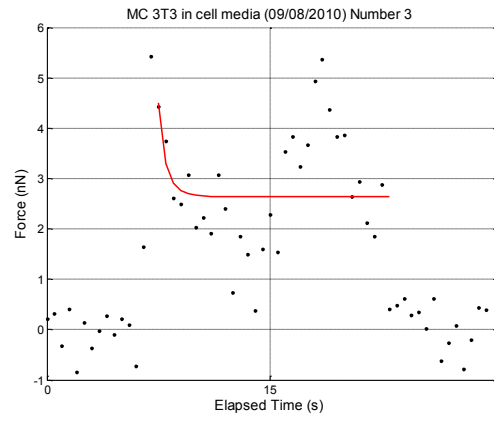
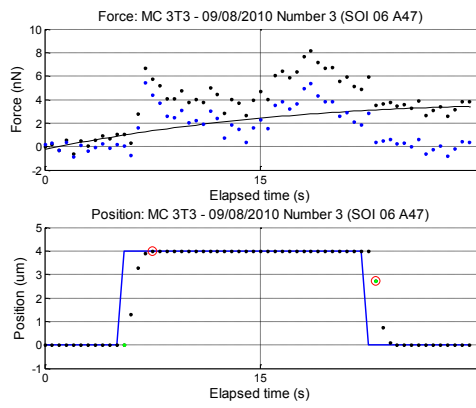
Raw Data and Model Fit Figures

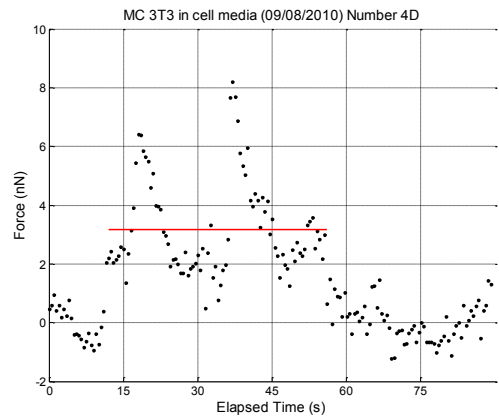
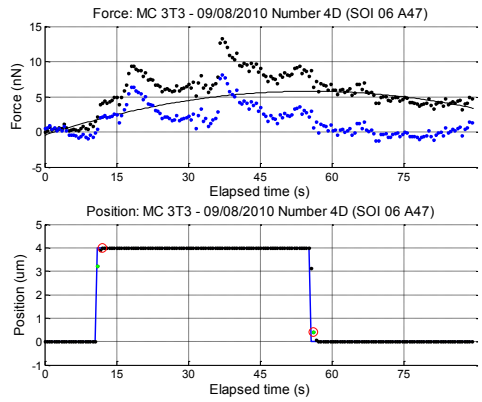
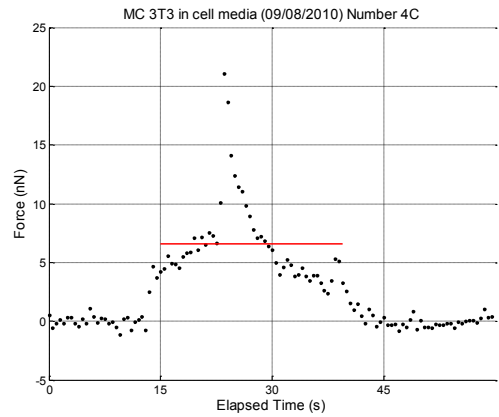
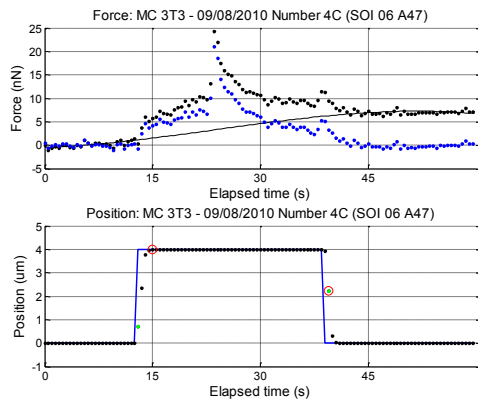
Measurements tagged with letters (e.g. Number 1a, 1b) indicated multiple measurements on the same cell.

In the tests results below, the left-hand figures show a chart split into two parts: the measured force (top) and the recorded position of the shuttle (bottom). The black dots show the data as recorded, the black line shows the trend line, and the blue dots show the data after the parabolic trend has been removed in order that the regions before and after the test appear flat. The right-hand figures show the force data with low frequency drift removed (this is the same as the blue plot on the left), and overlaid is the visco-elastic model fit (red) (see equation 82 above).









Tabulated Model Fit Parameters

Measurements tagged with letters (e.g. Number 1A, 1B) indicated multiple measurements on the same cell.

The one-pixel resolution for optical measurements is $0.335 \mu\text{m} / \text{px}$.

Table 71: MC3T3 fit to pure elastic model.

Device	Timestamp	Diameter (μm)	ΔD (μm)	E (Pa)	Tag
SOI 02 B55	20100908_153535	18.080	4.018	494.2	Number 1
SOI 06 A47	20110602_013459	12.388	3.683	348.8	Number 2A
SOI 06 A47	20110602_013459	12.388	4.018	272.2	Number 2B
SOI 06 A47	20110602_013459	12.723	4.687	371.6	Number 2C
SOI 06 A47	20110602_013935	13.728	3.683	82.9	Number 3
SOI 06 A47	20110602_013935	13.728	3.348	109.1	Number 4A
SOI 06 A47	20110602_013935	13.728	3.348	452.9	Number 4B
SOI 06 A47	20110602_013935	13.728	3.683	200.1	Number 4C
SOI 06 A47	20110602_013935	13.393	3.013	132.1	Number 4D
Average				273.8	
Std. Dev.				152	
Count				9	

Table 72: MC3T3 fit to standard linear solid model.

Device	Timestamp	Diameter (μm)	ΔD (μm)	E_1 (Pa)	E_2 (Pa)	Viscosity (Pa-s)	Tau (s)	R^2	Tag
SOI 02 B55	20100908_153535	18.08	4.018	0.0	2034	2.35E+04	11.5	50.1%	Number 1
SOI 06 A47	20110602_013459	12.388	3.683	465.1	0.0	2.49E-05	1.33	0.0%	Number 2A
SOI 06 A47	20110602_013459	12.388	4.018	363	0.0	9.88E-07	1.1	0.0%	Number 2B
SOI 06 A47	20110602_013459	12.723	4.687	486	104.4	248	2.37	6.8%	Number 2C
SOI 06 A47	20110602_013935	13.728	3.683	106.8	75.4	30.3	0.401	7.9%	Number 3
SOI 06 A47	20110602_013935	13.728	3.348	0.0	209.8	4.14E+03	19.7	43.8%	Number 4A
SOI 06 A47	20110602_013935	13.728	3.348	603.9	0.0	1.05E-05	1.57	0.0%	Number 4B
SOI 06 A47	20110602_013935	13.728	3.683	266.8	0.0	8.87E-05	2.81	0.0%	Number 4C
SOI 06 A47	20110602_013935	13.393	3.013	176.1	0.0	1.01E-05	4.93	0.0%	Number 4D
Average				0.0*	1122*	13820*	15.6*		
Std. Dev.				0.0*	1290*	13690*	5.8*		
Count (N)				2*	2*	2*	2*		

*Excluding values for R^2 values below 40%

Publications

Journals

Wenyue Zhang, Markus Gnerlich, Jonathan J Paly, Yaohua Sun, Gaoshan Jing, Arkady Voloshin, Svetlana Tatic-Lucic. "A polymer V-shaped electrothermal actuator array for biological applications." *Journal of Micromechanics and Microengineering*. vol. 18, pp. 075020, 2008. doi: [10.1088/0960-1317/18/7/075020](https://doi.org/10.1088/0960-1317/18/7/075020).

Markus Gnerlich, Susan F. Perry, Svetlana Tatic-Lucic. "A Submersible Piezoresistive MEMS Lateral Force Sensor for Cellular Biomechanics Applications." *Sensors & Actuators A: Physical*, submitted.

Conferences

Markus Gnerlich, Susan F. Perry, Svetlana Tatic-Lucic. "A Submersible Piezoresistive MEMS Lateral Force Sensor for Cellular Biomechanics Applications." *Proceedings of the 16th International Conference on Solid-State Sensors, Actuators and Microsystems*, Beijing (CN), 5-9 June 2011, pp. 2207-2210. doi: [10.1109/TRANSDUCERS.2011.5969365](https://doi.org/10.1109/TRANSDUCERS.2011.5969365).

Yaohua Sun, Yu Wang, Gaoshan Jing, Markus Gnerlich, Susan Fueshko Perry, Filbert Bartoli, Svetlana Tatic-Lucic. "Implementation of Nanoparticles for Patterning Cultured Cells." *Proceedings of the conference EUROSENSORS XXII*, Dresden (DE), 7-10 Sept. 2008, pp. 573-576.

Markus Gnerlich, Wenyue Zhang, Henry Donahue, Arkady Voloshin, Svetlana Tatic-Lucic. "Polymer Electrothermal Microactuator Operating in Deionized Water." *Proceedings of the conference EUROSENSORS XXII*, Dresden (DE), 7-10 Sept. 2008, pp. 708-711.

Markus Gnerlich, Wenyue Zhang, Henry Donahue, Arkady Voloshin, Svetlana Tatic-Lucic. "A Novel MEMS-Based Technology for Experimentally Measuring the Mechanical Properties of Single Living Biological Cells." *2008 SEM XI International Congress & Exposition on Experimental & Applied Mechanics*, Orlando, Florida (USA). 2-5 June 2008.

Svetlana Tatic-Lucic, Markus Gnerlich, Wenyue Zhang, Henry Donahue, Arkady Voloshin. "Towards a micromachined system for mechanical characterization of osteoblasts." *Microwaves, Communications, Antennas and Electronic Systems, 2008. COMCAS 2008. IEEE International Conference on*. Tel-Aviv (IL), 13-14 May 2008, pp. 1-6. doi: [10.1109/COMCAS.2008.4562775](https://doi.org/10.1109/COMCAS.2008.4562775).

Markus Gnerlich, Wenyue Zhang, Henry Donahue, Arkady Voloshin, Svetlana Tatic-Lucic. "Polymer-Based Microsystem for Mechanical Characterization of Cells." *Solid-State Sensors, Actuators, and Microsystems Workshop*. Hilton Head Island, South Carolina (USA), 1-5 June 2008, pp. 386-387.

Wenyue Zhang, Markus Gnerlich, Yaohua Sun, Gaoshan Jing, Jonathan J. Paly, Arkady Voloshin, Svetlana Tatic-Lucic. "Polymer MEMS System for Measuring the Mechanical Modulus of a Biological Cell." *BIODEVICES 2008: Proceedings of the First International Conference on Biomedical Electronics and Devices*, Funchal, Madeira (PT), 28-31 January 2008, vol.2, pp. 146-150.

Gaoshan Jing, Yi Yao, Markus Gnerlich, Susan Perry, Svetlana Tatic-Lucic. "Towards a Multi-Electrode Array (MEA) System for Patterned Neural Networks." *Proceedings of the EUROSENSORS XXIII conference, Procedia Chemistry*, September 2009, vol. 1, pp. 329-332. doi:[10.1016/j.proche.2009.07.082](https://doi.org/10.1016/j.proche.2009.07.082)

Vita

Markus H. Gnerlich was born in Bethlehem, PA, USA in 1976. His parents are Hans R. Gnerlich (Ph.D. Electrical Engineering, Lehigh University) and Karol L. Gnerlich (MFA Painting and Graphics, Pratt Institute). He earned his B.S. in Electrical Engineering in 2005 from the Pennsylvania State University (University Park) with Honors in Bioengineering, and he minored in Bioengineering and Philosophy. While completing his undergraduate degree he spent three years working for Xiomedia, a software startup in New York, NY that catered to the financial services industry. He recently received his M.S. in Electrical Engineering from Lehigh University in 2008 and will receive his Ph.D. in January 2011 under the supervision of Prof. Svetlana Tatic-Lucic. While at Penn State, Mr. Gnerlich was a Schreyer Honors Scholar, and at Lehigh University he was a P.C. Rossin College Doctoral Fellow and the recipient of the Sherman Fairchild Fellowship from 2008 to 2011. Mr. Gnerlich has been active in service to the community, from helping to found the Undergraduate Philosophy Club at Penn State, to serving on various academic committees at Lehigh University, to leading the Graduate Student Senate as President in 2009. He is a member of the Institute of Electrical and Electronics Engineers (IEEE) and Sigma Xi.